



Forschungszentrum Karlsruhe
in der Helmholtz-Gemeinschaft

Wissenschaftliche Berichte
FZKA 6664

Experimental and Computational Results of the QUENCH-06 Test (OECD ISP-45)

**L. Sepold, W. Hering, C. Homann,
A. Miassoedov, G. Schanz, U. Stegmaier,
M. Steinbrück, H. Steiner, J. Stuckert**

**Institut für Materialforschung
Institut für Reaktorsicherheit
Programm Nukleare Sicherheitsforschung**

Februar 2004

Forschungszentrum Karlsruhe

in der Helmholtz-Gemeinschaft

Wissenschaftliche Berichte

FZKA 6664

Experimental and Computational Results of the
QUENCH-06 Test (OECD ISP-45)

L. Sepold, W. Hering, C. Homann, A. Miassoedov, G. Schanz,
U. Stegmaier, M. Steinbrück, H. Steiner, J. Stuckert

Institut für Materialforschung
Institut für Reaktorsicherheit
Programm Nukleare Sicherheitsforschung

Forschungszentrum Karlsruhe GmbH, Karlsruhe

2004

Für diesen Bericht behalten wir uns alle Rechte vor

Forschungszentrum Karlsruhe GmbH
Postfach 3640, 76021 Karlsruhe

Mitglied der Hermann von Helmholtz-Gemeinschaft
Deutscher Forschungszentren (HGF)

ISSN 0947-8620

Zusammenfassung

Experimentelle und analytische Ergebnisse des Versuchs QUENCH-06 (OECD Internationales Standardproblem ISP-45)

In den QUENCH-Versuchen soll der Wasserstoffquellterm bei der Einspeisung von Notkühlwasser in einen trockenen, überhitzten Reaktorkern eines Leichtwasserreaktors (LWR) ermittelt werden. Mit dem Experiment QUENCH-06, das am 13. Dezember 2000 in der QUENCH-Versuchsanlage des Forschungszentrums Karlsruhe durchgeführt wurde, sollte das Verhalten von voroxidierten LWR-Brennstäben während des Abschreckens mit Wasser (Einspeisung von unten) untersucht werden. Der Test QUENCH-06 wurde bis auf die Einspeisung mit Wasser statt des Dampfes ganz ähnlich dem QUENCH-05-Experiment durchgeführt und dient ferner als Grundlage für Blindrechnungen mittels Rechenprogrammen zum LWR-Störfallverhalten (deklariert als OECD Internationales Standardproblem ISP-45).

Das QUENCH-Testbündel ist mit 21 Brennstabsimulatoren bestückt und hat eine Gesamtlänge von ca. 2,50 m. 20 Brennstabsimulatoren sind auf einer Länge von 1024 mm beheizt, der Zentralstab ist unbeheizt. Als Heizer werden Wolfram-Stäbe von 6 mm Durchmesser verwendet, die im Zentrum der Brennstabsimulatoren angeordnet und von ZrO_2 -Ringtabletten umgeben sind. Die Stabhüllen sind identisch denen der LWR-Hüllrohre: Zircaloy-4, 10,75 mm Außendurchmesser und 0,725 mm Wanddicke. Die Teststrecke ist mit Thermoelementen (TE) instrumentiert. Sie sind auf Messebenen zwischen -250 und 1350 mm an den Stabhüllen, dem Shroud und dem Kühlmantel befestigt. Zusätzlich waren im Zentralstab drei Zentral-TE und zwei TE auf der Hüllinnenseite montiert. In drei von vier Eckstäben war ebenfalls je ein Zentral-TE angebracht.

Während der Aufheizphase oder Transiente wird überhitzter Dampf zusammen mit Argon als Trägergas für die Wasserstoffanalyse am unteren Ende in die Teststrecke eingespeist und verlässt diese zusammen mit dem Wasserstoff, der sich durch die Zirkonium-Dampf-Reaktion gebildet hat, am oberen Ende. Der Wasserstoff wird mit Hilfe von drei Messgeräten analysiert: zwei Massenspektrometer und ein „Caldos-7G“-Analysegerät, das nach dem Wärmeleitfähigkeits-Messprinzip arbeitet.

Wie in den vorangegangenen Experimenten wurde das Versuchsbündel durch stufenweise Erhöhung der elektrischen Leistung von Raumtemperatur auf eine Bündeltemperatur von ~873 K gebracht. Im thermischen Gleichgewicht betrug die Leistung etwa 4 kW. Die Atmosphäre im Bündel bestand aus einem Dampf und Argonstrom von jeweils 3 g/s. Am Ende der Stabilisierungsphase wurde die Leistung stufenweise bis auf ca. 11 kW erhöht, um die Zieltemperatur für die Voroxidation von ~1473 K zu erreichen. Mit Hilfe der elektrischen Leistungsregelung wurde die Temperatur etwa 4600 s lang gehalten, um die gewünschte Oxidschichtdicke von rund 200 μm zu erreichen. Am Ende der Voroxidationsphase wurde die Leistung linear um 6 W/s angehoben. Diese Leistungssteigerung erbrachte eine zum Versuch QUENCH-05 identische Aufheizrate von 0,32 K/s (zwischen 1450 und 1750 K auf der Grundlage des TCRC 13-TE bei 950 mm Höhe). Während der transienten Phase kam es zu moderaten Temperaturskalationen zwischen 750 und 950 mm Höhe. Ab der Zeit stieg die Wasserstoffproduktion sichtbar an. Die Abschreckphase wurde unter den gleichen Bedingungen, die für den Versuch QUENCH-05 vorgegeben waren, ausgelöst. Zum Zeitpunkt der

Auslösung wurde eine maximale Stab-Hüllrohrtemperatur von ~ 2150 K bei 750 mm (TFS 2/11) erreicht.

Um den Teststreckeneinlauf vorzufüllen, wurden rund 4 kg Wasser innerhalb von 5 s eingespeist. Zum gleichen Zeitpunkt wurde die Quenchpumpe gestartet, um Wasser mit einer mittleren Rate von 40 g/s von unten in die Teststrecke einzuleiten (Dieser Mengenstrom entspricht einer Flutgeschwindigkeit von 1,4 cm/s am unteren Ende der Teststrecke). Anders als geplant erreichte das Hauptflutwasser das Testbündel mit einer Verzögerung von ca. 40 s. Deshalb fand die Abschreckung des Bündels in zwei Phasen statt: einer ersten und einer Haupt-Einspeisung.

26 s nach dem Beginn der Abschreckphase wurde die elektrische Leistung von 18,2 auf 4 kW innerhalb von 16 s reduziert. Das Niveau von 4 kW soll die Nachwärme eines LWR-Bündels simulieren. Nach ~ 255 s wurden die Wassereinspeisung und die elektrische Leistung abgeschaltet und das Experiment damit beendet.

Die gesamte freigesetzte Wasserstoffmenge während des Versuchs QUENCH-06 wurde mit den drei Messgeräten zu 35 g ermittelt, wobei die H_2 -Freisetzungsrates 0,24 g/s betrug. Von den 35 g wurden etwa 2 g während der Flutphase gebildet. Der Wert kann mit 1 g des Versuchs QUENCH-05 verglichen werden.

Nach dem Experiment war das QUENCH-06-Bündel insgesamt (und damit auch die Zircaloy-Hüllrohre) bis zu einer Höhe von ~ 850 mm in intaktem Zustand. Bis zu dieser Höhe war der Shroud nur leicht oxidiert. Zwischen ~ 870 mm and ~ 1010 mm hatte sich am Shroud eine lokal ausgeprägte Schmelzzone gebildet. Im Bündel selbst kam es zu keiner wesentlichen Schmelzbildung. Somit weist der Endzustand des Bündels eine intakte Bündelgeometrie auf. Die Quenchphase mit Wasser führte jedoch zu erheblicher Rissbildung und Fragmentierung von Stabhüllen und ZrO_2 Tabletten.

Das Oxidationsverhalten und die damit verbundene Wasserstofffreisetzung wurden nach dem Experiment mit dem FZK-Rechenprogramm CALUMO untersucht. Insgesamt waren die Rechenergebnisse in guter Übereinstimmung mit den Testdaten. Allerdings konnten die CALUMO-Rechnungen das Experiment QUENCH-06 nicht perfekt simulieren.

Thermohydraulik-Rechnungen mit der eigenen Version des Rechenprogramms SCDAP/RELAP5mod 3.2 wurden durchgeführt, um die experimentellen Einflussgrößen des QUENCH-Experiments zu definieren und die experimentellen Ergebnisse nach der Versuchsdurchführung zu interpretieren.

Abstract

The QUENCH experiments are to investigate the hydrogen source term that results from the water or steam injection into an uncovered core of a Light-Water Reactor (LWR). The QUENCH-06 experiment performed in the QUENCH facility at the Forschungszentrum Karlsruhe (Karlsruhe Research Center) on 13 December, 2000 was to investigate the behavior of pre-oxidized LWR fuel rods on cooling down with water from the bottom. This test is used as an OECD International Standard Problem (ISP-45) for blind and open calculations to assess the quality of severe accident codes. The test was planned to be as similar to QUENCH-05 as possible except that the bundle was quenched with water and not cooled down with steam. The test bundle is made up of 21 fuel rod simulators with a length of approximately 2.5 m. 20 fuel rod simulators are heated over a length of 1024 mm, the one unheated fuel rod simulator is located in the center of the test bundle. The rod cladding is identical to that used in LWRs: Zircaloy-4, 10.75 mm outside diameter, 0.725 mm wall thickness. Heating is carried out electrically using 6-mm-diameter tungsten heating elements, which are installed in the center of the rods and which are surrounded by annular ZrO₂ pellets. The test section is instrumented with thermocouples (TC) that are attached to the cladding, the shroud, and the cooling jackets at elevations between -250 mm and 1350 mm. Besides, inside the central rod three centerline TCs and two cladding inner surface TCs were installed, and three centerline TCs were mounted inside three of the four corner rods. The hydrogen is analyzed by three different instruments: a state-of-the-art mass spectrometer Balzers "GAM300", a commercialtype hydrogen analyzer "Caldos 7 G" that is based on the measurement of heat conduction, and a second, simpler mass spectrometer Balzers "Prisma" which was located close to the Caldos analyzer.

The superheated steam and argon as carrier gas for the detection of hydrogen enter the test bundle at the bottom and leave it at the top together with the hydrogen that is produced in the zirconium-steam reaction. As in the previous QUENCH experiments, the bundle was heated by a series of stepwise increases of electrical power from room temperature to ~873 K in an atmosphere of flowing argon (3 g/s) and steam (3 g/s). The bundle was stabilized at this temperature with the electrical power being ~4 kW.

At the end of the stabilization period the bundle was ramped by stepwise increases in power up to about 11 kW to reach ~1473 K, the target temperature for pre-oxidation. This temperature was maintained for about 4600 s by control of the electrical power to reach a desired oxide layer thickness of about 200 μm. At the end of the pre-oxidation period the bundle was ramped at 6 W/s. With this power ramp the transient heatup rate was identical to that of the QUENCH-05 experiment, i.e. 0.32 K/s between 1450 K and 1750 K (on the basis of TCRC 13, level 950 mm). Moderate temperature excursions occurred between the 750 and 950 mm elevation. From that time on the hydrogen release increased significantly. The quench phase was initiated when pre-defined criteria similarly to QUENCH-05 were reached. The maximum measured temperature was 2150 K at the 750 mm level (TFS 2/11) coinciding with the quench initiation.

Within 5 s 4 kg of water were pre-injected to fill the lower part of the test section. At the same time the quench pump was started to inject water into the bottom of the test section at a rate of ~40 g/s which corresponds to a flooding velocity of 1.4 cm/s at the bottom of the test

section. Different from planning the experiment the main quench water entered the bundle with a delay of about 40 s. Therefore the bundle was flooded in two stages, firstly by a first water injection and then by the main quench water injection.

26 s after the beginning of the quench phase the electrical power was reduced from 18.2 kW to 4 kW within 16 s. The 4 kW level is to simulate the decay heat. Cooling of the test section was completed within ~255 s; the water flow and the electrical power were then shut off, terminating the experiment.

The total hydrogen production measured by the three devices resulted in around 35 g with a maximum H₂ release rate of 0.24 g/s. Of the 35 g, ~2 g are estimated for the quenching phase. This compares with 1 g for the steam-cooling phase in the QUENCH-05 test.

After the experiment the QUENCH-06 bundle in total and the Zircaloy rod cladding appeared nearly intact up to ~850 mm elevation. Up to this elevation the shroud was only slightly oxidized whereas a localized molten zone is found between ~870 mm and ~1010 mm. No essential melt formation was observed in the test bundle itself. So, the final state of the bundle demonstrates an essentially intact bundle geometry, whereas considerable cracking and some fragmentation of clad and ZrO₂ pellets occurred during the phase of water quenching.

The oxidation and hydrogen behavior was investigated with the FZK code CALUMO. The results of the code are in the overall coherent with the experimental findings. However, the CALUMO bundle code calculations could not provide a perfect simulation of the experiment QUENCH-06.

Thermal hydraulic calculations were made with the in-house version of SCDAP/RELAP5mod 3.2 to define experimental parameters of the QUENCH experiment and to interpret the experimental results after the experiment.

Contents

List of Tables.....	1
List of Figures.....	2
Introduction	7
1 Description of the Test Facility	9
2 Test Bundle Assembly	11
3 Test Bundle Instrumentation	11
4 Hydrogen Measurement Devices.....	12
5 Data Acquisition and Process Control.....	13
6 Test Conduct.....	14
7 Test Results	16
7.1 General Results.....	16
7.2 Test Rod and Shroud Failure	17
7.3 Estimated Steam Conversion	17
7.4 Hydrogen Release.....	18
7.5 Temperature Differences Across the Rod Cladding	19
8 Posttest Examination	19
8.1 Posttest Appearance of the Shroud.....	19
8.2 Sectioning of the Test Bundle.....	20
8.3 Metallographic Examination	20
8.3.1 General state of the bundle	20
8.3.2 Physico-chemical state and behavior of the bundle	21
8.3.3 Lateral and axial oxidation profiles	24
8.3.4 Summary and conclusions	25
8.4 Hydrogen Absorption by Zircaloy	26
9 Calculational Support	27
9.1 Investigation of the oxidation and hydrogen behavior with the FZK code CALUMO ..	27
9.2 Calculational support with SCDAP/RELAP5	30
9.2.1 Modeling of the QUENCH facility	30
9.2.2 Pre-test calculations	31
9.2.3 Post-test calculations.....	31
9.2.4 Initial reflood conditions	32
References.....	34
Acknowledgements	37
Appendix	37
Steam measurements by MS.....	38

List of Tables

- Table 1: QUENCH test matrix
- Table 2: Design characteristics of the QUENCH test bundle
- Table 3: List of instrumentation for the QUENCH-06 test
- Table 4: QUENCH-06; Failure of thermocouples
- Table 5: QUENCH-06; Sequence of events
- Table 6: QUENCH-06; Excursion temperatures
- Table 7: QUENCH-06; Maximum measured test rod temperature of each elevation
- Table 8: QUENCH-06; Maximum measured shroud temperature of each elevation
- Table 9: QUENCH-06; Onset of cooling based on cladding TCs (TFS and TCR), central rod centerline TC (TCRC 13), corner rod TCs (TIT), and shroud TCs (TSH)
- Table 10: QUENCH-06; Onset of quenching based on cladding TCs (TFS and TCR), central rod centerline TCs (TCRC), corner rod TCs (TIT), and shroud TCs (TSH)
- Table 11: QUENCH-06; Cross sections for the metallographic examination
- Table A-1: Dependence of steam measurement by MS on the steam flow rate; results of pre-tests with a dummy bundle in the QUENCH Facility

List of Figures

- Fig. 1: Flow diagram of the QUENCH test facility
- Fig. 2: QUENCH Facility; main components
- Fig. 3: QUENCH Facility; containment and test section
- Fig. 4: QUENCH Test section; flow lines
- Fig. 5: QUENCH-06; Fuel rod simulator bundle (top view)
- Fig. 6: Heated fuel rod simulator
- Fig. 7: Unheated fuel rod simulator
- Fig. 8: QUENCH-06; Test bundle, TC instrumentation and rod designation
- Fig. 9: QUENCH; Test section instrumentation
- Fig. 10: QUENCH; High-temperature thermocouple
- Fig. 11: TC fastening concept for the QUENCH test rods
- Fig. 12: QUENCH-06; TC instrumentation of the unheated fuel rod simulator at levels 7 (350 mm) and 9 (550 mm)
- Fig. 13: QUENCH-06; TC instrumentation of the unheated fuel rod simulator
- Fig. 14: QUENCH-06; Schematic of the arrangement of the thermocouples inside the corner rods
- Fig. 15: QUENCH Facility; H₂ measurement with the mass spectrometer
- Fig. 16: QUENCH; Mass spectrometer sampling position at the off-gas pipe
- Fig. 17: QUENCH; Hydrogen measurement with the CALDOS analyzer
- Fig. 18: QUENCH-06; Test conduct
- Fig. 19: QUENCH-06, Test phases, top, and heatup rate during the transient phase determined on the basis of the centerline thermocouple TCRC 13, bottom
- Fig. 20: QUENCH-06; Total electric power
- Fig. 21: QUENCH-06; Coolant temperatures T 511 (at bundle inlet), T 512 (at bundle outlet), TFS 2/1 at-250 mm
- Fig. 22: QUENCH-06; Temperatures measured by rod surface (TFS), and shroud (TSH) thermocouples at -250 mm elevation
- Fig. 23: QUENCH-06; Oxide layer thickness of corner rod B (withdrawn from bundle during transient)
- Fig. 24: QUENCH-06; Temperatures measured by rod cladding outer surface (TFS), shroud (TSH), central rod centerline (TCRC), central rod cladding inner surface (TCRI), and central rod cladding outer surface (TCR) thermocouples at 350 mm elevation

-
- Fig. 25: QUENCH-06; Temperatures measured by rod cladding outer surface (TFS), shroud (TSH), central rod centerline (TCRC), central rod cladding inner surface (TCRI), central rod cladding outer surface (TCR), and corner rod internal (TIT) thermocouples at 550 mm elevation
- Fig. 26: QUENCH-06; Temperatures measured by rod cladding outer surface (TFS), shroud (TSH), and corner rod internal (TIT) thermocouples at 850 mm elevation
- Fig. 27: QUENCH-06; Temperatures measured by rod cladding outer surface (TFS), shroud (TSH), central rod centerline (TCRC), central rod cladding outer surface (TCR), and corner rod internal (TIT) thermocouples at 950 mm elevation
- Fig. 28: QUENCH-06; Temperatures measured by rod surface (TFS) and shroud (TSH) thermocouples at 1150 mm elevation
- Fig. 29: QUENCH-06; Temperature response of the shroud thermocouples, top, and cladding thermocouples up to 550 mm elevation, bottom, during the quenching phase
- Fig. 30: QUENCH-06; Axial temperature profile of TFS 2 (inner coolant channel), TFS 5 (outer channel), and TSH (shroud) thermocouples, left, and axial profile of all TFS thermocouples, right, at 6010 s (onset of transient).
- Fig. 31: QUENCH-06; Axial temperature profile of TFS 2 (inner coolant channel), TFS 5 (outer channel), and TSH (shroud) thermocouples, left, and axial profile of all TFS thermocouples, right, at 7000 s (transient phase).
- Fig. 32: QUENCH-06; Axial temperature profile of TFS 2 (inner coolant channel), TFS 5 (outer channel), and TSH (shroud) thermocouples, left, and axial profile of all TFS thermocouples, right, at 7179 s (onset of quenching).
- Fig. 33: QUENCH-06; Quench front progression based on TFS / TCR cladding thermocouples and on TSH shroud thermocouples. (Water injection velocity = 1.4 cm/s).
- Fig. 34: QUENCH-06; Indication of the collapsed water level in the test section (Lm 501) together with the time points of complete wetting based on cladding (TFS) and shroud (TSH) thermocouples
- Fig. 35: QUENCH-06; Maximum rod cladding temperature of each elevation, left, and maximum shroud temperature of each elevation, right
- Fig. 36: QUENCH-06; Rod failure at the onset of quenching indicated by P 411, top, and by the krypton concentration measured by the mass spectrometer, bottom
- Fig. 37: QUENCH-06; Shroud failure at the onset of quenching (7179 s) as indicated by the pressure P 406 measured in the space between shroud and inner cooling jacket and by the nitrogen concentration measured in the off-gas by the mass spectrometer
- Fig. 38: QUENCH-06; Rise of water level in the condensate collector (L 701) in [mm], top, and in [g], bottom
- Fig. 39: QUENCH-06; Steam flow measurements in the off-gas pipe (MS steam, F 601), in the condensate collector ($d(L701)/dt$), and mean steam flow data (thick line) compared to quench water input (F 104)
- Fig. 40: QUENCH-06; H₂ integral releases measured by the three analyzers, top, and H₂ release rate measured by the mass spectrometer, bottom

- Fig. 41: QUENCH-06; Synopsis of power input, rod temperature, quench water injection, and hydrogen generation
- Fig. 42: QUENCH-06; Posttest appearance of the shroud at the upper end of the heated zone, 0°
- Fig. 43: QUENCH-06; Posttest appearance of the shroud at the upper end of the heated zone, 90°
- Fig. 44: Shroud failure regions at the upper end of the heated zone of test bundles QUENCH-04, QUENCH-05, and QUENCH-06 (from left)
- Fig. 45: QUENCH-06; Sectioning of test bundle
- Fig. 46: QUENCH-06; Polished cross sections
- Fig. 47: QUENCH-06; Polished cross sections (continued)
- Fig. 48: QUENCH-06; Polished cross sections (continued)
- Fig. 49: QUENCH-06; Cross section QUE-06-10 at 950 mm depicting separately test rods 1–8
- Fig. 50: QUENCH-06; Cross section QUE-06-10 at 950 mm depicting separately test rods 9–16
- Fig. 51: QUENCH-06; Cross section QUE-06-10 at 950 mm depicting separately test rods 17–21
- Fig. 52: Cross section at 550 mm bundle elevation (QUE-06-2), overview, oxidation state of rod No. 8
- Fig. 53: Cross section at 750 mm bundle elevation (QUE-06-4), overview, rod No. 8 and its oxidation state
- Fig. 54: Cross section at 850 mm bundle elevation (QUE-06-6), overview, central rod and rod No. 21
- Fig. 55: Cross section at 850 mm bundle elevation (QUE-06-6), rod No. 14, showing a melt bridge from thermocouple to cladding, wetting of the duplex scale, and the partially molten cladding matrix
- Fig. 56: Cross section at 850 mm bundle elevation (QUE-06-6), rod No. 10, showing duplex external scale, non-molten metallic part of cladding without pellet interaction
- Fig. 57: Cross section at 850 mm bundle elevation (QUE-06-6), rod No. 3, showing duplex external scale, molten metallic part of the cladding, but no pellet interaction
- Fig. 58: Cross section at 850 mm bundle elevation (QUE-06-6), rod No. 2, showing wedge shaped crack in duplex scale, molten metallic cladding part and pellet interaction layer
- Fig. 59: Cross section at 900 mm bundle elevation (QUE-06-8), overview, state of rods No. 8 and 21
- Fig. 60: Cross section at 900 mm bundle elevation (QUE-06-8), central rod, showing defects in duplex scale and previously molten metallic part of cladding
- Fig. 61: Cross section at 900 mm bundle elevation (QUE-06-8), rod No. 11, showing duplex external scale and α -Zr(O) cladding with pellet interaction
- Fig. 62: Cross section at 900 mm bundle elevation (QUE-06-8), rod No. 5 and 19, showing through-wall cracking of duplex scale and metallic part of cladding

- Fig. 63: Cross section at 950 mm bundle elevation (QUE-06-10), overview, rods No. 4 and central rod, both in direct contact
- Fig. 64: Cross section at 950 mm bundle elevation (QUE-06-10), central rod, showing oxidized melt top layer, duplex external scale and α -Zr(O) cladding with local pellet interaction
- Fig. 65: Cross section at 950 mm bundle elevation (QUE-06-10), oxidation state of rod No. 4 on two opposite sides: advanced α -Zr(O) consumption (left), total oxidation (right)
- Fig. 66: Cross section at 950 mm bundle elevation (QUE-06-10), oxidation state of rod No. 14, showing local distribution of melt top layer, oxidative cladding consumption and void formation by internal cladding melt relocation
- Fig. 67: Cross section at 950 mm bundle elevation (QUE-06-10), rod No. 20 and 21, showing zirconia precipitation from metallic part of cladding, in solid or molten state, respectively
- Fig. 68: Cross section at 950 mm bundle elevation (QUE-06-10), internal scale of original shroud and oxidation of accumulated shroud melt
- Fig. 69: Cross section at 1000 mm bundle elevation (QUE-06-12), overview, rods No. 13 and 4 as examples
- Fig. 70: Cross section at 1000 mm bundle elevation (QUE-06-12), rods No. 8, showing strong external and slight internal oxidation by steam, and non-molten cladding
- Fig. 71: Cross section at 1150 mm bundle elevation (QUE-06-14), overview, rods No. 8, showing its components at electrode elevation and its cladding oxidation
- Fig. 72: QUENCH-06; Oxide layer thicknesses at bundle elevation 550 mm
- Fig. 73: QUENCH-06; Oxide layer thicknesses at bundle elevation 750 mm
- Fig. 74: QUENCH-06; Oxide layer thicknesses at bundle elevation 850 mm
- Fig. 75: QUENCH-06; Oxide layer thicknesses at bundle elevation 900 mm
- Fig. 76: QUENCH-06; Oxide layer thicknesses at bundle elevation 950 mm
- Fig. 77: QUENCH-06; Oxide layer thicknesses at bundle elevation 1000 mm
- Fig. 78: QUENCH-06; Oxide layer thicknesses at bundle elevation 1150 mm
- Fig. 79: QUENCH-06; Axial oxide layer thickness distribution
- Fig. 80: QUENCH-06; Calculational results with input of measured temperatures, top, and with input of temperatures according to the oxide profile measured at 6620 s, bottom
- Fig. 81: QUENCH-06; Axial profile of hydrogen absorbed by the remaining Zr(O) metal phases
- Fig. 82: QUENCH-06; Calculated average temperature of the entire bundle "trodz", average temperature of the inner cluster of nine fuel rod simulators "tcenz", and average shroud temperature "tshrz" compared to the available thermocouple readings at elevations 128–650 mm for the entire test duration
- Fig. 83: QUENCH-06; Calculated average temperature of the entire bundle "trodz", average temperature of the inner cluster of nine fuel rod simulators "tcenz", and average shroud temperature "tshrz" compared to the available thermocouple readings at elevations 128–650 mm for the test time 6500–7300 s.

- Fig. 84: QUENCH-06; Calculated average temperature of the entire bundle “trodz”, average temperature of the inner cluster of nine fuel rod simulators “tcenz”, and average shroud temperature “tshrz” compared to the available thermocouple readings at elevations 742–1250 mm for the entire test duration.
- Fig. 85: QUENCH-06; Calculated average temperature of the entire bundle “trodz”, average temperature of the inner cluster of nine fuel rod simulators “tcenz”, and average shroud temperature “tshrz” compared to the available thermocouple readings at elevations 742–1250 mm for the test time 6500–7300 s.
- Fig. 86: QUENCH-06; Calculated quench velocity and axial position of the quench front compared to test data.
- Fig. 87: QUENCH-06; Calculated steam production during the quench phase.
- Fig. 88: QUENCH-06; Axial distributions of the oxide scale thickness for 6640 s (withdrawal of the corner rod B), 7140 s (beginning of the temperature escalation), and 7400 s (after quenching).
- Fig. 89: QUENCH-06; Comparison of measured and calculated hydrogen production rate and accumulated total hydrogen values.
- Fig. 90: QUENCH-06; Detailed schematics of the inlet volumes including coaxial lower plenum with fluid inlet pipe, fast water injection system (right), and quench water pipe with realistic elevation changes (left) as used for FZK modelling.
- Fig. 91: QUENCH-06; Comparison of measured and calculated temperature developments at various axial levels in bundle and argon cooling.
- Fig. 92: QUENCH-06; Power, calculated clad temperatures, and oxide layer thickness, comparison of measured and calculated hydrogen production rate and cumulated hydrogen mass.
- Fig. 93: QUENCH-06; Comparison of measured and calculated temperature developments in the hot zone of the bundle.
- Fig. 94: QUENCH-06; Comparison of measured and calculated axial temperature profiles.
- Fig. 95: QUENCH-06; Comparison of measured and calculated axial temperature and oxide layer thickness profiles and calculated linear pin power profile.
- Fig. 96: QUENCH-06; Comparison of measured and calculated temperature developments at various axial levels in bundle and argon cooling during the quench phase.
- Fig. 97: QUENCH-06; Water level increase from experimental data and thermocouple readings compared with the S/R5irs calculation.

Introduction

The most important accident management measure to terminate a severe accident transient in a Light Water Reactor (LWR) is the injection of water to cool the uncovered degraded core. Analysis of the TMI-2 [1] accident and the results of integral out-of-pile (CORA [2, 3]) and in-pile experiments (LOFT [4]) have shown that before the water succeeds in cooling the fuel pins there will be an enhanced oxidation of the Zircaloy cladding that in turn causes a sharp increase in temperature, hydrogen production and fission product release.

Besides, quenching is considered a worst-case accident scenario regarding hydrogen release to the containment. For in- and ex-vessel safety analyses one has to prove that the hydrogen release rate and total amount do not exceed limits for the considered power plant. The hydrogen generation rate must be known to design appropriately accident mitigation measures for the following reasons.

- Passive autocatalytic recombiners require a minimum hydrogen concentration to start. Moreover, they work slowly, and their surface area and their position in the containment have to be quantified carefully.
- The air-steam-hydrogen mixture in the containment may be combustible for only a short time before detonation limits are reached. This limits the time period during which ignitors can be used.

The physical and chemical phenomena of the hydrogen release are, however, not sufficiently well understood. The increased hydrogen production during quenching cannot be determined on the basis of the available Zircaloy/steam oxidation correlations. Presently it is assumed that the following phenomena lead to an enhanced oxidation and hydrogen generation:

- Melt oxidation,
- Steam starvation conditions,
- Crack surfaces oxidation.

In most of the code systems describing severe fuel damage, these phenomena are either not considered or only modeled in a simplified empirical manner.

In addition, no models are yet available to predict correctly the thermal-hydraulic or the clad behavior of the quenching processes in the CORA and LOFT LP-FP-2 tests. An extensive experimental database is therefore needed as a basis for model development and code improvement.

The Forschungszentrum Karlsruhe has therefore started the QUENCH program on the investigation of coolability and determination of the hydrogen source term. The main objectives of this program are:

- The provision of an extensive experimental database for the development of detailed mechanistic fragmentation models,

- The examination of the physico-chemical behavior of overheated fuel elements under different flooding conditions,
- The provision of an improved understanding of the effects of water injection at different stages of a degraded core,
- The determination of cladding failure criteria, cracking of oxide layers, exposure of new metallic surfaces to steam
- The investigation of the oxide layer degradation under steam starvation conditions and influence of this phenomenon on subsequent flooding,
- The investigation of the melt oxidation process,
- The determination of the hydrogen source term.

The experimental part of the QUENCH program began with small-scale experiments with short Zircaloy fuel rod segments [5, 6]. On the basis of these results well-instrumented large-scale bundle experiments with fuel rod simulators under nearly adiabatic conditions are performed in the QUENCH facility at the Forschungszentrum Karlsruhe. The large-scale bundle experiments are more representative of prototypic reactor accident conditions than are the single-rod experiments. Important parameters of the bundle test program (see [Table 1](#)) are: quench medium, i.e. water or steam, fluid injection rate, cladding oxide layer thickness, and the temperature at onset of flooding. The results of the experiments with different thermo-hydraulic conditions, i.e. QUENCH-01, QUENCH-02, QUENCH-03, and QUENCH-04 are documented in references [7], [8], [9], and [11], respectively.

The sixth bundle experiment, QUENCH-06, was performed at the Forschungszentrum Karlsruhe on 13 December, 2000. It differed from the previous experiment QUENCH-05 [10] only in that the bundle was quenched with water instead of cooling it down by steam. This bundle was as well pre-oxidized before the transient and flooding phases began. In addition, the QUENCH-06 test was declared an International Standard Problem for blind calculations to assess the quality of the different severe accident codes. This report describes the test facility and the test bundle, and the main results of the QUENCH-06 experiment. In addition, one section refers to the calculational results obtained with the CALUMO oxidation behavior code and another one to those of the thermal-hydraulic computer code SCDAP/RELAP5 mod 3.2. The SCDAP/RELAP5 posttest calculations were used for guiding the participants in the ISP-45 task with respect to additional information for calculating the QUENCH-06 experiment [12].

1 Description of the Test Facility

The QUENCH test facility consists of the following component systems:

- the test section with 21 fuel rod simulators,
- the electric power supply for the test bundle heating,
- the water and steam supply system,
- the argon gas supply system,
- the hydrogen measurement devices,
- temperature, pressure, mass flow measurement devices,
- the process control system,
- the data acquisition system.

A simplified flow diagram of the QUENCH test facility is given in [Fig. 1](#), a three-dimensional schematic of the components in [Fig. 2](#). The main component of the facility is the test section with the test bundle ([Figs. 3 and 4](#)). The superheated steam from the steam generator and superheater together with argon as the carrier gas for the hydrogen detection systems enter the test bundle at the bottom end. The steam that is not consumed, the argon, and the hydrogen produced in the zirconium-steam reaction flow from the bundle outlet through a water-cooled off-gas pipe to the condenser ([Figs. 1 and 2](#)). Here the steam is separated from the non-condensable gases argon and hydrogen. The quenching phase is initiated by turning off the superheated steam of 3 g/s whereas the argon flow rate remains unchanged but the gas inlet position is switched to the upper plenum of the test section. At the same time quench water is injected at the bottom of the test bundle through a separate line.

Prior to the QUENCH-06 test a pre-injection system was added to the test facility to shorten the time of filling the pipes and the lower plenum of the test section (see [Figs. 1 and 2](#)). The pre-injection system consists of a tank which holds water under a pressure of around 0.6 MPa, a magnetic valve to activate the pre-injection, and a pipe connecting the tank with the test section inlet.

The design characteristics of the test bundle are given in [Table 2](#). The test bundle is made up of 21 fuel rod simulators, each with a length of approximately 2.5 m, and of four corner rods (see cross section in [Fig. 5](#)). The fuel rod simulators are held in their positions by five grid spacers, four of Zircaloy, and one of Inconel in the lower bundle zone ([Fig. 6](#)). The cladding of the fuel rod simulators is identical to that used in PWRs with respect to material and dimensions, i.e. Zircaloy-4, 10.75 mm outside diameter, 0.725 mm wall thickness. The rods are kept at a pressure of 0.22 MPa with a mixture of 95 % argon and 5 % krypton, i.e. a pressure slightly above the system pressure (0.2 MPa). The gas filling of all rods is realized by a channel-like connection system inside the lower sealing plate. The krypton additive allows to detect fuel rod failure during the experiment with help of the mass spectrometer.

Twenty fuel rod simulators are heated electrically over a length of 1024 mm, the unheated fuel rod simulator is located in the center of the test bundle. The unheated fuel rod simulator ([Fig. 7](#)) is filled with ZrO₂ pellets (bore size 2.5 mm ID). For the heated rods ([Fig. 6](#)) 6 mm

diameter tungsten heating elements are installed in the center of the rods and are surrounded by annular ZrO₂ pellets. The tungsten heaters are connected to electrodes made of molybdenum and copper at each end of the heater. The molybdenum and copper electrodes are joined by high-frequency/high-temperature brazing performed under vacuum. For electrical insulation the surfaces of both types of electrodes are plasma-coated with 0.2 mm ZrO₂. To protect the copper electrodes and the O-ring-sealed wall penetrations against excessive heat they are water-cooled (lower and upper cooling chamber). The copper electrodes are connected to the DC electric power supply by means of special sliding contacts at the top and bottom. The total heating power available is 70 kW, distributed among the two groups of heated rods with 35 kW each. The first group consists of the inner eight rods (rod numbers 2–9), the second group consists of the outer twelve rods (rod numbers 10–21). The rod designation can be taken from [Fig. 8](#).

The four corner positions of the bundle are occupied either by solid Zircaloy rods with a diameter of 6 mm or by solid rods (upper part) and Zry tubes (lower part) of $\varnothing 6 \times 0.5$ mm for thermocouple instrumentation at the inside ([Fig. 8](#)). The positioning of the four corner rods avoids an atypically large flow cross section at the outer positions and hence helps to obtain a rather uniform radial temperature profile. A solid Zry rod can be pulled out to determine the axial oxide layer thickness at that time.

The lower boundary for the lower cooling chamber is a sealing plate made of stainless steel with plastic inlays for electrical insulation, sealed to the system by O-shaped rings. The upper boundary of the lower cooling chamber is a sealing plate of stainless steel. An insulation plate made of plastic (PEEK) forms the top of the upper cooling chamber, and a sealing plate of Al₂O₃, functioning as a heat-protection shield, is the lower boundary of the upper cooling chamber (see [Fig. 6](#)).

In the region below the upper Al₂O₃ plate the copper electrode is connected firmly to the cladding. This is done by hammering the cladding onto the electrode with a sleeve of boron nitride put between electrode and cladding for electrical insulation. The axial position of the fuel rod simulator in the test bundle is fixed by a groove and a locking ring in the top Cu electrodes. Referred to the test bundle the fixing of the fuel rod simulators is located directly above the upper edge of the upper insulation plate. So, during operation the fuel rod simulators are allowed to expand downwards. Clearance for expansion of the test rods is provided in the region of the lower sealing plate. Also in this region relative movement between cladding and internal heater/electrode can take place.

The test bundle is surrounded by a 2.38 mm thick shroud (80 mm ID) made of Zircaloy with a 37 mm thick ZrO₂ fiber insulation and an annular cooling jacket made of stainless steel ([Figs. 4 and 5](#)). The 6.7 mm annulus of the cooling jacket is cooled by an argon flow. Above the heated zone, i.e. above the 1024 mm elevation there is no ZrO₂ fiber insulation to allow for higher radial heat losses. This region of the cooling jacket is cooled by a water flow ([Figs. 3 and 4](#)). Both the lack of ZrO₂ insulation above the heated region and the water cooling force the axial temperature maximum downward.

2 Test Bundle Assembly

The test section consists of three subassemblies pre-assembled separately. One subassembly comprises the cooling jacket with the bundle head casing; the second subassembly includes the instrumented shroud with the bundle foot; and the third subassembly is composed of the instrumented test bundle with the bundle head. The test bundle and the shroud, including the respective thermocouples, must be replaced for each experiment. The instrumentation of the bundle head and the foot as well as that of the cooling jacket, however, remains unchanged.

3 Test Bundle Instrumentation

The test bundle was instrumented with sheathed thermocouples attached to the rod claddings at 17 different elevations between -250 mm and 1350 mm and at different orientations ([Figs. 8 and 9](#)). The elevations of the surface-mounted shroud thermocouples are from -250 mm to 1250 mm. In the lower bundle region, i.e. up to the 550 mm elevation, NiCr/Ni thermocouples (1 mm diameter) are used for temperature measurement of rod cladding and shroud as is illustrated in [Fig. 9](#). The thermocouples of the hot zone are high-temperature thermocouples with W-5Re/W-26Re wires, HfO₂ insulation, and a duplex sheath of tantalum (internal)/Zircaloy with an outside diameter of 2.1 mm ([Fig. 10](#)). The leads of the thermocouples from -250 mm to 650 mm leave the test section at the bottom whereas the TCs above 650 mm penetrate the test section at the top.

The thermocouple attachment technique for the surface-mounted high-temperature TCs is illustrated in [Fig. 11](#). The TC tip is held in place by two clamps of zirconium. As these clamps are prone to oxidation and embrittlement in a steam environment an Ir-Rh wire of 0.25 mm diameter is additionally used in the experiments with pre-oxidation as was the case in test bundle QUENCH-06.

The designations of the surface-mounted cladding and shroud thermocouples are "TFS" and "TSH", respectively. The unheated fuel rod simulator of the QUENCH-06 bundle was especially instrumented to provide information on the accuracy of the temperature measurement with externally mounted thermocouples, particularly during cooldown. Therefore, two thermocouples were inserted in the center of the central rod (designation "TCRC"), two thermocouples at the rod cladding inner surface (designation "TCRI", \varnothing 0.5 mm), and two thermocouples at the rod cladding outer surface (designation "TCR", \varnothing 1 mm). These three thermocouple positions were realized at the 350 and 550 mm elevation (see [Figs. 12 and 13](#)).

The wall of the inner tube of the cooling jacket is instrumented between -250 mm and 1150 mm with 22 NiCr/Ni thermocouples (designation "TCI"). Five NiCr/Ni thermocouples are fixed at the outer surface of the outer tube of the cooling jacket ("TCO"). The designation of the thermocouples inside the Zircaloy instrumentation rods (corner positions) is "TIT" ([Fig. 14](#)). Three of the four corner rods of the QUENCH-06 test bundle were instrumented as follows:

- Rod A: W/Re, 2.1 mm diameter, Zr/Ta duplex sheath, 950 mm elevation (TIT A/13)
- Rod C: NiCr/Ni, 1 mm diameter, stainless steel sheath, 550 mm elevation (TIT C/9)
- Rod D: W/Re, 2.1 mm diameter, Zr/Ta duplex sheath, 850 mm elevation (TIT D/12).

A list of the instruments for experiment QUENCH-04 installed in the test section and at the test loop are given in [Table 3](#). The thermocouples that failed prior or during the test are listed in [Table 4](#).

4 Hydrogen Measurement Devices

The hydrogen is analyzed by three different measurement systems: (1) a Balzers mass spectrometer (MS) "GAM 300" ([Fig. 15](#)) located at the off-gas pipe, approx. 2.7 m downstream from the test section outlet, (2) a hydrogen detection system "Caldos 7 G" ([Fig. 17](#)) located in a bypass to the off-gas line behind the condenser, (3) a second, simpler mass spectrometer "Prisma" made by Balzers installed close to the Caldos device. So, the off-gas, i.e. the argon/hydrogen mixture, downstream the condenser passed at first the mass spectrometer "Prisma" and then the Caldos analyzer before it exited to the outside. Due to their different locations in the facility the mass spectrometer "GAM 300" responds almost immediately (less than 5 s) to a change in the gas composition whereas the mass spectrometer "Prisma" and the Caldos device have a delay time of about 20–30 s. The time delay of the off-gas analyzing systems has been determined with several bundle flows and gas injections at the 700 mm level of a dummy test section particularly installed for calibration purposes. A first series was performed at room pressure and temperature with 3 and 6 g/s argon flow in the bundle and hydrogen as injection gas. A second series was performed at 1000 K maximum rod surface temperature with a mixture of 3 g/s argon and 3 and 50 g/s steam flow in the bundle at a system pressure of 0.2 MPa and with helium as injection gas. Besides the time delay, the signal shapes are different for the H₂ detection systems, i.e. the CALDOS analyzer gives a broader peak due to the diffusion of the hydrogen in the fluid.

The mass spectrometer "BALZERS GAM 300" used is a completely computer-controlled quadrupole MS with an 8 mm rod system which allows quantitative measurement of gas concentrations down to about 10 ppm. For the MS measurement a sampling tube is inserted in the off-gas pipe ([Fig. 16](#)). It has several holes at different elevations to guarantee that the sampling of the gas to be analyzed is representative. To avoid steam condensation in the gas pipes between the sampling position and the MS the temperature of the gas at the MS inlet is controlled by a heat exchanger to be between 110 °C and 150 °C (the upper operating temperature of the MS inlet valves). This allows the MS to analyze the steam production rate. Besides, the concentrations of the following species were continuously measured by the mass spectrometer during all test phases: argon, hydrogen, steam, nitrogen, oxygen, and krypton. As the fuel rod simulators are filled with krypton as a tracer gas in addition to the argon, i.e. a mixture of argon and 5% krypton, the measurement of krypton can be used as an indicator for a cladding failure. Additionally, the MS is used to control the atmosphere in the facility, e.g., to monitor the gas composition at the beginning of the test.

The temperature and pressure of the analyzed gas are measured near the inlet valve of the MS. The MS is calibrated for hydrogen with well-defined argon/hydrogen mixtures and for steam with mixtures of argon and steam supplied by the steam generator of the QUENCH facility. The MS off-gas is released into the atmosphere because the amount of hydrogen taken out of the system is negligible.

The principle of measurement of the Caldos system is based on the different heat conductivities of different gases. The Caldos device is calibrated for the hydrogen-argon gas mixture. To avoid any moisture in the analyzed gas a gas cooler, which is controlled at 296 K, is connected to the gas analyzer (Fig. 16). The response time of the gas analyzer is documented by the manufacturer to be 2 s, i.e. a time in which 90 % of the final value should be reached. In contrast to the mass spectrometer the Caldos device only measures the hydrogen content. Gases other than H₂ cannot be analyzed by this system.

For the Caldos device as well as for the MS the hydrogen mass flow rate is calculated by referring the measured H₂ concentration to the known argon mass flow rate according to equation (1):

$$\dot{m}_{H_2} = \frac{M_{H_2}}{M_{Ar}} \cdot \frac{C_{H_2}}{C_{Ar}} \cdot \dot{m}_{Ar} \quad (1)$$

with M representing the molecular masses, C the concentrations in vol-% and \dot{m} the mass flow rates of the corresponding gases.

With an argon-hydrogen (two-component) mixture that in fact exists at the location of the Caldos analyzer equation (1) can be written as follows

$$\dot{m}_{H_2} = \frac{M_{H_2}}{M_{Ar}} \cdot \frac{C_{H_2}}{100 - C_{H_2}} \cdot \dot{m}_{Ar} \quad (2)$$

5 Data Acquisition and Process Control

A computer-based control and data acquisition system is used in the QUENCH facility. Data acquisition, data storage, online visualization as well as process control, control engineering and system protection are accomplished by three computer systems that are linked in a network.

The data acquisition system allows recording of about 200 measurement channels at a maximum frequency of 25 Hz per channel. The experimental data and the date and time of the data acquisition are stored as raw data in binary format. After the experiment the raw data are converted into SI units and stored as ASCII data.

For process control, a system flow chart with the most important actual measurement values is displayed on the computer screen. Furthermore, the operating mode of the active

components (pumps, steam generator, superheater, DC power system, valves) is indicated. Blocking systems and limit switches ensure safe plant operation. Operating test phases, e.g. heating or quenching phases, are pre-programmed and can be started on demand during the experiment. The parameter settings of the control circuits and devices can be modified online.

Online visualization allows to observe and to document the current values of selected measurement positions in the form of tables or plots. Eight diagrams with six curves each can be displayed as graphs. This means that altogether 48 measurement channels can be selected and displayed online during the course of the experiment.

The data of the main data acquisition system and of the mass spectrometers were stored on different computers. Both computers were synchronized by radio-controlled clocks.

The data of the main acquisition system were stored at frequencies of 1 Hz (until 5921 s), and 5 Hz (from 5922 s on), respectively. The mass spectrometer data were recorded at a frequency of approx. 1 Hz during the entire test.

6 Test Conduct

The test conduct and the test phases are illustrated in [Fig. 18](#) and [Fig. 19, top](#), respectively. The sequence of events is summarized in [Table 5](#).

The bundle was heated by a series of stepwise increases of electrical power from room temperature to 873 K in an atmosphere of flowing argon (3 g/s) and steam (3 g/s).

At the end of the stabilization period the bundle was ramped by stepwise increases in power. The electric power history is given in [Fig. 20](#). The temperature was stabilized at the 1473 K level (axial maximum) with a power of about 11 kW. The temperature was maintained constant by control of the electrical power during this pre-oxidation phase for 4046 s. The coolant inlet temperature TFS 2/1 was 640 K throughout the test until the quenching phase began (see [Fig. 21 and 22](#)). At the end of the pre-oxidation period the bundle was ramped at 6.0 W/s to start the transient phase, in the same way as in QUENCH-04 and QUENCH-05. The heatup rate of the rod bundle evaluated on the basis of TCRC 13, level 950 mm, was 0.32 K/s between 1450 K and 1750 K ([Fig. 19, bottom](#)). During the transient period, prior to any temperature excursion the withdrawal of corner rod B was started at ~1606 K to check the amount of oxidation at that time. The analysis performed after the experiment by metallographic examination resulted in a maximum oxide layer thickness of ~210 μm at the 950 mm elevation as can be taken from [Fig. 23](#).

The temperatures measured at the 350, 550, 850, 950, and 1150 mm elevations are given separately for the axial levels in [Figs. 24 through 28](#) and - as an overview - rod cladding and shroud temperatures in one diagram each in [Fig. 29, bottom and top](#), respectively. The TFS-thermocouples at 750 mm and 850 mm show (at ~7100 s) moderate temperature excursions

during the transient phase . Also at ~7100 s the upper shroud thermocouples (above 1000 mm) show a moderate increase in the signal^{*)}.

The conditions for starting the quenching sequence were: a minimum of three rod thermocouples should have exceeded 1973 K, and the central rod thermocouple TCRC 13 should have reached ~1873 K at this time. In this way the initiation temperature for the cooldown was comparable to that of test QUENCH-05. The thermocouples of the hot region, i.e. at 750–950 mm elevation, reached the 1973 K level:

TFS 4/11	at ~7134 s
TFS 5/11	at ~7136 s
TFS 2/11	at ~7151 s
TFS 3/12	at ~7139 s
TFS 5/12	at ~7142 s
TIT A/13	at ~7140 s
TSH 13/270	at ~7160 s.

At ~7140 s TCRC 13 was then at ~1873 K as it was planned.

For starting the quenching sequence, the flow of 3 g/s superheated steam was turned off at 7179 s, the argon flow was switched over to the bundle head, and the valve of the fast injection system was opened for 5 s allowing approx. 4 l of quench water for pre-filling the pipes and the lower plenum of the test section. At the same time the quench pump was started to inject water into the bottom of the test section for 255 s at a mean rate of ~42 g/s (F 104). This mass flow corresponds to a flooding velocity of 1.4 cm/s at the bottom of the test section (one-phase flow, no evaporation assumed).

Before the main water injection affected the bundle cooling an unforeseen delay was encountered in the water flow through the bundle. A detailed examination of available experimental data, done recently in [22], suggests that the delay of quench water injection into the test section is 34 to 41 s.

26 s after starting the injection (7179 s) the electrical power was reduced from ~18.2 kW to ~4 kW (to simulate decay heat levels in nuclear power reactors) within 16 s. The bundle flooding was terminated when the shroud thermocouples at the 1150 mm elevation, i.e. TSH 15/0 and TSH 15/180, indicated local wetting. Cooling of the test section to around 400 K was complete about 250 s after its initiation; the quench water and electrical power were shut off 255 s after the water injection, terminating the experiment.

^{*)}) The new analysis [21, Appendix 2] showed that thermocouple readings of the TFS thermocouples at 750 mm and at 850 mm as well as of the TSH thermocouples above 950 mm are questionable at high temperatures (>1000 K) because of the “hot zone effect”.

7 Test Results

7.1 General Results

The evolution of the axial temperature profile is presented in [Figs. 30–32](#) for the onset of the transient phase, i.e. at 6010 s, for the middle of the transient phase, i.e. at 7000 s, and for the onset of quenching, i.e. at 7179 s.

After the first water injection a prompt cooling of the test bundle started resulting from the fast pre-injection with a total of ~4 kg H₂O. At axial levels up to 250 mm the cladding temperature drops to the saturation temperature of around 400 K. 10–20 s later the cladding temperatures increase again due to the evaporation of the pre-injected water at the bottom of the test section. The increase in the bundle temperature is then followed by the main cooling phase. As found in the previous QUENCH experiments without pre-injection this main cooling phase is characterized by (a) a relatively moderate cooldown mainly due to two-phase flow cooling and (b) a rapid cooling period with a drastic improvement in heat transfer. The temperatures evaluated for the first period are given as “onset of cooling” in [Table 9](#). The beginning of the latter period is called “quench temperature” or “onset of quenching” and can be taken from [Table 10](#). In the upward direction this onset of quenching occurs stepwisely later so that a quench front progression can be evaluated. The quench front progression based on cladding thermocouples (types TFS and TCR) and on the shroud thermocouple readings (TSH) as a function of elevation is depicted in [Fig. 33](#). Particularly the shroud data show a linear behavior with a velocity of approx. 0.5 cm/s. (For comparison: The water injection velocity amounts to 1.4 cm/s).

As was already noticed in previous experiments, the externally mounted cladding thermocouples (TFS and TCR types) demonstrate a more pronounced temperature drop than the internal thermocouples (TCRC and TCRI types) and the shroud thermocouples (TSH). In any case, there is no complete wetting of the test rods during the temperature drop. Complete wetting could not begin before the cladding temperatures stay at the saturation temperature level for the rest of the experiment (see e.g. [Fig. 29](#), bottom). The time points of complete wetting based cladding and shroud data are plotted in [Fig. 34](#) together with the liquid level indicator Lm 501, a differential pressure (Δp) measurement between bottom and top of the bundle. The Lm 501 signal reflects well the periods of pre-injection and main water injection. The wetting points, in particular those of the shroud data, are in good agreement with the Δp curve up to around 800 mm elevation.

The maximum rod cladding temperatures are identical to the temperature at the onset of cooldown or 1 s later. The maximum measured rod temperature of 2150 K was measured with thermocouple TFS 2/11 (750 mm level) at 7180 s, i.e. at the onset of the quenching phase (see [Table 7](#)). The maximum measured shroud temperatures of each elevation are provided in [Table 8](#). The axial distributions of the maximum measured cladding and shroud temperature of each elevation are plotted in [Fig. 35](#). In contrast to the previous experiments there were no large azimuthal differences in the shroud temperature at the 1150 mm and 1250 mm elevations (see e.g. [Fig. 28](#) for the 1150 mm elevation).

7.2 Test Rod and Shroud Failure

A first rod failure is usually indicated by a sudden drop in the rod internal pressure P 411 as well as in the sudden increase in the krypton concentration of the off-gas which can be measured by the mass spectrometer. According to both signals a failure of at least one test rod occurred at the onset of cooling, i.e. at 7179 s, in the QUENCH-06 experiment as is presented in [Fig. 36](#).

The shroud was detected to fail as well directly after the initiation of the quench phase. P 406, the pressure measured in the space between shroud and inner cooling jacket, increased at 7180 s and dropped to the bundle pressure level one second later ([Fig. 37](#)). This behavior might be explained by some kind of ballooning and subsequent rupture of the shroud. At the same time the nitrogen concentration measured in the off-gas by the mass spectrometer shows some spikes reflecting shroud failure (see also [Fig. 37](#)). Prior to the test the nitrogen as part of the air is still entrained in the void volume of the shroud insulation (ZrO₂ fiber). During heatup the air is released from the insulation into the volume between inner cooling jacket and shroud and enters the test section upon shroud failure.

7.3 Estimated Steam Conversion

The integral values of water and steam evaluated for test bundle QUENCH-06 are as follows:

- Total mass of water injected: ~14.6 kg;
- Total mass of water pre-injected: ~4.0 kg,
- Total mass of water injected based on the F 104 data: ~10.6 kg,
- Total mass of water that remained in the test section (determined one day after the experiment): ~6.0 kg,
- Total mass of water accumulated (from the onset of quenching to one day after the experiment) in the condensate collection tank (L 701): ~7.8 kg.

[Fig. 38](#) gives the rise of the water level in the condensate collection tank (L 701) as a function of time. The lower plot of this figure is the conversion to the unit mass, i.e. g, which is based on a calibration that 1 mm H₂O corresponds to 13.84 g. The amount of 7.8 kg is assumed to have been steam in the test section during the experiment.

To evaluate the evaporation that results from the quench water injection into the hot test bundle as a rate, i.e. as a function of time, data from three independent instruments were evaluated: mass spectrometer (MS) data, F 601 orifice data, and L 701 condensate collector data. MS and F 601 measurement devices are located at and in the off-gas pipe, respectively, whereas the L 701 data are deduced from the accumulated water level downstream the condenser.

With respect to the MS data special calibration tests with different steam flow rates were performed prior to QUENCH-06 (see Appendix). The tests revealed a partial steam condensation in the off-gas pipe at low steam flows and hence low temperatures: When

operating with 3 g/s approx. 46 % of the steam are condensed in the off-gas pipe. With an elevated steam flow which is realistic for the quenching phase, e.g. 10 g/s, the temperature in the off-gas pipe (T 601) increases avoiding condensation so that almost the entire steam reaches the MS. So, correcting the MS for the partial steam condensation leads to reasonable results. F 601 is a standard orifice plate designed for measuring volumetric flow rates under steady-state conditions and with a fixed and well-known gas composition. So, to use the F 601 data it has to be assumed that gas in the off-gas pipe is mainly composed of steam. This assumption seems justified: (a) Converting the Δp signal of the orifice to mass flow rates results in reasonable values when applying the density of steam for the off-gas composition. (b) The onset of the increase in the F 601 signal coincides with the startup of the water/steam injection to initiate cooldown.

The L 701 data represent the water level in the condensate collector. With a calibration value of 13.84 g/mm H₂O the accumulated mass of water is obtained. Deriving these data leads to a steam mass flow rate ($d(L\ 701)/dt$) because the water collected in the tank had been steam in the test section during the quenching phase of the experiment.

In [Fig. 39](#) the three different steam determination methods described above are compared for the quenching phase, among each other and to the quench water input F 104. In addition, an average of the three curves by a coarse approximation (thick line in the diagram) is presented as mean steam flow data. According to these data indicate that the mass rate ratio of steam produced to water injected seems to change mainly during the first period of the quenching phase. From the mass rates plotted in [Fig. 39](#) the following accumulated masses were evaluated: The total mass of steam measured by the mass spectrometer is ~3.4 kg, that of L 701 is ~3.5 kg (~7.8 kg is the value for the entire test), and ~4.7 kg is the integrated value of the F 601 standard orifice plate. The total quench water input amounts to 10.6 kg (F 104) plus 4 kg (fast injection).

7.4 Hydrogen Release

The total hydrogen production is ~36 g according to the integral values of the GAM 300 mass spectrometer, the Prisma mass spectrometer, and the Caldos analyzer ([Fig. 40](#)). The peak production rate of ~0.24 g/s was measured by the main mass spectrometer GAM 300 which is believed to present the most reliable data. The peak value coincides with the onset of quenching ([Fig. 40](#), bottom). Of the 36 g, ~4 g is estimated for the quenching phase. The total value for the quenching phase compares with 2 g for the steam-cooling phases in the QUENCH-04 and -05 experiments.

[Fig. 41](#) gives the synopsis of the electric bundle power input, the bundle temperature TCRC 13, the quench water flow rate, and the hydrogen release rate measured by the main mass spectrometer. It can be seen that the hydrogen release rate increases with the onset of the temperature excursion decreases promptly with the water injection indicating an effective cooling. In addition, the steam flow rate evaluated from the mass spectrometer data is added in the lower graph.

7.5 Temperature Differences Across the Rod Cladding

With respect to the “real” wall temperature one must note that the cladding thermocouples of the types TFS and TCR are externally mounted and thus do not measure the wall temperature correctly. To account for the deviation of external surface Thermocouples, the central rod was equipped at levels 350 mm and 550 mm with Thermocouples on the cladding inner surface (TCRI 7 and TCRI 9) and in the rod center (TCRC 7 and TCRC 9) in addition to the Thermocouples on the cladding outer surface (TCR 7 and TCR 9). The differences of internal and external rod cladding temperatures turned out to be relatively small during the transient of test QUENCH-06 in the steam-argon atmosphere (3 g/s + 3 g/s), e.g. at 6000 s during a power plateau when the total electric power was at 10.9 kW and at 7100 s during a power ramp when the total electric power was at 17.6 kW:

Thermo-couple	Temperature at 6000 s	Temperature at 7100 s	Thermo-couple	Temperature at 6000 s	Temperature at 7100 s
TFS 2/7	1045 K	1193 K	TFS 2/9	1138 K	1327 K
TCR 7	1007 K	1165 K	TCR 9	1120 K	1302 K
TCRI 7	1024 K	1184 K	TCRI 9	1123 K	1302 K
TCRC 7	1020 K	1176 K	TCRC 9	1120 K	1302 K

In the temperature range of 1020–1320 K during the transient the internal thermocouples “TCRI” and “TCRC” and the pertinent external cladding thermocouples “TCR” of the central rod resulted in temperature differences of 17-19 K for axial level 9 (550 mm) and negligible differences for level 7 (350 mm), respectively.

The results with respect to the quenching phase can be taken from the bottom graphs of Figs. 23 and 24. The temperature differences are also relatively small during cooling phase.

8 Posttest Examination

8.1 Posttest Appearance of the Shroud

After the experiment the QUENCH-06 bundle in total (including the Zircaloy rod cladding) appeared nearly intact up to ~850 mm elevation. Up to this elevation the shroud was only slightly oxidized on the external side whereas a localized molten zone is found between ~870 mm and ~1010 mm, between ~270° and ~0° orientation as can be seen in [Figs. 42 and 43](#). On the basis of the shroud thermocouples no large azimuthal differences in the shroud temperature existed at the upper end or above the heated zone during the experiment to explain the asymmetric behavior of the shroud. Besides this failure region the shroud is intact and so are the thermocouples apart from this region. There they are still attached to the shroud surface. [Fig. 44](#) compares the shroud failure regions of test bundle QUENCH-04 [9], QUENCH-05 [10], and QUENCH-06. The similarities are evident.

8.2 Sectioning of the Test Bundle

To allow a detailed posttest analysis of the test bundle by means of cross sections the bundle had to be encapsulated. The test bundle was set up vertically for the encapsulation, which was performed in three steps. First, a cap was placed over the bottom of the copper electrodes and a low-melting metal alloy (containing Pb, Bi, Sn, and In; density of $\sim 10 \text{ kg/dm}^3$; melting point of 331 K) was used to seal the bottom of the bundle. Secondly, a small amount of the same resin to be used for the encapsulation of the bundle was placed on top of the metal to generate an interface of around 0.2 m that prevents the metal from being liquefied after starting to epoxy the bundle together with its shroud. The mould for filling the bundle with epoxy resin mainly consists of a tube made of PMMA ($\text{Ø}133 \times 6.5 \text{ mm}$, 2 m length) that surrounds the shroud over the entire bundle length. The bundle is filled from the bottom with approx. 20 kg of resin and hardener (epoxy system Rütapox 0273 with the hardener designated LC manufactured by Bakelite GmbH, Iserlohn). The epoxying process generally shows little heating during the curing stage due to the exothermal reaction. After epoxying the bundle the resin is allowed to harden for a minimum of one week. To obtain the cross sections a saw with a 2.0 mm-thick diamond blade (mean diamond size 138 μm) of 350 mm OD is used to cut the slabs at 1300 rpm. As an overview the sectioning map is given for test bundle QUENCH-06 in [Fig. 45](#). The exact elevations are listed in [Table 11](#). The 13 mm thick cross sections that were selected for metallographic examination (see also [Table 11](#)) were polished. For this purpose, the samples were infiltrated by "Araldit" resin to close up residual voids, then they were ground and polished. The work is performed using a semi-automatic machine with a closed water circuit for grinding and an automatic lubricant feeder for the polishing steps. In addition to the 13-mm thick sections, cross sections of 5 mm thickness were cut to use their claddings for the analysis of the hydrogen absorption in the Zircaloy metal.

8.3 Metallographic Examination

8.3.1 General state of the bundle

With reference to the cross sections of [Figs. 46 through 48](#) some features of the general state of the bundle are given. The missing corner rod B had been removed from the bundle during the transient test phase. For the elevations 737 and 750 mm the pellets and heater rod stubs of about half of the rods are missing, due to handling after cutting of the cross section slabs. Those could fall off as they did not stick to the cladding, which had not interacted with the pellets at those positions. At the elevations 837 and 850 mm, (where only some pellets were lost during preparation,) a fragment of corner rod A is seen after movement from above. At 887 and 900 mm the fragmentation of corner rod A is obvious as well, and a spacer grid fragment is found. At 937 and 950 mm fragmentation and downward movement of corner rod fragments are confirmed by their partial or total absence. At 987 and 1000 mm the spacer grid survived only partly, confirming the rubble relocation mentioned before. At 1137 and 1150 mm, i.e. within the upper electrode zone, corner rod A is missing as below. The cross sections between the two grid spacers, i.e. between 592 and 1050 mm, indicate considerable displacement of some test rods, due to rod bending.

Shroud melting and melt agglomeration at the external side is pronounced, but restricted to the orientation range $\sim 270^\circ$ to $\sim 0^\circ$. At 937 and 950 mm the damaged shroud region is seen to be split into an internal and an external part of residual metallic material, both supported by the corresponding scale. Few amounts of re-solidified shroud melt remained. Strong lateral bending of the residual rod and shroud structures occurred due to scale growth stress.

Within the test bundle no melt distribution can be detected within the magnification given by the cross section overview macrographs. As the test QUENCH-06 was the reference for the OECD ISP No. 45 exercise, preservation of the bundle arrangement and avoiding of gross melt relocation was thus successfully obtained as intended. More details, especially on stronger cladding damage remain to be described. As introduction to the next section the 21 individual rods of the 950 mm level (cross section QUE-06-10) are displayed in [Figs. 49 through 51](#).

8.3.2 Physico-chemical state and behavior of the bundle

Procedures

Based on the metallographic preparation of the cross section slabs by careful grinding and polishing, comprehensive investigation and photo documentation, the evaluation uses a choice of available examples for illustration. The interpretation of the bundle behaviour is explained by composing micrographs into thematic figures. The final bundle state is described, and the mechanisms of physico-chemical components' interaction and of the oxidation are deduced as far as possible. It was helpful to proceed from the lower bundle elevations upward, in the direction of increasing temperatures, and thus increasing extent of interaction. Thus, the state at lower elevations could be used to understand intermediate states of the higher elevations. Special attention was paid to the quench related phenomena.

For all prepared cross sections the scale thickness on simulator and corner rod surfaces as well as inner and outer shroud surfaces was measured. This was done at four positions around the rods and eight around the shroud, for the lowest elevation only half of that program. The results are collected in axial profiles for the different bundle components and their average.

Cross section QUE-06-02, bundle elevation 550 mm

At this cross section the fuel rod simulators are in original arrangement and undamaged within the intact spacer grid and shroud ([Fig. 52](#)). The corner rod B (on 45° , i.e. south-west position), pulled-off during the experiment just before the transient phase, is consequently missing; rod C on NW position is massive, whereas rods A and D at the SE and NE corners show their hollow TC instrumentation type. A few elongated rubble fragments are present. At the moderate temperature, reached here, the oxidation of all zircaloy components remained quite limited, as shown for the cladding example of rod No. 8 ([Fig. 52, right](#)). The scalloped scale growth front is a typical item of long-term pre-transition exposure to steam at moderate temperatures.

Cross section QUE-06-04, bundle elevation 750 mm

The overview on this cross section consists of the intact shroud, the slightly distorted fuel rod simulator arrangement, the corner rods as described, and an additional, massive corner rod stub at SE position, which obviously sunk down as fragment of corner rod A (Fig. 53). Since no tight contact between the epoxy resin and the inner rod components was provided, cross section slab preparation did not avoid the loss of pellet and heater rod stubs, which are missing for about half of the simulators. Together with the overview, rod No. 8 is documented as example for the oxidation state. In this respect the thermocouple and its attachment to rod No. 8 are intact. Not shown in detail is the strong oxidation and the partial missing of the Zircaloy tape, spot welded to rod No. 14 for TC attachment. Thus, the oxidation can be judged as important, but not yet advanced.

Cross section QUE-06-06, bundle elevation 850 mm

Here, the shroud is found slightly oval and the rod arrangement more distorted than below. The massive zone of the corner rod D is reached, and most interior simulator components remain present (Fig. 54). Items, identified by closer view, are the damaged TC attachment to rod No. 9, and a melt bridge between TC and rod No. 14. The latter rod and this pore containing melt is shown in higher magnification in Fig. 55. According to the duplex cladding scale (tetragonal external double layer with tin enriched interface, and cubic internal layer with characteristic decomposition microstructure, developed during cooling), the peak temperature at that position of the outer ring of rods was evaluated to be around 1900 K.

The temperature range up to 2100 K reached at this bundle elevation together with the slight lateral temperature profile across it allows to present with Figs. 56 to 58 a series of rods, showing the sequence of items, contributing to advancing damage: Fig. 56, documenting rod No. 10 of the outer ring, again shows the presence of duplex cladding scale, the non-melted metallic part of the cladding and the absence of interaction with the ZrO₂ pellet. The next in the series, rod No. 3 of the inner ring exhibits a previously molten metallic part of the cladding, due to the higher temperature, but not yet pellet interaction (Fig. 57). The last example (rod No. 2) shows filling of the gap by molten cladding and formation of an interaction layer at positions of pellet contact (Fig. 58). As introduction to the next higher elevation it shall be mentioned finally that rod-internal downward relocation of cladding melt was not observed at 850 mm.

Cross section QUE-06-08, bundle elevation 900 mm

The most striking item of this elevation overview (Fig. 59) is the melt accumulation at the outer side of the shroud on one third of the circumference in SE orientation, together with the bent shroud contour. Obviously, still another fragment of the tube of corner rod A, essentially not oxidized, has found its final position here during cool-down or due to posttest handling. (The melt relocation void within the tube of corner rod A marks the rod cut, which stayed at original elevation.) All pellets and heater stubs have survived cross section preparation. The advanced shroud oxidation on its inner side is mentioned next, as not illustrated. The melt, attached to rod No. 8 (see Fig. 59, top right) is related to the originally close thermocouple, and seems to have relocated downward from TC failure position. Other melt between the

bundle structures is very scarce, and therefore not considered in detail. Rod-internal melt formation is more frequently seen than in the previous elevation, the same holds for gap filling and pellet interaction; but internal void formation by melt relocation is seldom found, obviously because additional melt was provided from above. All fuel rods are examined in through-wall cracked condition. Generally no crack surface oxidation took place, indicating late crack formation during quenching. However, a few rod circumference positions show widened surface cracks (flaws), interpreted to have formed at temperature. Nevertheless, consequences of steam access were generally not identified. Examples for the advanced rod damage are shown in Figs. 60 to 62:

Fig. 60 depicts the central rod, interpreted to have exceeded 1900 K according to duplex scale, but to have not reached complete cladding melting, according to the kept contour and gap towards the pellet. By creeping of the weak metal in response to scale growth stress, some large “voids” may have formed at temperature. After cooling, especially at those positions the embrittled or even pre-cracked material is easily damaged further during cross section preparation. Consequently, the dark features within the metal zone are not all to be interpreted as voids, but as consequence of the mentioned creep and artefact formation. Fig. 61 illustrates details at one position of rod No. 11 in much more perfect preservation, the columnar external scale sub-layer, the decomposed cubic internal sub-layer, showing characteristic α -Zr(O) phase precipitation and a cool-down influenced growth front, the precipitation-free α -Zr(O) matrix, the pellet/cladding interaction layer and the pellet, the latter two separated due to gap formation during quenching. Finally documented are rods No. 19 and No. 5 in comparison, which show quite comparable features, but no pellet interaction (Fig. 62).

Cross section QUE-06-10, bundle elevation 950 mm

Further 50 mm above, the hottest zone is depicted by the cross section overview, given in Fig. 63. The external shroud melting and melt accumulation is covering more than half of the circumference. Only the NW oriented corner rod is found at place. All simulator rods are still in fairly compact shape and separately arranged. Only a few rubble fragments are seen. The central rod (see Fig. 63, bottom right) has caught some melt wetting the rod outer surface. Details, observed for this rod are shown in Fig. 64: The external melt, assumed to be cladding melt, but mostly oxidized by steam, can be distinguished from the substrate cladding scale with its duplex morphology. Next follows the metallic cladding residual layer, partly and locally consumed by internal melt relocation on the one hand and pellet interaction on the other. A thinner cover layer on some internal surface positions, apart from pellet contact, can be only explained by ingress of steam in a rather late test phase. The metallic cladding matrix shows precipitates of ceramic phase, most probably ZrO_2 , which might have formed at temperature according to the melt pool oxidation interpretation given in [13].

For rod No. 4 two quite different aspects, observed at opposite sides, are reported in Fig. 65. A broad opening through cladding scale is seen (towards west), and the fully oxidized residual structures below allow to conclude that they were oxidized by steam ingress. Their form indicates the reverse conclusion, that a fraction of the previous metallic melt had found its way out of the rod. Close and continued pellet/cladding contact (at east position) has resulted in a thick interaction layer, which has contributed to the almost complete metal

conversion. Melt of the cladding type, as described to have been distributed from rod No. 4, was e.g. found on rod No. 3, where it formed a wetting, but somewhat porous cover layer, which has completely oxidized at the final position.

Detailed inspection of rod No. 14 allows again, to document the combined effect of different mechanisms at the same place, as depicted in [Fig. 66](#): Relocated melt covers the cladding partly, whereas at the inner cladding surface pellet interaction as well as void formation due to cladding melt relocation took place. Advanced oxidation of the residual metallic cladding part went on in molten state and precipitation of ZrO_2 phase took place. The described cladding melt oxidation is also illustrated in [Fig. 67](#) for rods No. 20 and 12. Whereas the precipitation seems to have occurred in the solid state for rod No. 20, dendritic growth features for rod No. 12 indicate formation at temperature by melt decomposition.

Melt oxidation is observed for only a smaller part of the pool of melt, accumulated between the internal shroud scale and the surrounding ZrO_2 fiber insulation. Melting of the shroud has occurred, melt relocation from above, and penetration into the fiber material by its dissolution. But the more effective oxidation source was the outward penetrating steam, according to the thickness of scale on surfaces, resulting from the exposure history (see [Fig. 68](#), bottom, left). This more directly steam exposed melt zone is showing a considerable amount of ceramic precipitates, interpreted to have formed at temperature, according to the pool oxidation mechanism, which was already cited [13]. In contrast, the bulk of the melt is found to be almost purely metallic. (As an exception, a banded zone, which is not documented in the figure, was identified to contain tiny precipitates in regular distribution, interpreted to indicate the position of the original shroud surface).

Cross section QUE-06-12, bundle elevation 1000 mm

At the upper end of the electrically heated zone and a spacer grid elevation the bundle is found less damaged than below: Shroud bending, and thinning due to melt relocation, are restricted to SE direction. Spacer grid remnants survived at S and N, and all rods are complete. (Note the missing of SE corner rod, as it broke and fell in parts.) Together with the overview, [Fig. 69](#) shows rods No. 13 and 4, spacer and shroud. Details, given for the example of rod No. 8 ([Fig. 70](#)) indicate no cladding melting, but still thick scale, some oxidation of through-wall crack surfaces and some inner surface oxidation.

Cross section QUE-06-14, bundle elevation 1150 mm

Within the upper electrode zone ([Fig. 71](#)) the simulators, consisting of molybdenum rods and Zry cladding, show intact plasma sprayed ZrO_2 protection layer and moderate external cladding oxidation.

8.3.3 Lateral and axial oxidation profiles

The results of this measurement task are illustrated in [Figs. 72 to 78](#). Compared to the scale thickness of $\sim 20 \mu m$ at 550 mm elevation ([Fig. 72](#)) at least fivefold thickness is determined at 750 mm ([Fig. 73](#)). Here, local variations are observed, a flat general profile across the bundle, retarded inner surface shroud oxidation and traces of external scale. At 850 mm ([Fig.](#)

74) similar features hold for scales of more than twofold thickness compared to the previous elevation.

At 900 mm (Fig. 75) the oxidation profile through bundle and shroud reflects the shroud melting at SE orientation. Here, important external and strong internal shroud oxidation contrasts to the opposite side (NW), which shows less internal shroud oxidation and no external one. Rod oxidation gives a comparable trend from SE to NW or W. At 950 mm (Fig. 76), where the highest bundle temperatures were recorded, the scale thickness range, obtained, includes complete cladding conversion to ZrO_2 (data underlined in Fig. 76). The profile is as oblique as found for the elevation below. Very similar results are obtained for the elevation 1000 mm, further 50 mm higher (Fig. 77): The scale thickness values for the rods rise in a clear trend from W to E. Besides this, the extent of oxidation marks the general decrease above the temperature maximum. Fig. 78, giving scale thickness values mostly below $\sim 100 \mu\text{m}$ for 1150 mm elevation, concludes the series.

The reasons for the development of asymmetric scale thickness profiles at 900 mm and above cannot be completely traced. It is plausible to assume, that some minor rod and consequently electrical heat source re-arrangement, might have caused some steam flow re-distribution, thus allowing a positive feedback for increasing the distortion of the temperature profile. As such profiles have not been obtained in previous QUENCH experiments, the observation seems to indicate some variability in response of a small test bundle to coupled triggering aspects. This might be the standard case for a real fuel element, which is not dependent on fixed boundary conditions. Unfortunately, such integral phenomena between deterministic and statistic can hardly be studied experimentally as well as analytically.

The results of the obtained lateral temperature profiles are summarized in axial profiles for the different rod types and the shroud, and further reduced to the common profile for all structures and the range of deviation from mean values. [Fig. 79](#) gives this condensed information.

Finally included is an approach towards the temporal oxidation profile, using the mechanistic SVECHA code. The intention was to provide information on the oxide layer thickness at the time of flooding, 7120 s, for comparison with results of ISP-45 calculations. Direct experimental information on the oxide layer thickness of the corner rod is available for 6620 s, the time of its removal, but not for the bundle at 7120 s, i.e. the time at flooding, 500 s later. In the upper diagram of [Fig. 80](#) the results of posttest calculations with the SVECHA code at 6620 and 7120 s are presented together with the measured oxide layer thickness at 6620 s (corner rod data). On the basis of this measured oxide scale profile the temperatures were recalculated to match the measured oxide layer thickness at this time. The recalculation was then extended to 7120 s, the time of flooding. The lower diagram of Fig. 80 therefore shows the results of SVECHA code calculations at both times, 6620 and 7120 s.

8.3.4 Summary and conclusions

The shroud failure range between 870 and 1010 mm elevation and 0° to 270° (south to east) orientation reflects the peak temperature zone of the bundle. Breach formation, steam penetration, external shroud melt accumulation and oxidation took place there. The

metallographic preparation and inspection of cross sections allowed a detailed mechanistic analysis of the bundle damage and its history: Rod bending after loss of sufficient spacer grid support are assumed to have caused modified rod arrangements at the different elevations, local development of hot spots, an asymmetry in the temperature profile, shroud bending and melting. All those items should have contributed to the broad lateral range of cladding scale thickness, observed especially for the elevations, which saw the highest temperatures. However, the combination of the lateral scale profiles, determined for every rod and elevation, gave a pronounced axial profile of quite regular form.

The QUENCH-06 bundle has withstood the experimental transient with essentially intact rod geometry, whereas considerable cracking and some fragmentation occurred during the phase of water quenching. The behavior was dominated by the strong steam oxidation of the fuel rod simulator cladding (external side), the corresponding ZrO_2 scale growth, and the embrittlement of the residual metallic material. In comparison, the cladding interaction with the ZrO_2 simulator pellets, the rod-internal melt formation, and the internal oxidation by steam ingress along through-wall cracks were of local and secondary importance. The QUENCH-06 post-test examination results correspond reasonably well to those of the temperature and hydrogen evolution measurements.

Close similarities are seen for the QUENCH-06 bundle after water quenching in comparison to QUENCH-04 and QUENCH-05, both rapidly steam-cooled, with respect to the moderate response of bundle temperature and H_2 production on fast cool-down.

In contrast, QUENCH-01 had shown important crack surface oxidation, whereas in QUENCH-02 and QUENCH-03 considerable melt relocation and oxidation had taken place. For both different types of test conditions much more violent hydrogen evolution had been observed. The interpretation of the hydrogen signal remains the task of the ongoing QUENCH program, which, among other parameters, includes meanwhile the presence of an absorber arrangement.

In the blind phase of the OECD/NEA ISP-45 exercise [14] the comparison of results indicated code-to-code differences in the mechanistic treatment of phenomena, and occasionally, inadequate balancing between them. It will be most important for the simulation of more severe accident situations, not only to re-consider all pertinent phenomena and to revise their ranking, but also to account for their inter-dependencies. Integral experiments towards such phenomena and their interaction will provide the improved mechanistic basis for future code development and verification efforts.

8.4 Hydrogen Absorption by Zircaloy

Various 5 mm thick cross sections were used for hydrogen absorption analysis (see Table 11). The amount of absorbed hydrogen in specimens of that slices was analyzed by hot extraction under flowing argon gas and determination of the released hydrogen by mass spectroscopy.

Fig. 81 summarizes the results of these analyses showing the axial profile of the hydrogen absorbed by the Zircaloy-4 metal. Most data of specimens from the hot zone are between 5 and 10 at-% of dissolved hydrogen in the metal phase. A maximum of 24 at-% was measured at elevation 900 mm at rod 2. The integral amount of hydrogen absorbed was estimated to be 1-2 g (assuming a mean hydrogen absorption of 5 at-% over 500 mm bundle length). This value is comparable with the results obtained after the water quench tests QUENCH-01 and QUENCH-02 (1 g and 5 g, respectively) and higher than for the steam cooling tests QUENCH-04 and QUENCH-05 (0.1 g and 0.4 g, respectively).

9 Calculational Support

9.1 Investigation of the oxidation and hydrogen behavior with the FZK code CALUMO

Blind posttest calculations for the QUENCH-06 experiment have been done with the standard version of the CALUMO code [15] in the state as obtained for the calculation campaign of QUENCH-05 [10]. The quench model implemented in the code has been developed for QUENCH-01 [17] and has since then never again been tested as only steam-cooled tests, as QUENCH-05 and QUENCH-07, were calculated. Thus, the posttest calculations for QUENCH-06 mean a check of this important model. The other main interest of the calculations with CALUMO is with the oxidation and hydrogen production phenomena. A good simulation of the temperature evolutions in the fuel rod simulators and the shroud must, of course, be achieved by the code, otherwise one has no chance to obtain reasonable results. It should also be noted that the oxidation correlations of Leistikow et al. [16] have been used as was the case for all the other QUENCH posttest calculations done so far. It appears that these correlations allow a good simulation of the experimental findings of the oxidation behavior.

Results of code calculations in comparison to the respective measured data are given in Figs. 82 to 89. These are the temperature evolutions between 150 and 1250 mm, the axial profiles of oxide scale thickness of the fuel rod simulators and the shroud, and the results on hydrogen production, i.e. rates and total production.

In Figs. 82 through 85 the average temperature in the bundle “trodz”, the average temperature in the inner cluster of 9 fuel rod simulators “tcenz” and the average shroud temperature “tshrz” are plotted. They are compared to the available thermocouple readings.

In the overall, the temperature evolution in the bundle and the shroud is simulated in a satisfactory way by the code. Most of the features of the temperature evolution are rather well reproduced, especially in the heated zone below 750 mm. The temperature rise to steady-state conditions (calibration phase), the pre-oxidation phase, the temperature transient, and the cooldown phase match well to a certain extent although the temperatures in the lower part of the heated zone (150-450 mm) are a bit low.

As was the case for the QUENCH-05 results [10] there is some serious difference between measured and calculated temperature values between 750 and 950 mm during the pre-oxidation phase. The flat temperature evolution could not be well reproduced by the code. The calculated rod and shroud temperatures rise distinctly, i.e. 100-150 K above the measured ones. That means that the calculated oxide scales grow faster than in reality. This effect ends a further rise of the temperatures, so that towards the end of the pre-oxidation phase the calculated temperatures approach the measured ones.

In the transient phase there is limited information on the temperature rise from shroud thermocouple readings and from only one rod thermocouple at 750 mm. At 750 mm the temperature seems to be rather well met by the code during the first part of the transient phase, but at 850 and 950 mm the calculated temperature rise is below the measured one even from the very beginning of the transient. There are indications from the thermocouple readings that a temperature escalation occurred in the second half of the transient phase in the upper part of the heated zone (about 700-1000 mm). The assumption is that this was caused by the bending of the fuel rods. Most probably, the escalation evolves first in the inner part of the bundle. Heat transfer by radiation then leads to a delayed temperature increase in the outer part of the bundle and the shroud. This effect is not yet modeled in the code, and a temperature escalation cannot be simulated.

Due to some modification in the model for axial heat transfer, the situation in the upper unheated zone was considerably improved compared to earlier calculations for QUENCH-01 [17] and QUENCH-04 [15] although the calculated bundle temperatures between 1050 and 1150 mm are a bit low. Except for the temperature escalations in the shroud thermocouples, which rise towards the end of the transient phase, the situation for the CALUMO code is not so bad.

These temperature escalations of the shroud thermocouples are observed in all QUENCH tests done so far irrespective of the test conditions. The mechanism of convective heat transfer in the Ar-filled volume between shroud and cooling jacket above the heated zone given in [10], and [18] can explain the experimental fact that only the respective shroud thermocouples show this effect but not the cladding thermocouples. Up to now there is no model for convective heat transfer in the Ar volume implemented in the CALUMO code.

The bundle code CALUMO was not meant to serve as a sophisticated thermo-hydraulic code, but the aim was to implement a simple quench model which should reproduce the most important features of the quench phase in a satisfying way as there is the cooldown of the fuel rod simulators and the shroud, the production of steam, and the propagation of the quench front. Of course, all these effects are interlinked, and it would be insufficient if the code simulates only one or two of these three features.

In order to provide a good visualization of the temperature evolution during the transient and the quench phase the time scale was extended in Figs. 1 and 2 for this period. It is obvious from this that in the in the quench phase the cooldown is in the overall relatively well reproduced by the code. In Fig. 86 the calculated values of the velocity of the quench front and its axial position in comparison with an experimental curve obtained from evaluations of

thermocouple readings are shown. The calculated quench front rises too fast, and the evolution of the quench velocity shows some indentations which are not yet understood.

The steam production during the quench phase (see Fig. 87) is also rather perturbed and seems a bit low. As there are 40 g/s of quench water injected into the test section, we would expect a steam production somewhat above 20 g/s. A higher steam production would lead to a lower velocity of the quench front. As the temperature in the lower and especially in the upper part of the heated zone was indeed higher than calculated by the code, it is clear that the calculated steam production is too low and therefore the quench velocity too high. The amount of steam produced during the quench phase increases, of course, with the heat stored in the bundle and the shroud.

The calculated profiles of axial scale thickness are plotted in [Fig. 88](#) together with experimental values from posttest examinations, with "dox" denoting the oxide scales of the inner cluster of nine fuel rods, "doxa" that of the outer ring of 12 fuel rods and four corner rods, and "doxsh" the oxide scale of the shroud. Calculated profiles are shown for three different times, namely for the time when a corner rod was withdrawn ($t = 6640$ s), second at the time of the beginning of the temperature escalation ($t = 7140$ s), and at the time when the calculation is finished. The comparison at 6620 s shows that up to this time the growth of the oxide scales is relatively well met. The measured axial profile of the withdrawn corner rod is to be compared with the curve for „doxa“. As concerns the end state, the calculated axial profile for the 9 fuel rod simulators of the inner part of the bundle compares relatively well with the measured profile. But for the outer part of the bundle and for the shroud the calculated values of oxide scale thickness are much too low between about 700 and 1100 mm. The strong growth of the oxide scales occurred presumably during the temperature escalation, a phenomenon, which is not simulated by the code. This should explain the difference between measured and calculated values. It is, however, not clear why the temperature escalation did not have a greater impact on the inner part of the bundle. In [Fig. 88](#) only the mean values of the heated fuel rod simulators are given. It could be that the effect of the temperature escalation could be seen on the maximum values of the oxide scale thickness not shown in [Fig. 88](#). There is a downward shift for all the calculated profiles by about 50 to 100 mm. The reason for this systematic discrepancy is not clear at the moment.

A comparison of measured and calculated hydrogen values for production rate and time integrated values is to be seen in [Fig. 89](#). The agreement is satisfactory up to nearly the end of the transient phase. There is then a very high peak in the experimentally measured hydrogen production rate which is not reproduced by the CALUMO code. As this peak starts well before the onset of quenching it is presumably no quench effect. It seems to be caused by the temperature escalation in the inner part of the bundle arising in the upper part of the heated zone (about 700-1000 mm). This effect is also well-known from tests QUENCH-04 and QUENCH-05.

There is a second peak albeit of much lower height observed in the hydrogen production rate a bit after the onset of quenching. This seems to be a true quench effect which could be linked to cracking effects of the oxide scale. As these two peaks in the hydrogen production rate are not reproduced by the code, the calculated overall hydrogen production is low by

about 10 g. This is also in accordance with the findings on the oxidation behavior between about 750 and 1100 mm.

The CALUMO bundle code could not provide a perfect simulation of the experiment QUENCH-06. There are some problems with the temperature evolution during the pre-oxidation phase, and the temperatures in the second part of the transient phase are underestimated to some extent in the upper part of the heated zone. Especially the temperature escalation, which occurred there was not simulated, as this is outside the scope of the modelling. This leads to an underestimation of the oxidation in the transient phase and of course to an underestimation of the hydrogen production. Despite these problems one can note that the results of the code are in the overall coherent with the experimental findings. An overprediction of the hydrogen production would have been a bad indication in view of the underestimation of the temperatures and the oxidation in certain axial regions.

9.2 Calculational support with SCDAP/RELAP5

Within FZK institutional R&D activities calculations are made to define experimental parameters of the QUENCH experiments and to interpret the experimental results after the experiment had been performed, using the in-house version of SCDAP/RELAP5mod 3.2, S/R5irs. It contains an improved model for heat transfer in the transition boiling region [19], an adaptation of the CORA heater rod model to the conditions of the QUENCH facility, and the material property data for ZrO_2 instead of those for UO_2 to model the pellets. The various calculations also rely on the experience gained from calculations, done up to then. Especially the adjustment of the electrical resistance of the circuit outside the electrical heater rods, performed on the basis of test QUENCH-01 [7], was kept.

9.2.1 Modeling of the QUENCH facility

As for previous QUENCH tests a 16-nodes facility model as defined hereafter is used for pre- and post-test calculations. In the radial direction the whole facility including the containment is modeled, because the radial heat losses out of the bundle depend ultimately on the ambient room temperature. This modeling is mandatory for all work performed before experimental data are available, and it is desirable for all post-test analyses, because the calculated data are more detailed than the experimental ones.

Axially 16 axial nodes are used in sum: the heated part is modeled with ten 0.1 m long meshes; in the lower and upper electrode zones 0.45 and 0.6 m, respectively, of the test section are considered, each by three meshes, assuming molybdenum as electrode material. The unheated rod, the two rows of rods to be heated independently, the four Zircaloy corner rods, the inner and outer cooling jacket, and the containment are modeled as separate SCDAP components. In this way two-dimensional heat conduction within the structures and radiation between adjacent structures are taken into account. The temperature at the end of the rods is set to 300 K. For the electrical resistance of the circuit outside the electrical heater rods the same value of 4.2 m Ω per rod was used as for test QUENCH-01 [7]. The ZrO_2 fiber insulation is modeled to end at the upper end of the heated zone. With this exception all structures must be modeled to have the same length because of limitations in the code. Therefore the upper and lower head cannot be modeled in all details.

The bundle flow and the gas atmospheres outside the outer cooling jacket, e.g. in the containment, are represented by a single channel each. Besides the gas atmospheres outside the outer cooling jacket are assumed to be stagnant, thus neglecting natural convection in these regions. Because of restrictions in the code, where only a limited number of materials can be specified, these atmospheres are modeled to consist of argon.

The off-gas pipe is taken into account with its whole length of 3 m, including the orifice at the position where the gas sample for the mass spectrometer is taken and the orifice at the outlet of the off-gas pipe. The mass flows in the off-gas pipe and the adjacent cooling jacket are modeled to be one-dimensional, the structures are modeled as RELAP heat structures, thus taking into account radial heat transfer within the structures.

In addition a 32 nodes bundle model has been created as a fast running approximate solution, where all axial mesh lengths in the heater and the electrode zones are halved. All heated rods are simulated as a single SCDAP component; the corner rods are not modeled. The facility outside the argon and water cooling flows is not considered. Therefore the flow area for the cooling flow is changed on the basis of the 16 nodes facility model to result in realistic radial heat losses out of the bundle. The lower plenum, the inlet pipes and the fast water injection system ([Fig. 90](#)) were modeled in much more detail and with finer mesh lengths than in the 16 nodes facility model.

Meanwhile a 32 nodes facility model is available, where the whole facility is modeled as in the 16 nodes facility model, but all axial mesh lengths in the heated zone and the electrode zones are halved and the lower plenum, the inlet pipes and the fast water injection system are modeled as in the 32 nodes bundle model. Besides the radial discretization of the fuel simulator rods has been refined.

9.2.2 Pre-test calculations

Since test QUENCH-06 was intended to be run as test QUENCH-05 except for the quench phase, the test relied on the experience from that test and on pre-test calculations for QUENCH-05, where the main task consisted in determining the parameters of the pre-oxidation phase.

9.2.3 Post-test calculations

Post-test calculations were performed on the basis of the exact experimental values of inlet temperatures, mass flow rates, and power history. Fluid inlet temperature has been adjusted according to the reading of thermocouple TFS 2/1, bent into the flow channel to measure fluid inlet temperature. All three models were used, but the following presentation concentrates on the 16 and 32 nodes facility model, using the latter as a standard. [Fig. 91](#) indicates that the agreement between measured and calculated temperatures in the bundle is quite good for both facility models. The agreement for the argon cooling is a hint that calculated radial heat transfer out of the bundle is not too bad. A good agreement is also obtained for hydrogen production ([Fig. 92](#)), which is a sensible measure for the quality of the modelling. Radial differences in measured temperatures can only partly be reproduced by the calculations, because radiation heat transfer gives a certain radial temperature decrease,

but the thermal-hydraulic modelling of the bundle is one-dimensional, such giving the same fluid temperature for all components in the bundle at a given axial level. Detailed inspection shows that the first larger deviation from measured temperatures begins when at level 11 a temperature escalation is detected in the experiment (Fig. 93). Up to now temperature escalations are calculated to begin at the end of the heated zone, i. e. at the hottest spot. The reason for this discrepancy is still unclear.

For various times of the experiment axial temperature profiles (Fig. 94) the quite good agreement between calculated and measured values can also be seen. The figure shows furthermore that differences between the two nodalizations occur mainly in the upper electrode zone, giving better results for the finer discretization. Measured and calculated temperatures and oxide layer thickness at the time, when one of the corner rods was withdrawn are shown in Fig. 95. The oxide layer thickness is overestimated in the lower half of the heated zone. Several reasons may contribute to this finding, so the inadequate modelling of oxidation for low temperatures which are not of special interest in a severe accident code, and locally also the enhanced heat transfer in the vicinity of the grid spacer at 550 mm. Underestimation of the maximum value may also be due to a code error in post-processing the values calculated in the main part of the code. The axial profile of linear pin power demonstrates the necessity of an adequate model for the electrical heater, taking into account the positive feedback of local power input with temperature.

During the quench phase saturation temperature is calculated to be reached earlier with the 32 nodes version (Fig. 96), which seems to be more realistic. When quench water is switched off, 26,1 and 31.7 g of H₂, respectively, for the 32 and 16 nodes facility model are calculated to be produced in comparison to 35.7 g in the experiment. Filling of the bundle during quenching is calculated quite well up to 1 m with the 32 nodes model and for the lower half of the bundle with the 16 nodes version, but afterwards an unidentified code error, communicated to the code developer long ago, leads to unacceptably high mass errors and physically wrong results. With the 32 nodes version temperature escalation in the heated zone is overestimated. A complete flooding of the bundle is calculated, but in a shorter time than observed in the experiment. The mass error is much smaller than for each of the facility models.

9.2.4 Initial reflood conditions

During the post-test analyses of QUENCH-06 the comparison between measured data and those obtained by post-test calculations with S/R5irs revealed some inconsistencies with respect to the reflood initiation, as mentioned in the ISP-45 specification report [20]. An unexpected time delay was found between calculated water level and that deduced from measured temperatures and differential pressure. To identify the origin of this delay, a series of calculations with the 32 nodes bundle model and a profound comparison with experimental data as well as a detailed inspection of the facility revealed the reason for this delay.

Due to an unexpected leakage of a check-valve at the quench pump the quench inlet pipe must have drained out partially before quench initiation. Consequently, the specified mass flow rate is only relevant at the position of the quench pump, where it is measured, and not at the entrance into the lower plenum, where it is needed. Before adding to the fast quench

water injection system, the quench water had to refill the voided pipe, thus giving a certain delay. On the basis of these investigations the mass flow rate in the lower plenum, to be used for the calculations, could be specified and made available to the participants of ISP-45.

In Fig. 97 the calculated collapsed water level (sc16 final) as a measure for water level rise is added to the experimental values of liquid level quench water (Lm 501 raw and smoothed data, derived from a pressure difference sensor) and TC wetting data as derived visually from temperature readings. The sharp peak of Lm501 at 7180 s indicates the violent water injection and cannot be interpreted as a water level. The result of the S/R5irs posttest analysis is in the vicinity of the detected wetting signals. In this context the shroud outer surface thermocouples (TSH) are more relevant, because they are not influenced by dispersed droplet flow.

References

- [1] J.M. Broughton, P. Kuan, and D.A. Petti, "A Scenario of the Three Mile Island Unit 2 Accident," *Nuclear Technology*, 87, 34, 1989.
- [2] P. Hofmann, S. Hagen, V. Noack, G. Schanz, L. Sepold, "Chemical-Physical Behavior of Light Water Reactor Core Components Tested under Severe Reactor Accident Conditions in the CORA Facility," *Nuclear Technology*, vol. 118, 1997, p. 200.
- [3] S. Hagen, P. Hofmann, V. Noack, L. Sepold, G. Schanz, G. Schumacher, "Comparison of the Quench Experiments CORA-12, CORA-13, CORA-17," FZKA 5679, Forschungszentrum Karlsruhe, 1996.
- [4] S.M. Modro and M.L. Carboneau, "The LP-FP-2 Severe Fuel Damage Scenario; Discussion of the Relative Influence of the Transient and Reflood Phase in Affecting the Final Condition of the Bundle," OECD/LOFT Final Event, ISBN 92-64-03339-4, 1991, p. 388.
- [5] P. Hofmann, V. Noack, M.S. Veshchunov, A.V. Berdyshev, A.V. L.V. Matweev, A.V. Palagin, V.E. Shestak: „Physico-Chemical Behavior of Zircaloy Fuel Rod Cladding Tubes During LWR Severe Accident Reflood“, FZKA 5846, Forschungszentrum Karlsruhe, 1997
- [6] P. Hofmann, A. Miassoedov, L. Steinbock, M. Steinbrück, M. Veshchunov et al.: "Quench Behavior of Zircaloy Fuel Rod Cladding Tubes. Small-Scale Experiments and Modeling of the Quench Phenomena," FZKA 6208, Forschungszentrum Karlsruhe, 1999
- [7] P. Hofmann, W. Hering, C. Homann, W. Leiling, A. Miassoedov, D. Piel, L. Schmidt, L. Sepold, M. Steinbrück, "QUENCH-01, Experimental and Computational Results," FZKA 6100, Forschungszentrum Karlsruhe, 1998.
- [8] P. Hofmann, C. Homann, W. Leiling, A. Miassoedov, D. Piel, G. Schanz, L. Schmidt, L. Sepold, M. Steinbrück, "Experimental and Computational Results of the Experiments QUENCH-02 and QUENCH-03," FZKA 6295, 2000.
- [9] "Investigation of an Overheated PWR-Type Fuel Rod Simulator Bundle Cooled Down by Steam," Part I: L. Sepold, P. Hofmann, C. Homann, W. Leiling, A. Miassoedov, D. Piel, G. Schanz, L. Schmidt, U. Stegmaier, M. Steinbrück, H. Steiner, "Experimental and Computational Results of the QUENCH-04 Test," Part II: M.S. Veshchunov, A.V. Berdyshev, A.V. Boldyrev, A.V. Palagin, V.E. Shestak, "Application of SVECHA/QUENCH Code to the Analysis of the QUENCH-01 and QUENCH-04 Bundle Tests," FZKA 6412, 2002.

-
- [10] L. Sepold, C. Homann, A. Miassoedov, G. Schanz, U. Stegmaier, M. Steinbrück, H. Steiner, "Experimental and Computational Results of the QUENCH-05 Test," FZKA 6615, 2002.
- [11] L. Sepold, P. Hofmann, W. Leiling, A. Miassoedov, D. Piel, L. Schmidt, M. Steinbrück, "Reflooding Experiments with LWR-Type Fuel Rod Simulators in the QUENCH Facility," Nuclear Engineering and Design 204 (2001), 205-220.
- [12] W. Hering, C. Homann, J.-S. Lamy, "Interpretation and Comparison Report of the OECD International Standard Problem No. 45 (ISP-45/QUENCH-06)," FZKA 6677, 2002
- [13] M. S. Veshchunov, J. Stuckert, A. V. Berdyshev: „Modelling of Zr-O and U-Zr-O Melts Oxidation and New Crucible Tests." FZKA 6792, SAM-COLOSS-P040, Dec. 2002.
- [14] W. Hering, Ch. Homann, J.-S. Lamy, A. Miassoedov, G. Schanz, L. Sepold, M. Steinbrück; "Comparison and Interpretation Report of the OECD International Standard Problem No. 45 Exercise (QUENCH-06)." FZKA 6722, Jul. 2002.
- [15] H. Steiner, M. Heck, "The code CALUMO, a tool for the analysis for temperature transients in QUENCH tests," FZKA 6501, 2000.
- [16] S. Leistikow, et al, "Kinetik und Morphologie der isothermen Dampfoxidation von Zircaloy-4 bei 700 bis 1300 °C," KFK 2587, 1978.
- [17] H. Steiner, M. Heck: "Recalculation of the temperature transient in QUENCH-03 with the code CALUMO," Contribution to PSF Annual Report 2000, FZKA 6653, 2001, p.259
- [18] G. Choi and S.T. Korpela, "Stability of the Conduction Regime of Natural Convection in a Tall Vertical Annulus," J. Fluid Mech. 99, 1980, pp. 725–738.
- [19] V. Sanchez, E. Elias, Ch. Homann, W. Hering, D. Struwe, "Development and Validation of a Transition Boiling Model for the RELAP5/MOD3 Reflood Simulation," FZKA 5954, 1997.
- [20] W. Hering, Ch. Homann, A. Miassoedov, M. Steinbrück, "Specification of the International Standard Problem ISP-45 (QUENCH-06)," OECD/NEA/CSNI/R, 2001.
- [21] M. Steinbrück, C. Homann, A. Miassoedov, G. Schanz, L. Sepold, U. Stegmaier, H. Steiner, J. Stuckert, „Results of the QUENCH-09 Experiment with a B₄C Control Rod," FZKA 6829, 2004.
- [22] Ch. Homann, W. Hering, A. Miassoedov, L. Sepold, "Investigation of the Reflood Phase in QUENCH Experiments," accepted for the 12. International Conferene on Nuclear Eng. (ICONE 12), April 25-29, 2004, Arlington, Virginia, USA

Acknowledgements

At the Karlsruhe Research Center the broad support needed for preparation, execution, and evaluation of the experiment is gratefully acknowledged. In particular, the authors would like to thank Messrs. L. Anselment and S. Horn for the assembly of the heated test rods and for the instrumentation of the central rod, Messrs. J. Moch and R. Vouriot for assembling and instrumenting the test bundle, Mr. S. Horn for the preparation of the hydrogen measurement with the "Caldos" analyzer and the support for the test data selection. Furthermore, the authors would like to express their gratitude to Mr. D. Piel for the test data acquisition, Dr. W. Krauss for the hydrogen measurement with the "Prisma" mass spectrometer, to Mr. L. Anselment for sectioning the epoxied bundle, to Mrs. J. Laier and Mrs. I. Werner for processing the test data, and to Mrs. M. Heck for processing the results of the metallographic examination.

Table 1: QUENCH Test Matrix

Test	Quench medium	Flooding rate ¹⁾	Heat-up rate	Max. ZrO ₂ layer thickness ²⁾	Temp. at onset of flooding ³⁾	Remarks, objectives	Date of test conduct
QUENCH-00	Water	2.8 cm/s from bottom	1.0 K/s	≈ 500 μm	≈ 1800 K	COBE Project; commissioning tests.	Oct. 9 - 16, 97
QUENCH-01	Water	1.6 cm/s; from the bottom	0.5 K/s	≈ 300 μm	≈ 1900 K	COBE Project; partial fragmentation of pre-oxidized cladding.	February 26, 98
QUENCH-02	Water	1.6 cm/s; from the bottom	0.5 K/s	completely oxidized	> 2400 K	COBE Project; no additional pre-oxidation, quenching from high temperatures.	July 7, 98
QUENCH-03	Water	1.4 cm/s from the bottom	0.6 K/s	completely oxidized	> 2400 K	No additional pre-oxidation, quenching from high temperatures.	January 20, 99
QUENCH-04	Steam	≈ 50 g/s; from the bottom	0.5 K/s	≈ 170 μm	≈ 2300 K	Cooldown behavior of slightly pre-oxidized cladding by cold steam injection.	June 30, 99
QUENCH-05	Steam	≈ 50 g/s from the bottom	0.5 K/s	≈ 400 μm	≈ 2300 K	Cooldown behavior of pre-oxidized cladding by cold steam injection.	March 29, 2000
QUENCH-06	Water	1.4 cm/s from the bottom	0.5 K/s	≈ 660 μm	≈ 2300 K	OECD-ISP 45; blind test predictions by different computer codes.	December, 13 2000
QUENCH-07	Steam	≈ 15 g/s from the bottom	0.5 K/s	completely oxidized	> 2300 K	COLOSS Project; impact of B ₄ C absorber rod failure on H ₂ , CO, CO ₂ , and CH ₄ generation.	July 25, 2001

1) Flooding rate for water: rise of the water level at the -250 mm bundle elevation (single-phase flow).

2) Measured posttest at the bundle elevation of max. temperature.

3) Maximum measured or estimated temperature in test section

2002

Revised: March,

Table 2: Design characteristics of the QUENCH test bundle

Bundle type		PWR, 21 rods
Pitch		14.3 mm
Number of heated rods		20
Number of unheated rods		1
Cladding	heated rod	Zircaloy-4, \varnothing 10.75 / 9.3 mm L = 2278 mm (EL -593 to 1685)
Cladding	unheated (central) rod	Zircaloy-4, \varnothing 10.75 / 9.3 mm L = 2203 mm (EL -593 to 1610)
Overall rod length	heated rod (levels) unheated rod (levels)	2480 mm (EL -690 to 1790) 2842 mm (EL -827 to 2015, incl. extension piece)
Heater material		Tungsten (W)
Heater length		1024 mm
Heater diameter		6 mm
Annular pellet	heated rod unheated rod	ZrO ₂ ; \varnothing 9.15/6.15 mm; L=11 mm ZrO ₂ ; \varnothing 9.15/2.5 mm; L=11 mm
Pellet stack length	heated rod unheated rod	EL 0 to 1024 mm EL 0 to 1554 mm
Grid spacer (5)	material length location of lower edge	Zircaloy-4 (Zry), Inconel 718 (Inc) Zry 42 mm, Inc 38 mm Inc: -200 mm; Zry: 50, 550, 1050, 1410 mm
Shroud	material wall thickness outside diameter length (extension)	Zircaloy-4 2.38 mm 84.76 mm 1600 mm (EL -300 to 1300)
Shroud insulation	material insulation thickness extension	ZrO ₂ fiber ~ 37 mm EL -300 to 1000 mm
Molybdenum-copper electrodes:		
length of upper electrodes		766 mm (576 Mo, 190 mm Cu)
length of lower electrodes		690 mm (300 Mo, 390 mm Cu)
diameter of electrodes:	- prior to coating - after coating with ZrO ₂	8.6 mm 9.0 mm
Cooling jacket	material inner tube outer tube	1.4541 stainless steel \varnothing 158.3 / 168.3 mm \varnothing 181.7 / 193.7 mm

Table 3: List of instrumentation for the QUENCH-06 Test 31.01.01

Channel	Designation	Instrument, location	Output in
1	TFS 2/11	TC (W/Re) fuel rod simulator 8 (type 2), 750 mm, 135°	K
2	TFS 2/13	TC (W/Re) fuel rod simulator 2 (type 2), 950 mm, 225°	K
3	TFS 2/15	TC (W/Re) fuel rod simulator 4 (type 2), 1150 mm, 315°	K
4	TFS 2/17	TC (W/Re) fuel rod simulator 6 (type 2), 1350 mm, 45°	K
5	TSH 15/180	TC (W/Re) shroud outer surface, 1150 mm, 206°	K
6	TFS 3/10	TC (W/Re) fuel rod simulator 7 (type 3), 650 mm, 135°	K
8	TFS 3/13	TC (W/Re) fuel rod simulator 3 (type 3), 950 mm, 315°	K
9	TFS 3/14	TC (W/Re) fuel rod simulator 5 (type 3), 1050 mm, 45°	K
10	TFS 4/11	TC (W/Re) fuel rod simulator 14 (type 4), 750 mm, 45°	K
11	TFS 4/13	TC (W/Re) fuel rod simulator 20 (type 4), 950 mm, 135°	K
12	TSH 14/90	TC (W/Re) shroud outer surface, 1050 mm, 116°	K
13	TFS 5/11	TC (W/Re) fuel rod simulator 13 (type 5), 750 mm, 45°	K
15	TFS 5/13	TC (W/Re) fuel rod simulator 16 (type 5), 950 mm, 135°	K
17	TSH 16/180	TC (W/Re) shroud outer surface, 1250 mm, 206°	K
18	TSH 13/90	TC (W/Re) shroud outer surface, 950 mm, 116°	K
20	TSH 11/0	TC (W/Re) shroud outer surface, 750 mm, 26°	K
21	TSH 12/0	TC (W/Re) shroud outer surface, 850 mm, 26°	K
23	TFS 2/7	TC (NiCr/Ni) fuel rod simulator 6 (type 2), 350 mm, 45°	K
25	FM 401	Argon gas mass flow rate	g/s
32	TIT A/13	TC (W/Re) corner rod A, centre, 950 mm	K
33	TCRC 13	TC (W/Re) central rod, centre, 950 mm	K
35	TSH 9/90	TC (NiCr/Ni) shroud outer surface, 550 mm, 116°	K
36	TSH 9/270	TC (NiCr/Ni) shroud outer surface, 550 mm, 296°	K
37	TFS 3/16	TC (W/Re) fuel rod simulator 7 (type 3), 1250 mm, 135°	K
38	TFS 5/9	TC (NiCr/Ni) fuel rod simulator 10 (type 5), 550 mm, 315°	K
39	TFS 2/9	TC (NiCr/Ni) fuel rod simulator 8 (type 2), 550 mm, 135°	K
40	TIT D/12	TC (W/Re) corner rod D, centre, 850 mm	K
41	TCR 13	TC (We/Re) central rod, cladding outer surface, 950 mm, 225°	K
42	TFS 5/8	TC (NiCr/Ni) fuel rod simulator 21 (type 5), 450 mm, 135°	K
43	TFS 3/8	TC (NiCr/Ni) fuel rod simulator 5 (type 3), 450 mm, 45°	K
46	TIT C/9	TC (NiCr/Ni) corner rod C, centre, 550 mm	K
47	TFS 5/15	TC (W/Re) fuel rod simulator 19 (type 5), 1150 mm, 225°	K
48	TFS 5/16	TC (W/Re) fuel rod simulator 21 (type 5), 1250 mm, 135°	K
49	TFS 5/17	TC (W/Re) fuel rod simulator 10 (type 5), 1350 mm, 315°	K

Chan-nel	Designation	Instrument, location	Output in
50	TFS 3/12	TC (W/Re) fuel rod simulator 9 (type 3), 850 mm, 225°	K
51	TFS 5/12	TC (W/Re) fuel rod simulator 15 (type 5), 850 mm, 315°	K
52	TSH 13/270	TC (W/Re) shroud outer surface, 950 mm, 296°	K
53	TSH 14/270	TC (W/Re) shroud outer surface, 1050 mm, 296°	K
54	TSH 11/180	TC (W/Re) shroud outer surface, 750 mm, 206°	K
55	TSH 12/180	TC (W/Re) shroud outer surface, 850 mm, 206°	K
58	TCRC 9	TC (NiCr/Ni) central rod, centre, 550 mm	K
66	TSH 15/0	TC (W/Re) shroud outer surface, 1150 mm, 26°	K
67	TSH 16/0	TC (W/Re) shroud outer surface, 1250 mm, 26°	K
68	T 512	Gas temperature bundle outlet	K
72	TFS 2/1	TC (NiCr/Ni) fuel rod simulator 4 (type 2), -250 mm, 315°	K
73	TFS 2/2	TC (NiCr/Ni) fuel rod simulator 6 (type 2), -150 mm, 45°	K
74	TFS 2/3	TC (NiCr/Ni) fuel rod simulator 8 (type 2), -50 mm, 135°	K
75	TCRI 7	TC (NiCr/Ni) central rod, cladding inner surface, 350 mm	K
76	TFS 2/6	TC (NiCr/Ni) fuel rod simulator 4 (type 2), 250 mm, 315°	K
77	TCRI 9	TC (NiCr/Ni) central rod, cladding inner surface, 550 mm	K
78	TFS 5/4/0	TC (NiCr/Ni) fuel rod simulator 15 (type 5), 50 mm, 315°	K
79	TFS 5/4/180	TC (NiCr/Ni) fuel rod simulator 21 (type 5), 50 mm, 135°	K
80	TFS 5/5	TC (NiCr/Ni) fuel rod simulator 16 (type 5), 150 mm, 135°	K
81	TFS 5/6	TC (NiCr/Ni) fuel rod simulator 18 (type 5), 250 mm, 45°	K
82	TFS 5/7	TC (NiCr/Ni) fuel rod simulator 19 (type 5), 350 mm, 225°	K
83	TSH 4/270	TC (NiCr/Ni) shroud outer surface, 50 mm, 296°	K
84	TSH 3/180	TC (NiCr/Ni) shroud outer surface, -50 mm, 206°	K
85	TSH 4/180	TC (NiCr/Ni) shroud outer surface, 50 mm, 206°	K
86	TSH 7/180	TC (NiCr/Ni) shroud outer surface, 350 mm, 206°	K
87	TSH 4/90	TC (NiCr/Ni) shroud outer surface, 50 mm, 116°	K
88	TSH 1/0	TC (NiCr/Ni) shroud outer surface, -250 mm, 26°	K
89	TSH 4/0	TC (NiCr/Ni) shroud outer surface, 50 mm, 26°	K
90	TSH 7/0	TC (NiCr/Ni) shroud outer surface, 350 mm, 26°	K
91	TCI 9/270	TC (NiCr/Ni) cooling jacket inner tube wall, 550 mm, 270°	K
92	TCI 10/270	TC (NiCr/Ni) cooling jacket inner tube wall, 650 mm, 270°	K
93	TCI 11/270	TC (NiCr/Ni) cooling jacket inner tube wall, 750 mm, 270°	K
94	TCI 13/270	TC (NiCr/Ni) cooling jacket inner tube wall, 950 mm, 270°	K
95	TCR 7	TC (NiCr/Ni) central rod, cladding outer surf., 350 mm, 315°	K
96	TCI 1/180	TC (NiCr/Ni) cooling jacket inner tube wall, -250 mm, 180°	K
97	TCI 4/180	TC (NiCr/Ni) cooling jacket inner tube wall, 50 mm, 180°	K

Chan- nel	Designation	Instrument, location	Output in
98	TCI 7/180	TC (NiCr/Ni) cooling jacket inner tube wall, 350 mm, 180°	K
99	TCI 11/180	TC (NiCr/Ni) cooling jacket inner tube wall, 750 mm, 180°	K
100	TCI 12/180	TC (NiCr/Ni) cooling jacket inner tube wall, 850 mm, 180°	K
101	TCI 13/180	TC (NiCr/Ni) cooling jacket inner tube wall, 950 mm, 180°	K
103	TCR 9	TC (NiCr/Ni) central rod, cladding outer surf., 550 mm, 315°	K
104	TCI 9/90	TC (NiCr/Ni) cooling jacket inner tube wall, 550 mm, 90°	K
105	TCI 10/90	TC (NiCr/Ni) cooling jacket inner tube wall, 650 mm, 90°	K
106	TCI 11/90	TC (NiCr/Ni) cooling jacket inner tube wall, 750 mm, 90°	K
107	TCI 13/90	TC (NiCr/Ni) cooling jacket inner tube wall, 950 mm, 90°	K
109	TCI 1/0	TC (NiCr/Ni) cooling jacket inner tube wall, -250 mm, 0°	K
110	TCI 4/0	TC (NiCr/Ni) cooling jacket inner tube wall, 50 mm, 0°	K
111	TCI 7/0	TC (NiCr/Ni) cooling jacket inner tube wall, 350 mm, 0°	K
112	TCI 11/0	TC (NiCr/Ni) cooling jacket inner tube wall, 750 mm, 0°	K
113	TCI 12/0	TC (NiCr/Ni) cooling jacket inner tube wall, 850 mm, 0°	K
114	TCI 13/0	TC (NiCr/Ni) cooling jacket inner tube wall, 950 mm, 0°	K
115	TCI 15/0	TC (NiCr/Ni) cooling jacket inner tube wall, 1150 mm, 0°	K
116	TCRC 7	TC (NiCr/Ni) central rod, centre, 350 mm	K
117	TCO 9/270	TC (NiCr/Ni) cooling jacket outer tube surface, 550 mm, 270°	K
118	TCO 4/180	TC (NiCr/Ni) cooling jacket outer tube surface, 50 mm, 180°	K
120	TCO 1/0	TC (NiCr/Ni) cooling jacket outer tube surface, -250 mm, 0°	K
121	TCO 7/0	TC (NiCr/Ni) cooling jacket outer tube surface, 350 mm, 0°	K
123	T 601	Temperature before off-gas flow instrument F 601	K
128	T 104	Temperature quench water	K
131	T 205	Temperature before steam flow instrument location 10 g/s	K
134	T 303	Temperature before total flow instrument location	K
135	T 401	Temperature before gas flow instrument location	K
136	T 403	Temperature at inlet cooling gas	K
137	T 404	Temperature at outlet cooling gas	K
138	T 501	Temperature at containment	K
139	T 502	Temperature at containment	K
140	T 503	Temperature at containment	K
141	T 504	Temperature at containment	K
142	T 505	Temperature at containment	K
143	T 506	Temperature at containment	K
144	T 507	Temperature at containment	K
145	T 508	Temperature at containment	K

Chan- nel	Designation	Instrument, location	Output in
147	T 510	Temperature at containment	K
148	T 511	Gas temperature at bundle inlet	K
149	T 901	Temperature before off-gas flow instrument F 901, behind condensor	K
154	P 205	Pressure at steam flow instrument location 10 g/s	bar
155	P 303	Pressure before total flow instrument location	bar
157	P 511	Pressure at bundle inlet	bar
158	P 512	Pressure at bundle outlet	bar
159	P 601	Pressure before off-gas flow instrument F 601	bar
160	P 901	Pressure before off-gas flow instrument F 901, behind condensor	bar
165	P 411	Pressure Ar-Kr supply	bar
166	P 403	Pressure Ar cooling of cooling jacket	bar
167	P 406	Pressure insulation shroud/cooling jacket	bar
168	F 104	Flow rate quench water	l/h
170	F 205	Flow rate steam 10 g/s	g/s
171	F 303	Flow rate at bundle inlet (steam + argon), orifice	mbar
174	F 601	Flow rate off-gas (orifice)	mbar
178	E 501	Electric current inner ring of fuel rod simulators	A
179	E 502	Electric current outer ring of fuel rod simulators	A
180	E 503	Electric voltage inner ring of fuel rod simulators	V
181	E 504	Electric voltage outer ring of fuel rod simulators	V
	E 505	Electric power inner ring of fuel rod simulators	W
	E 506	Electric power outer ring of fuel rod simulators	W
	Ptot	Total electric power	W
	Fm 104	Flow rate quench water	g/s
	Fm 403	Flow rate cooling gas	g/s
	Lm 501	Liquid level quench water	mm
	Lm 701	Liquid mass condensation vessel	g

Remarks:

1. Tip of thermocouple TFS 2/1 is bent into flow channel to measure the fluid temperature.
2. The angles refer to the azimuthal position (approximate values) of the respective structure.
3. Data without a channel number are not part of the instrumentation list, but are included in the set of available experimental data.

Table 4: QUENCH-06; Failure of thermocouples

Thermocouple	Elevation [mm]	Time at failure [s]	Failure temperature [K]
TFS 2/5	150	Pre-test failure	
TFS 5/10	650	Pre-test failure	
TFS 4/11	750	7124	1906
TFS 2/12	850	Pre-test failure	
TFS 3/12	850	7131	1879
TFS 2/13	950	6799	1636
TFS 3/13	950	6754	1602
TFS 5/13	950	6901	1625
TCR 13	950	6881	1653
TCO 13/0	950	Pre-test failure	
TFS 5/14	1050	Pre-test failure	
TSH 14/270	1050	Pre-test failure	
TCI 15/180	1150	Pre-test failure	

Table 5: QUENCH-06; Sequence of events

Time [s]	Event
0	Start of data recording, test bundle at ~873 K, data acquisition frequency 0.25 Hz
30	Start of heatup from ~873 K to ~1473 K
1965	Start of pre-oxidation phase at ~1473 K
5922	Data acquisition frequency 5 Hz
6011	Start of transient phase
6620	Withdrawal of corner rod B initiated at T ~1606 K (TFS 3/13 and TIT A13)
6640	End of pulling corner rod B
~7100	Begin of temperature escalations at the 750 and 850 mm level (bundle) and at the 1050 mm level (shroud) and begin of significant H ₂ production, based on the mass spectrometer data
7179	Start of water injection and of cooldown at TFS 2/1 (-250 mm); Rod failure
7180	Shroud failure
7181	Steam flow at zero
7205	Start of electric power reduction from 18.2 kW to 3.9 kW
7221	Electric power at 3.9 kW
7431	Electric power shutoff (< 0.5 kW)
7431	Quench water shutoff
7434	Quench water at zero
11420	End of data recording

0 s = 13:20:00 h on December 13, 2000

Table 6: QUENCH-06; Excursion temperatures

Elevation [mm]	Thermocouple	Time at excursion [s]	Excursion temperature [K]
850	TSH 12/0	~7150	1738
850	TSH 12/180	~7150	1758
950	TIT A/13	~7100	1884
950	TCR 13	~7150	1841
950	TSH 13/90	~7110	1741
950	TSH 13/270	~7100	1814
1050	TFS 3/14	~7100	1639

Table 7: QUENCH-06; Maximum measured test rod temperature of each elevation

Elevation [mm]	Thermocouple	Time [s]	Maximum temperature [K]
- 250	TFS 2/1	7177	648
- 150	TFS 2/2	7179	735
- 50	TFS 2/3	7179	796
50	TFS 5/4/180	7179	846
150	TFS 5/5	7179	989
250	TFS 2/6	7178	1100
350	TFS 2/7	7179	1210
450	TFS 3/8	7179	1287
550	TFS 2/9	7179	1356
650	TFS 3/10	7179	1475
750	correct measurement not available		
850	TIT D/12	7181	1856
950	TCR 13	7180	2056
1050	TFS 3/14	7180	1930
1150	TFS 2/15	7180	1648
1250	TFS 3/16	7180	1356
1350	TFS 2/17	7180	1228

Table 8: QUENCH-06; Maximum measured shroud temperature of each elevation

Elevation [mm]	Thermocouple	Time [s]	Maximum temperature [K]
- 250	TSH 1/0	7178	603
- 50	TSH 3/180	7179	722
50	TSH 4/90	7176	790
350	TSH 7/180	7179	1131
550	TSH 9/270	7180	1287
750	TSH 11/180	7180	1625
850	TSH 12/180	7180	1847
950	TSH 13/270	7180	2007
1050	correct measurement not available		
1150	correct measurement not available		
1250	correct measurement not available		

Table 9: QUENCH-06; Onset of cooling based on cladding TCs (TFS and TCR), central rod centerline TC (TCRC 13), corner rod TCs (TIT), and shroud TCs (TSH)

Thermocouple	Elevation [mm]	Onset of cooling		Mean value per elevation	
		Time [s]	Temp. [K]	Time [s]	Temp. [K]
TFS 2/1	- 250	7178	648		
TFS 2/2	- 150	7179	735		
TFS 2/3	- 50	7179	796		
TFS 5/4/0	50	7179	842	7179	843
TFS 5/4/180	50	7179	844		
TFS 5/5	150	7179	986		
TFS 2/6	250	7180	1095	7180	1095
TFS 5/6	250	7180	1095		
TFS 2/7	350	7180	1209	7180	1190
TFS 5/7	350	7180	1181		
TCR 7	350	7179	1181		
TFS 3/8	450	7180	1284	7180	1272
TFS 5/8	450	7179	1259		
TFS 2/9	550	7179	1354	7179	1330
TFS 5/9	550	7179	1312		
TCR 9	550	7179	1326		
TFS 3/10	650	7180	1473		
TFS 2/11	750	7180	2100	7180	2052
TFS 5/11	750	7181	2004		
TFS 5/12	850	7180	2114		
TFS 4/13	950	7180	2242		
TFS 3/14	1050	7180	1931		

Thermocouple	Elevation [mm]	Onset of cooling		Mean value per elevation	
		Time [s]	Temp. [K]	Time [s]	Temp. [K]
TFS 2/15	1150	7180	1645	7180	1532
TFS 5/15	1150	7180	1419		
TFS 3/16	1250	7180	1356	7180	1324
TFS 5/16	1250	7180	1291		
TFS 2/17	1350	7179	1238	7180	1155
TFS 5/17	1350	7180	1071		
TCRI 7	350	7180	1200		
TCRC 7	350	7183	1191		
TCRC 9	550	7184	1314		
TCRI 9	550	7180	1326		
TCRC 13	950	7186	1955		
TIT C/9	500	7180	1310		
TIT D/12	800	7181	1853		
TIT A/13	950	7179	2056		
TSH 1/0	- 250	7179	603		
TSH 3/180	- 50	7180	722		
TSH 4/0	50	7180	773	7180	777
TSH 4/90	50	7180	790		
TSH 4/180	50	7180	779		
TSH 4/270	50	7180	767		
TSH 7/0	350	7180	1126	7180	1126
TSH 7/180	350	7180	1126		

Thermocouple	Elevation [mm]	Onset of cooling		Mean value per elevation	
		Time [s]	Temp. [K]	Time [s]	Temp. [K]
TSH 9/90	550	7180	1276	7180	1281
TSH 9/270	550	7180	1286		
TSH 11/0	750	7180	1582	7180	1604
TSH 11/180	750	7180	1625		
TSH 12/0	850	7180	1810	7180	1828
TSH 12/180	850	7180	1846		
TSH 13/90	950	7180	1899		
TSH 14/90	1050	7182	1878		
TSH 15/0	1150	7181	2008	7181	2005
TSH 15/180	1150	7181	2001		
TSH 16/0	1250	7180	1992	7181	2008
TSH 16/180	1250	7181	2024		

Table 10: QUENCH-06; Onset of quenching based on cladding TCs (TFS and TCR), central rod centerline TCs (TCRC), corner rod TCs (TIT), and shroud TCs (TSH)

Thermocouple	Elevation [mm]	Onset of quenching		Mean value per elevation	
		Time [s]	Temp. [K]	Time [s]	Temp. [K]
TFS 2/1	- 250	7178	648		
TFS 2/2	- 150	7179	735		
TFS 2/3	- 50	7183	540		
TFS 5/4/0	50	7182	582	7182	571
TFS 5/4/180	50	7182	560		
TFS 5/5	150	7183	634		
TFS 2/6	250	7253	757	7253	758
TFS 5/6	250	7252	759		
TFS 2/7	350	7272	775	7274	786
TFS 5/7	350	7277	873		
TCR 7	350	7272	710		
TFS 3/8	450	7292	542	7292	663
TFS 5/8	450	7292	784		
TFS 2/9	550	7314	666	7314	688
TFS 5/9	550	7313	780		
TCR 9	550	7316	619		
TFS 3/10	650	7313	877		
TFS 5/11	750	7376	722		
TFS 3/14	1050	7353	959		
TFS 2/15	1150	7404	697	7377	735
TFS 5/15	1150	7350	772		

Thermocouple	Elevation [mm]	Onset of quenching		Mean value per elevation	
		Time [s]	Temp. [K]	Time [s]	Temp. [K]
TFS 3/16	1250	7374	610	7377	689
TFS 5/16	1250	7380	768		
TFS 2/17	1350	7293	907	7304	861
TFS 5/17	1350	7315	814		
TCRI 7	350	7281	886		
TCRC 7	350	7283	889		
TCRC 9	550	7323	842		
TCRI 9	550	7319	805		
TCRC 13	950	7409	1045		
TIT C/9	500	7309	853		
TIT D/12	800	7382	904		
TIT A/13	950	7411	652		
TSH 1/0	- 250	7179	603		
TSH 3/180	- 50	7233	589		
TSH 4/0	50	7239	594	7241	597
TSH 4/90	50	7241	591		
TSH 4/180	50	7243	598		
TSH 4/270	50	7240	604		
TSH 7/0	350	7294	753	7294	760
TSH 7/180	350	7293	766		
TSH 9/90	550	7344	683	7339	701
TSH 9/270	550	7333	718		

Thermocouple	Elevation [mm]	Onset of quenching		Mean value per elevation	
		Time [s]	Temp. [K]	Time [s]	Temp. [K]
TSH 11/0	750	7380	757	7378	815
TSH 11/180	750	7375	873		
TSH 12/0	850	7399	804	7403	815
TSH 12/180	850	7407	826		
TSH 13/90	950	7435	749	7427	729
TSH 13/270	950	7419	709		
TSH 14/90	1050	7410	592		
TSH 15/0	1150	7427	533	7424	573
TSH 15/180	1150	7420	612		

Table 11: QUENCH-06; Cross sections for the metallographic examination

06.04.01

Sample	Sample length (mm)	Axial position		Remarks
		Bottom (mm)	Top (mm)	
QUE-06-a			48	Remnant
Cut	2	48	50	Coarse cut #1 *)
QUE-06-b	8	50	58	
Cut	2	58	60	
QUE-06-1	13	60	73	Reference, 73 mm polished
Cut	2	73	75	
QUE-06-c	249	75	324	
Cut	2	324	326	Coarse cut #2 ⇒ slab length = 274 mm
QUE-06-d	209	326	535	
Cut	2	535	537	
QUE-06-2	13	537	550	Elevation 9, 550 mm polished
Cut	2	550	552	
QUE-06-3	5	552	557	Sample for H ₂ absorption
Cut	2	557	559	
QUE-06-e	41	559	600	
Cut	2	600	602	Coarse cut #3 ⇒ slab length = 274 mm
QUE-06-f	133	602	735	
Cut	2	735	737	
QUE-06-4	13	737	750	Elevation 11, 750 mm polished
Cut	2	750	752	
QUE-06-5	5	752	757	Sample for H ₂ absorption
Cut	2	757	759	
QUE-06-g	76	759	835	
Cut	2	835	837	
QUE-06-6	13	837	850	Elevation 12, 850 mm polished
Cut	2	850	852	
QUE-06-7	5	852	857	Sample for H ₂ absorption
Cut	2	857	859	
QUE-06-h	26	859	885	

Sample	Sample length (mm)	Axial position		Remarks
		Bottom (mm)	Top (mm)	
Cut	2	885	887	
QUE-06-8	13	887	900	900 mm polished
Cut	2	900	902	
QUE-06-9	5	902	907	Sample for H ₂ absorption
Cut	2	907	909	
QUE-06-i	26	909	935	
Cut	2	935	937	
QUE-06-10	13	937	950	Elevation 13, 950 mm polished
Cut	2	950	952	
QUE-06-11	5	952	957	Sample for H ₂ absorption
Cut	2	957	959	
QUE-06-j	26	959	985	
Cut	2	985	987	
QUE-06-12	13	987	1000	1000 mm polished
Cut	2	1000	1002	
QUE-06-13	5	1002	1007	Sample for H ₂ absorption
Cut	2	1007	1009	
QUE-06-k	126	1009	1135	
Cut	2	1135	1137	
QUE-06-14	13	1137	1150	Elevation 15, 1150 mm polished
Cut	2	1150	1152	
QUE-06-15	5	1152	1157	Sample for H ₂ absorption
Cut	2	1157	1159	
QUE-06-l	11	1159	1170	
Cut	2	1170	1172	Coarse cut #4 ⇒ slab length = 568 mm
QUE-06-m		1172		Remnant

*) The coarse cuts are made with help of a machine which can handle the entire length of the test bundle. Afterwards the slabs of a length < 600 mm are cut into slices of a higher precision in a different machine.

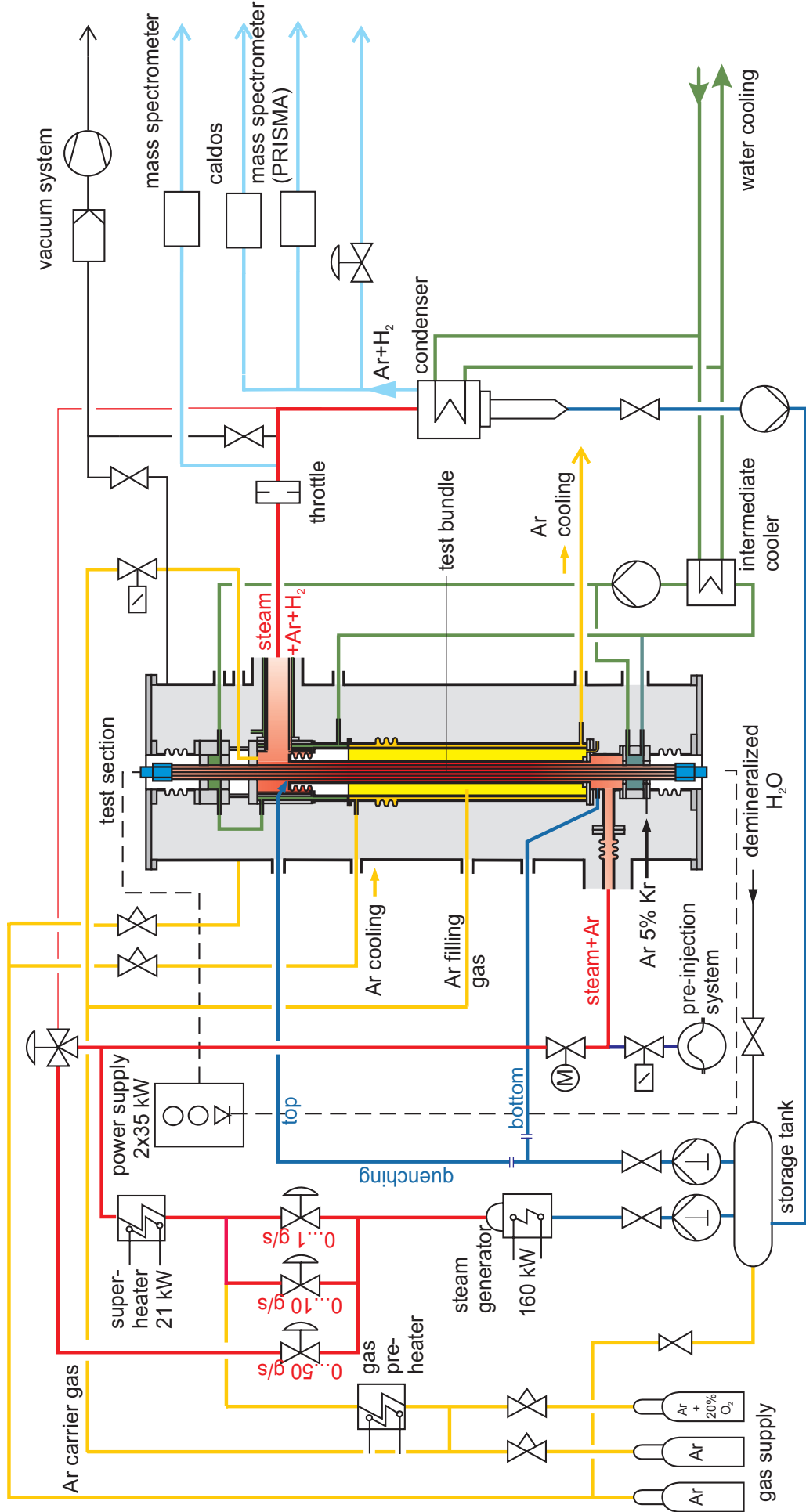


Fig.1-QUE06-Flow diagram.cdr
26.05.03 - IMF

Fig. 1: Flow diagram of the QUENCH test facility

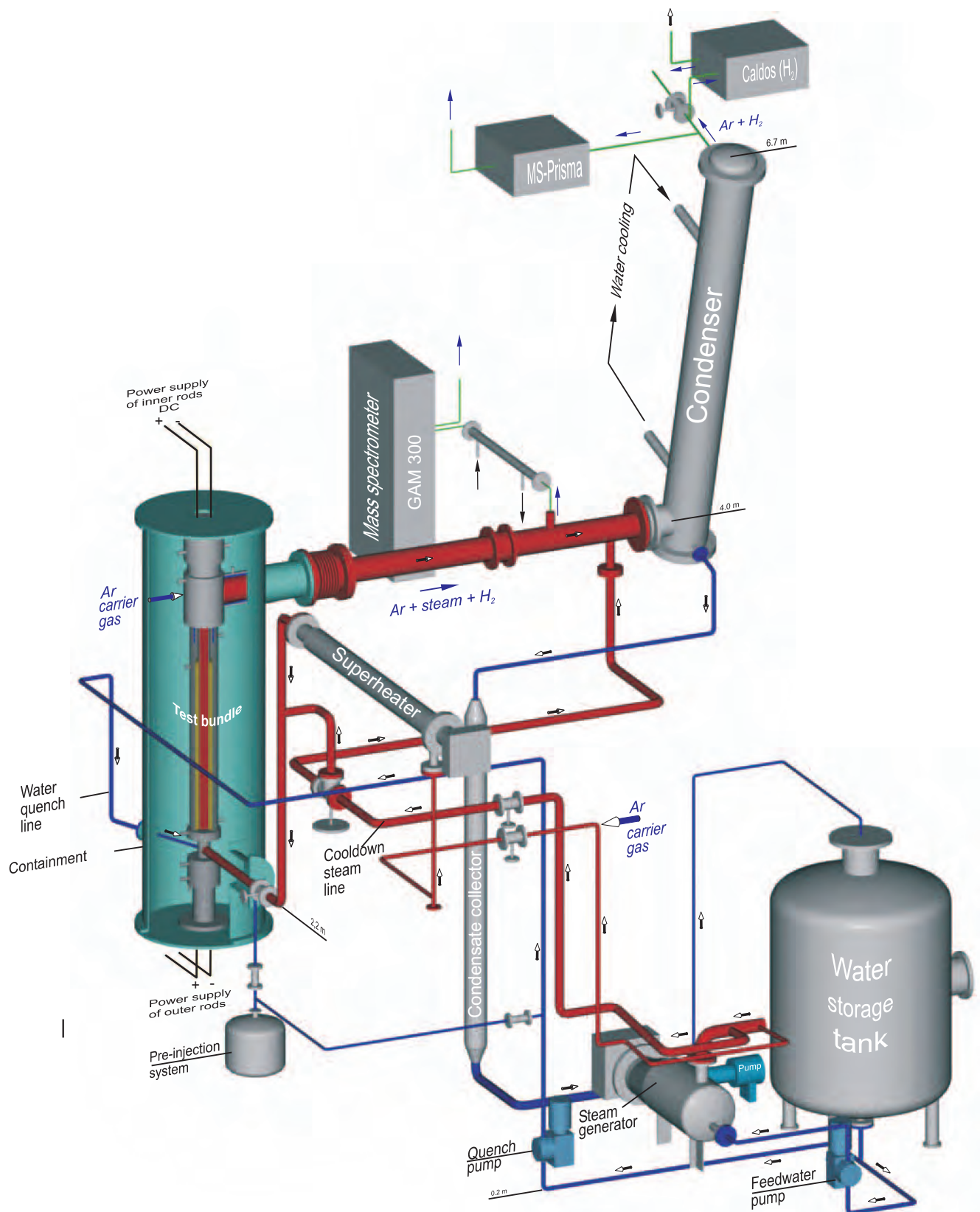


Fig.2-QUE06 Gesamtanlage 3D.cdr
06.05.02 - IMF

Fig. 2: QUENCH Facility; main components

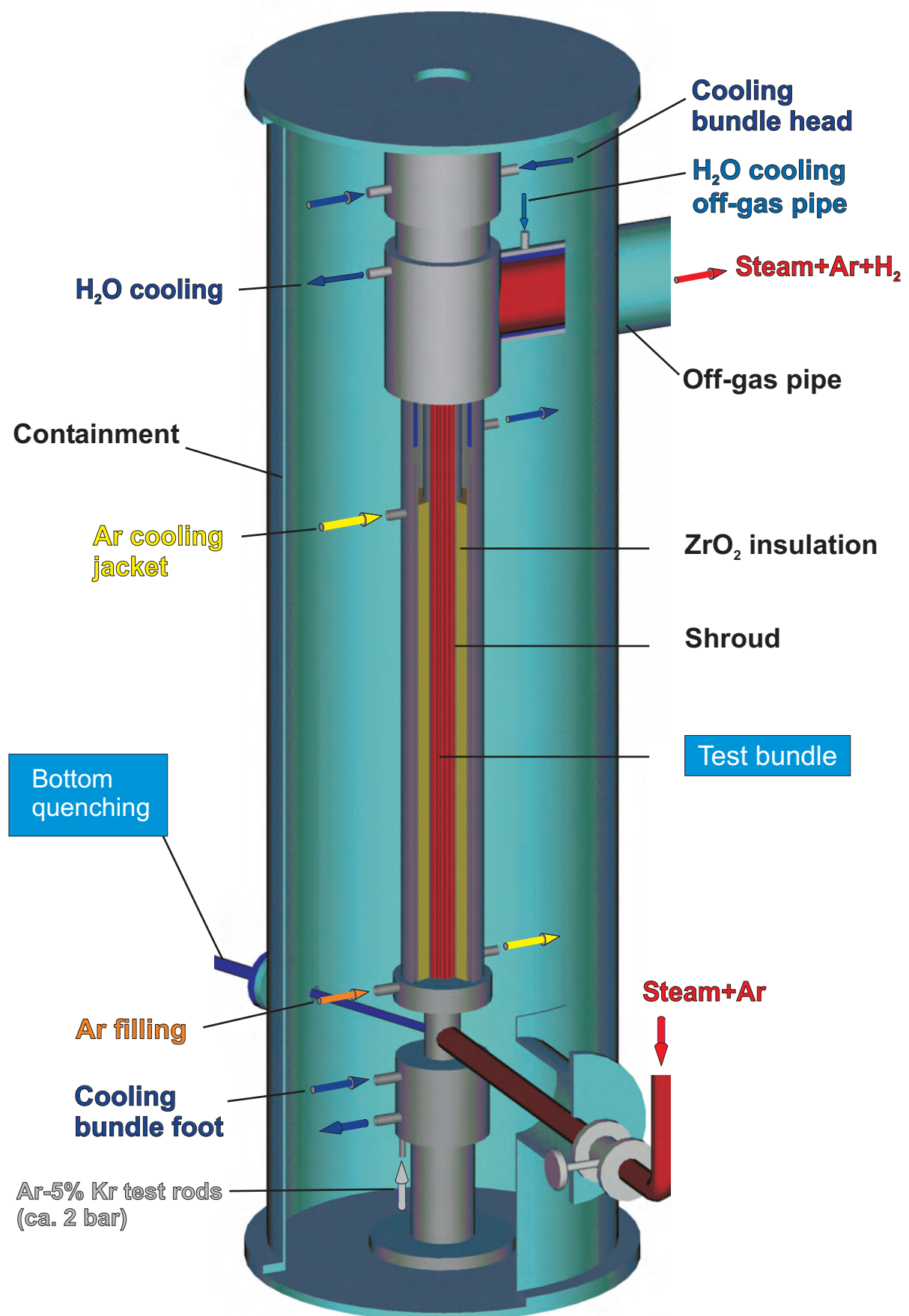


Fig.3-QUE06 Containment 3D.cdr
03.02.04 - IMF

Fig. 3: QUENCH Facility; containment and test section

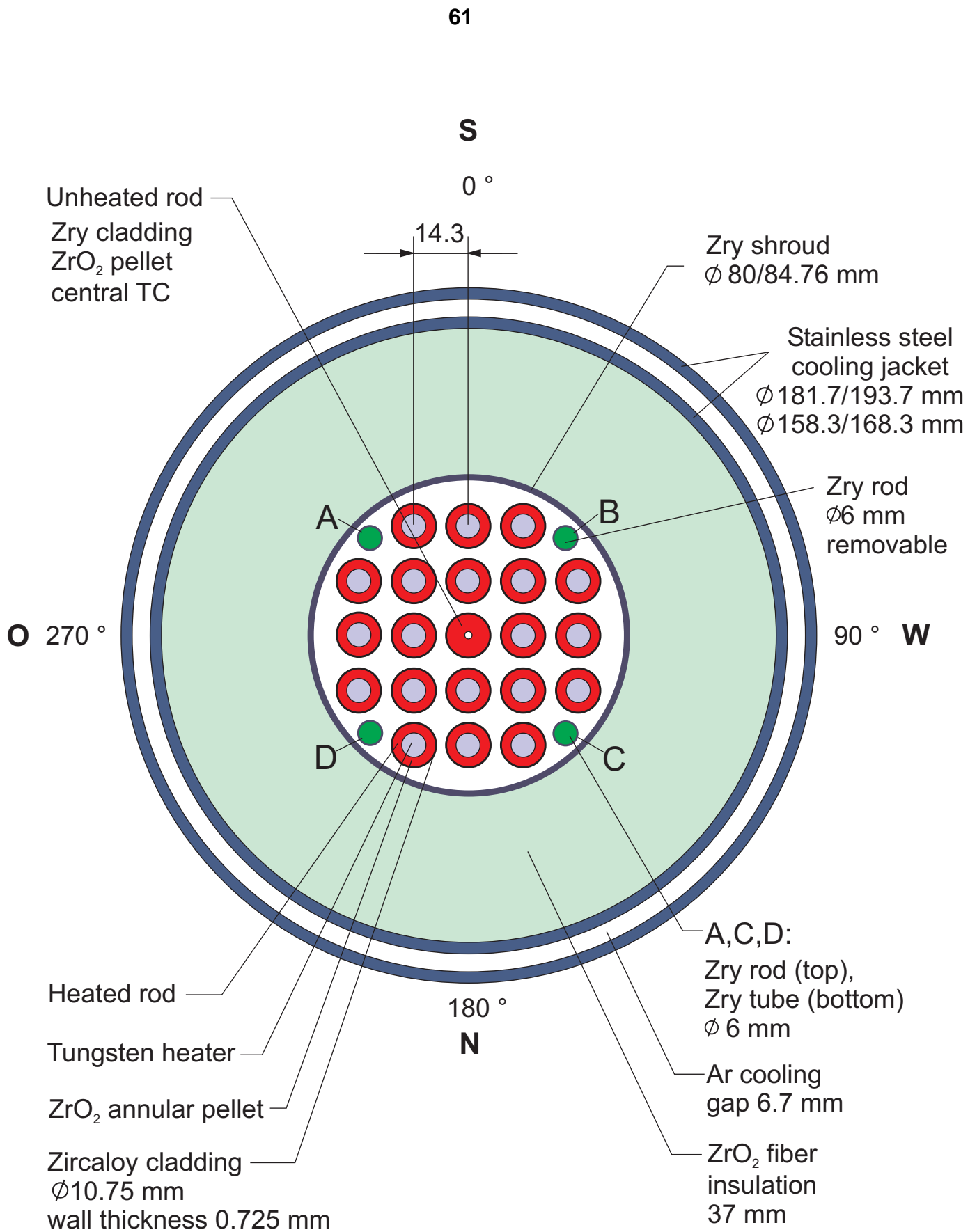


Fig.5-QUE06 Cross section.cdr
06.05.02 - IMF

Fig. 5: QUENCH-06; Fuel rod simulator bundle (Top view)

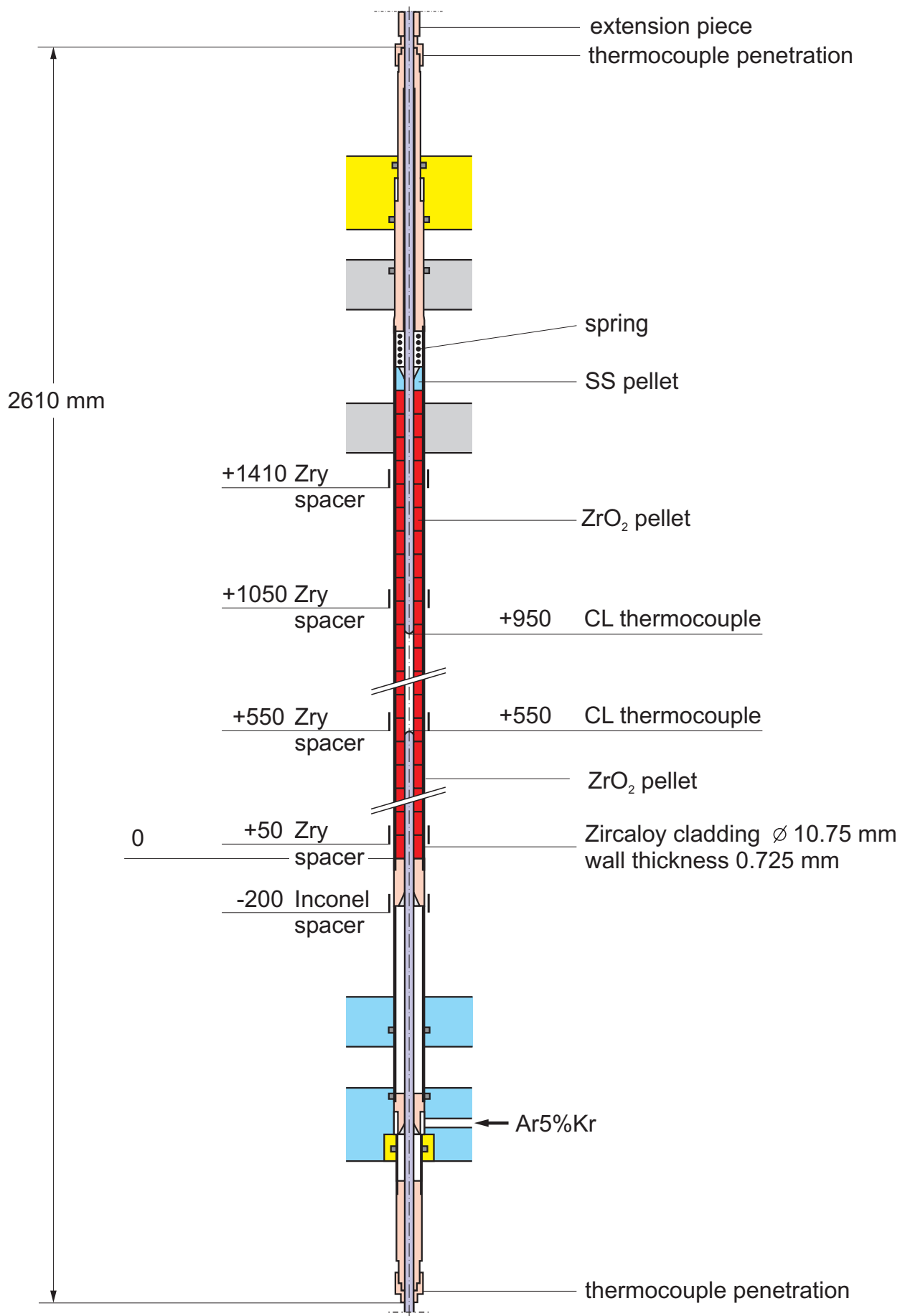


Fig. 7: Unheated fuel rod simulator

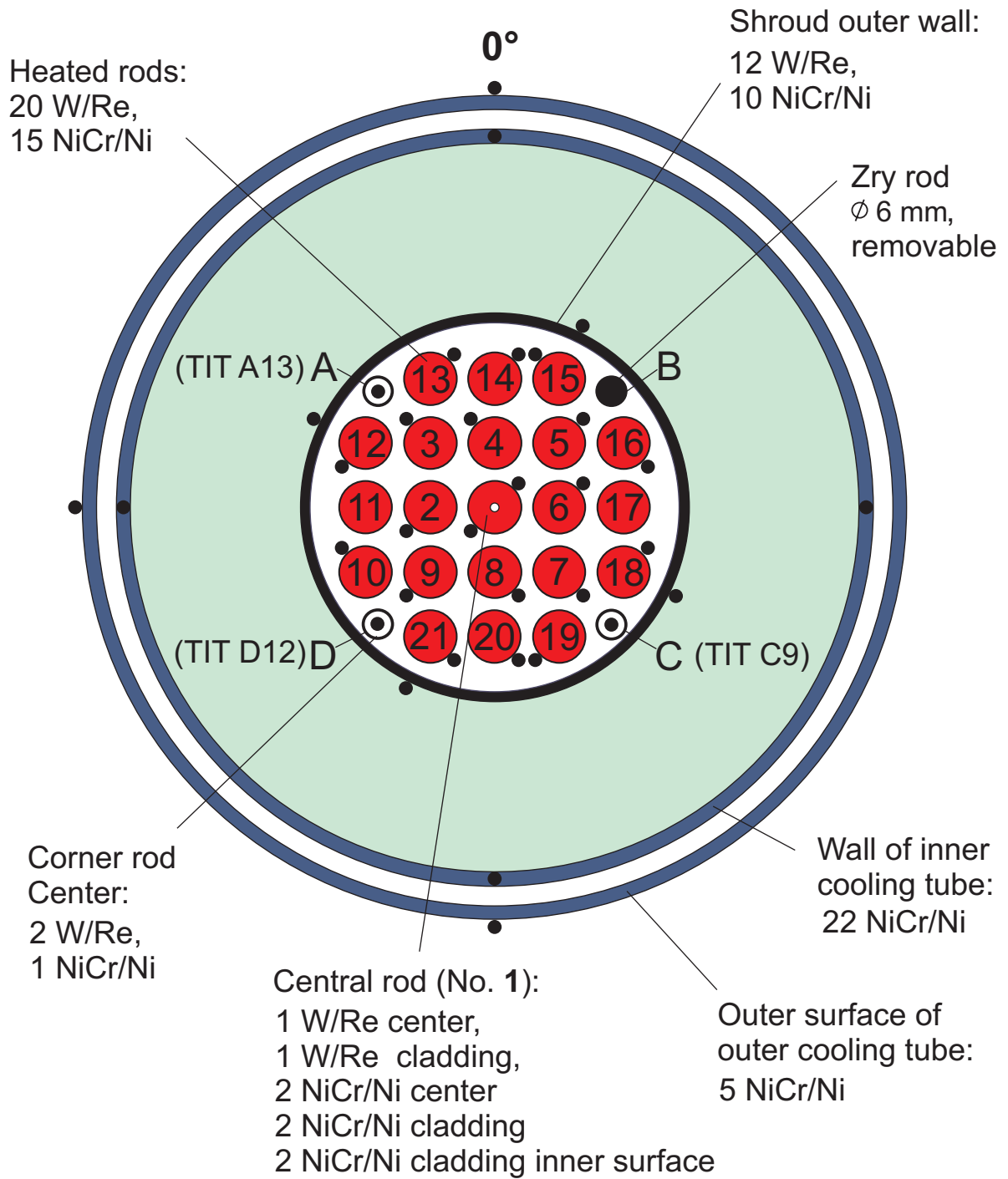


Fig.8-QUE06 TC instr.cdr
06.05.02 - IMF

Fig. 8: QUENCH-06; Test bundle; TC instrumentation and rod designation (top view)

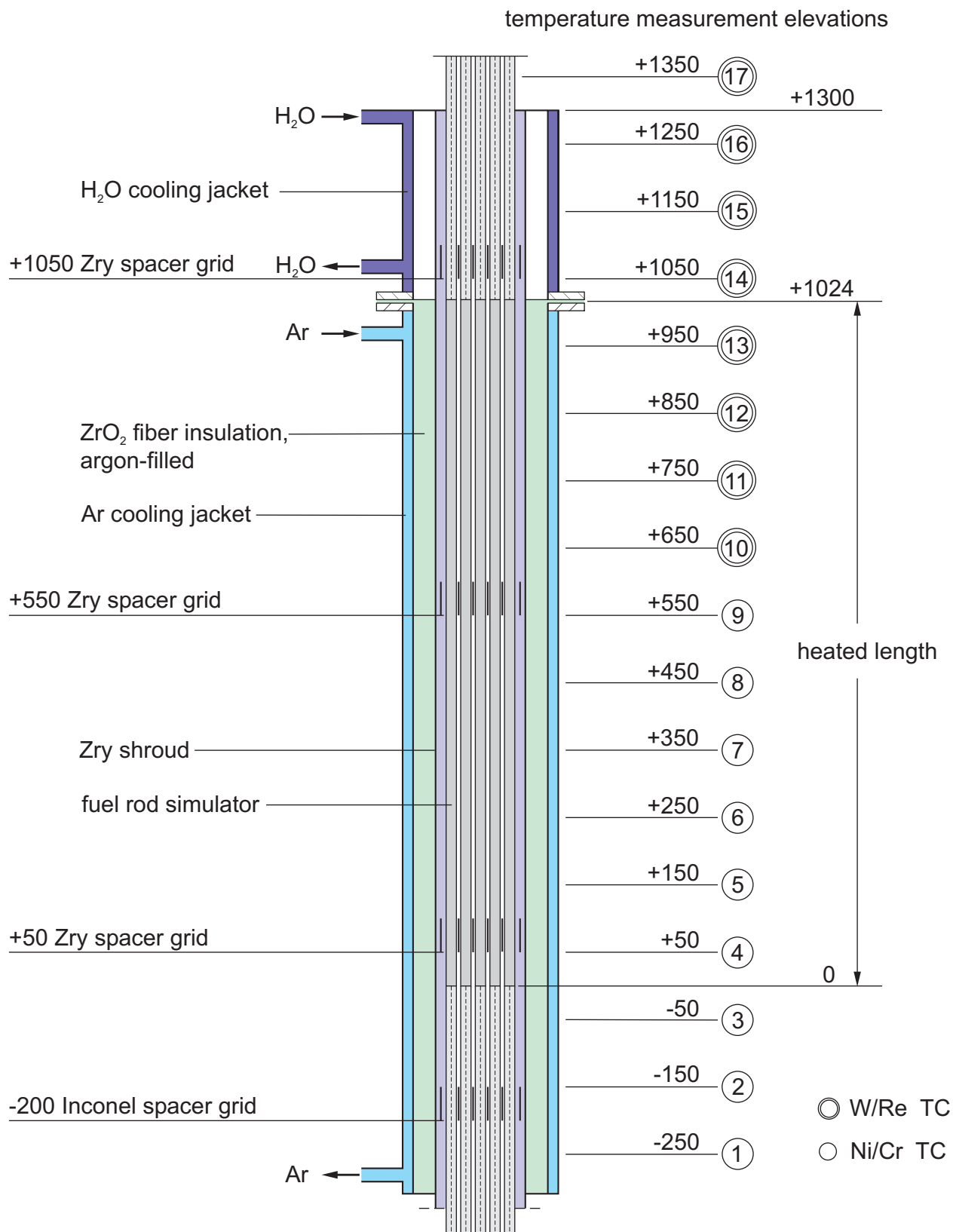
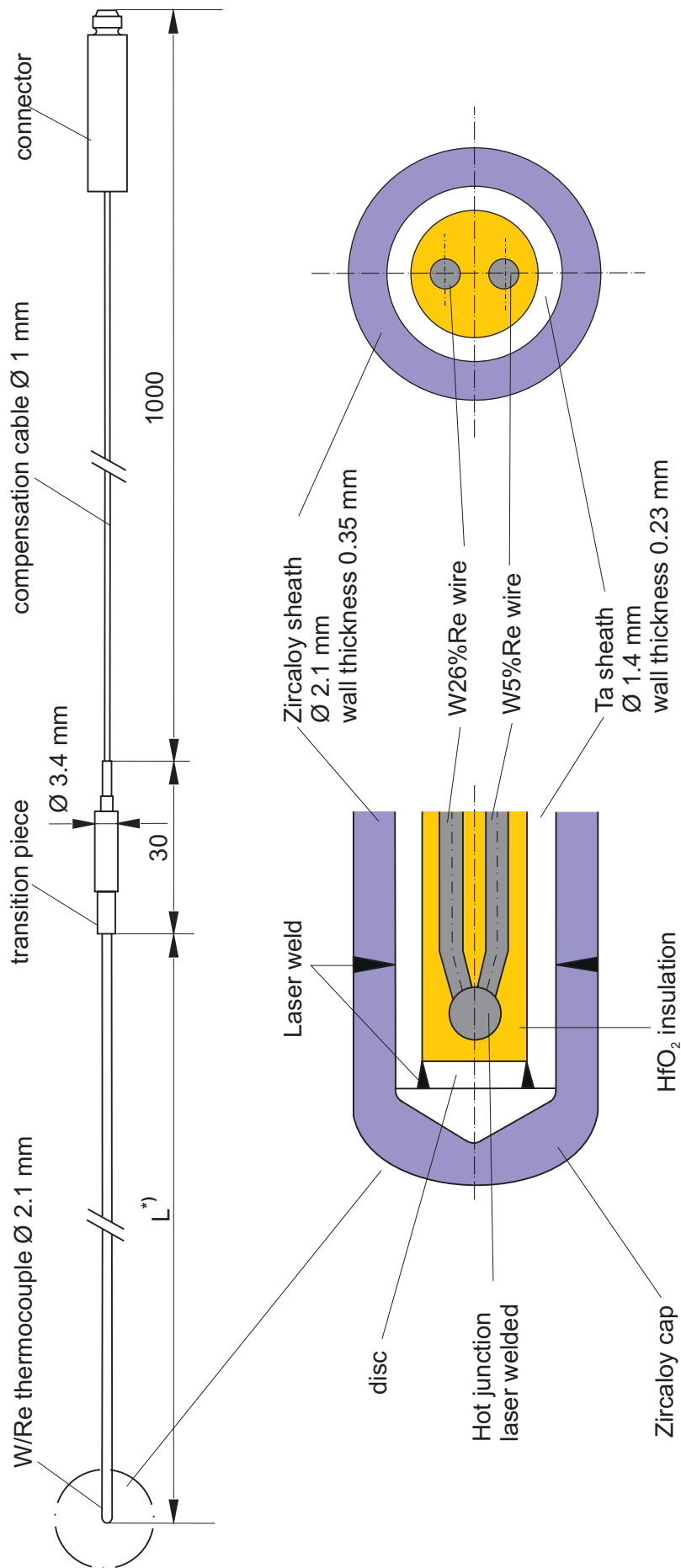


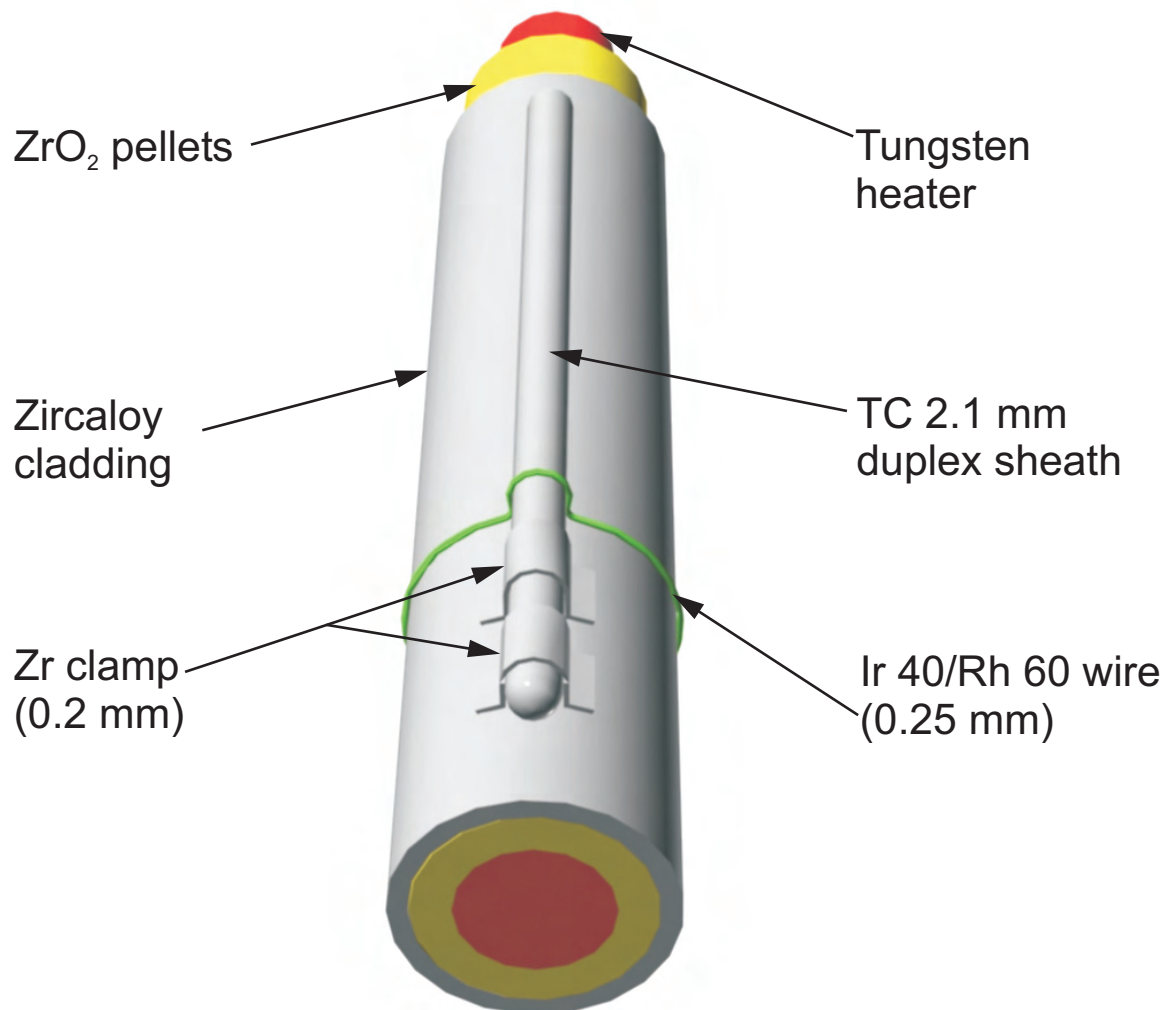
Fig.9-QUE06 TC elevations.cdr
06.05.01 - IMF

Fig. 9: QUENCH; Test section instrumentation



*) L: high-temperature section length dependent on the TC position in the test bundle 500 mm - 1700 mm

Fig. 10: QUENCH; High-temperature thermocouple



Tests with pre-oxidation: Zr clamp + wire

Tests without pre-oxidation: Zr clamp

Fig. 11: TC fastening concept for the QUENCH test rods

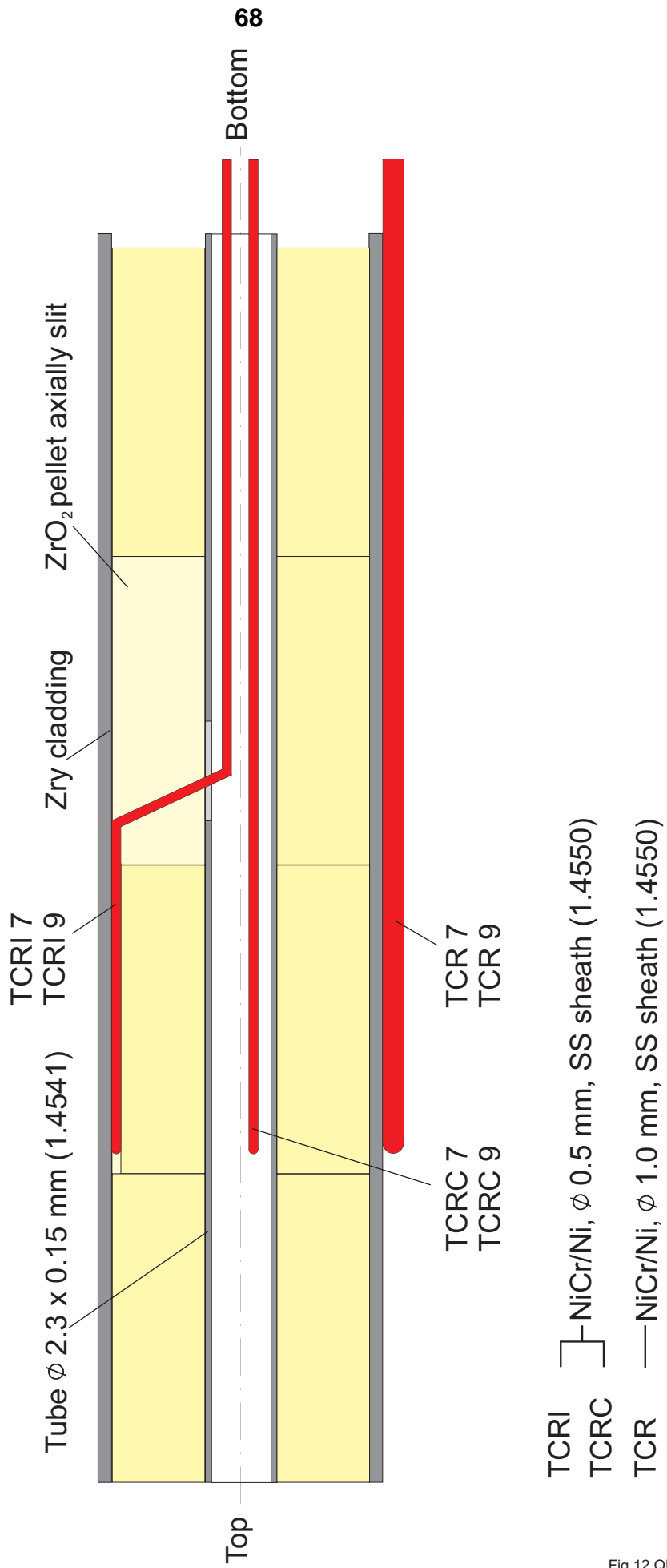


Fig. 12: QUENCH-06; TC instrumentation of the unheated fuel rod simulator at levels 7 (350 mm) and 9 (550 mm)

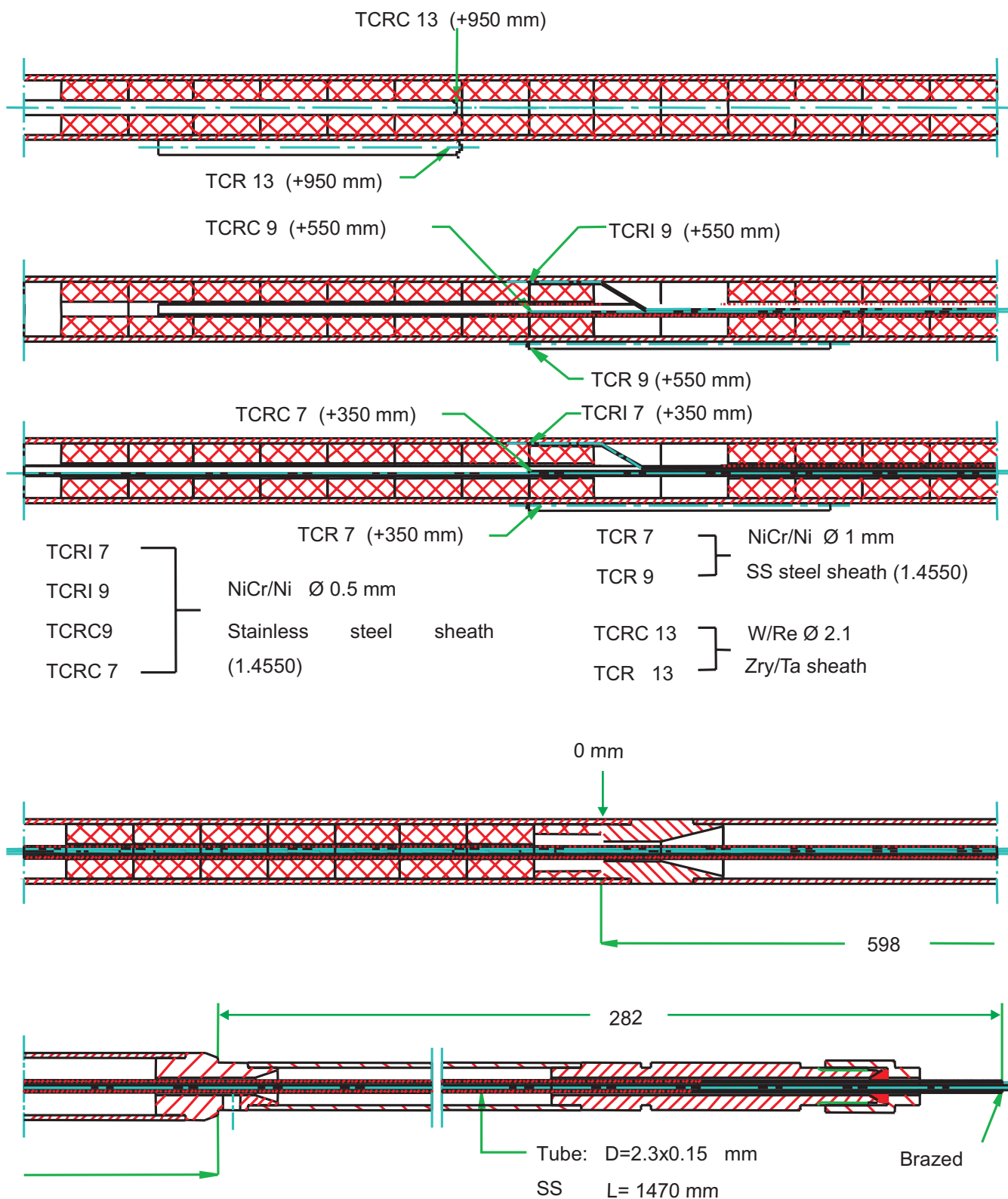
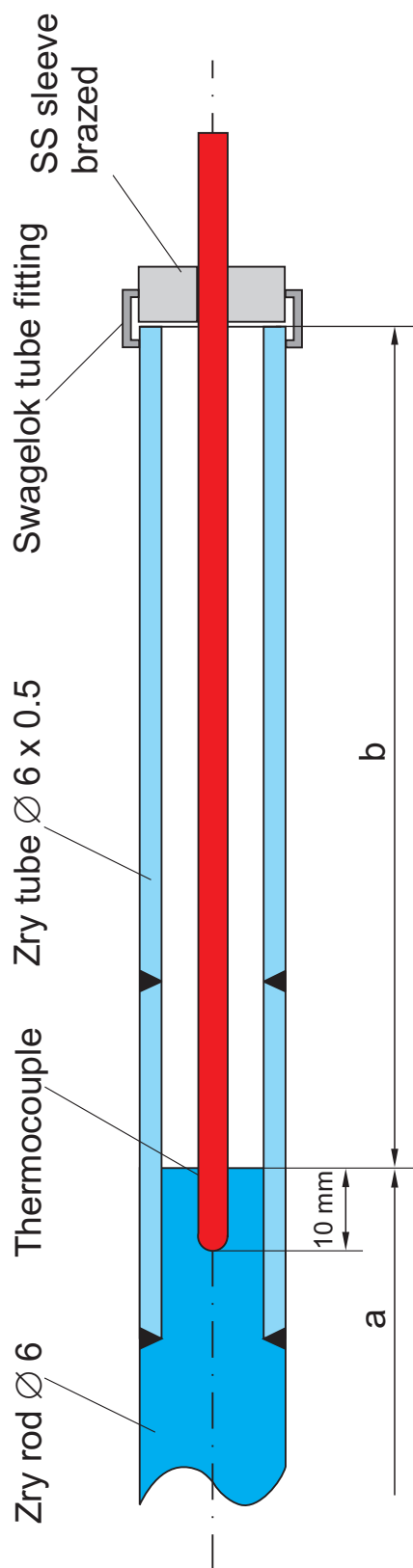


Fig 13 QUE06-Stab unbeheizt.cdr
06.05.02 - IMF

Fig. 13: QUENCH-06; TC instrumentation of the unheated fuel rod simulator

(TIT A13, TIT D12, TIT C9)



Rod A: TIT A13 (950 mm), W/Re, Ø 2.1 mm, a = 360 mm, b = 2080 mm

Rod D: TIT D12 (850 mm), W/Re, Ø 2.1 mm, a = 460 mm, b = 1980 mm

Rod C: TIT C 9 (550 mm), NiCr/Ni, Ø 1 mm, a = 760 mm, b = 1680 mm

(Rod B: Zry-4 rod, Ø 6 mm, removable)

Fig. 14: QUENCH-06; Schematic of the arrangement of the thermocouples inside the corner rods

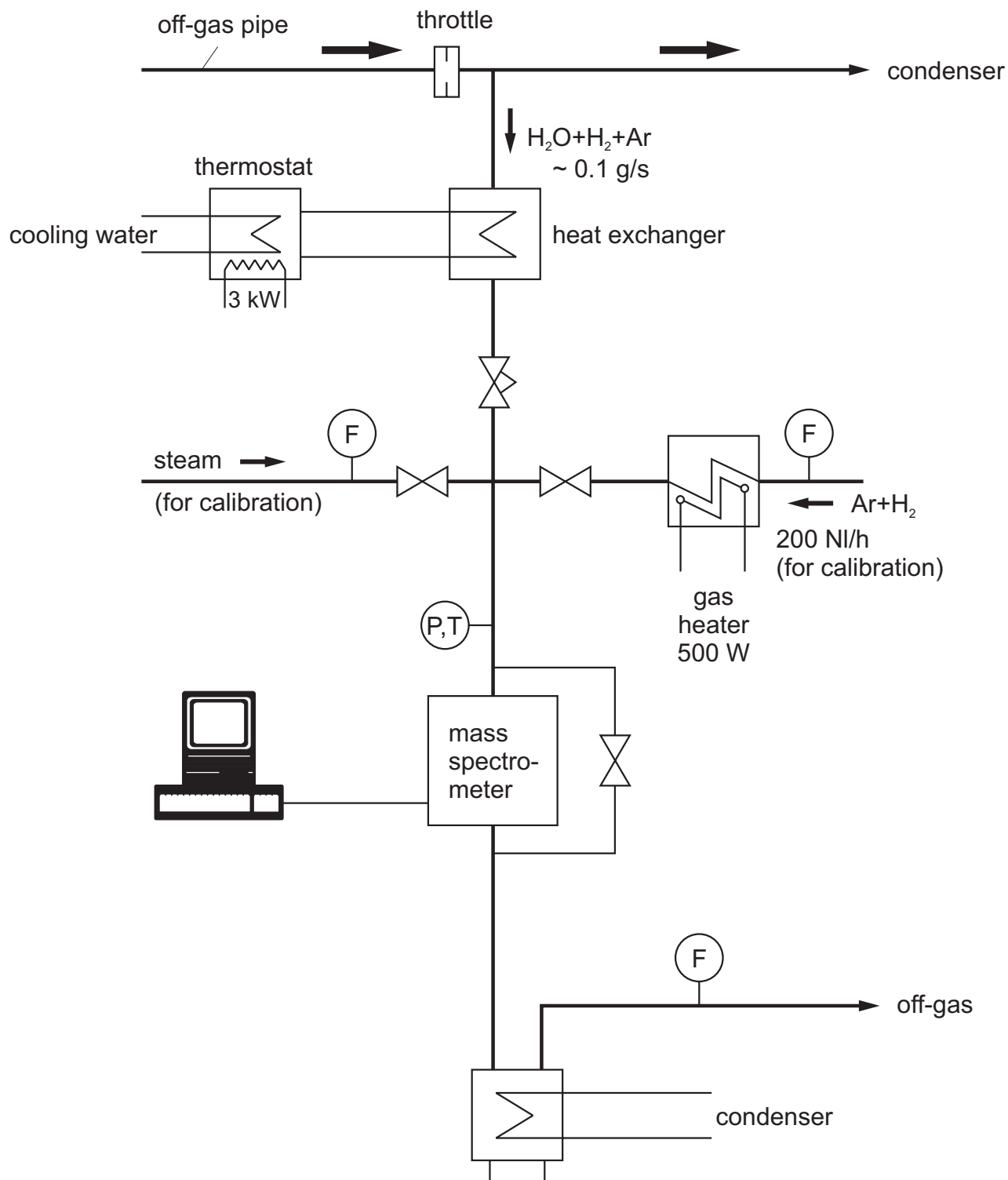


Fig 15 QUE06 MS QUENCH-Facility.cdr
07.05.02 - IMF

Fig. 15: QUENCH-Facility; H_2 measurement with the mass spectrometer

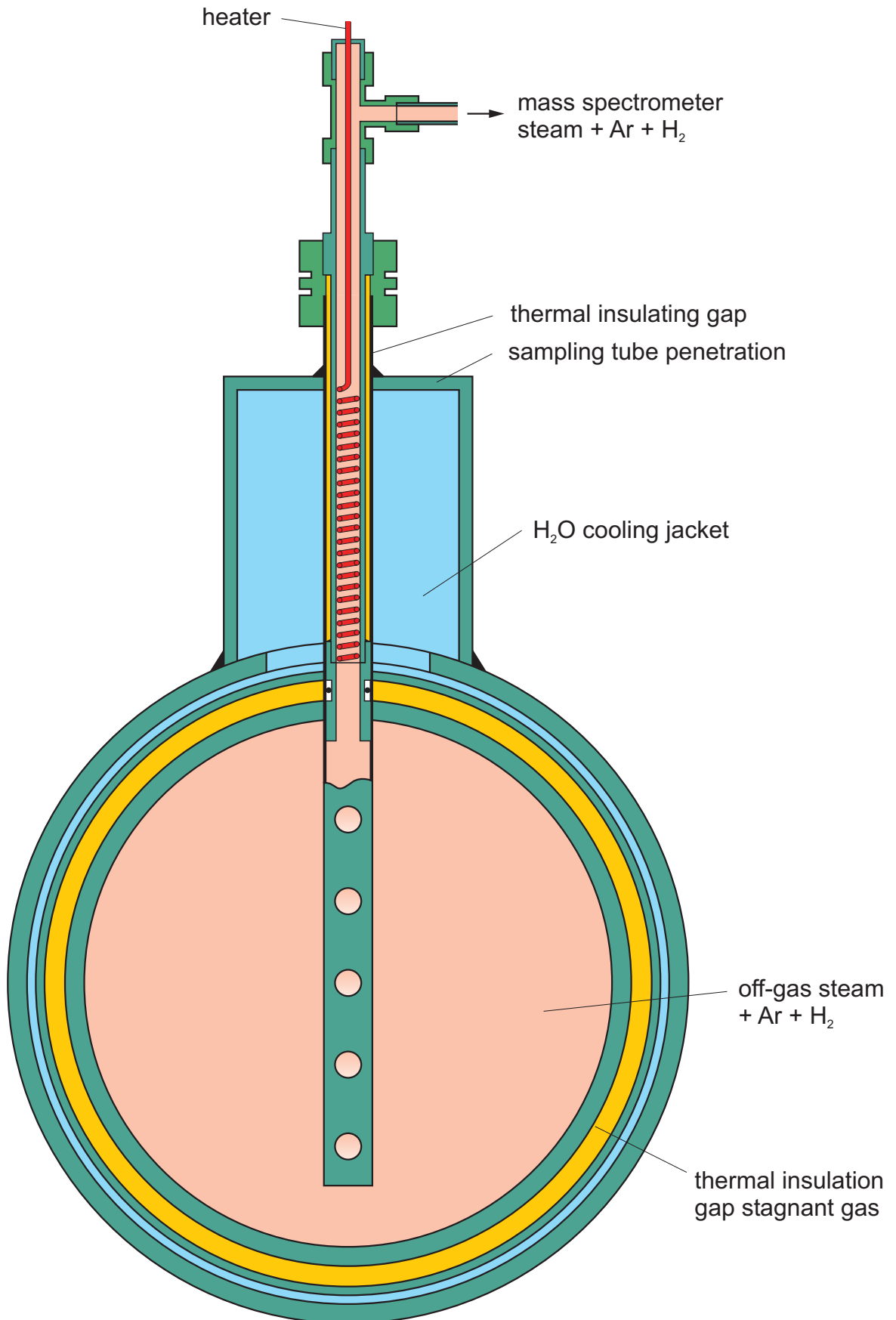


Fig 16 QUE06 MS sampling position new.cdr
07.05.02 - IMF

Fig. 16: QUENCH; Mass spectrometer sampling position at the off-gas pipe

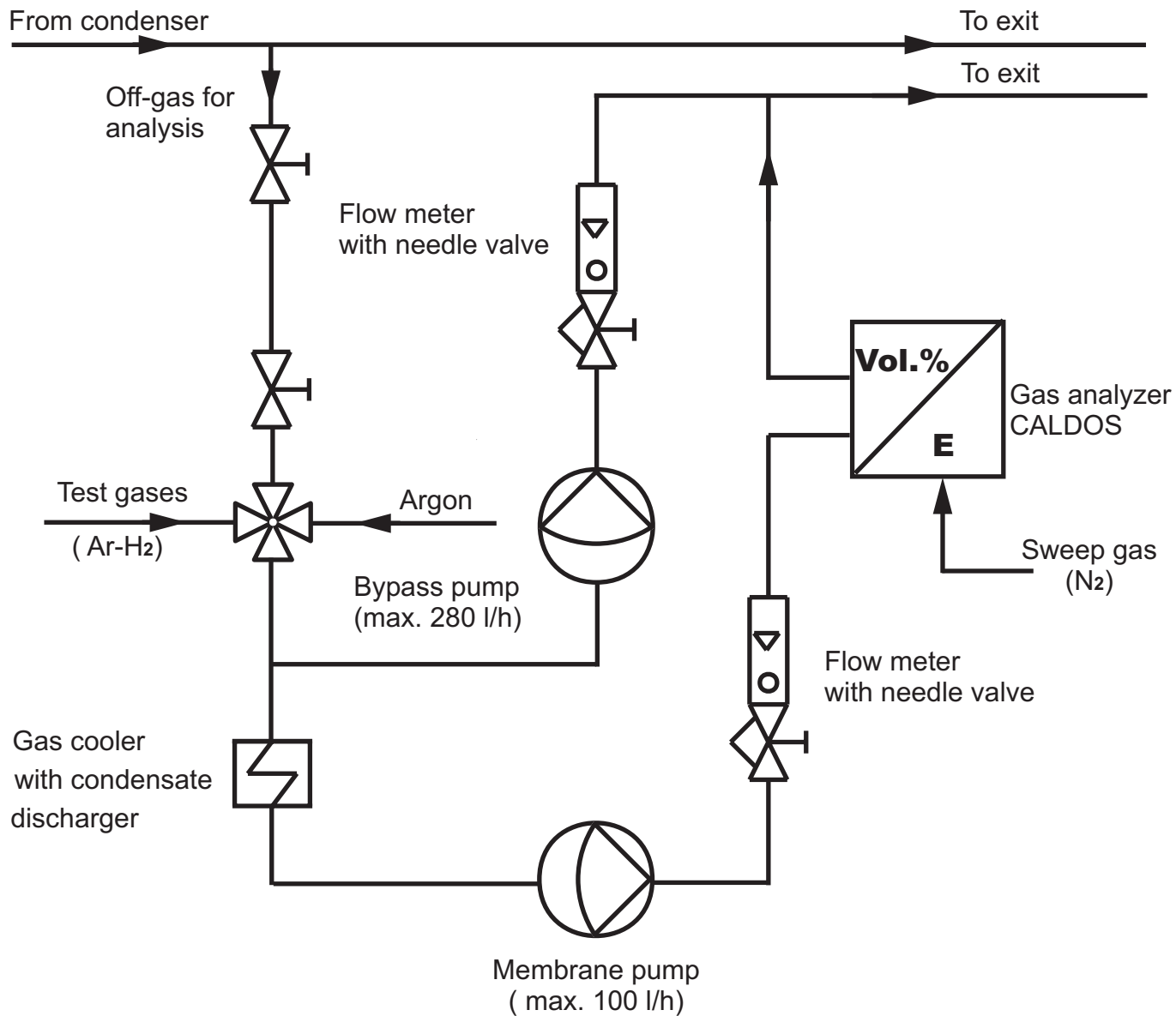


Fig 17 QUE06 Caldos Schema (ab QUE04).cdr
07.05.02 - IMF

Fig. 17: QUENCH-06; Hydrogen measurement with the CALDOS analyzer

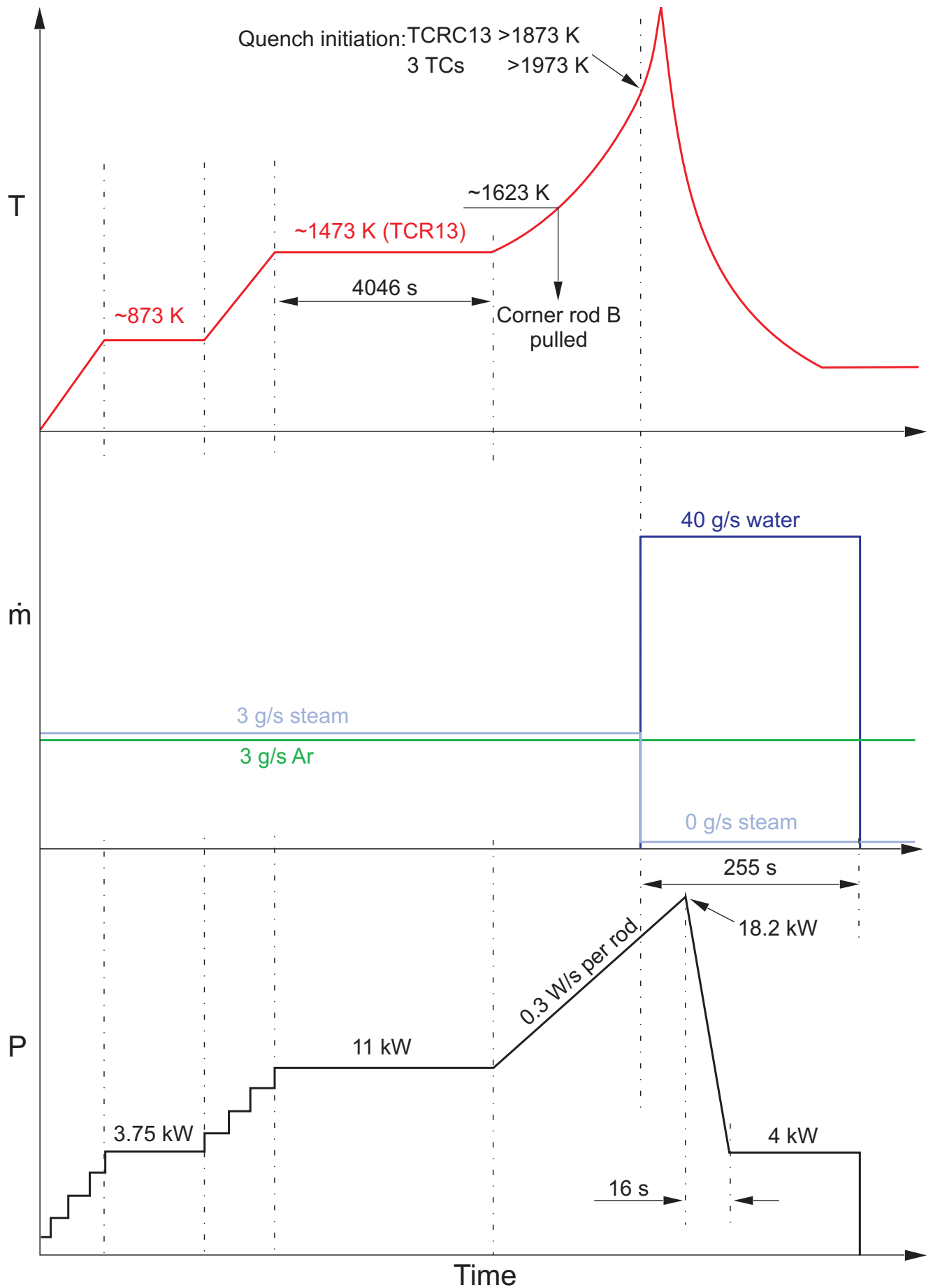


Fig 18 QUE06 Test conduct.cdr
12.06.02 - IMF

Fig. 18: QUENCH-06; Test conduct (schematic)

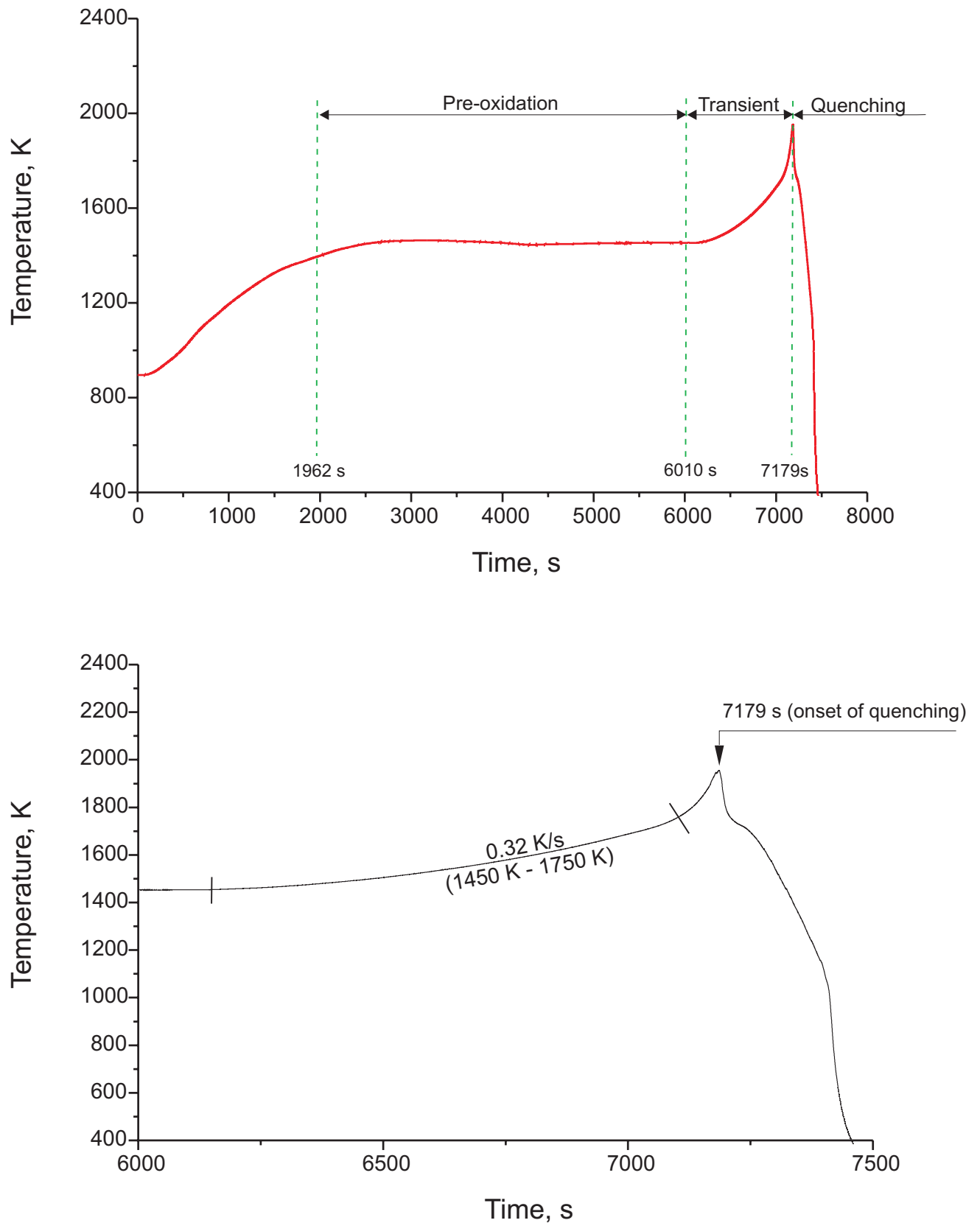


Fig.19 QUE06 Temp-Zeit-TCRC13.cdr
12.06.02 - IMF

Fig. 19: QUENCH-06; Test phases, top, and heatup rate during the transient phase determined on the basis of the centerline thermocouple TCRC 13, bottom

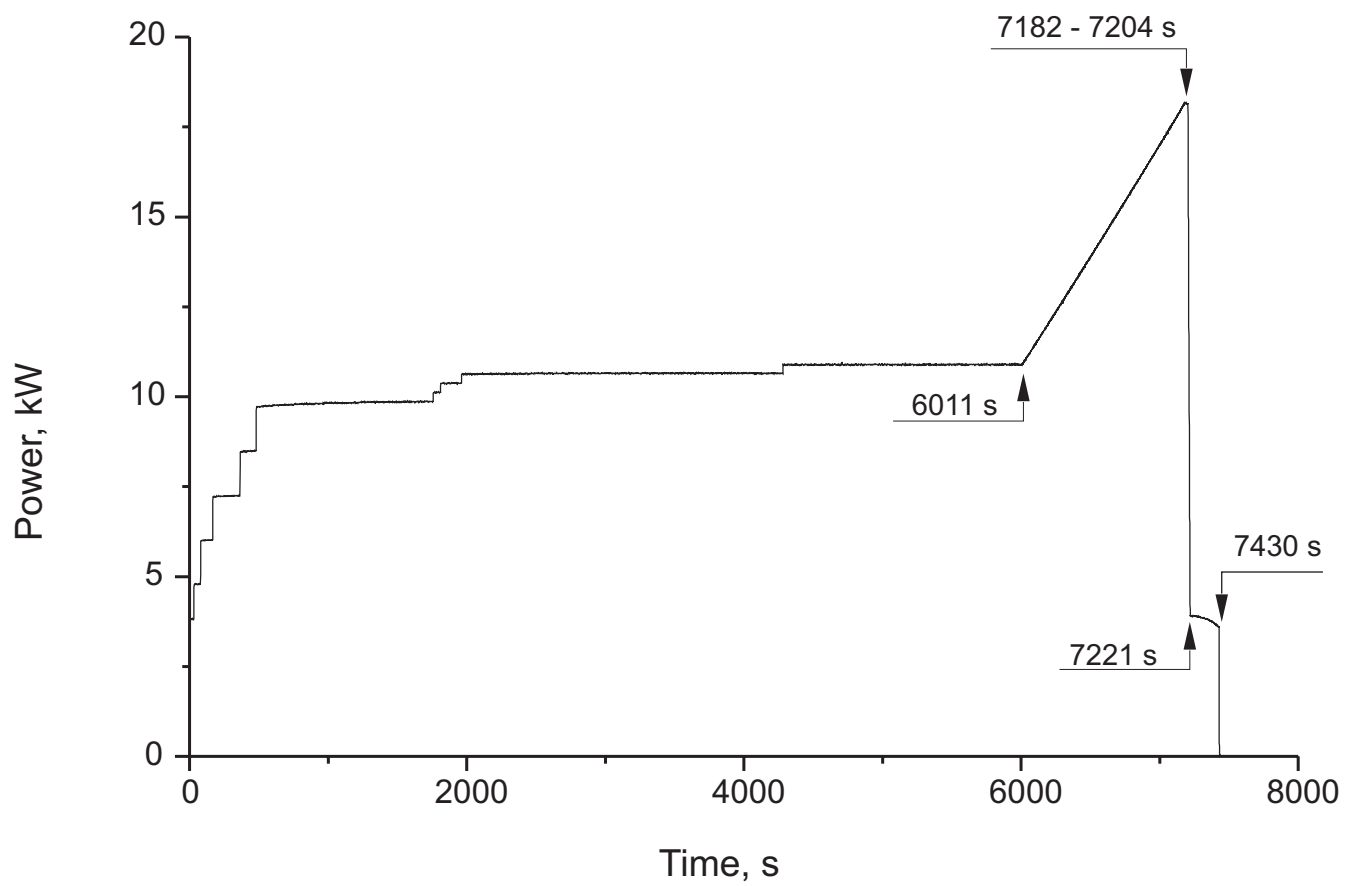


Fig.20-QUE06-Leistung.cdr
06.05.02 - IMF

Fig.20: QUENCH-06; Total electric power

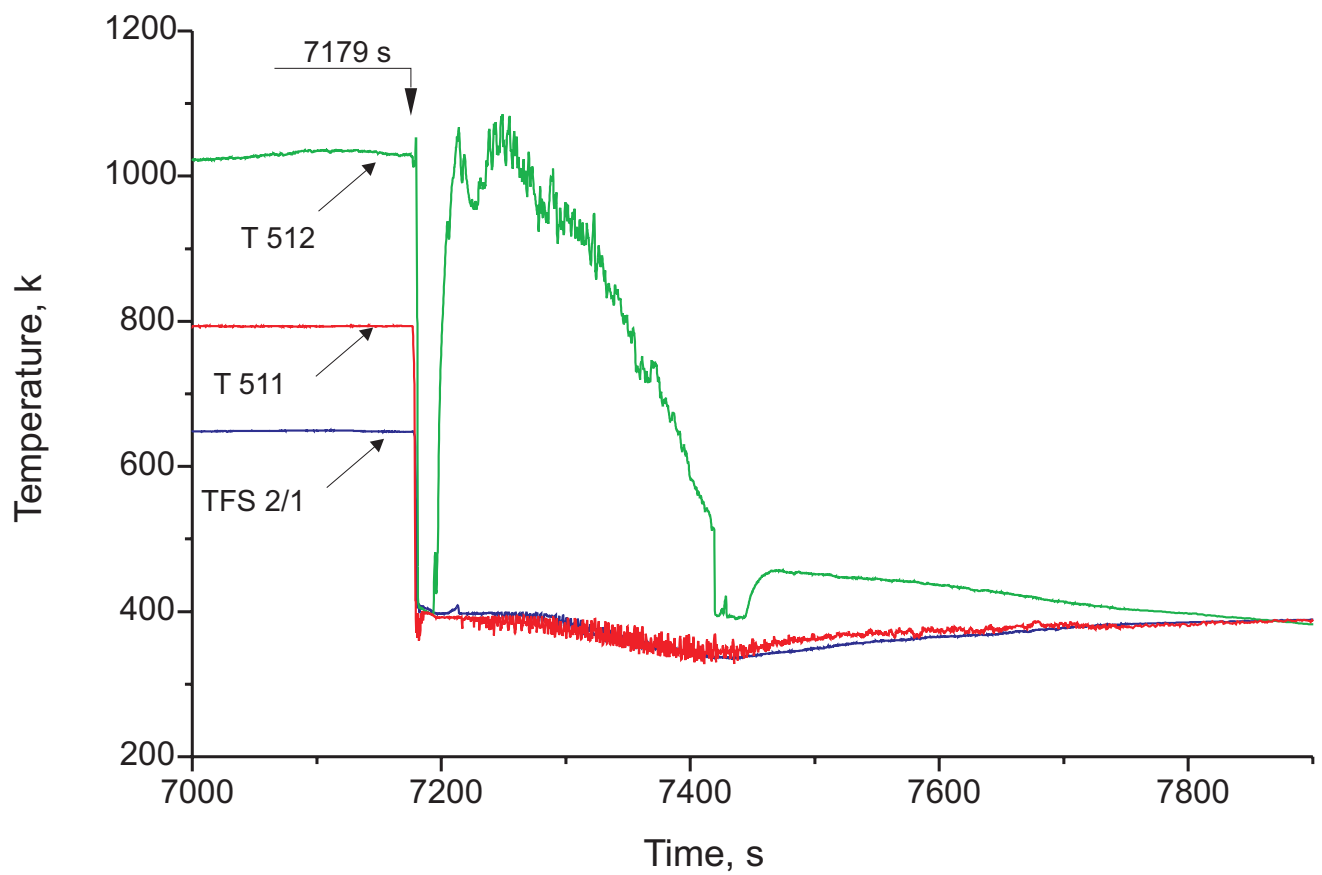
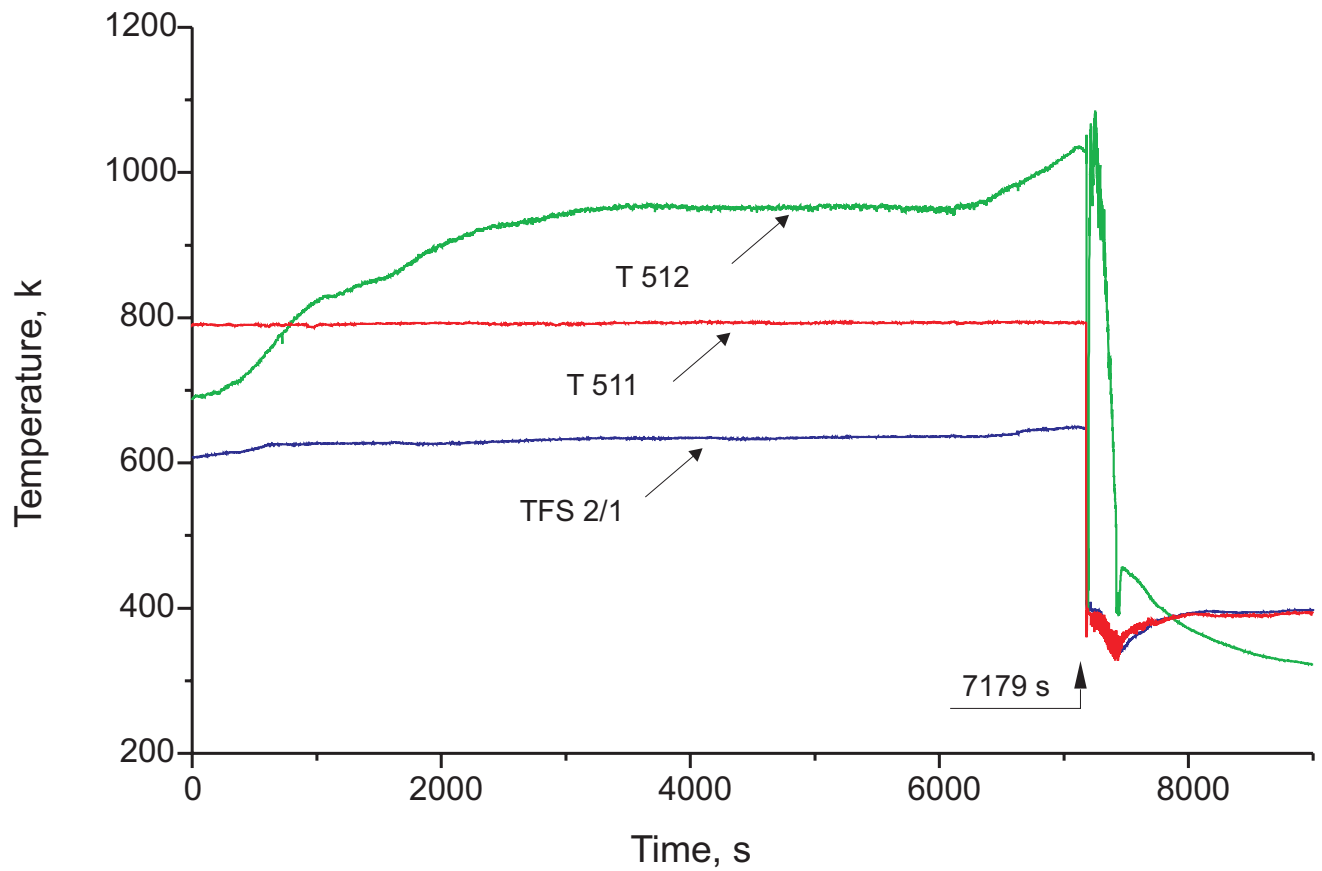


Fig.21-QUE06_Anlage_T511_T512.cdr
08.05.02 - IMF

Fig.21: QUENCH-06; Coolant temperatures
T 511 at bundle inlet, T 512 at bundle outlet, TFS 2/1 at -250 mm

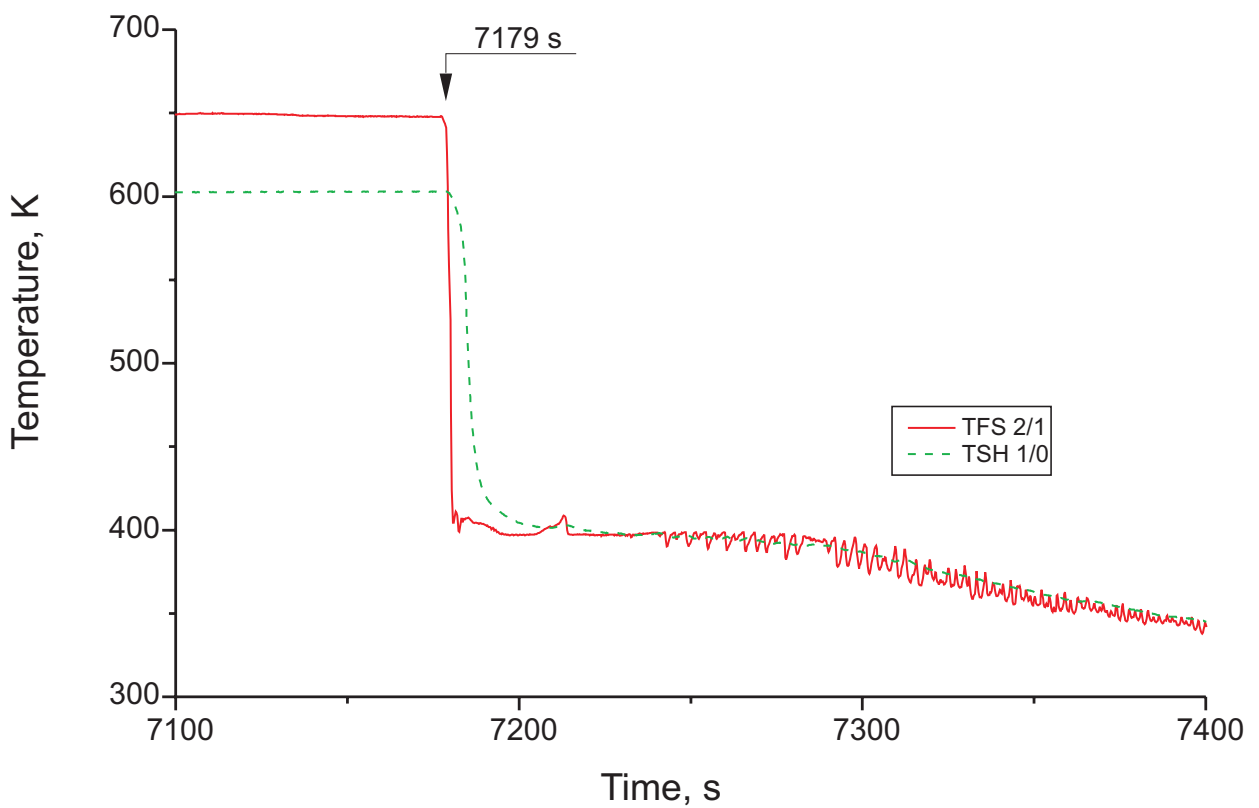
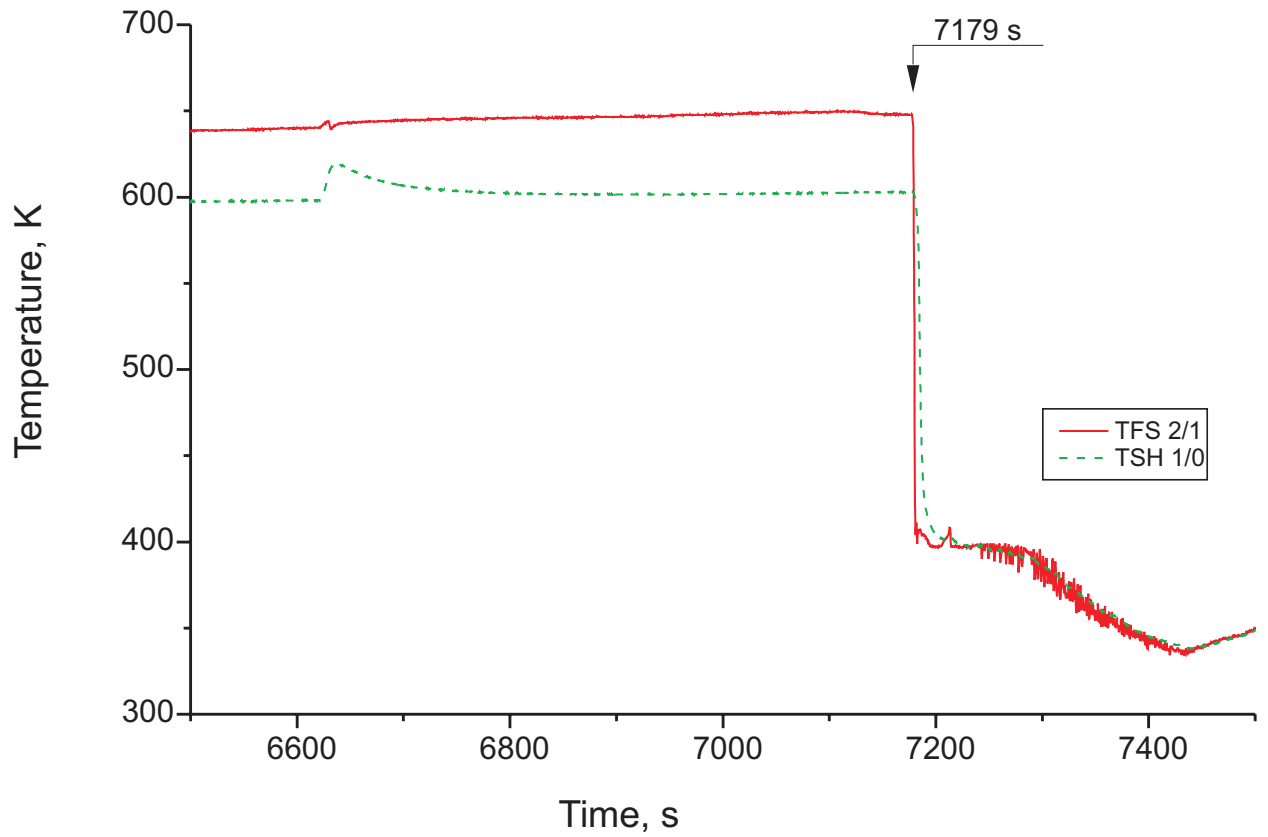


Fig. 22: QUENCH-06; Temperatures measured by rod surface (TFS), and shroud (TSH) thermocouples at -250 mm elevation

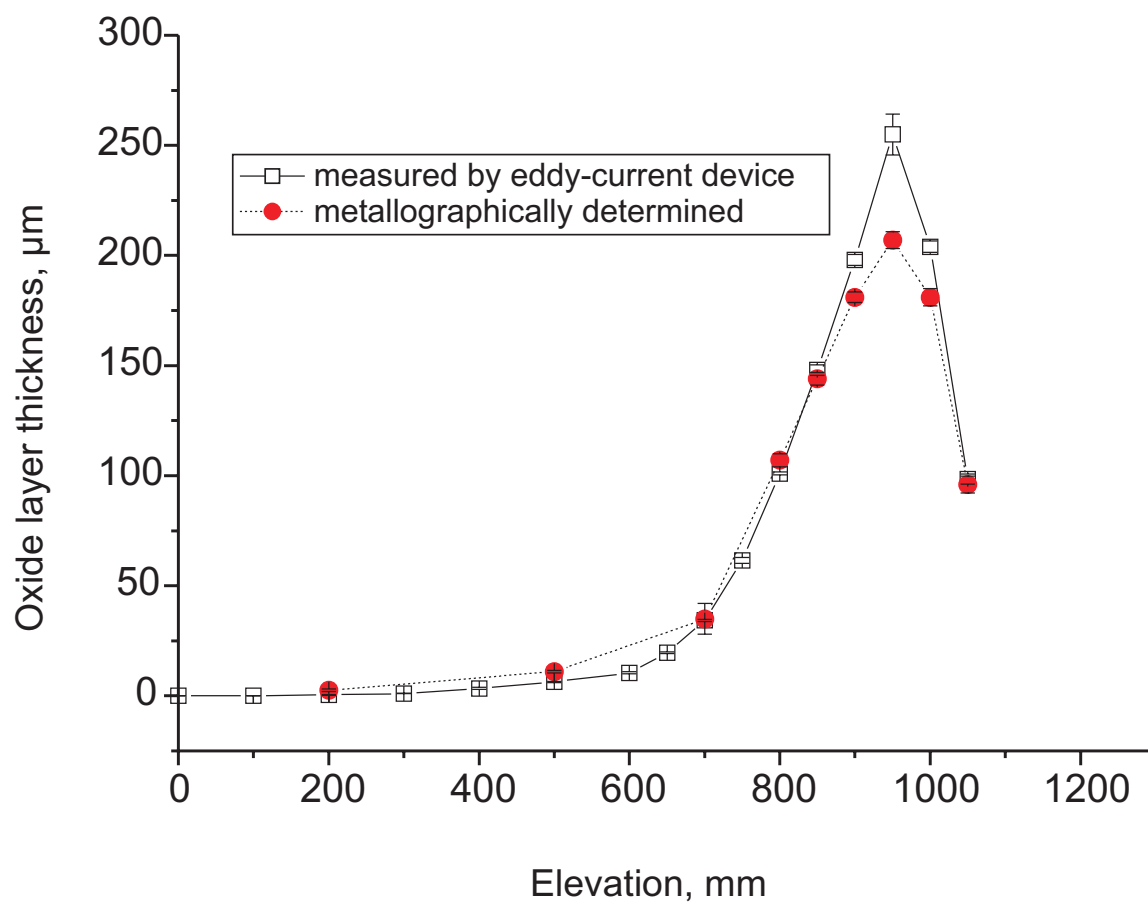


Fig.23-QUE06-eckstab oxid.cdr
05.06.02 - IMF

Fig. 23: QUENCH-06; Oxide layer thickness of corner rod B (withdrawn from bundle during transient)

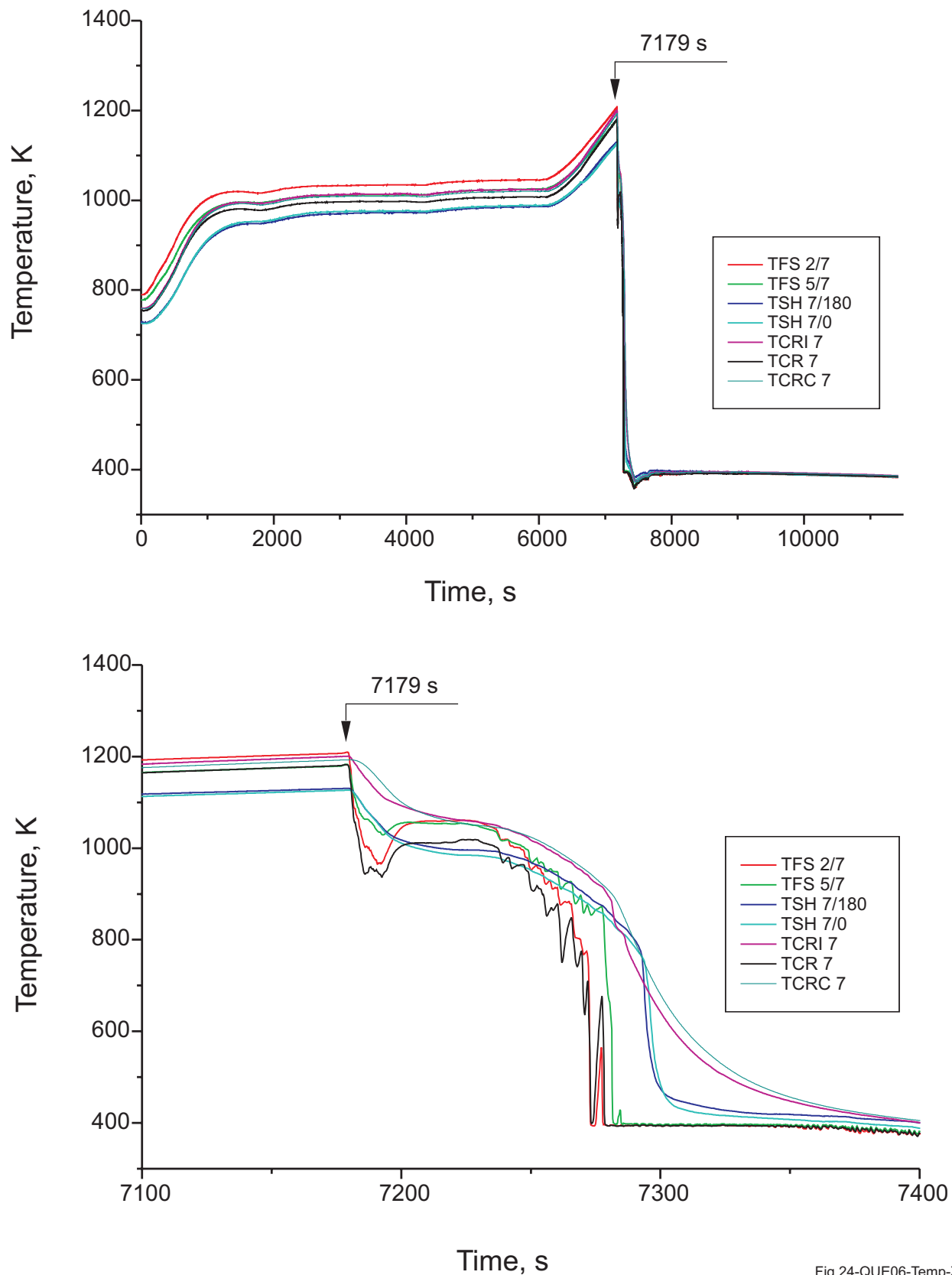


Fig.24-QUE06-Temp-Zeit-ebe7.cdr
15.05.01 - IMF

Fig. 24: QUENCH-06; Temperatures measured by rod cladding outer surface (TFS), shroud (TSH), central rod centerline (TCRC), central rod cladding inner surface (TCRI), and central rod cladding outer surface (TRC) thermocouples at 350 mm elevation

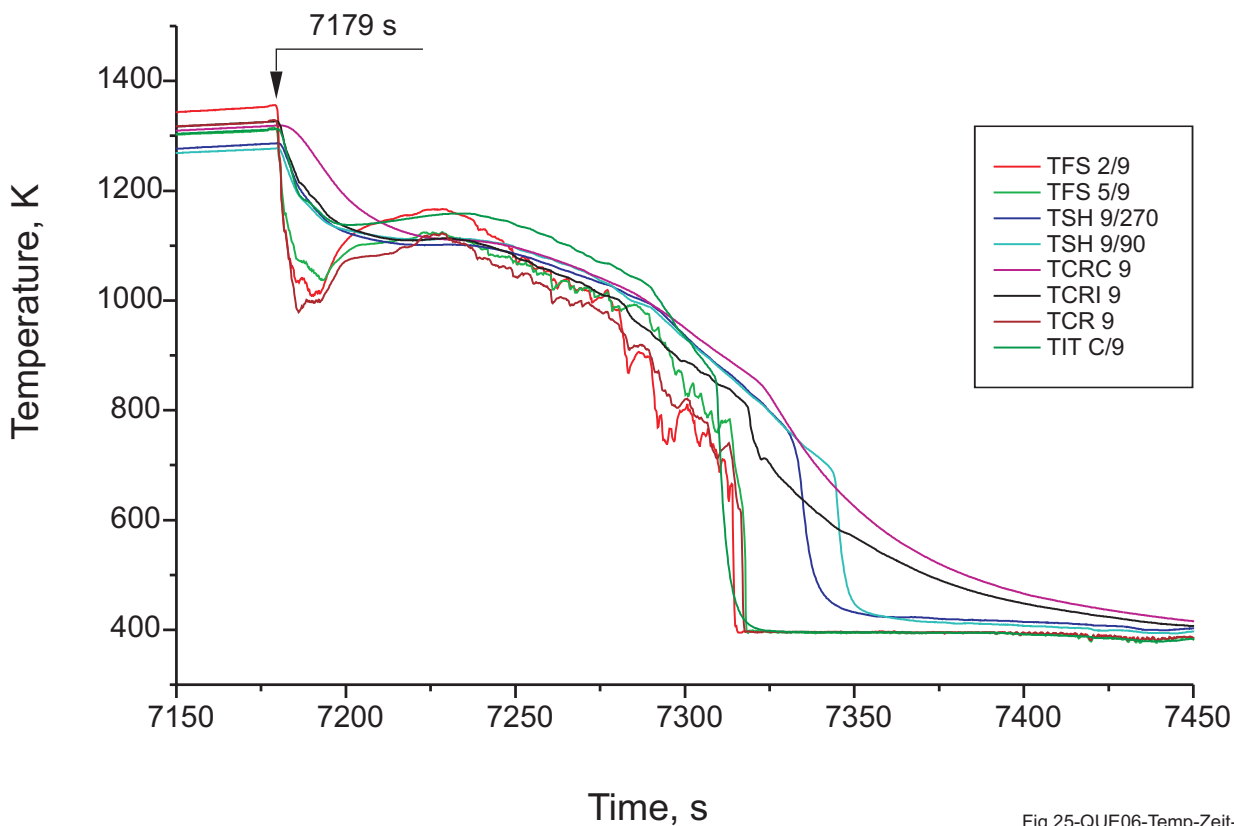
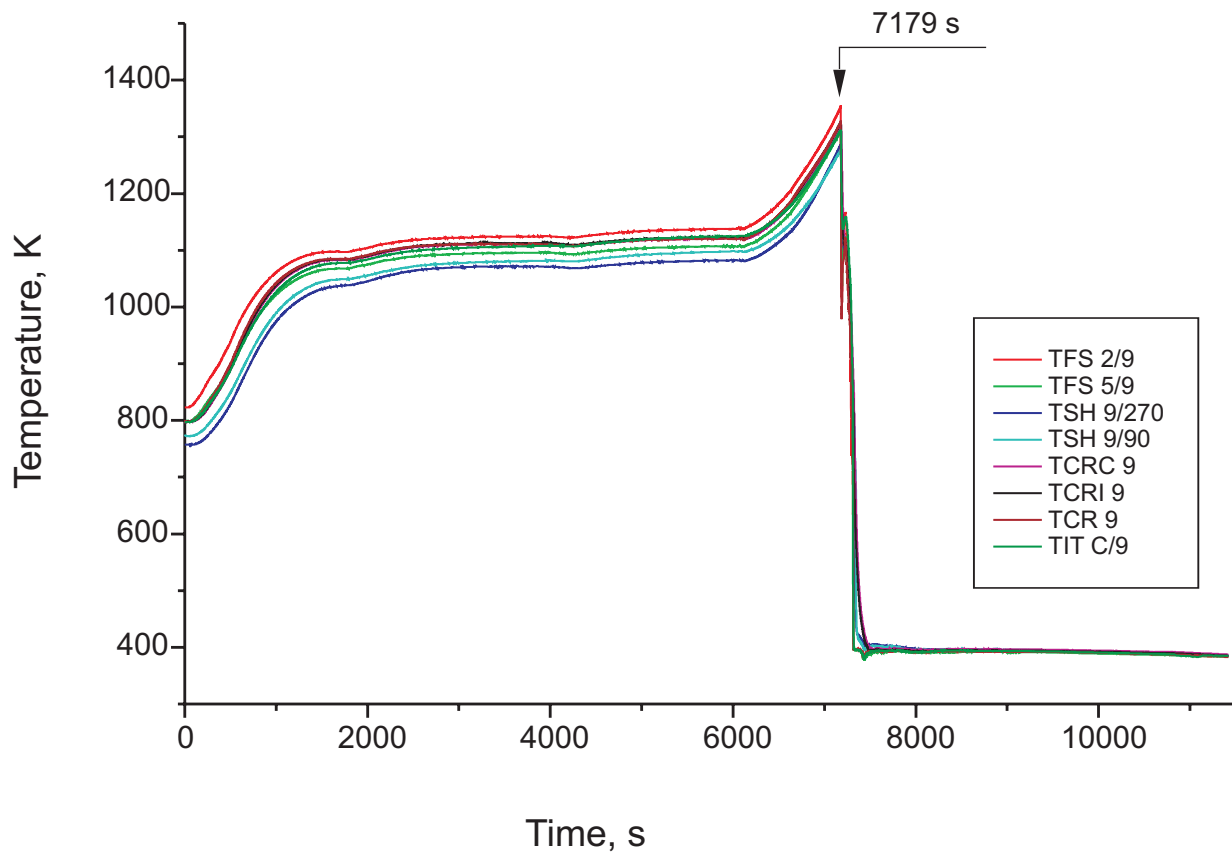


Fig.25-QUE06-Temp-Zeit-ebe9.cdr
15.05.01 - IMF

Fig. 25: QUENCH-06; Temperatures measured by rod cladding outer surface (TFS), shroud (TSH), central rod centerline (TCRC), central rod cladding inner surface (TCRI), central rod cladding outer surface (TRC), and corner rod internal (TIT) thermocouples at 550 mm elevation

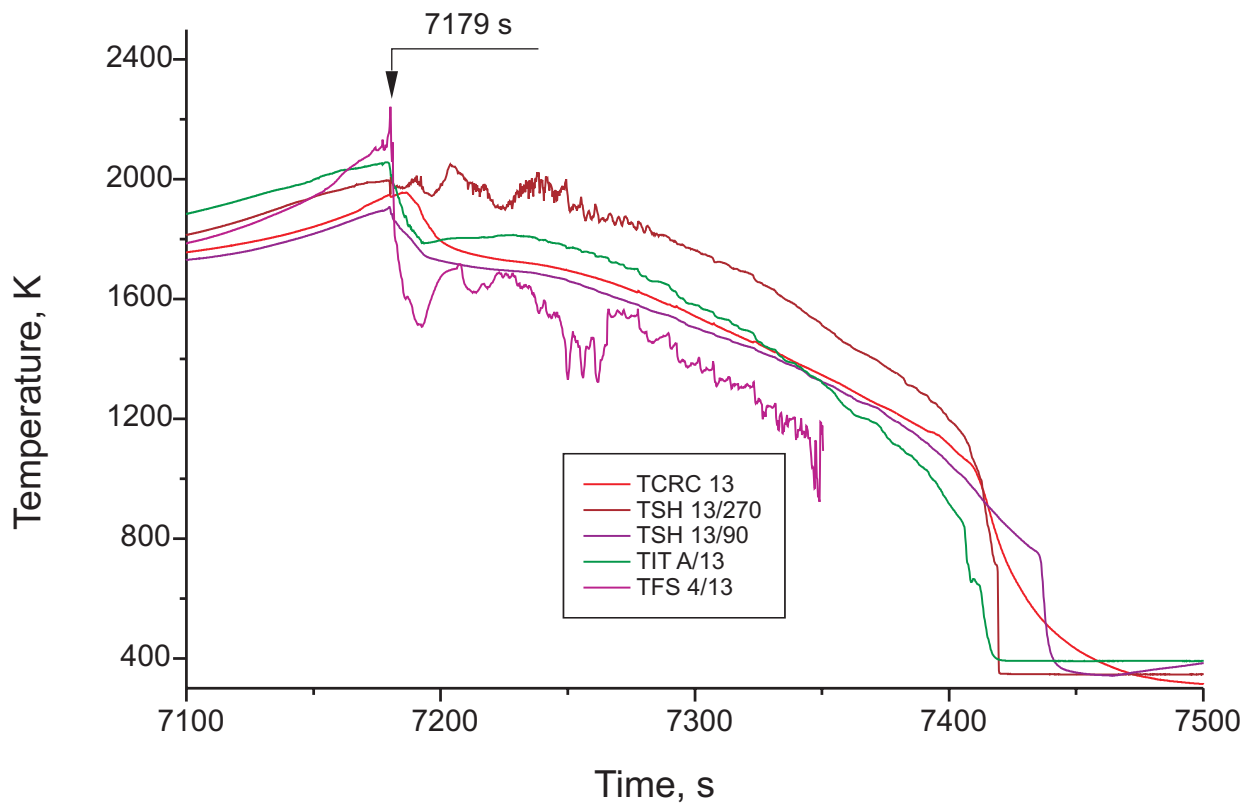
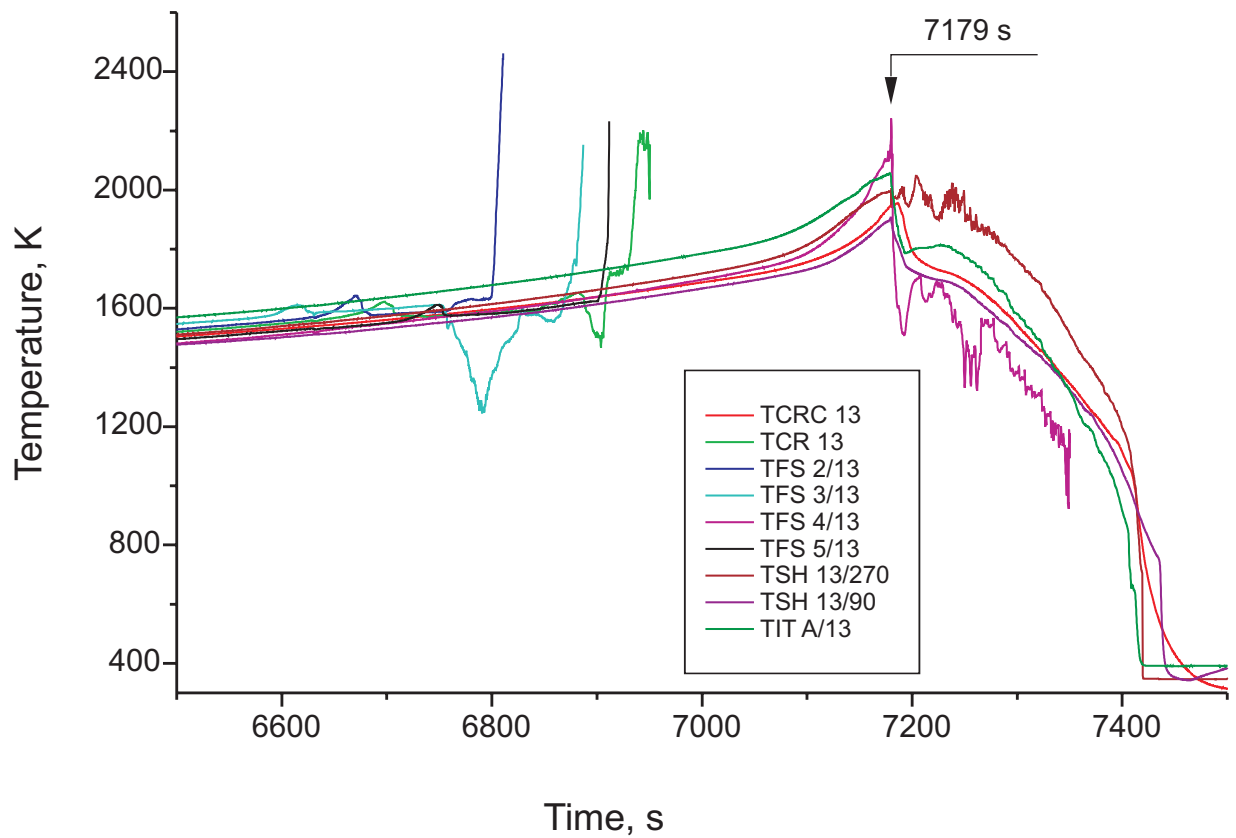


Fig.27-QUE06-Temp-Zeit-ebe13.cdr
12.06.02 - IMF

Fig. 27: QUENCH-06; Temperatures measured by rod cladding outer surface (TFS), shroud (TSH), central rod centerline (TCRC), central rod cladding outer surface (TCR), and corner rod internal (TIT) thermocouples at 950 mm elevation

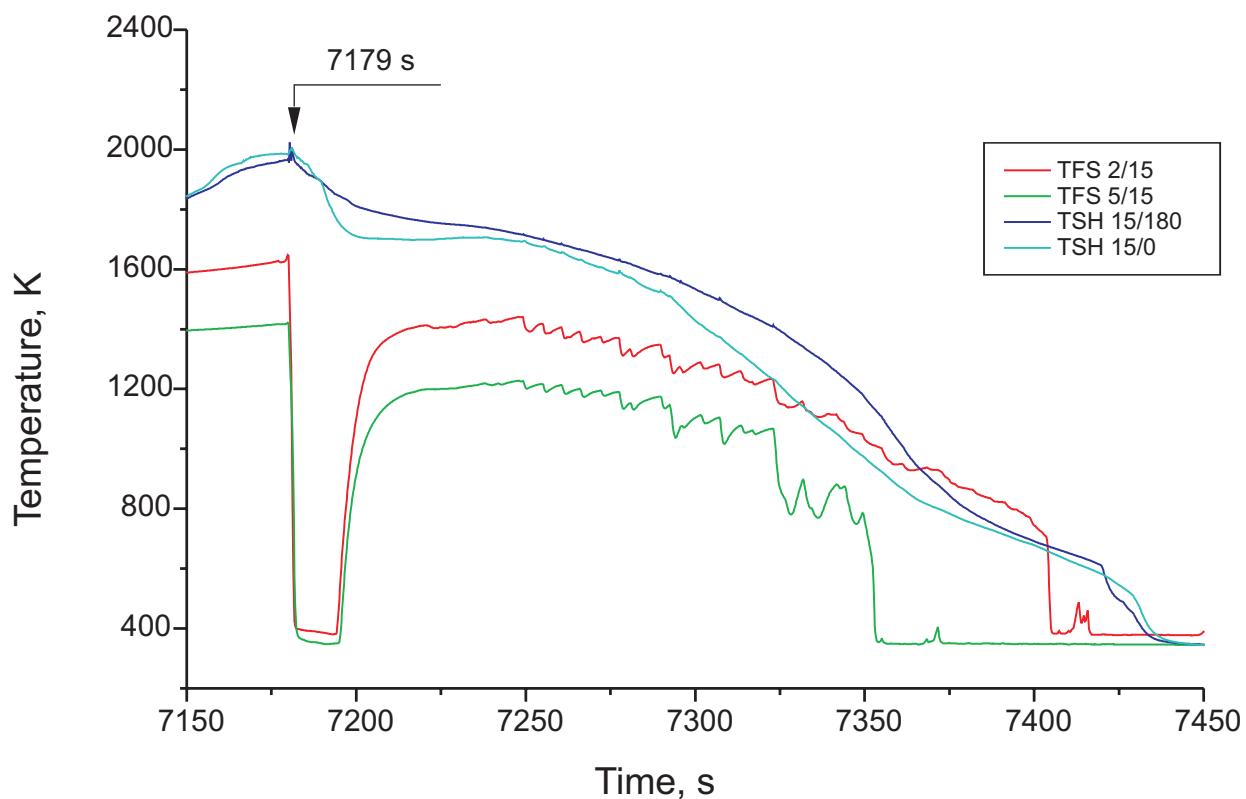
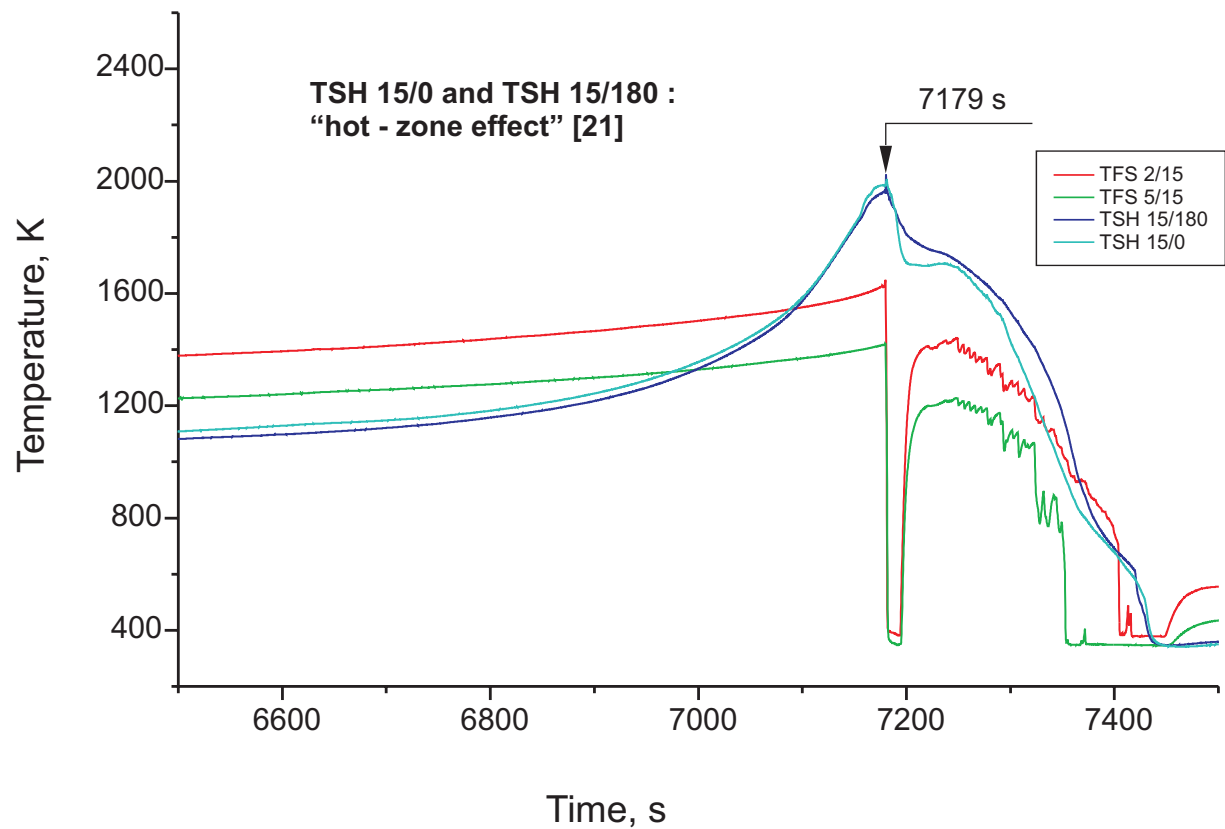


Fig.28-QUE06-Temp-Zeit-ebe15.cdr
20.01.04 - IMF

Fig. 28: QUENCH-06; Temperatures measured by rod surface (TFS), and shroud (TSH) thermocouples at 1150 mm elevation

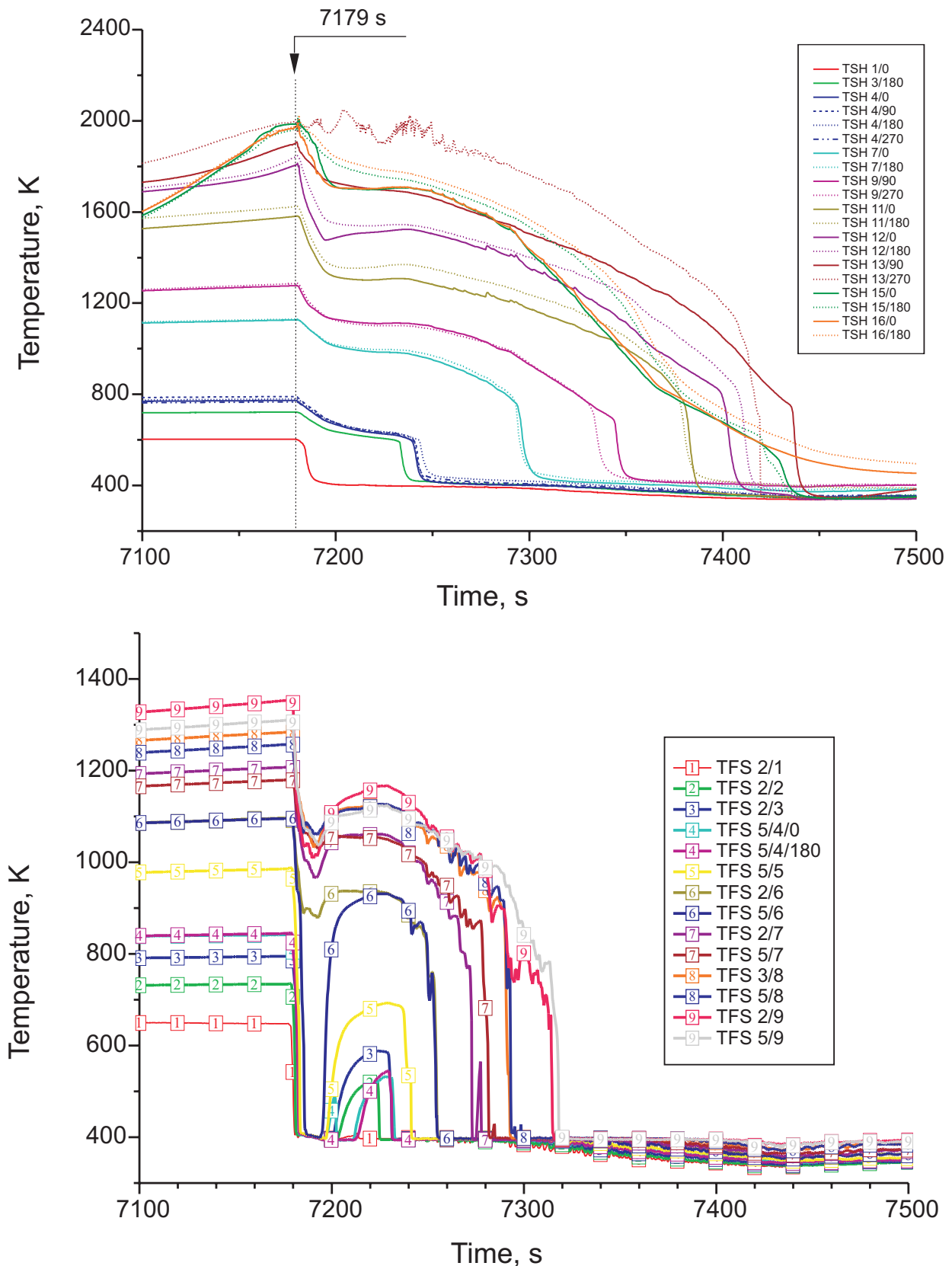


Fig.29-QUE06-alle TSH.cdr
03.06.02 - IMF

Fig. 29: QUENCH-06; Temperature response of the shroud thermocouples , top, and cladding thermocouples up to 550 mm elevation, bottom, during the quenching phase

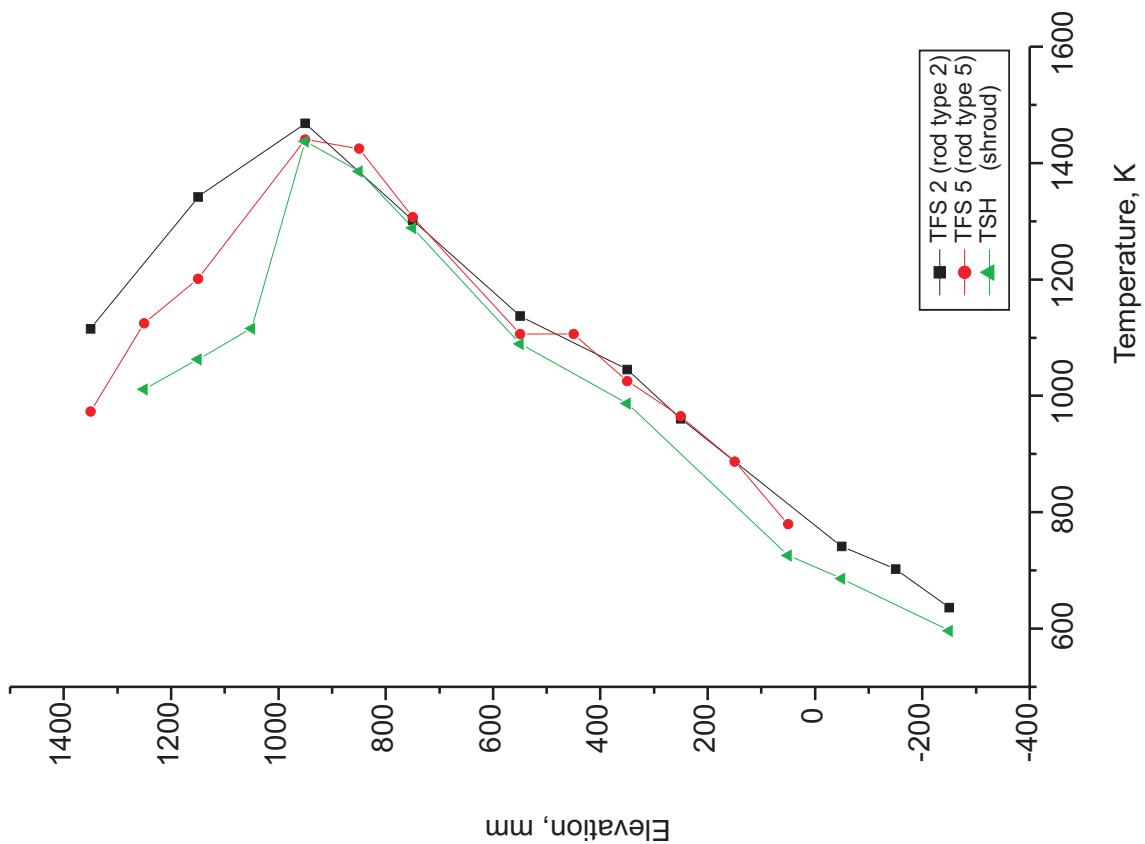
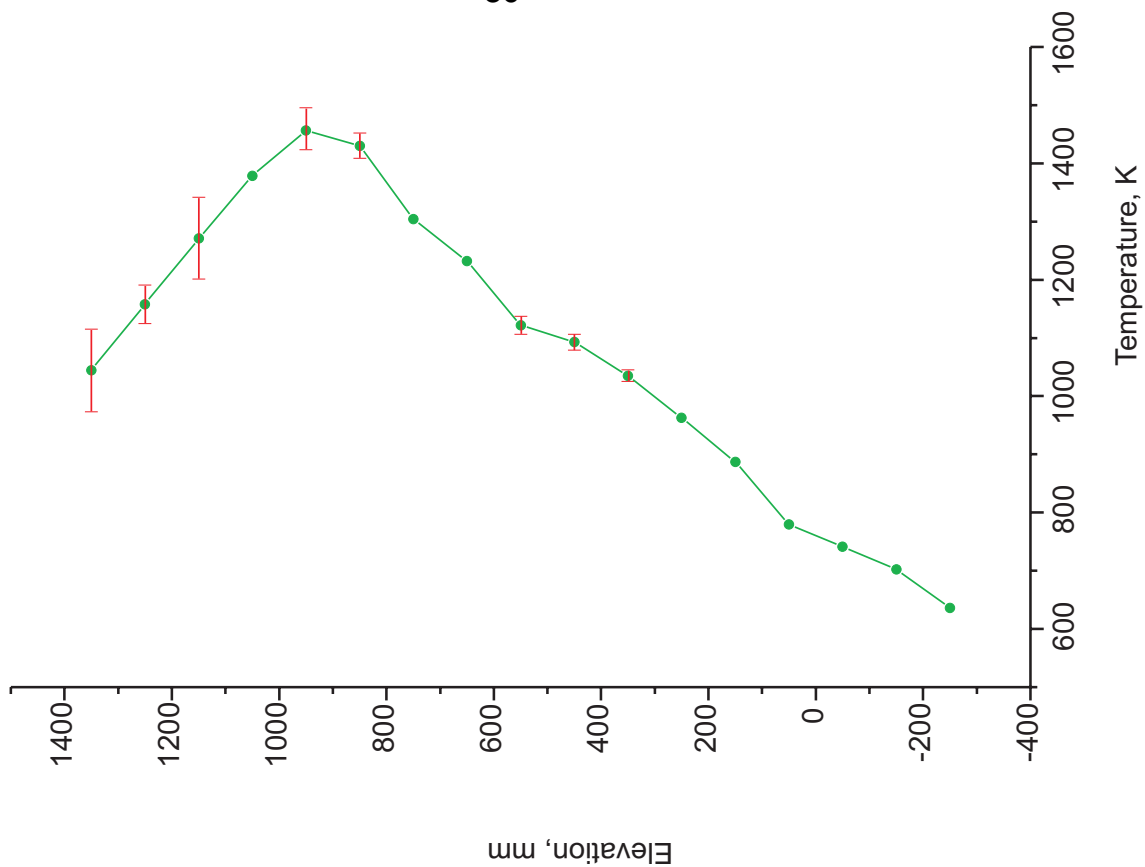


Fig.30-QUE06-axial-6010s.cdr
04.06.03 - IMF

Fig. 30: QUENCH-06; Axial temperature profile of TFS 2 (inner coolant channel), TFS 5 (outer channel), and TSH (shroud) thermocouples, left, and axial profile of all TFS thermocouples, right, at 6010 s (onset of transient).

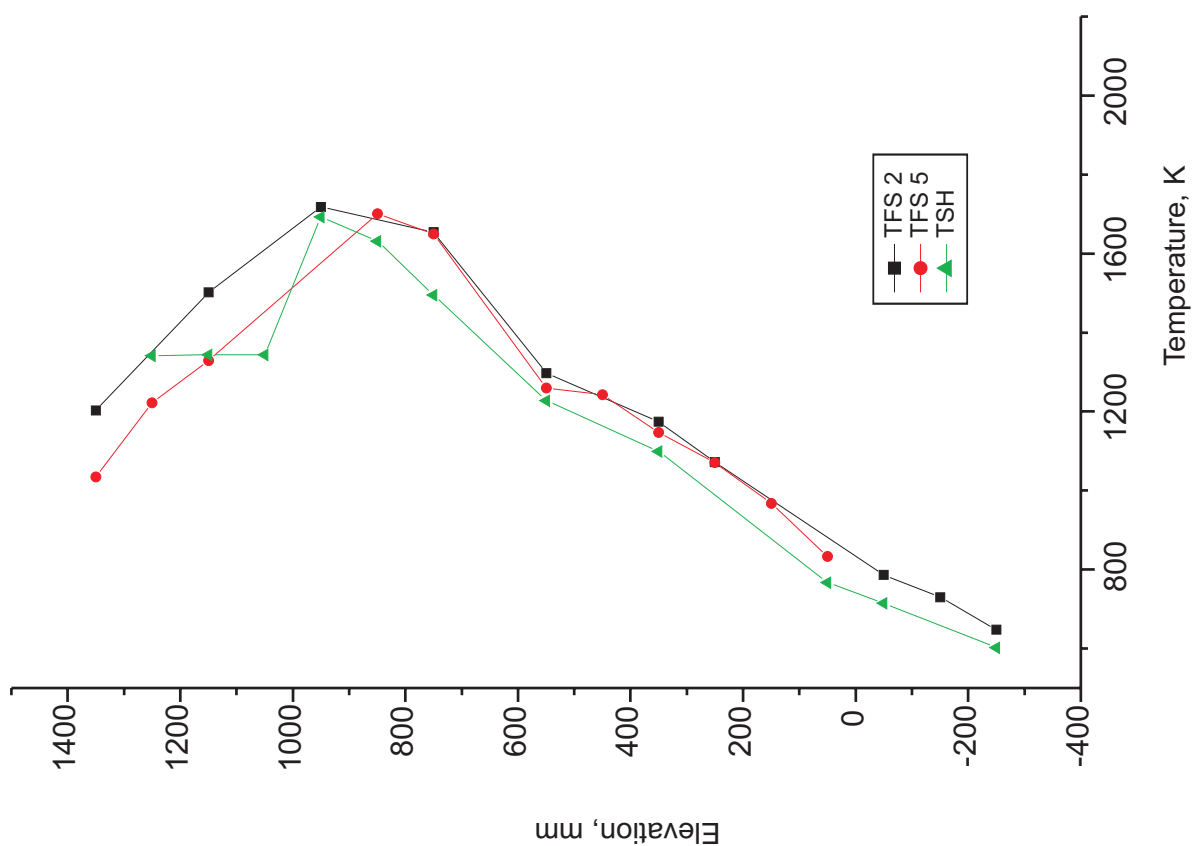
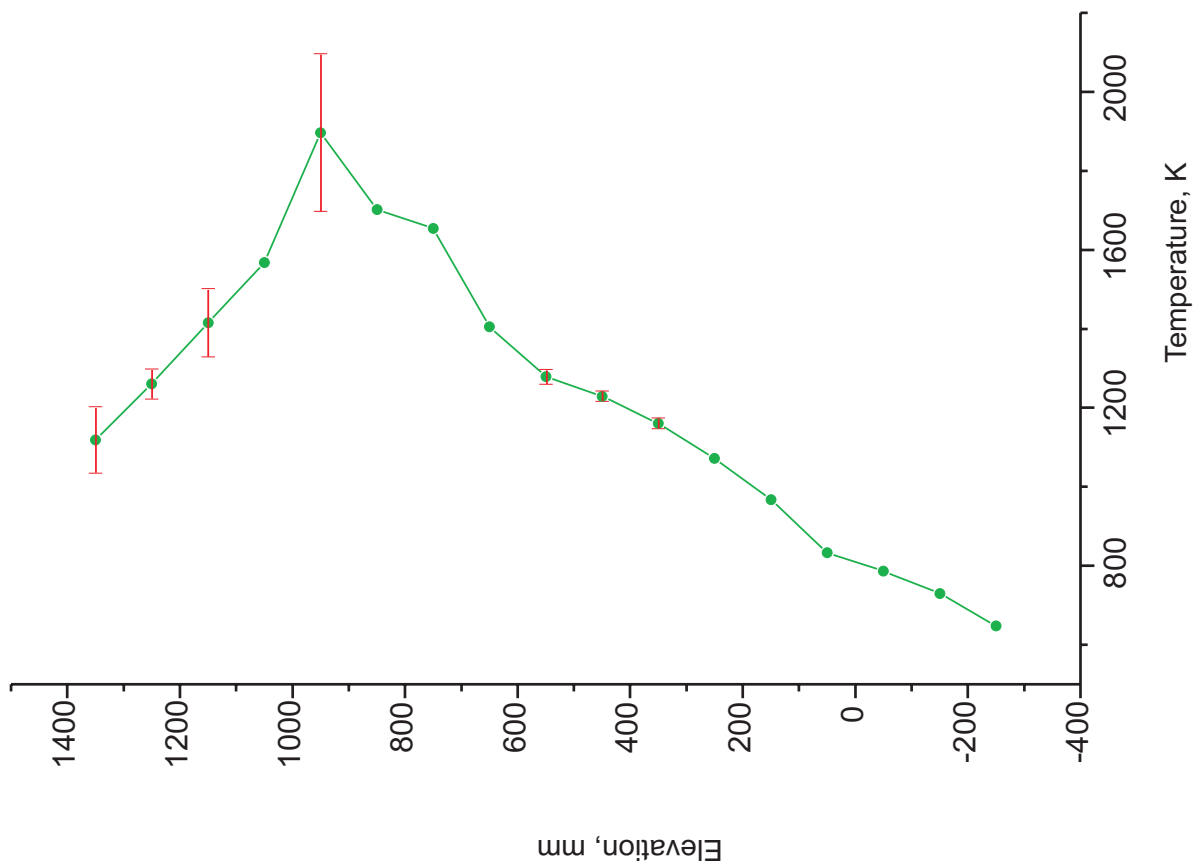


Fig.31-QUE06-axial-7000s.cdr
04.06.03 - IMF

Fig. 31: QUENCH-06; Axial temperature profile of TFS 2 (inner coolant channel), TFS 5 (outer channel), and TSH (shroud) thermocouples, left, and axial profile of all TFS thermocouples, right, at 7000 s (transient phase).

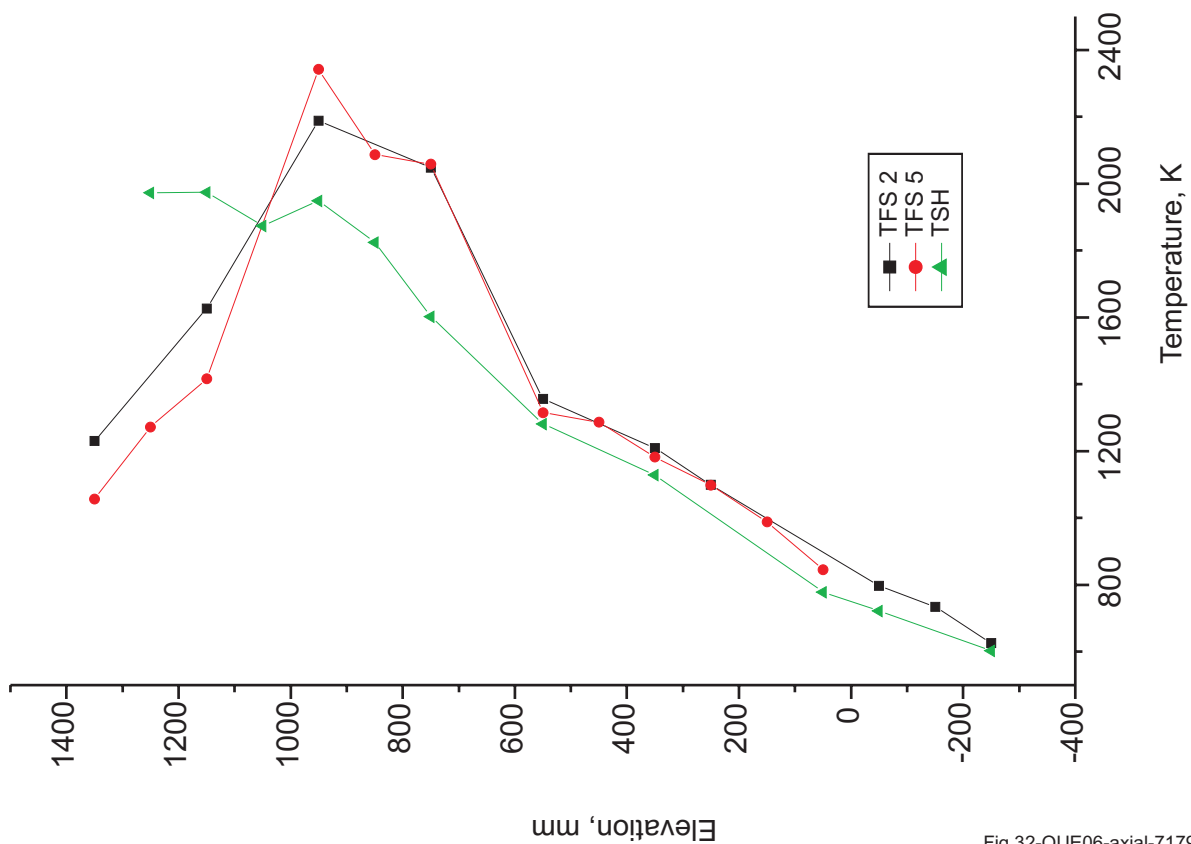
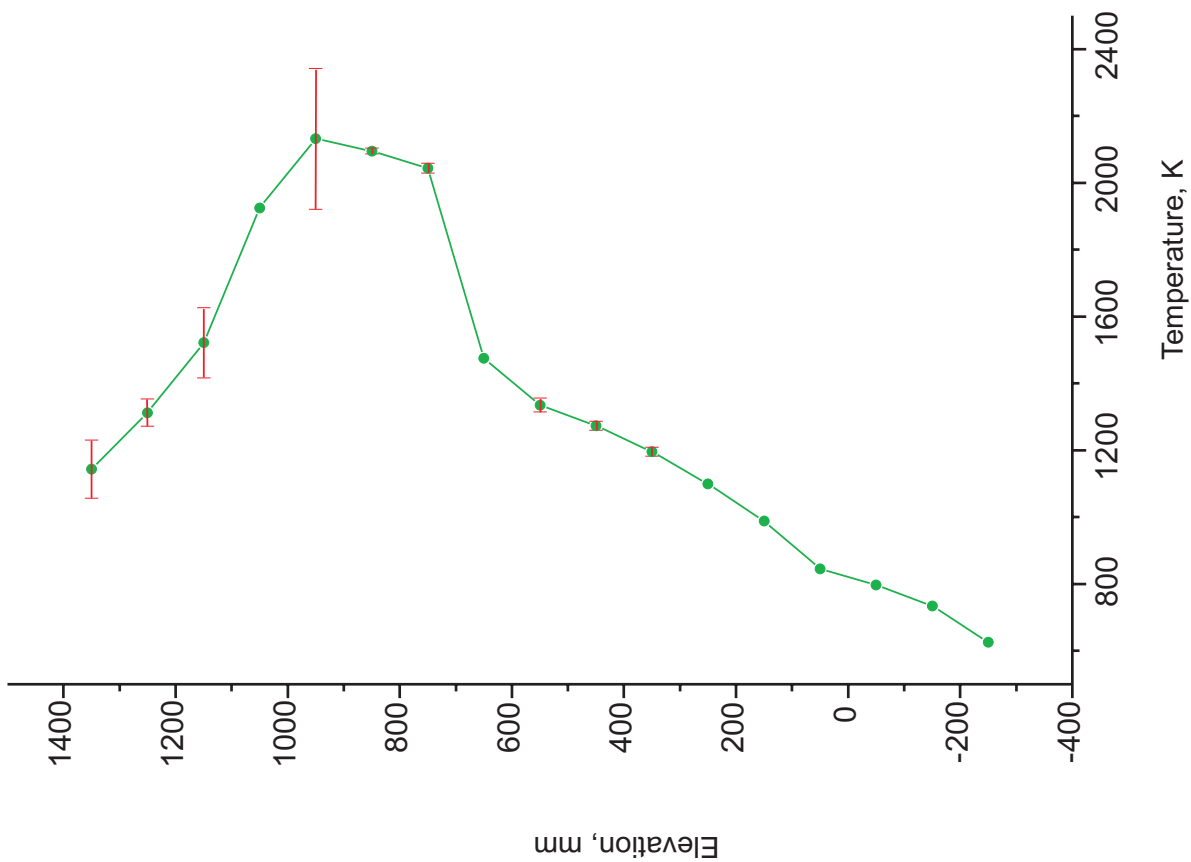


Fig.32-QUE06-axial-7179s.cdr
04.06.03 - IMF

Fig. 32: QUENCH-06; Axial temperature profile of TFS 2 (inner coolant channel), TFS 5 (outer channel), and TSH (shroud) thermocouples, left, and axial profile of all TFS thermocouples, right, at 7179 s (onset of quenching).

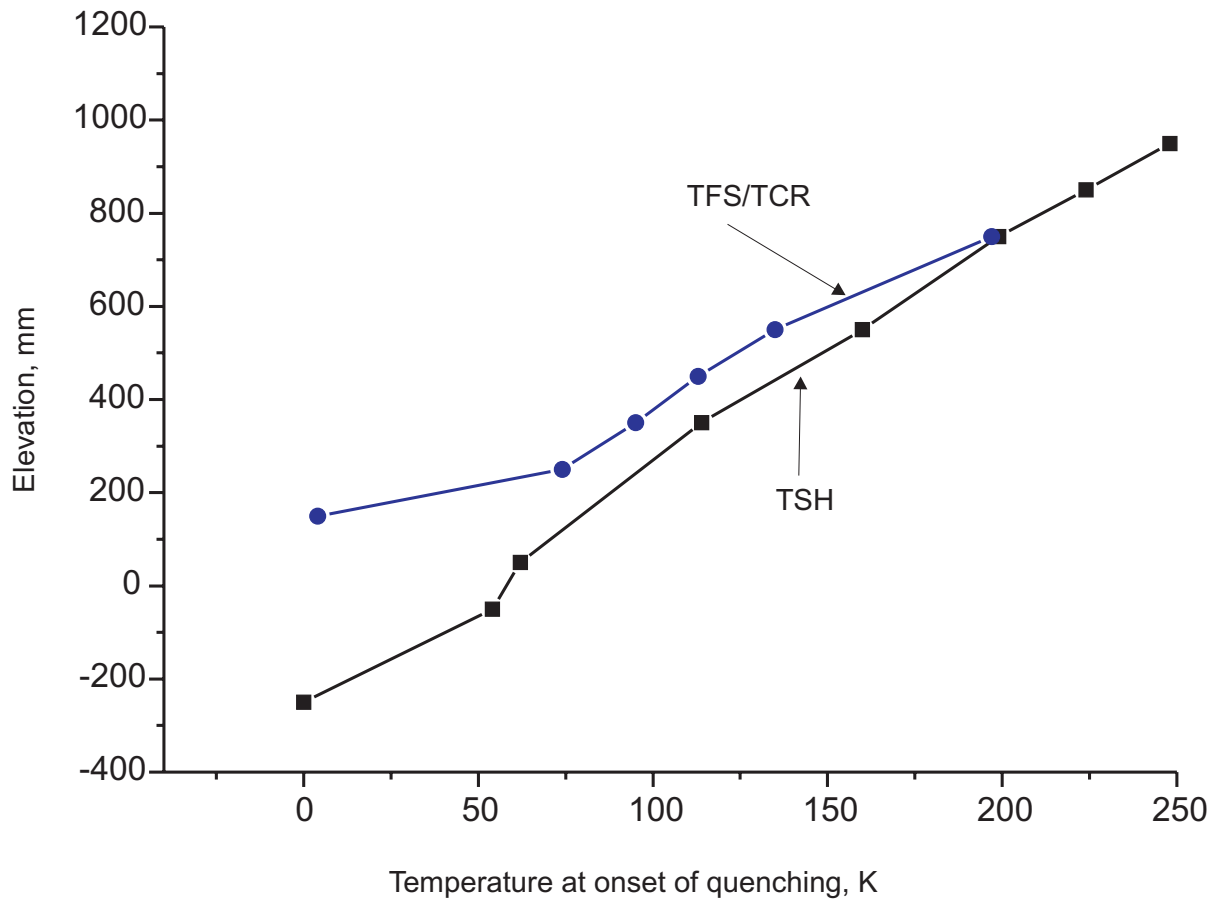


Fig.33-QUE06-TFS+TSH quench progression2.cdr
05.06.02 - IMF

Fig. 33: QUENCH-06; Quench front progression based on TFS/TCR cladding thermocouples and on TSH shroud thermocouples. (Water injection velocity - 1.4 cm/s).

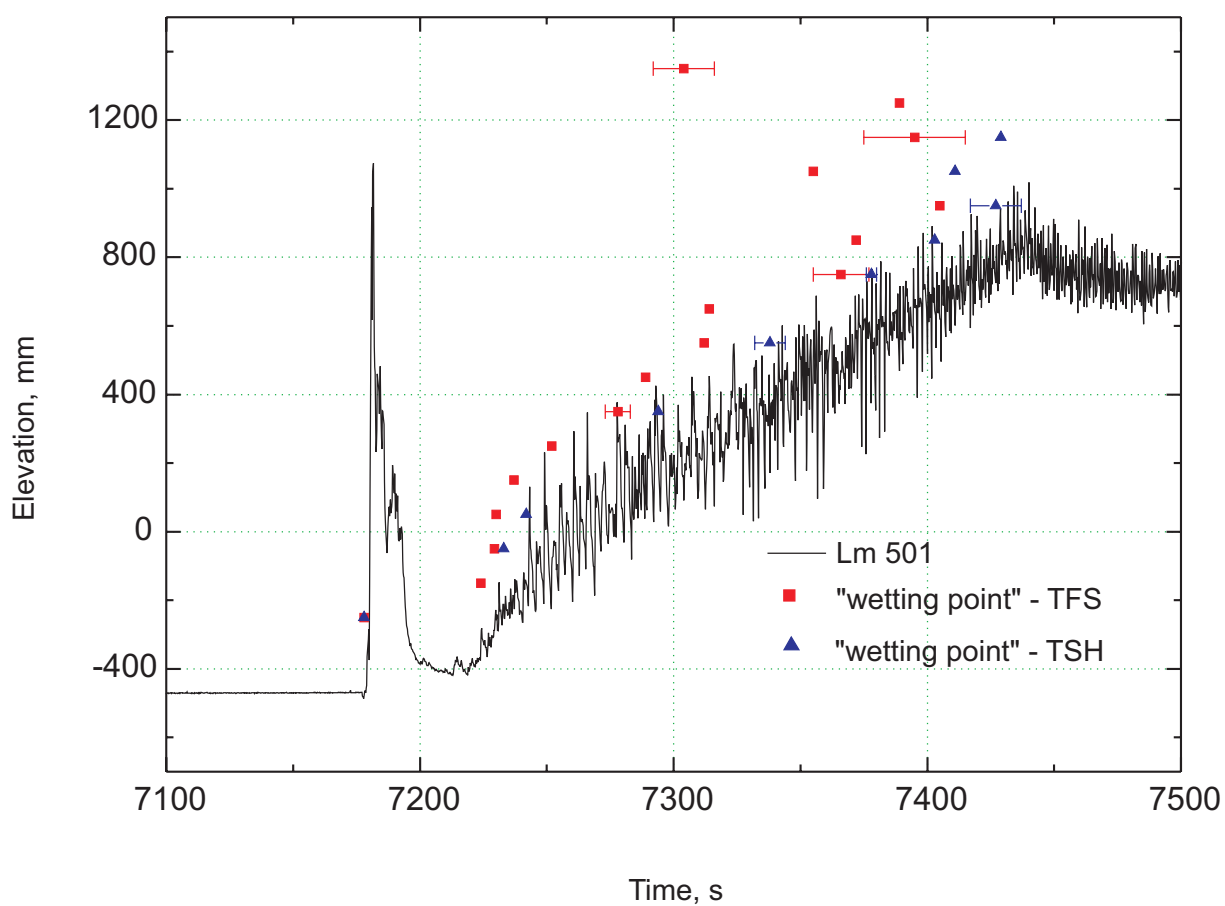


Fig.34-QUE06-Anlage-Lm501.cdr
12.06.02 - IMF

Fig. 34: QUENCH-06; Indication of the collapsed water level in the test section (Lm 501) together with the time points of complete wetting based on cladding (TFS) and shroud (TSH) thermocouples

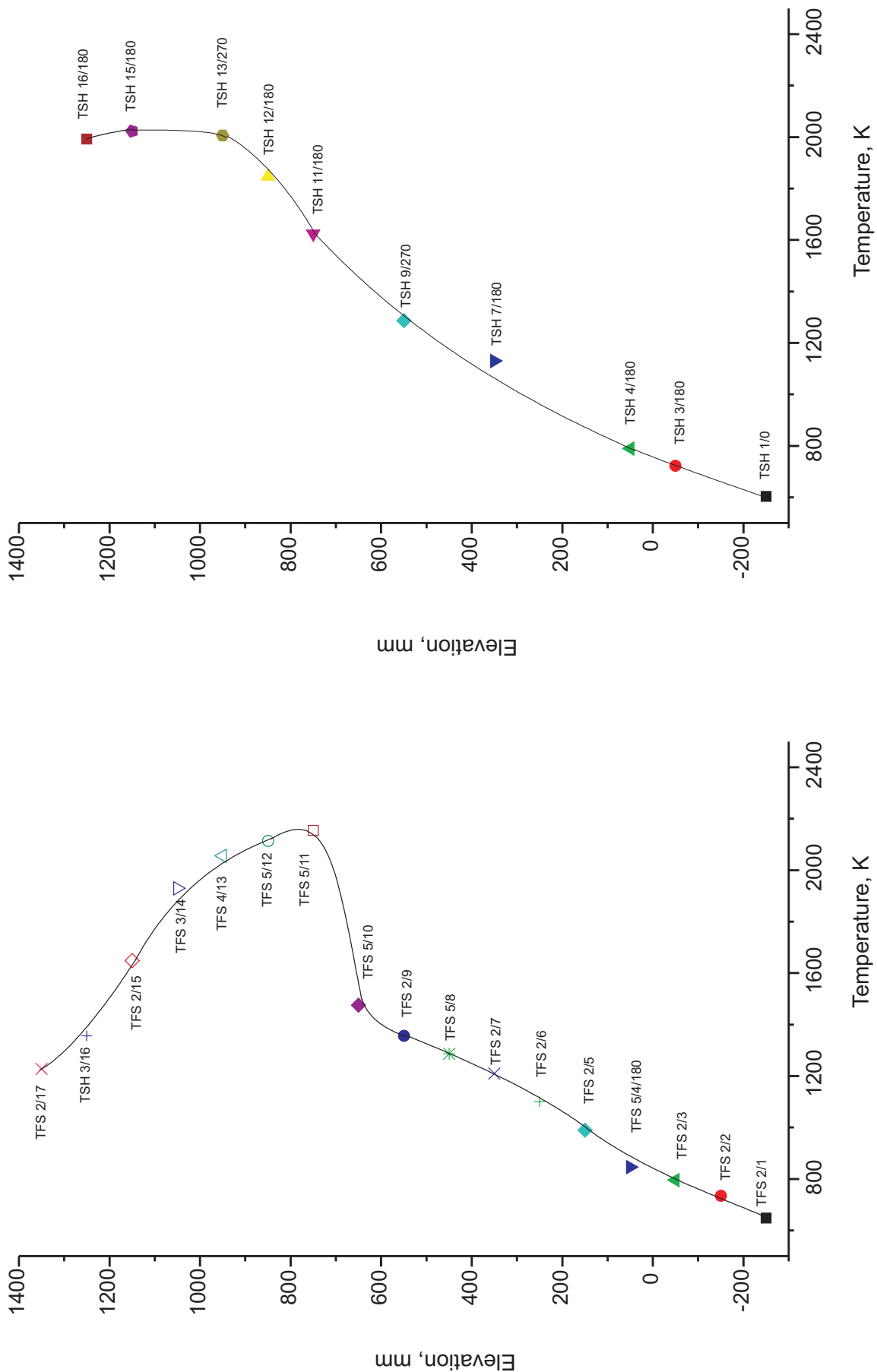


Fig.35-QUE06-maxTFS-TSH.cdr
04.06.03 - IMF

Fig. 35: QUENCH-06; Maximum rod cladding temperature of each elevation, left, and maximum shroud temperature of each elevation, right

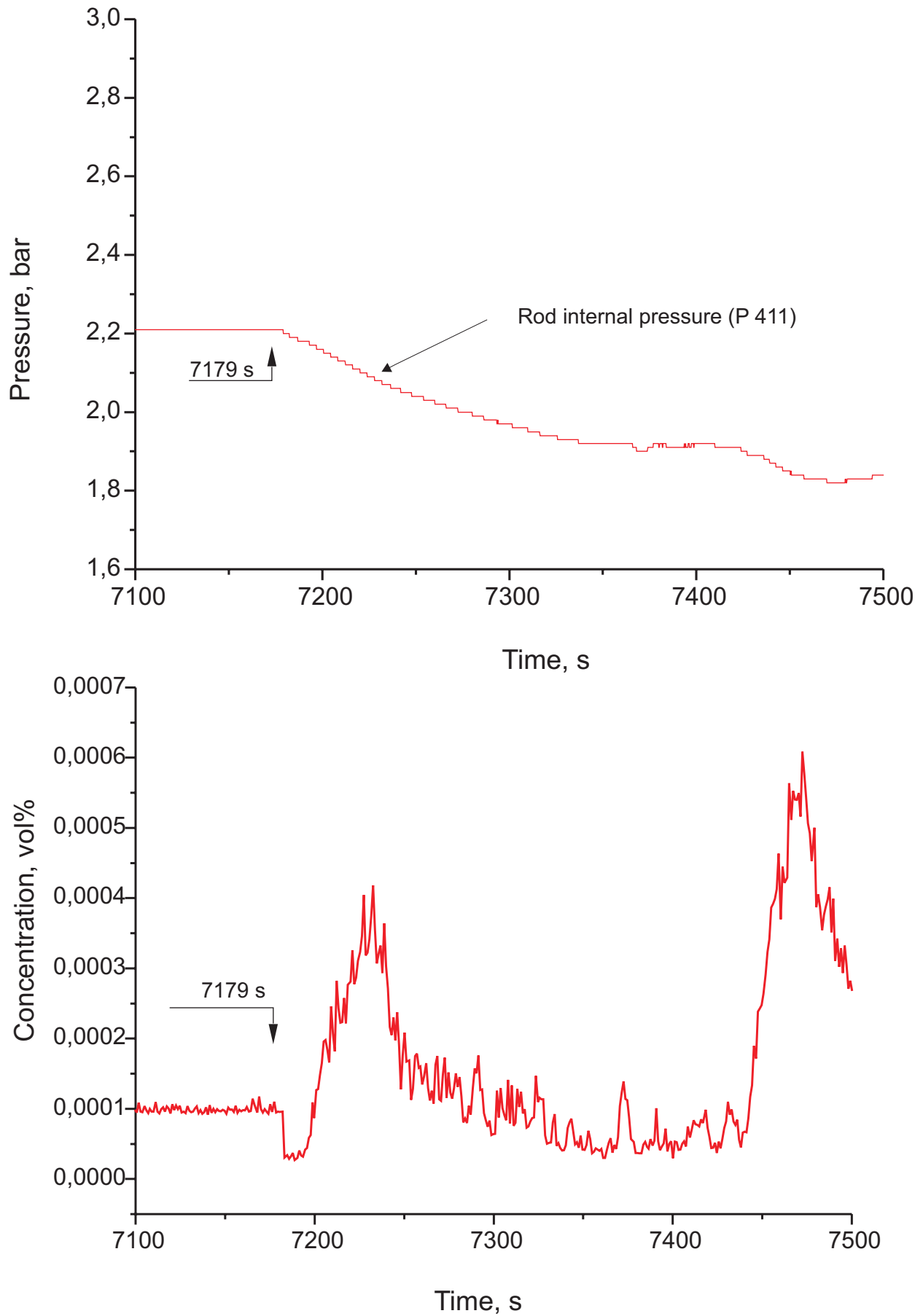


Fig.36-QUE06-P411-krypton.cdr
12.06.02 - IMF

Fig. 36: QUENCH-06; Rod failure at the onset of quenching indicated by P 411, top, and by the krypton concentration measured by the mass spectrometer, bottom.

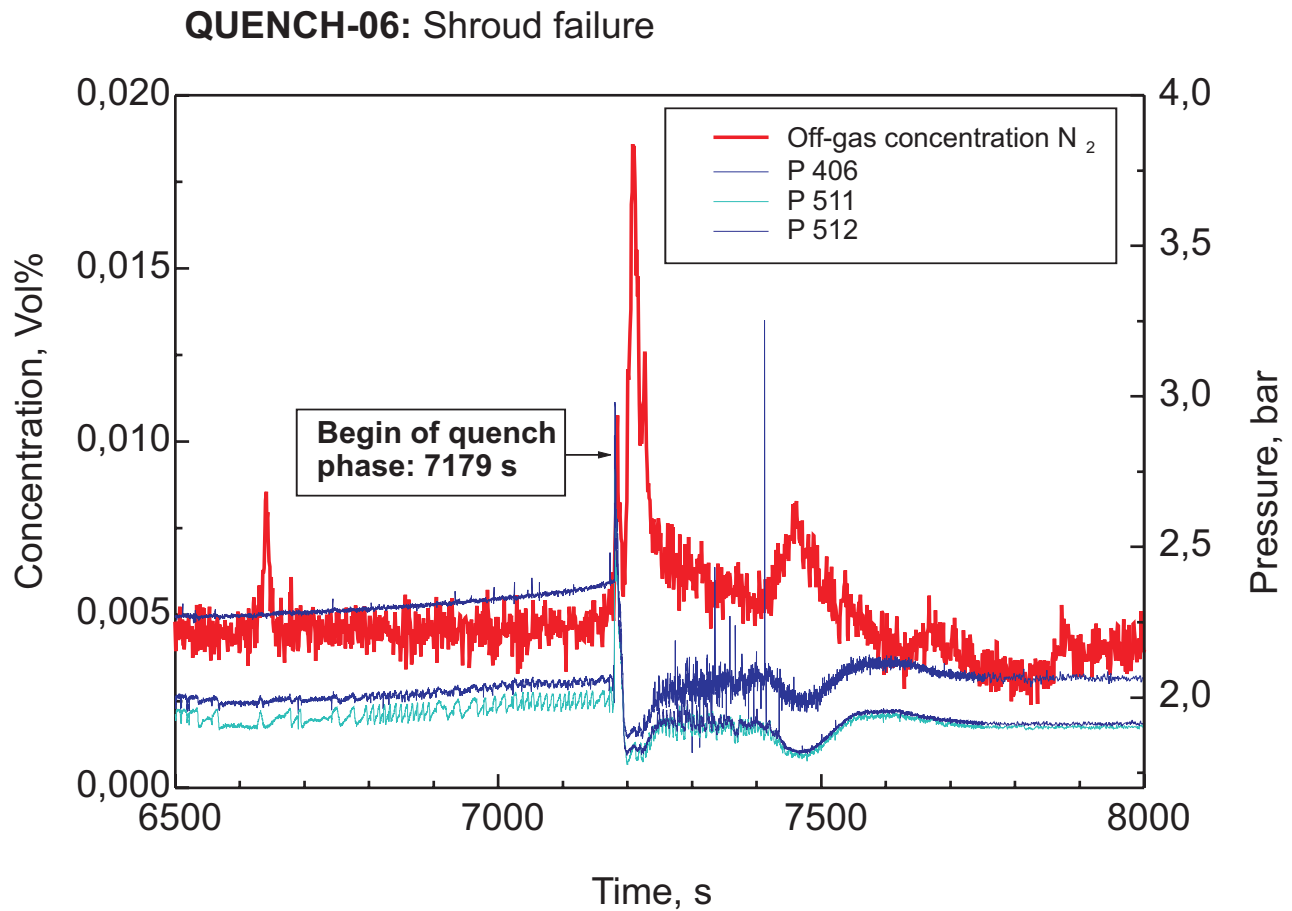


Fig.37-QUE06-shroud failure.cdr
12.06.02 - IMF

Fig. 37: QUENCH-06; Shroud failure at the onset of quenching (7179 s) as indicated by the pressure P 406 measured in the space between shroud and inner cooling jacket and by the nitrogen concentration measured in the off-gas by the mass spectrometer.

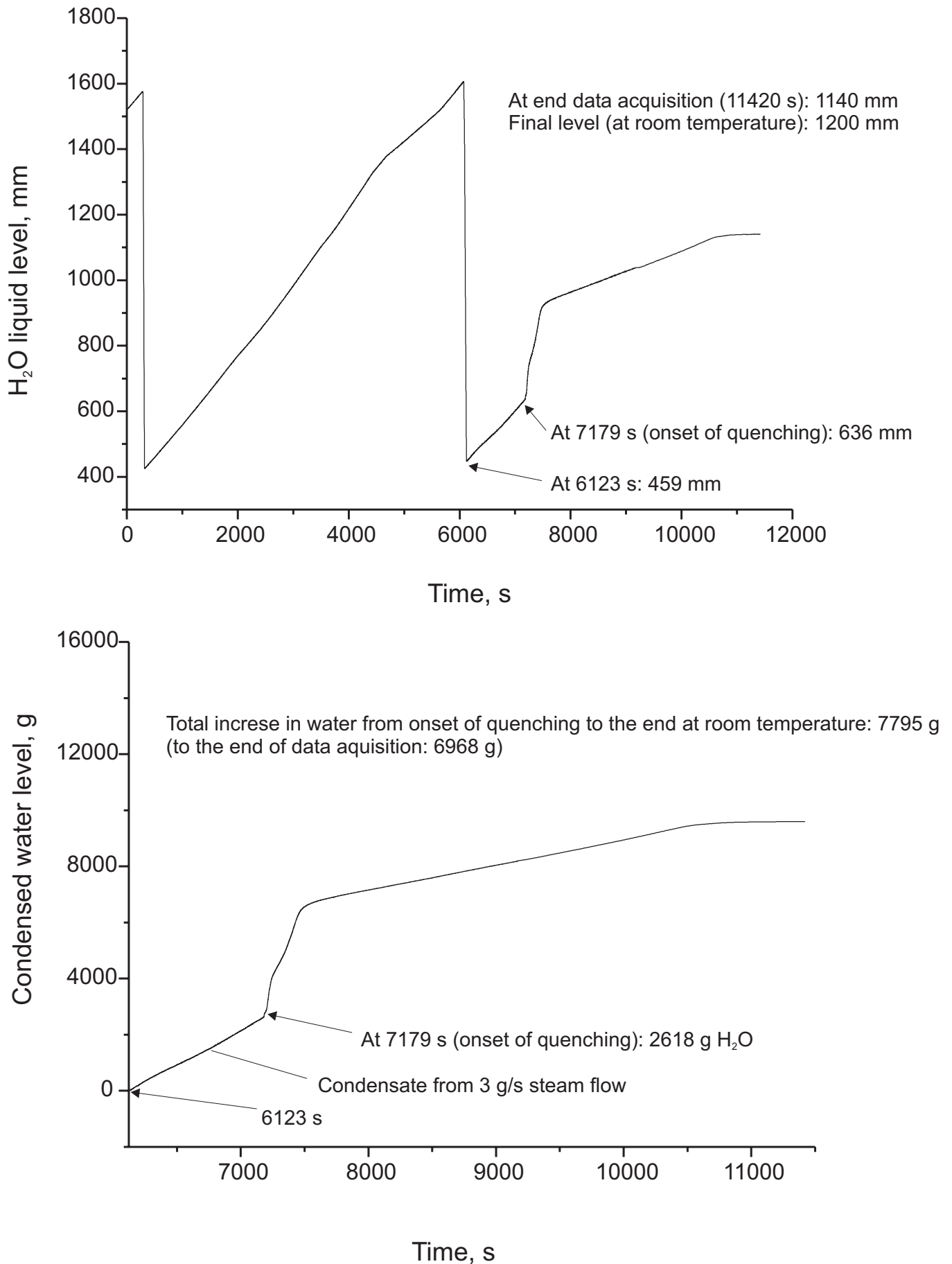
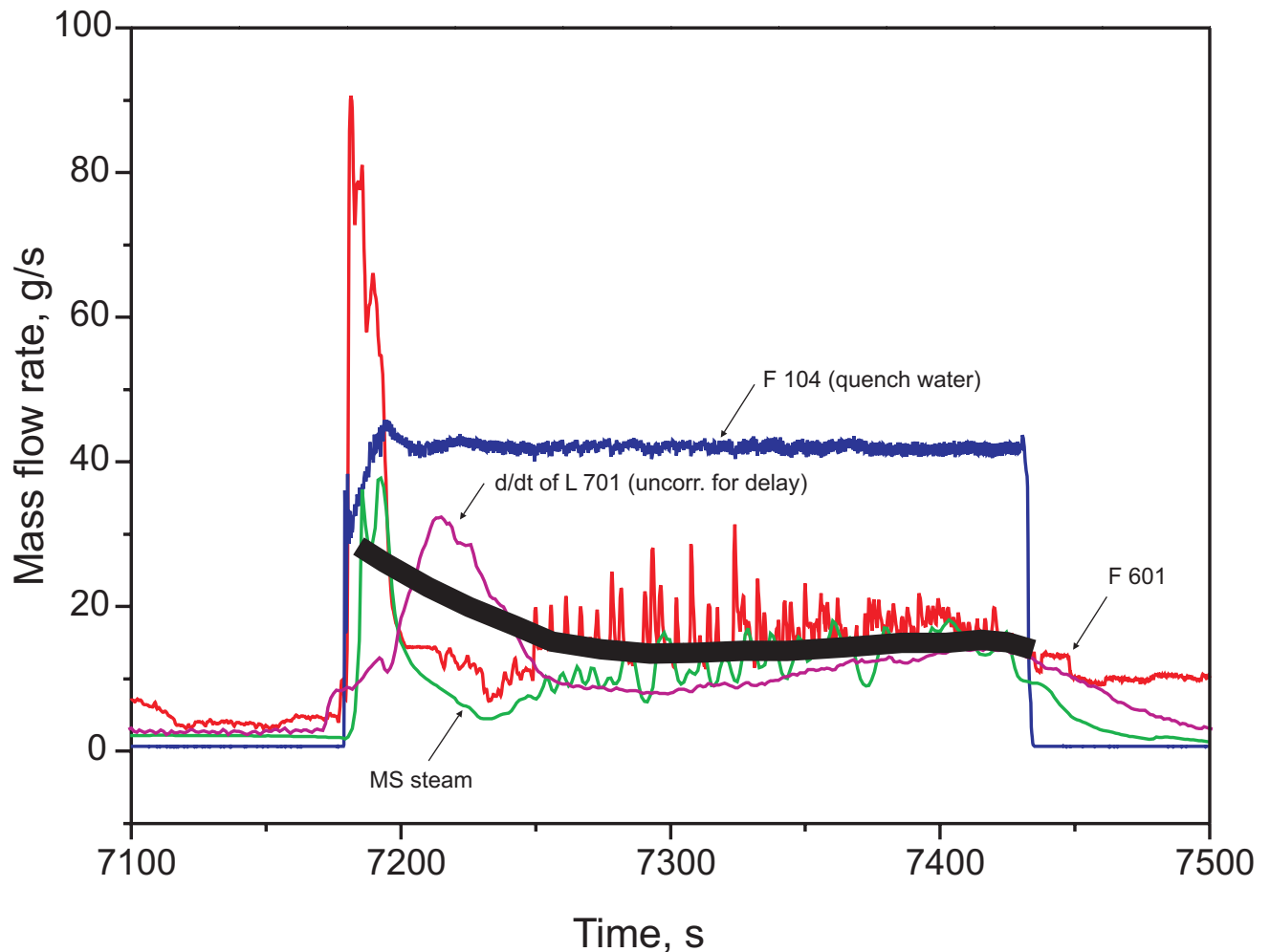


Fig. 38: QUENCH-06; Rise of water level in the condensate collector (L 701) in [mm], top, and in [g], bottom



Total steam measured during the quenching phase:
 F 601 = 4.7 kg, MS steam = 3.4 kg, L 701 = 3.5 kg.
 Total quench water injected: F 104 = 10.6 kg.

Fig. 39-QUE06 F601+L701+MS+K.cdr
 13.06.02 - IMF

Fig. 39: QUENCH-06; Steam flow measurements in the off-gas pipe (MS steam, F 601), in the condensate collector ($d(L 701)/dt$), and mean steam flow data (thick line) compared to quench water input (F 104)

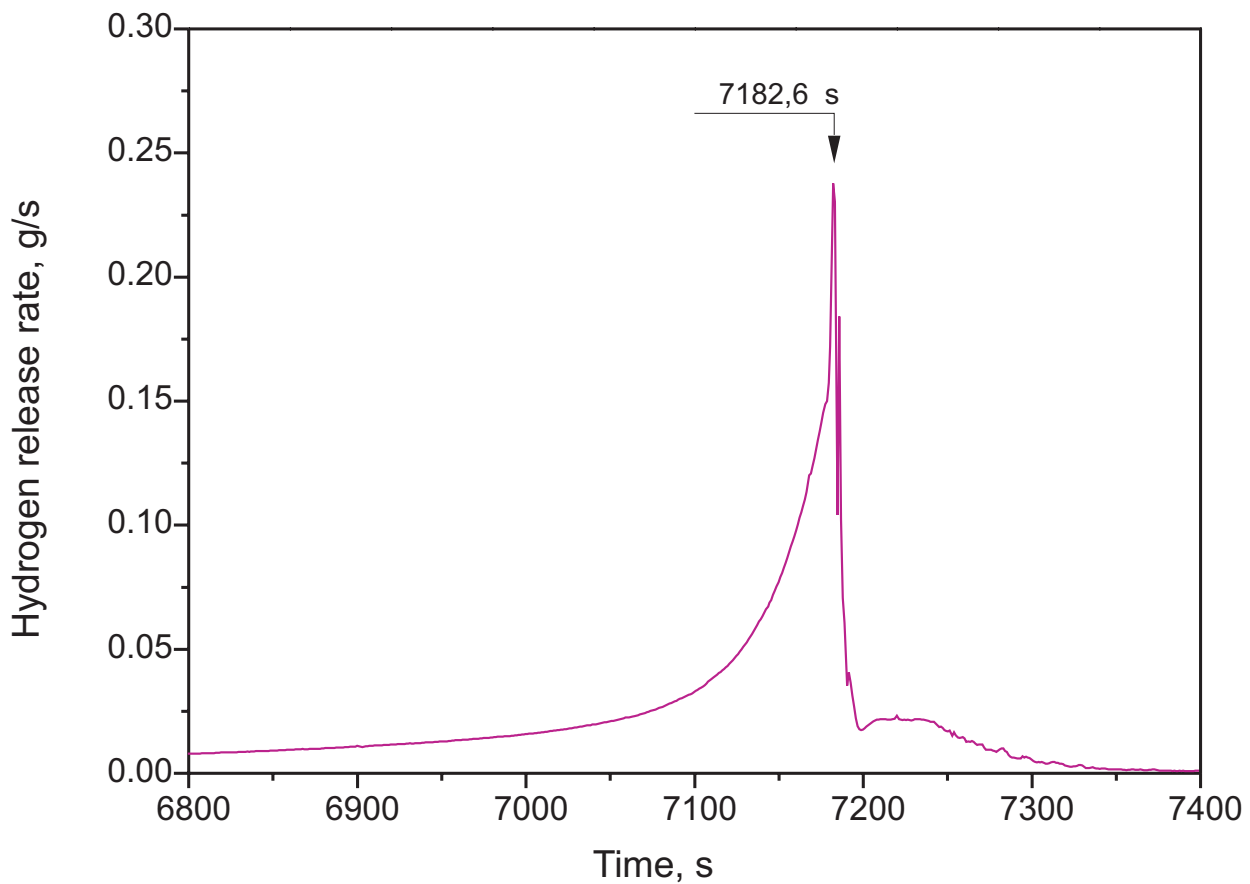
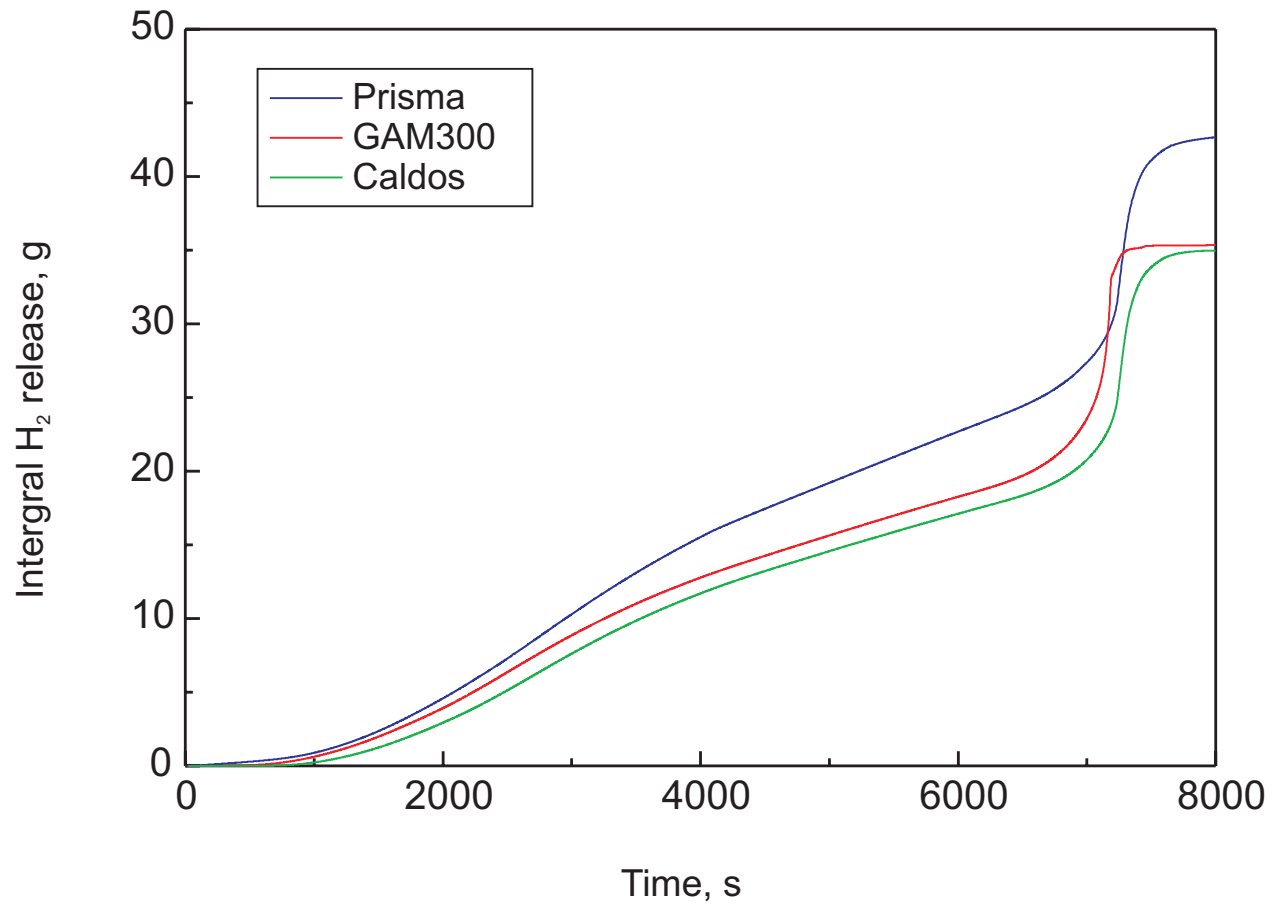


Fig.40-QUE06-H2.cdr
13.06.02 - IMF

Fig. 40: QUENCH-06; H₂ integral releases measured by the three analyzers, top, and H₂ release rate measured by the mass spectrometer, bottom

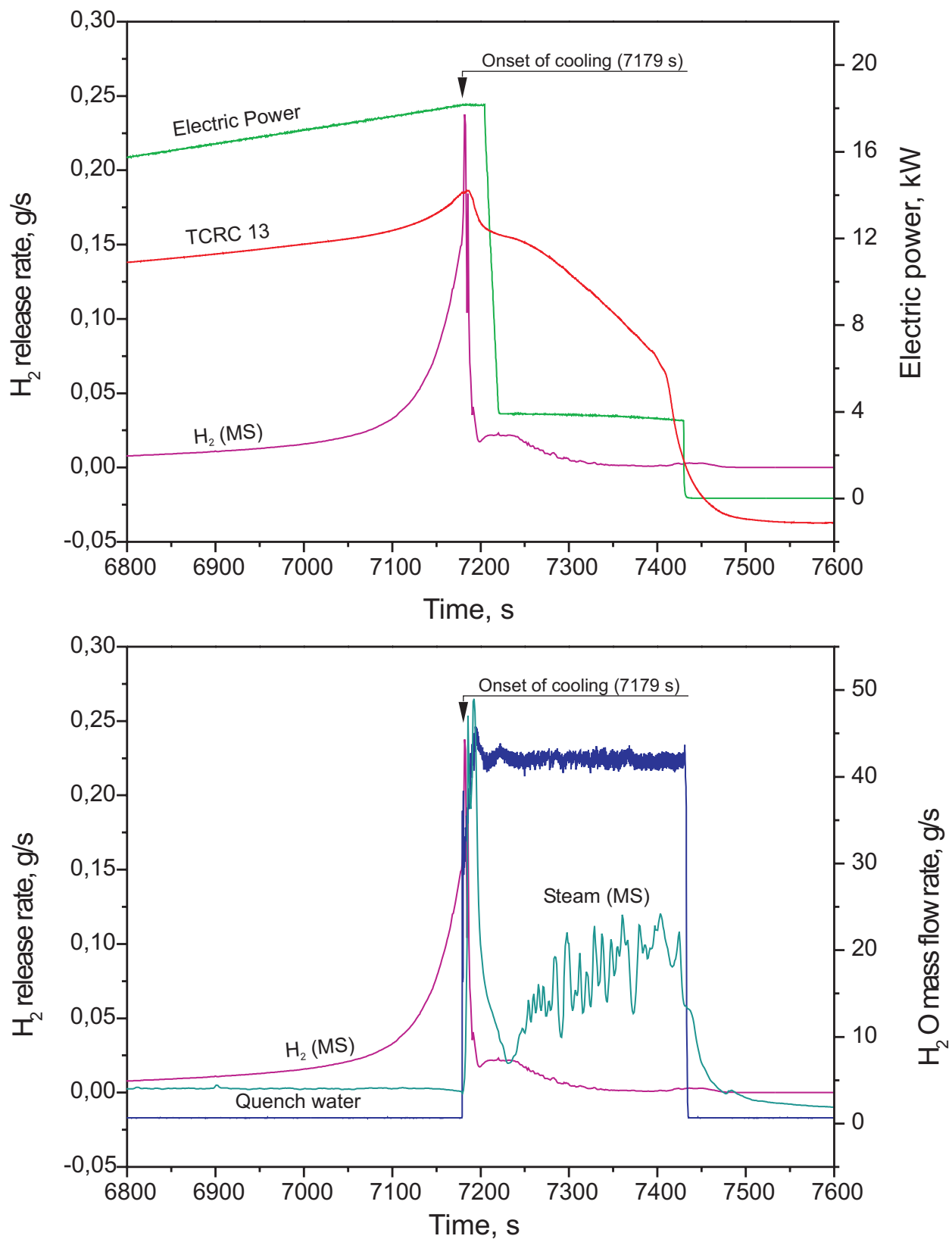


Fig 41-QUE06 Zeitbezug.cdr
10.06.02 - IMF

Fig. 41: QUENCH-06; Synopsis of power input, rod temperature, quench water injection, and hydrogen generation



Fig 42-QUE06 Posttest b.cdr
10.06.02 - IMF

Fig. 42: QUENCH-06; Posttest appearance of the shroud at the upper end of the heated zone, 0°



Fig 43-QUE06 Posttest c.cdr
11.06.02 - IMF

Fig. 43: QUENCH-06; Posttest appearance of the shroud at the upper end of the heated zone, 90°

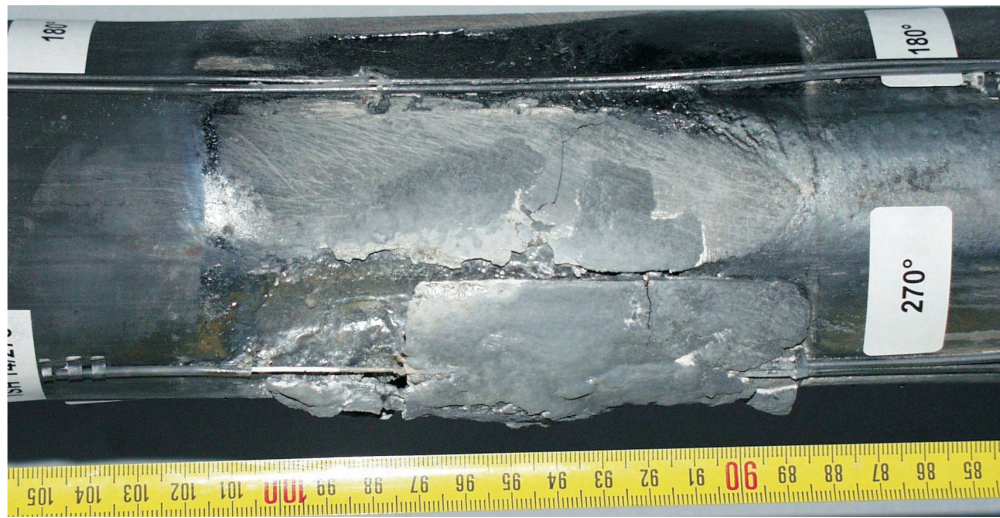


Fig 43-QUE06 Posttest c.cdr
13.06.02 - IMF

Fig. 44: Shroud failure regions at the upper end of the heated zone of test bundles QUENCH-04, QUENCH-05, and QUENCH-06 (from left)

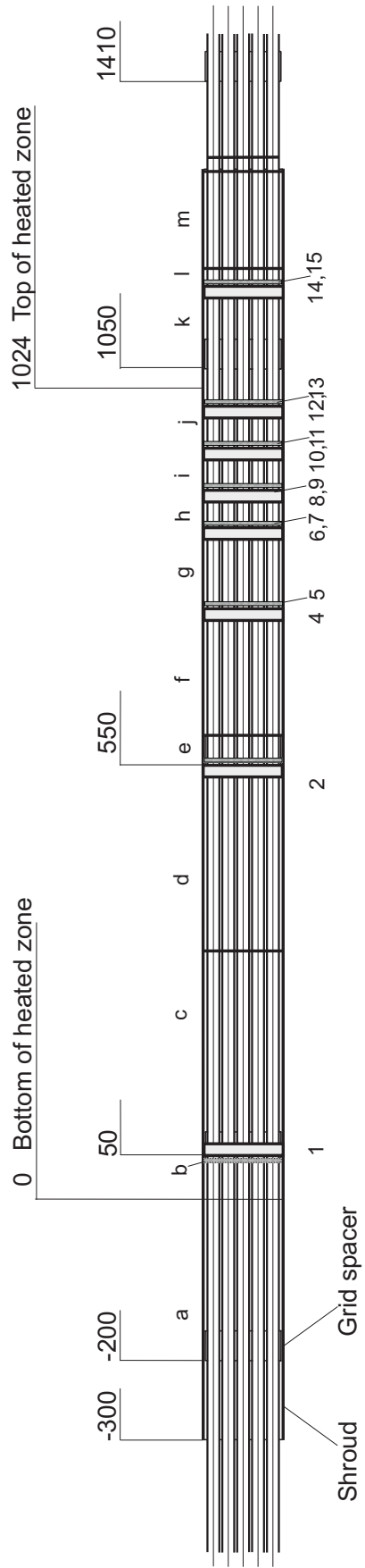


Fig. 45: QUENCH-06; Sectioning of test bundle

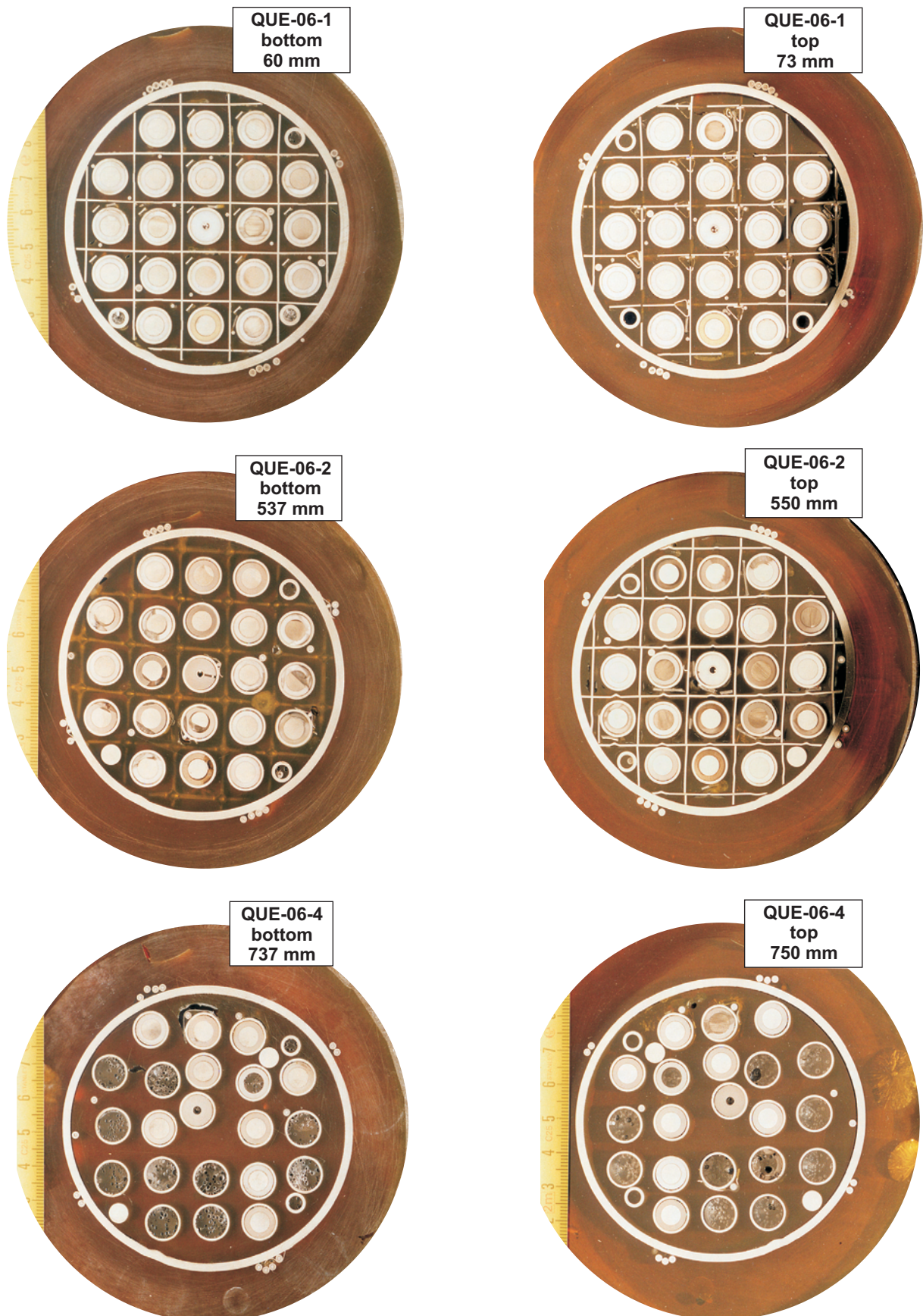


Fig 46-QUE06 cross sections1.cdr
11.06.02 - IMF

Fig. 46: QUENCH-06; Polished cross sections.

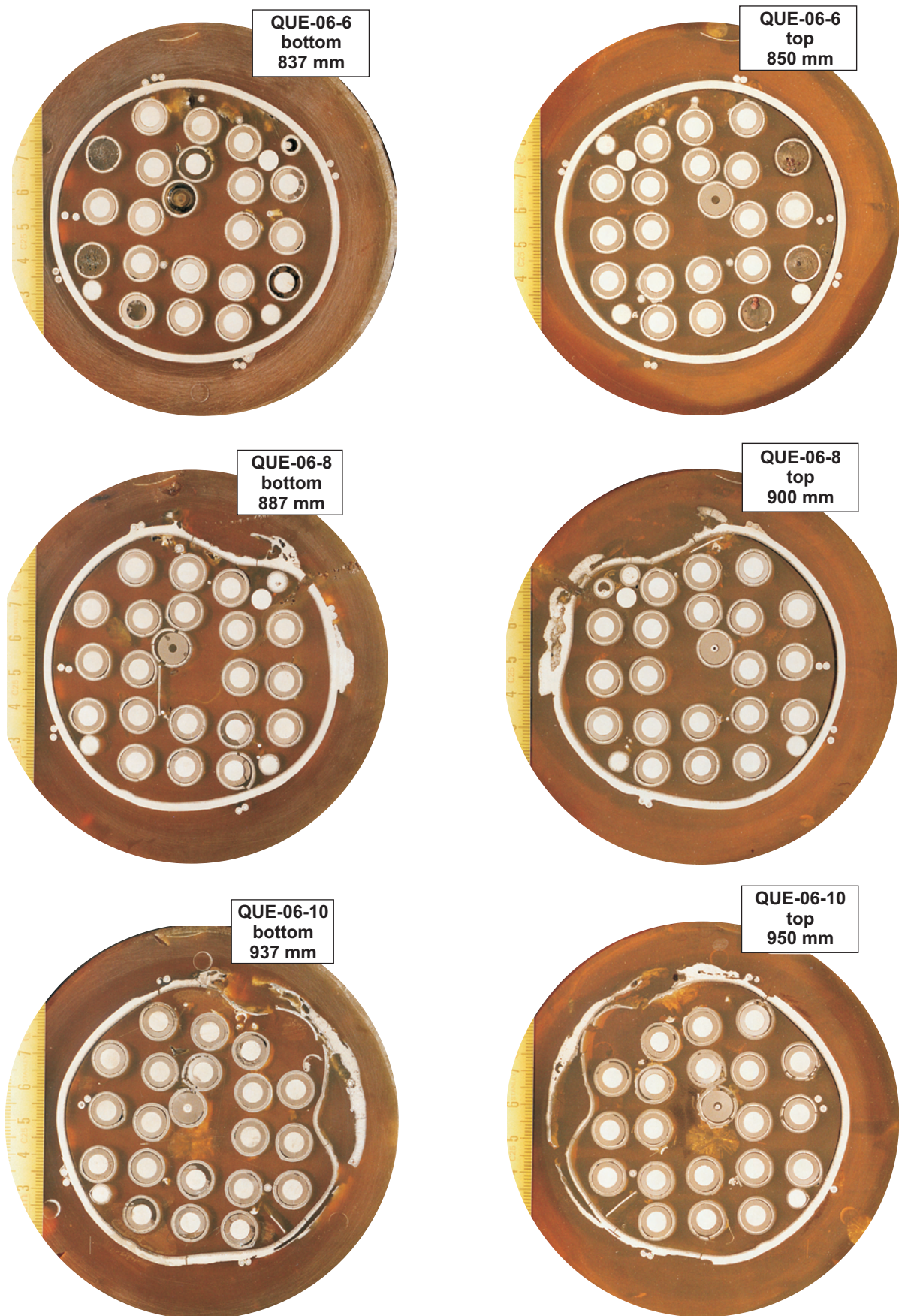


Fig 47-QUE06 cross sections2.cdr
10.06.02 - IMF

Fig. 47: QUENCH-06; Polished cross sections (continued).

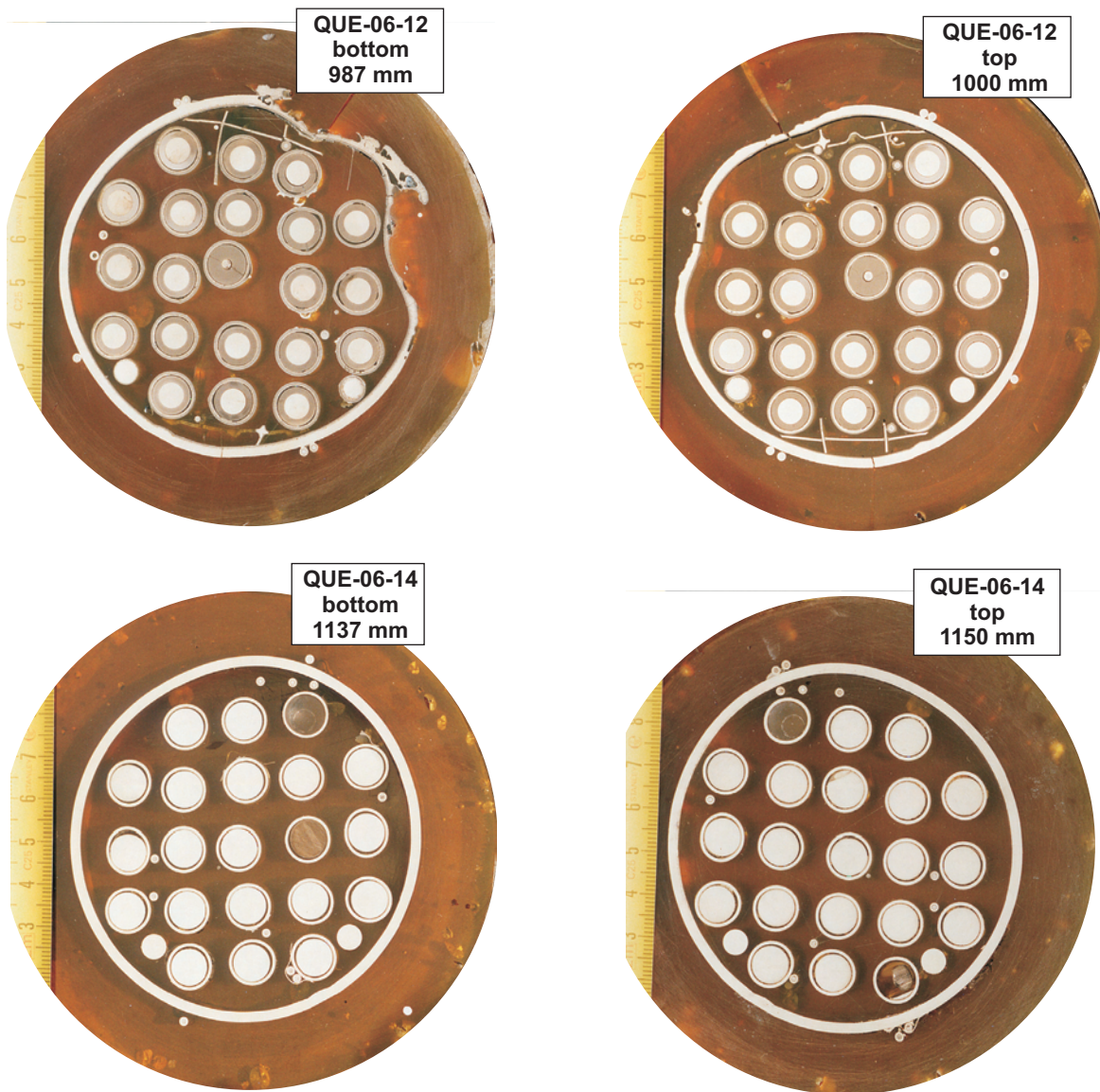


Fig 48-QUE06 cross sections3.cdr
10.06.02 - IMF

Fig. 48: QUENCH-06; Polished cross sections (continued).

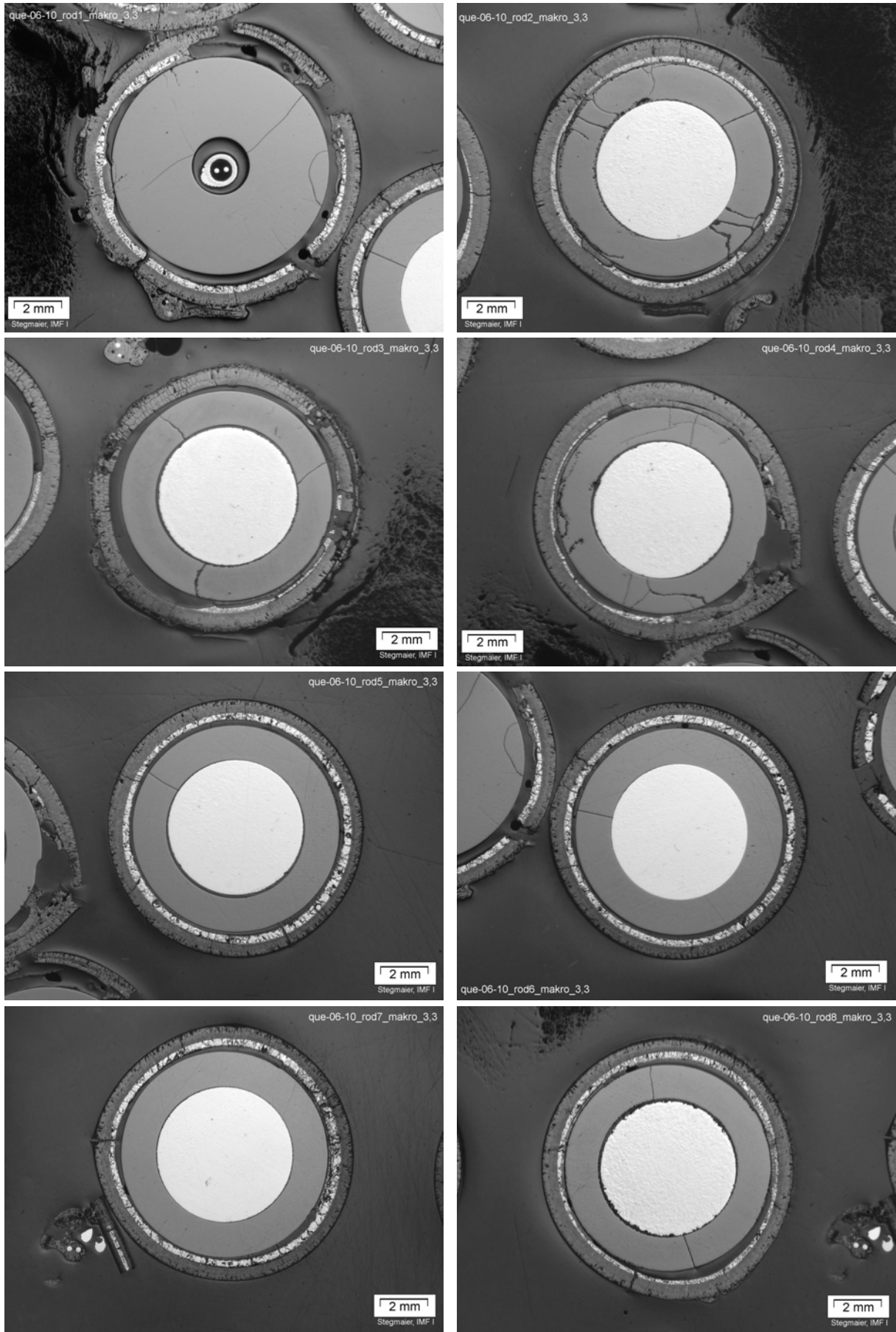


Fig 49-QUE06-overview1.doc
11.06.02 – IMF

Fig. 49: QUENCH-06; Cross section QUE-06-10 at 950 mm depicting separately test rods 1 – 8

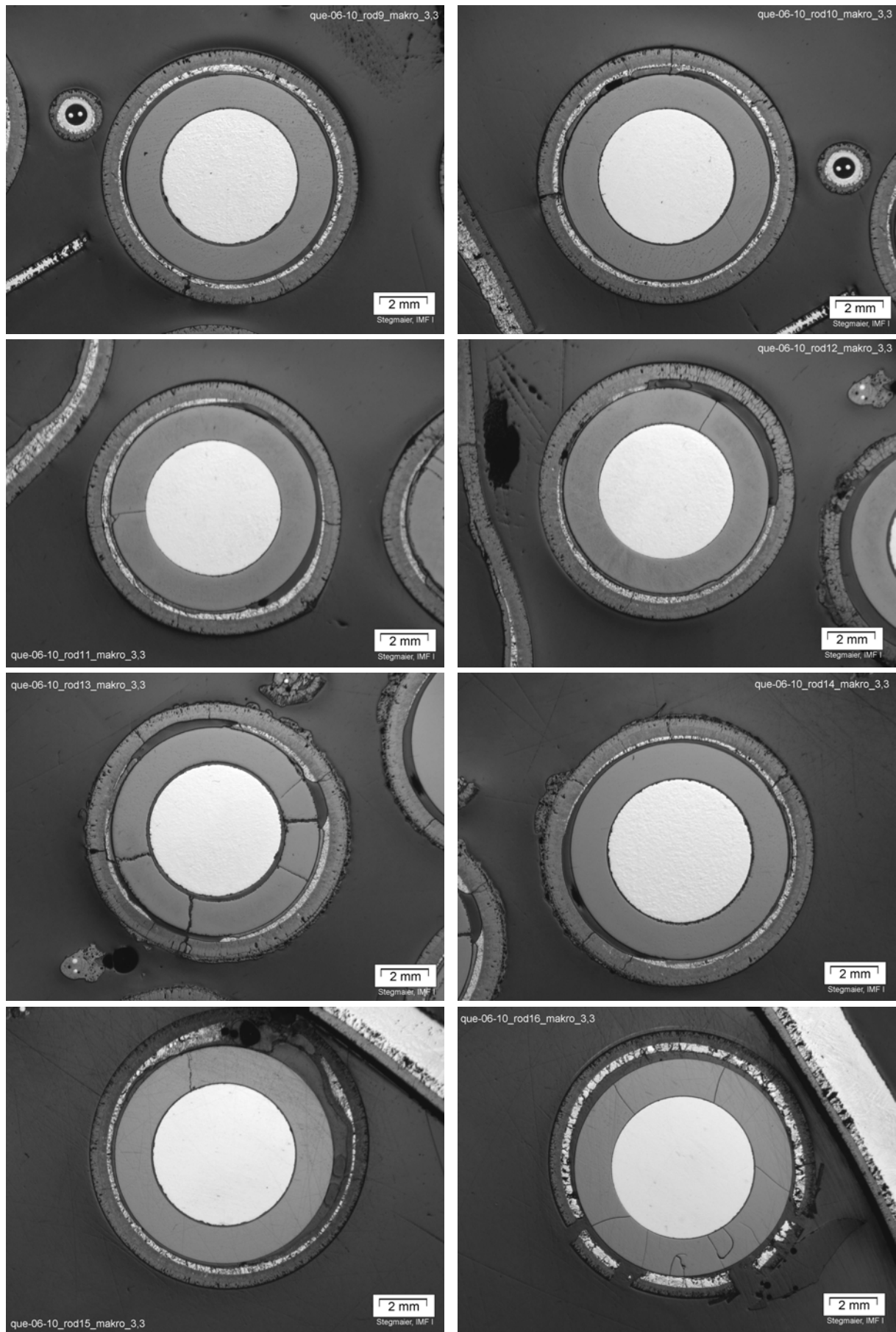


Fig 50-QUE06 overview2.doc
11.06.02 – IMF

Fig. 50: QUENCH-06; Cross section QUE-06-10 at 950 mm depicting separately test rods 9 – 16

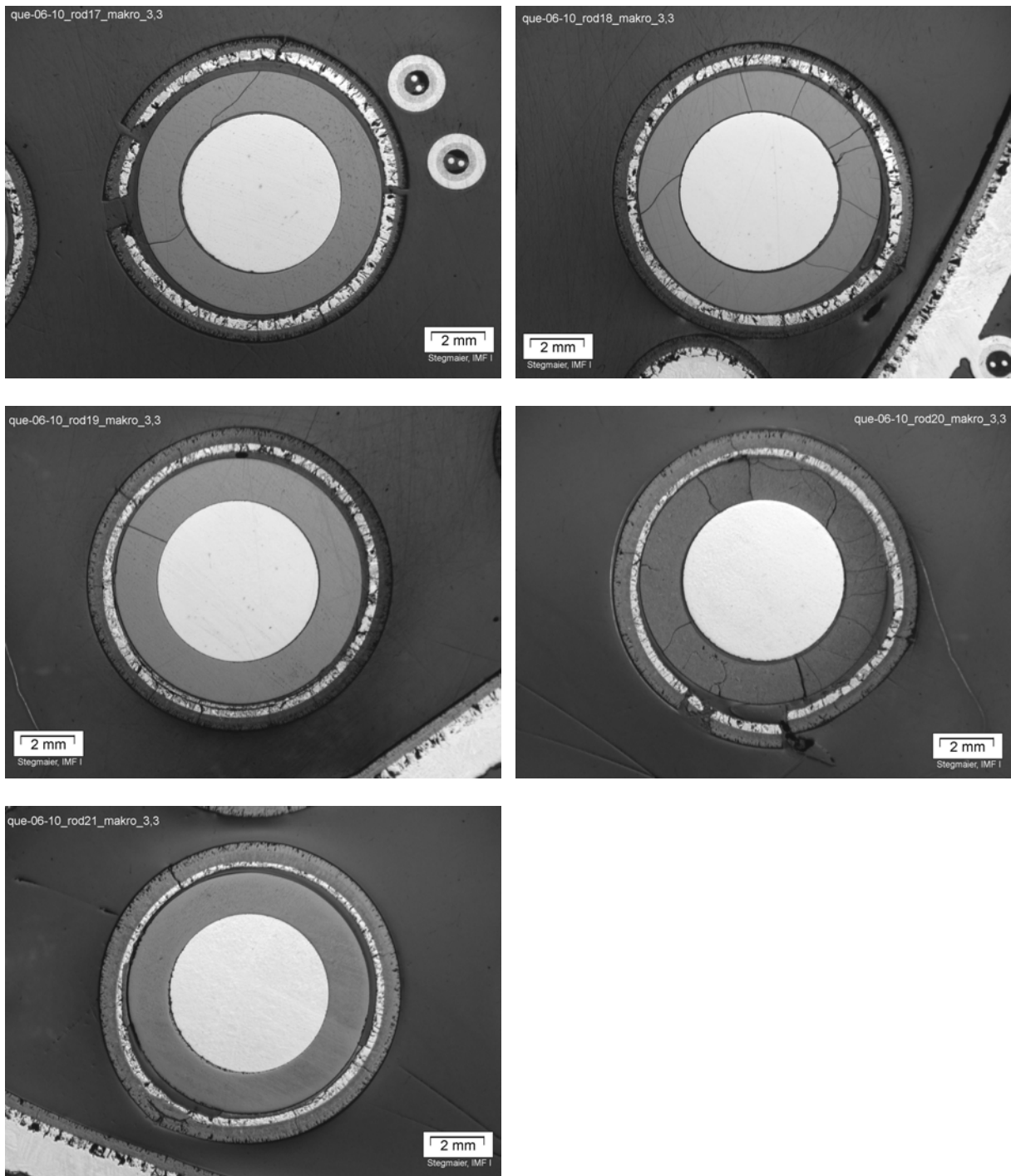


Fig 51-QUE06 overview3.doc
11.06.02.02 – IMF

Fig. 51: QUENCH-06; Cross section QUE-06-10 at 950 mm depicting separately test rods 17 – 21

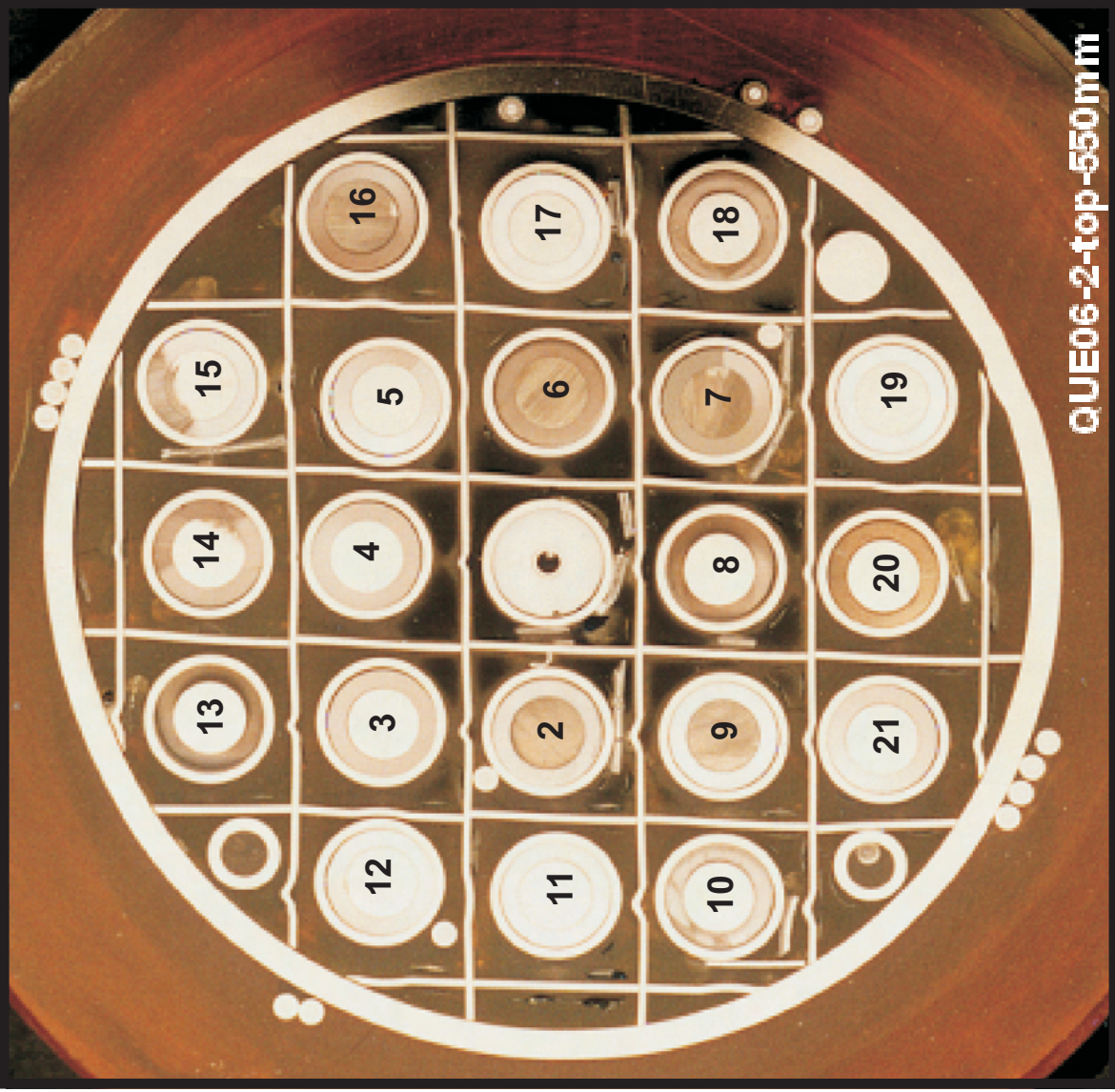
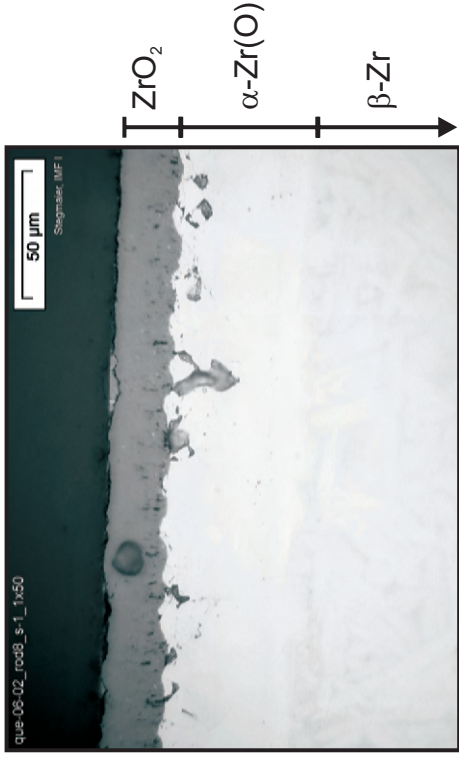
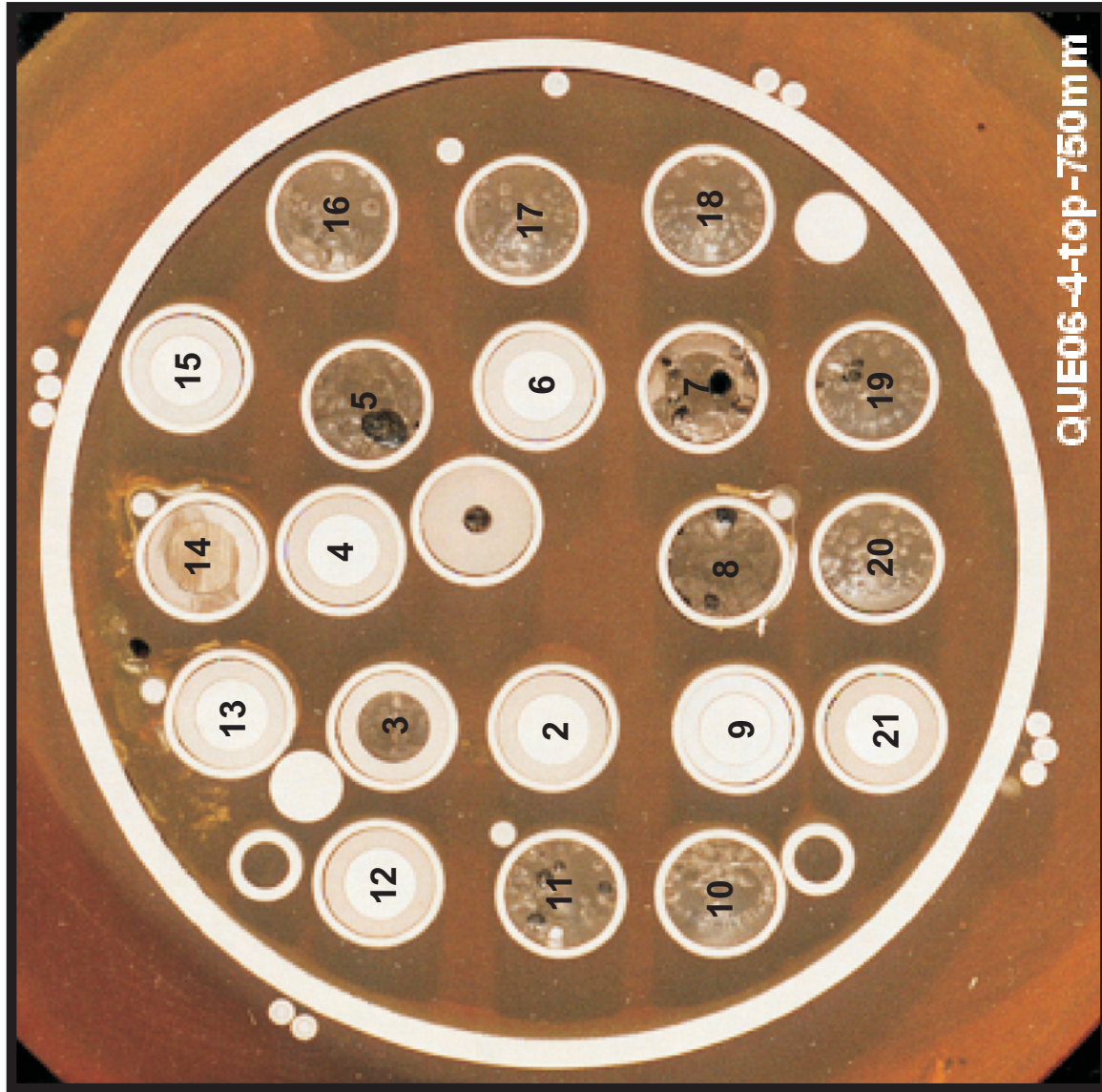


Fig. 52: Cross section at 550 mm bundle elevation (QUE-06-2); overview, oxidation state of rod No. 8



Micrograph of rod No. 8, showing state of cladding oxidation: Scale, with scalloped growth front, relatively thick α -Zr(O) layer, and β -Zr matrix. Those features are typical for moderate-temperature / long-term pre-transition morphology.

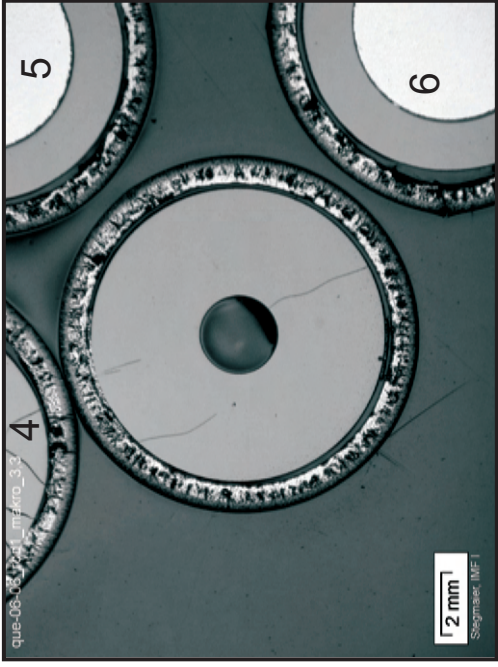


Rod No. 8, together with attached thermocouple



Micrograph, showing state of cladding oxidation

Fig. 53: Cross section at 750 mm bundle elevation (QUE-06-4); overview, rod No. 8 and its oxidation state



Central rod and close neighbours (rods No. 4, 5, 6)

Rod No. 21, shroud, corner rod D,

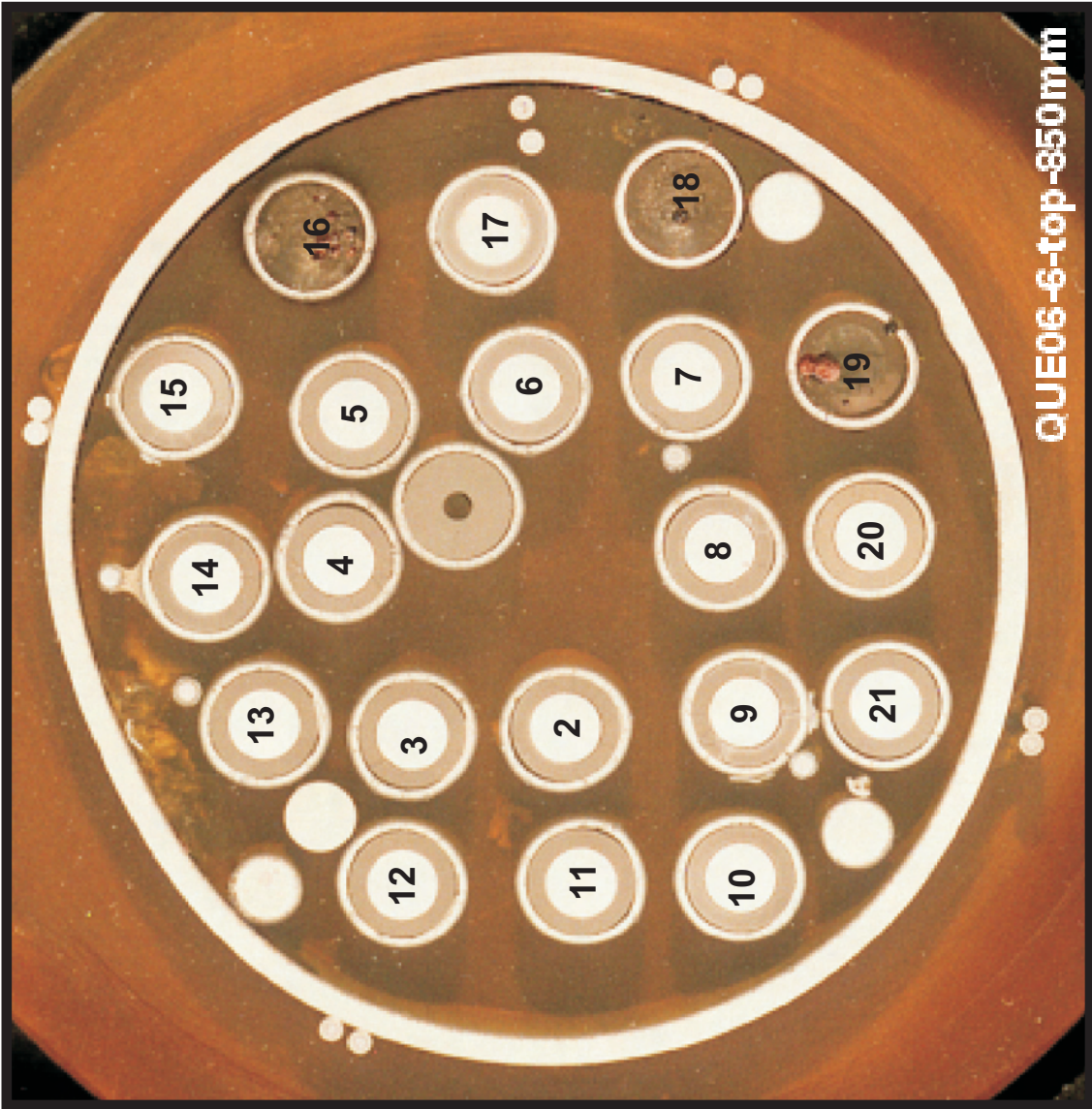
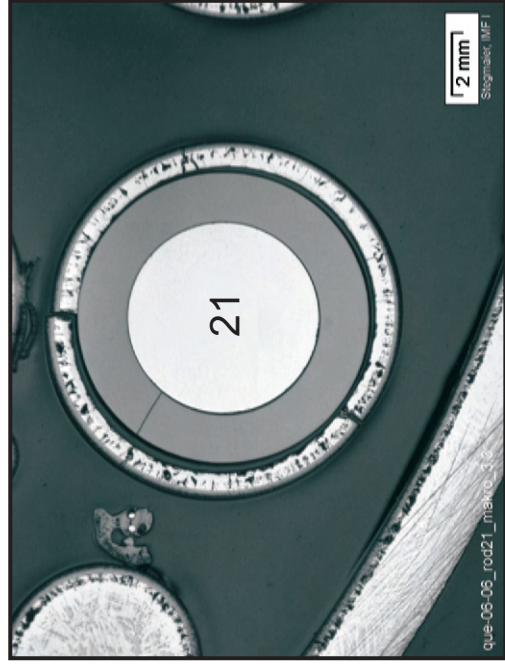
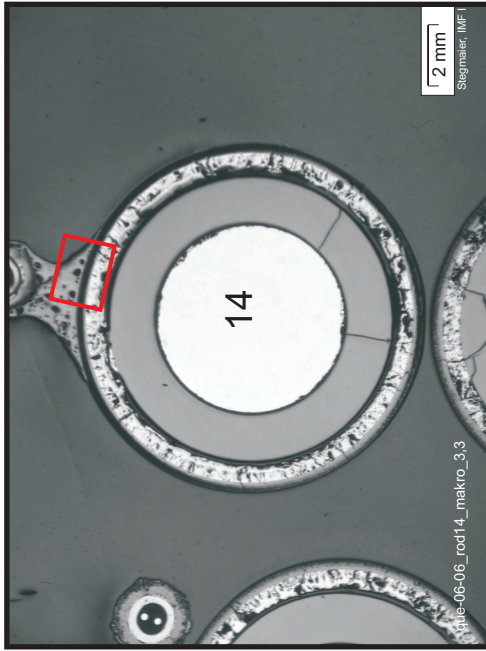
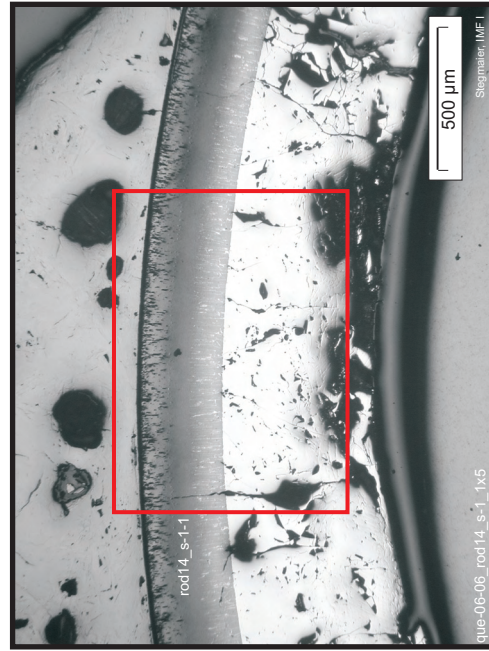


Fig. 54: Cross section at 850 mm bundle elevation (QUE-06-6); overview, central rod and rod No. 21



top and bottom: Overviews



Melt top layer on duplex scale (tetragonal/cubic) of partially molten cladding



Fig. 55: Cross section at 850 mm bundle elevation (QUE-06-6); rod No. 14, showing a melt bridge from thermocouple to cladding, wetting of the duplex scale, and the partially molten cladding matrix

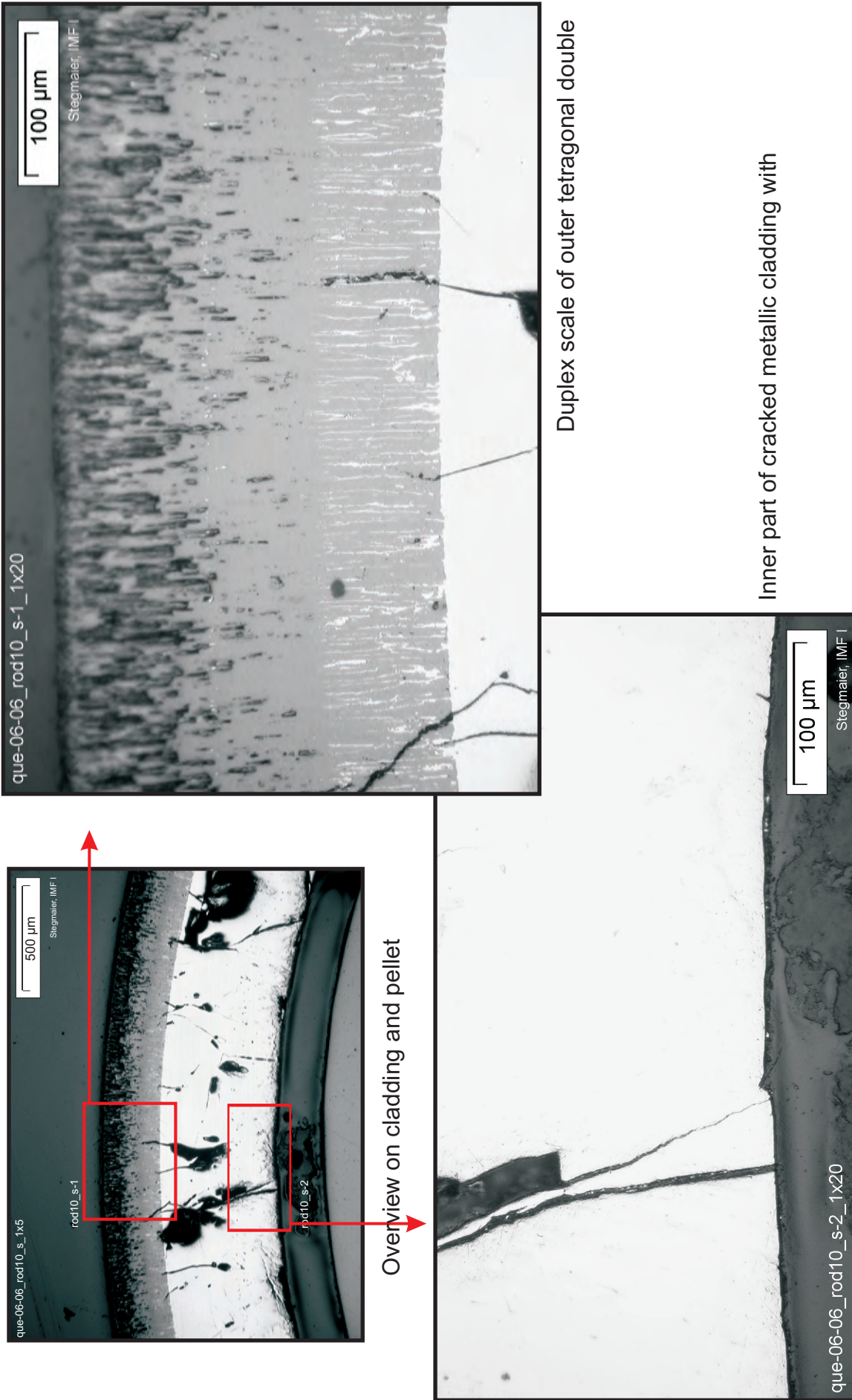


Fig. 56: Cross section at 850 mm bundle elevation (QUE-06-6); rod No. 10, showing duplex external scale, non-molten metallic part of cladding without pellet interaction.

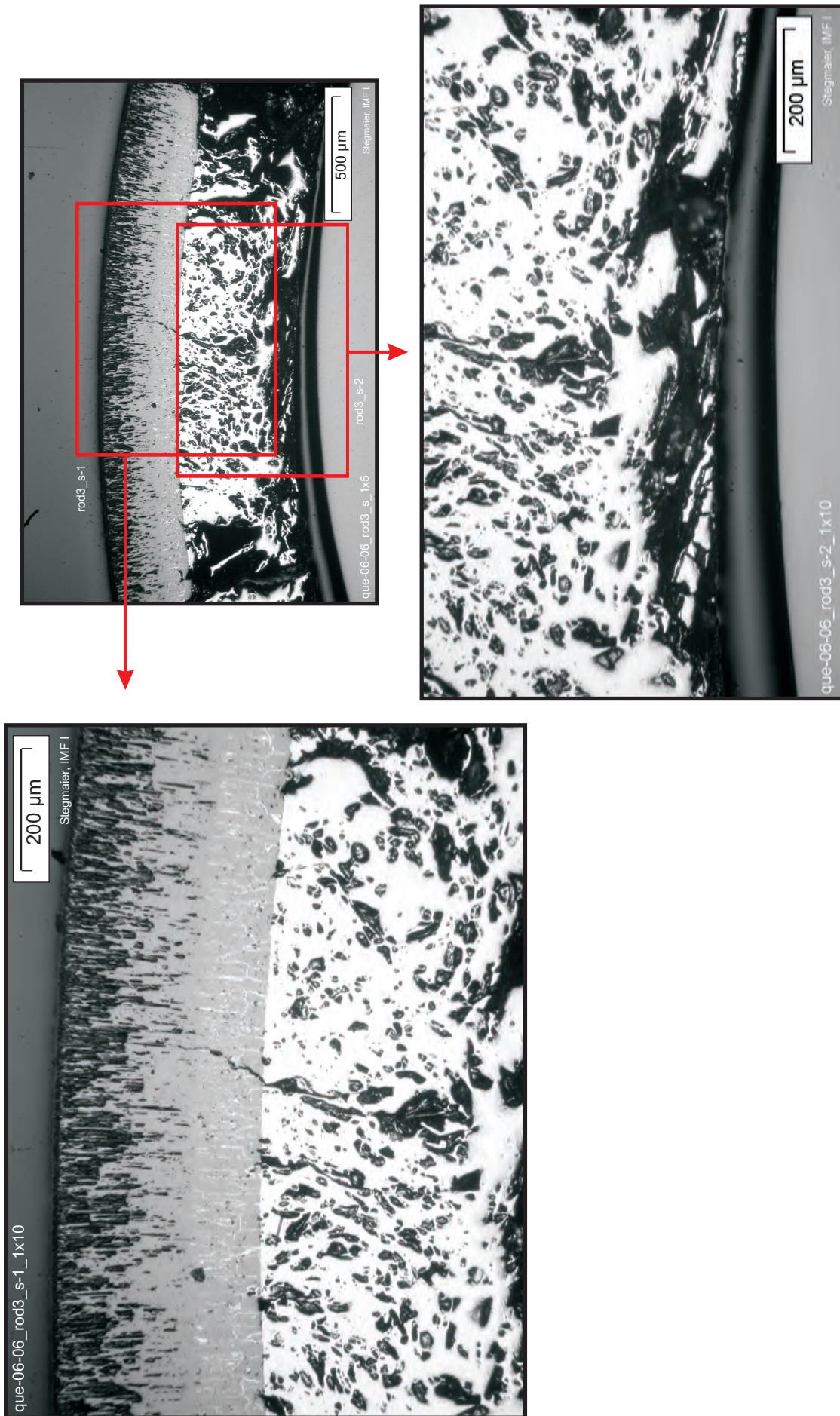


Fig. 57: Cross section at 850 mm bundle elevation (QUE-06-6); rod No. 3, showing duplex external scale, molten metallic part of the cladding, but no pellet interaction

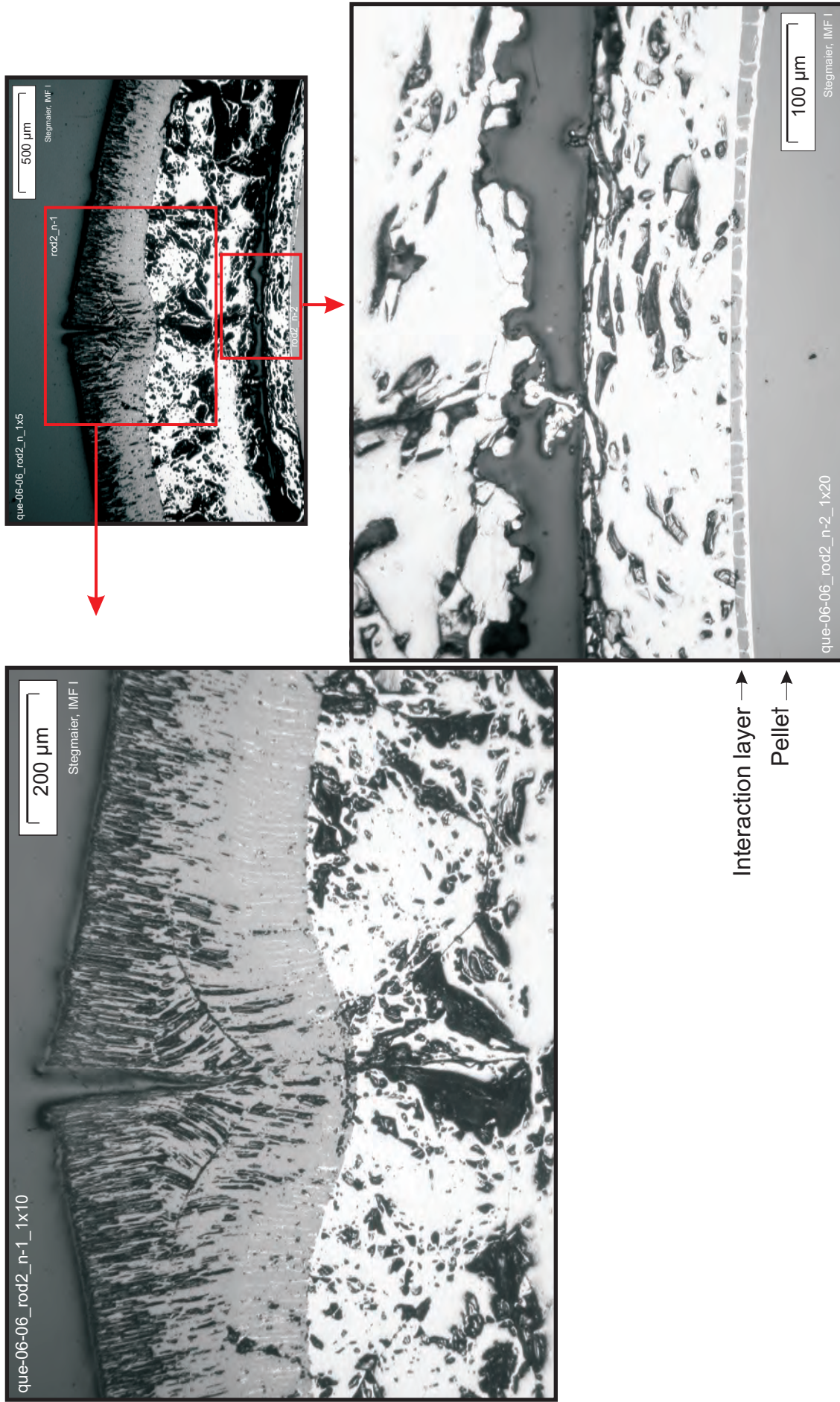
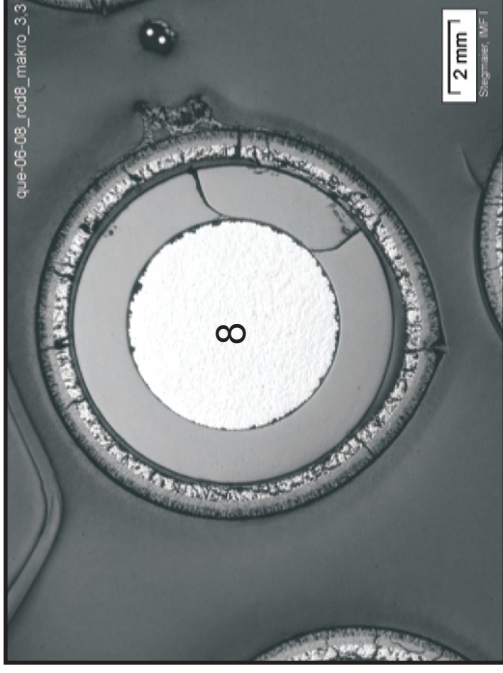
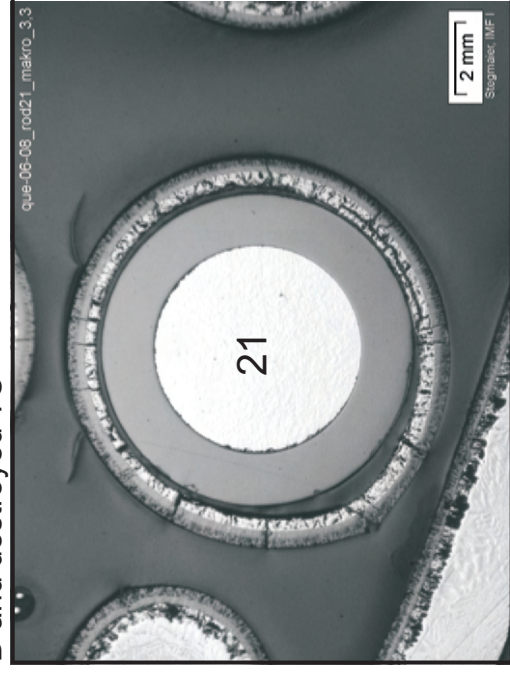


Fig. 58: Cross section at 850 mm bundle elevation (QUE-06-6); rod No. 2, showing wedge shaped crack in duplex scale, molten metallic cladding part and pellet interaction layer



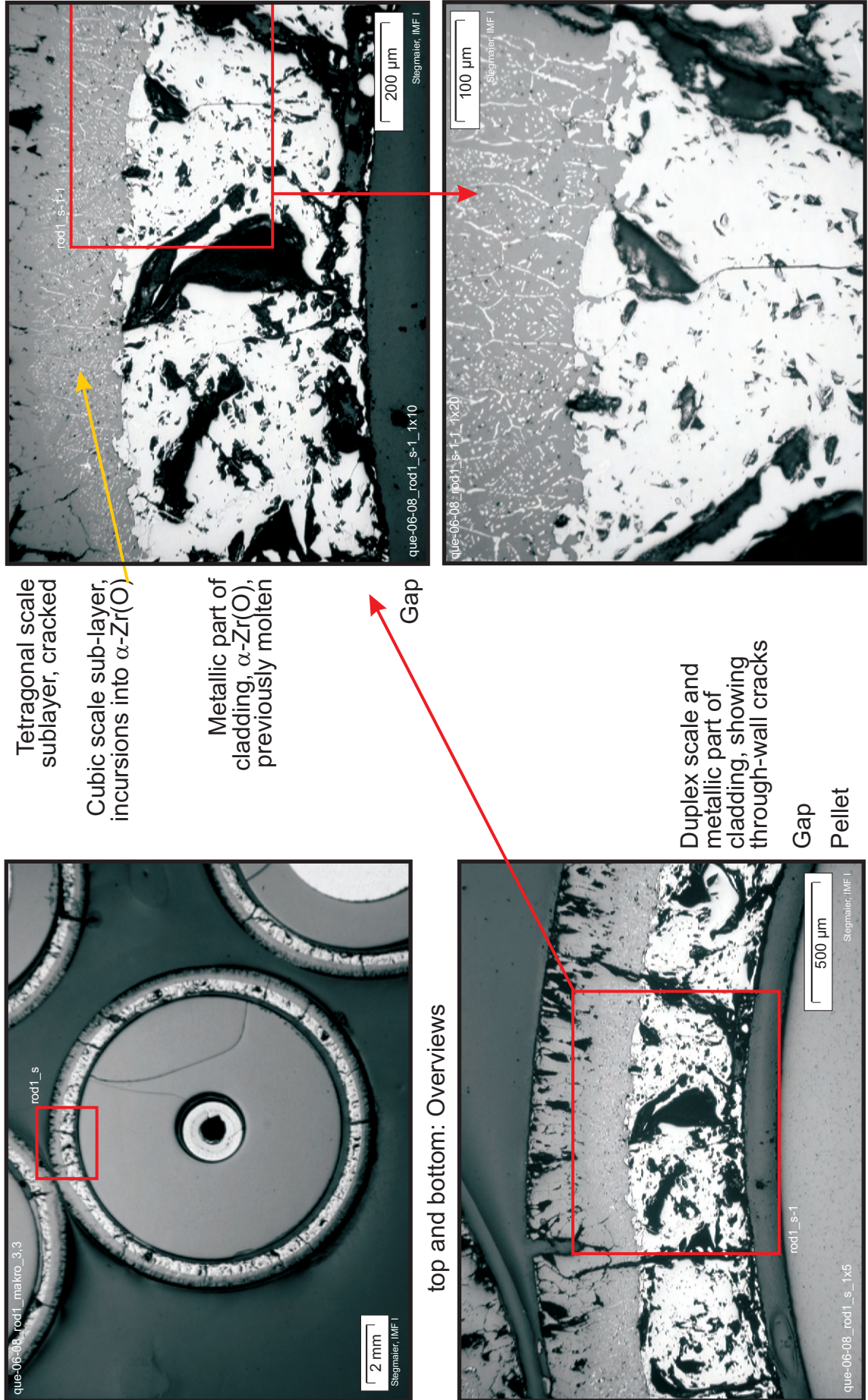
Rod No. 8, remnants of TC and related melt (see other elevations)



Rod No. 21 together with shroud, corner rod D and destroyed TC



Fig. 59: Cross section at 900 mm bundle elevation (QUE-06-8); overview, state of rods No. 8 and 21



Tetragonal scale sublayer, cracked
Cubic scale sub-layer, incursions into α -Zr(O)

Metallic part of cladding, α -Zr(O), previously molten

Gap

Duplex scale and metallic part of cladding, showing through-wall cracks

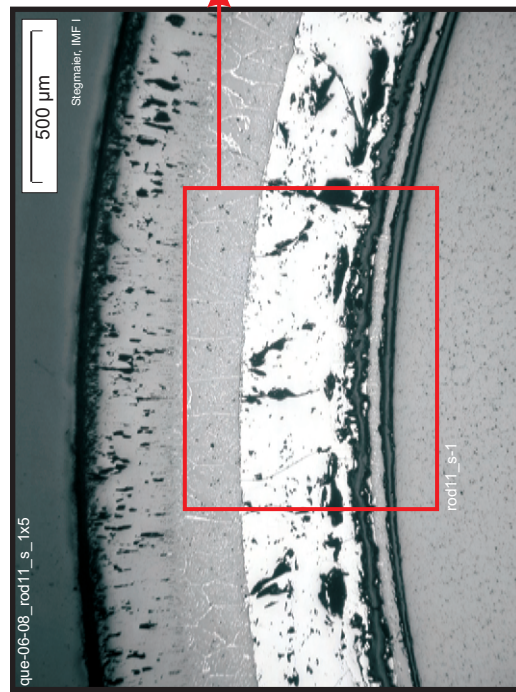
Gap
Pellet

top and bottom: Overviews

Fig. 60: Cross section at 900 mm bundle elevation (QUE-06-8); central rod, showing defects in duplex scale and previously molten metallic part of cladding



top and bottom: Overviews



Inner part of duplex scale and metallic part of cladding, showing no through-wall cracking defects. Pellet/cladding interaction layer is found separated by gaps, formed during quenching.

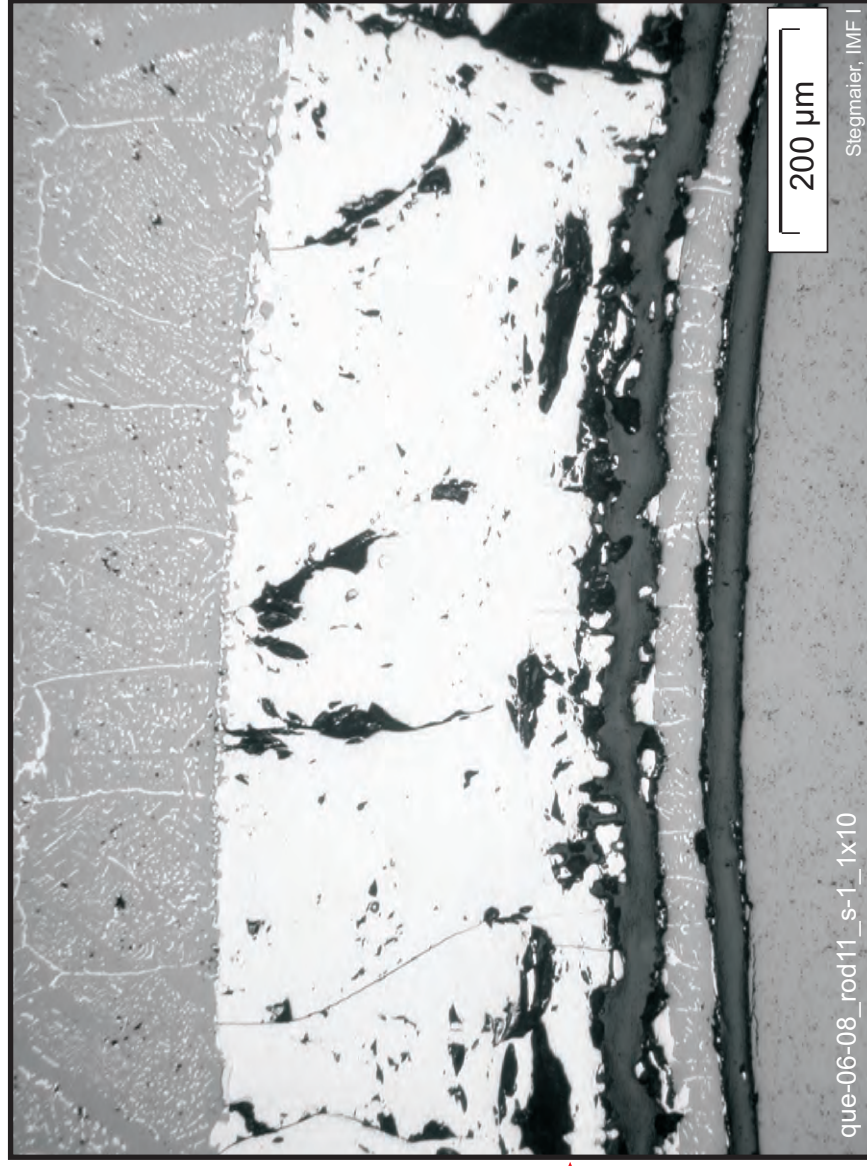


Fig. 61: Cross section at 900 mm bundle elevation (QUE-06-8); rod No. 11, showing duplex external scale and α -Zr(O) cladding with pellet interaction.

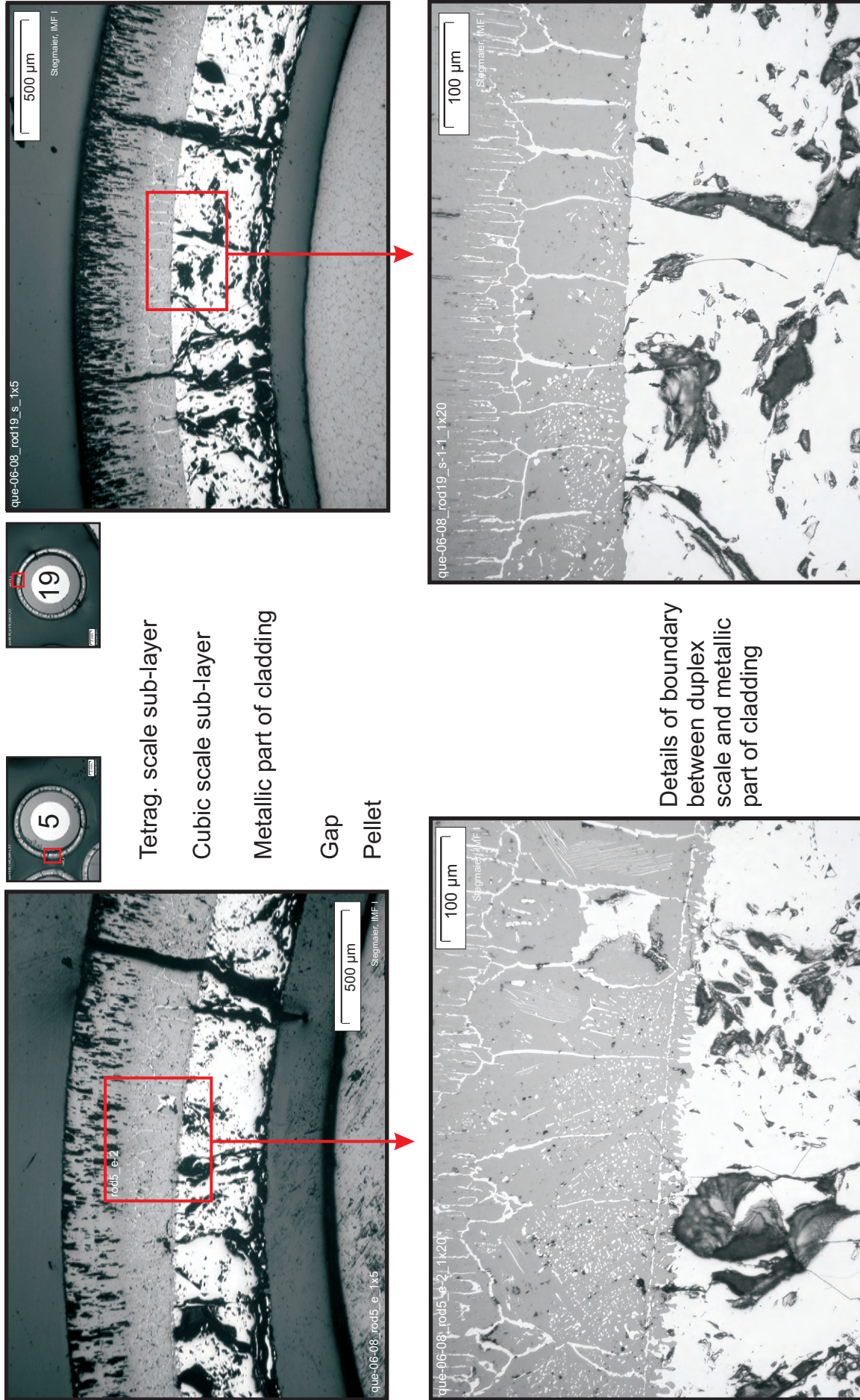
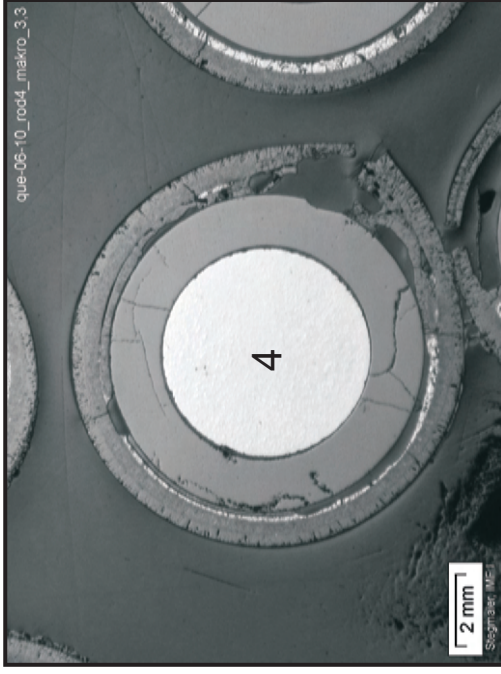


Fig. 62: Cross section at 900 mm bundle elevation (QUE-06-8); rods No. 5 and 19, showing through-wall cracking of duplex scale and metallic part of cladding



Rod No. 4, showing clad failure, and indicating loss of released melt

Central rod, showing partial coverage by melt top layer and late fragmentation

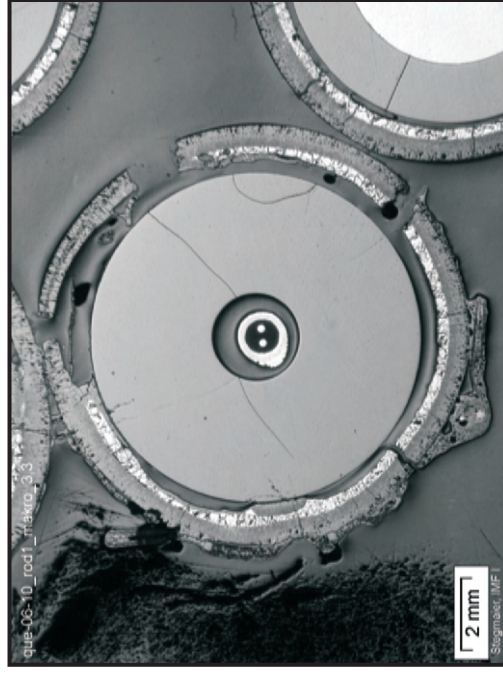
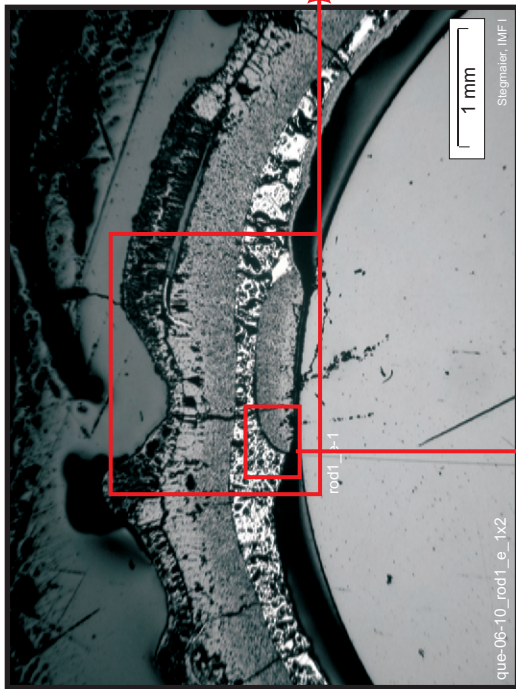


Fig. 63: Cross section at 950 mm bundle elevation (QUE-06-10); overview, rod No. 4 and central rod, both in direct contact

Cladding, consisting of duplex scale, metallic part and local pellet interaction zone, covered by a mostly oxidised melt top layer. See thin oxide on free inner surface at bottom right corner, indicating some steam ingress



top: Overview of cladding and pellet
bottom: Details of pellet interaction zone

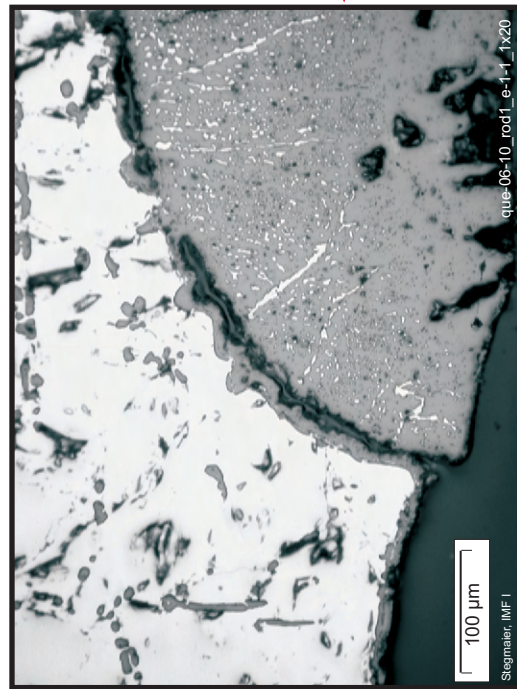
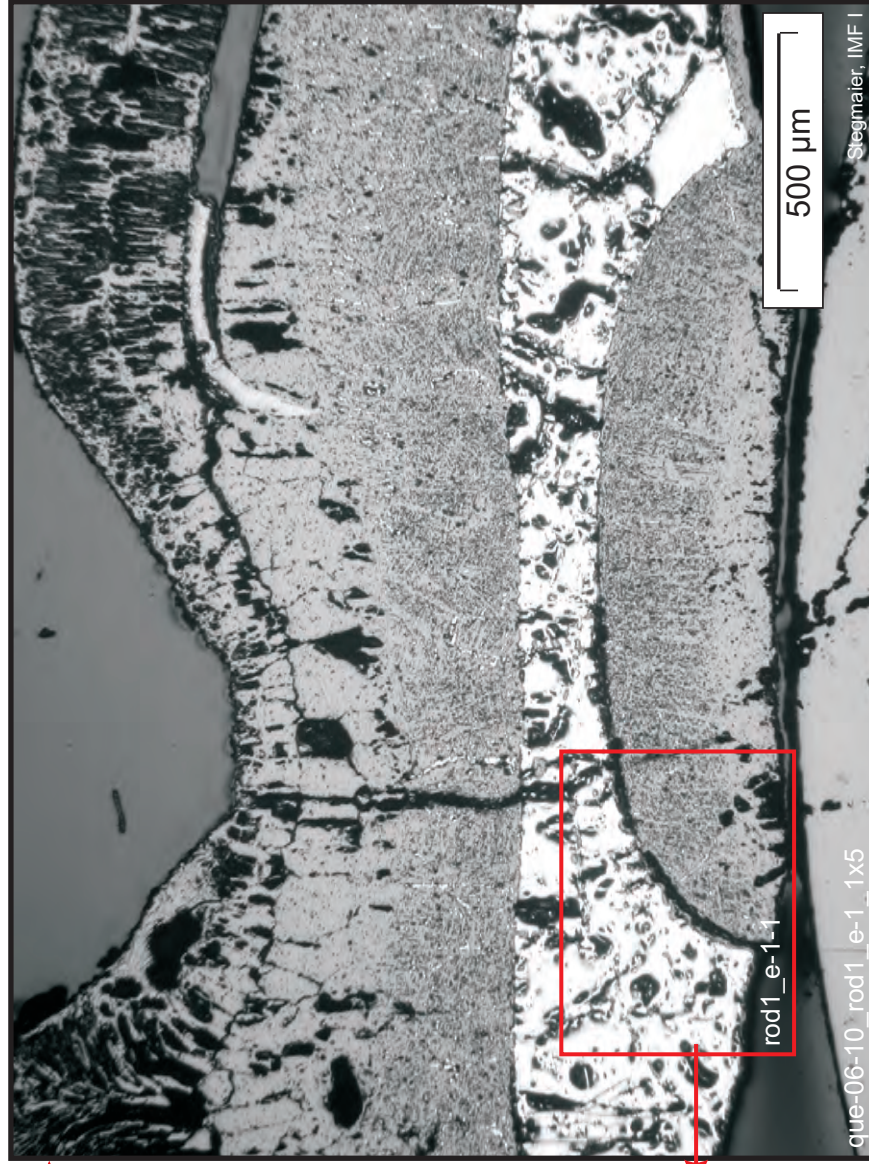


Fig. 64: Cross section at 950 mm bundle elevation (QUE-06-10); central rod, showing oxidised melt top layer, duplex external scale and α -Zr(O) cladding with local pellet interaction.

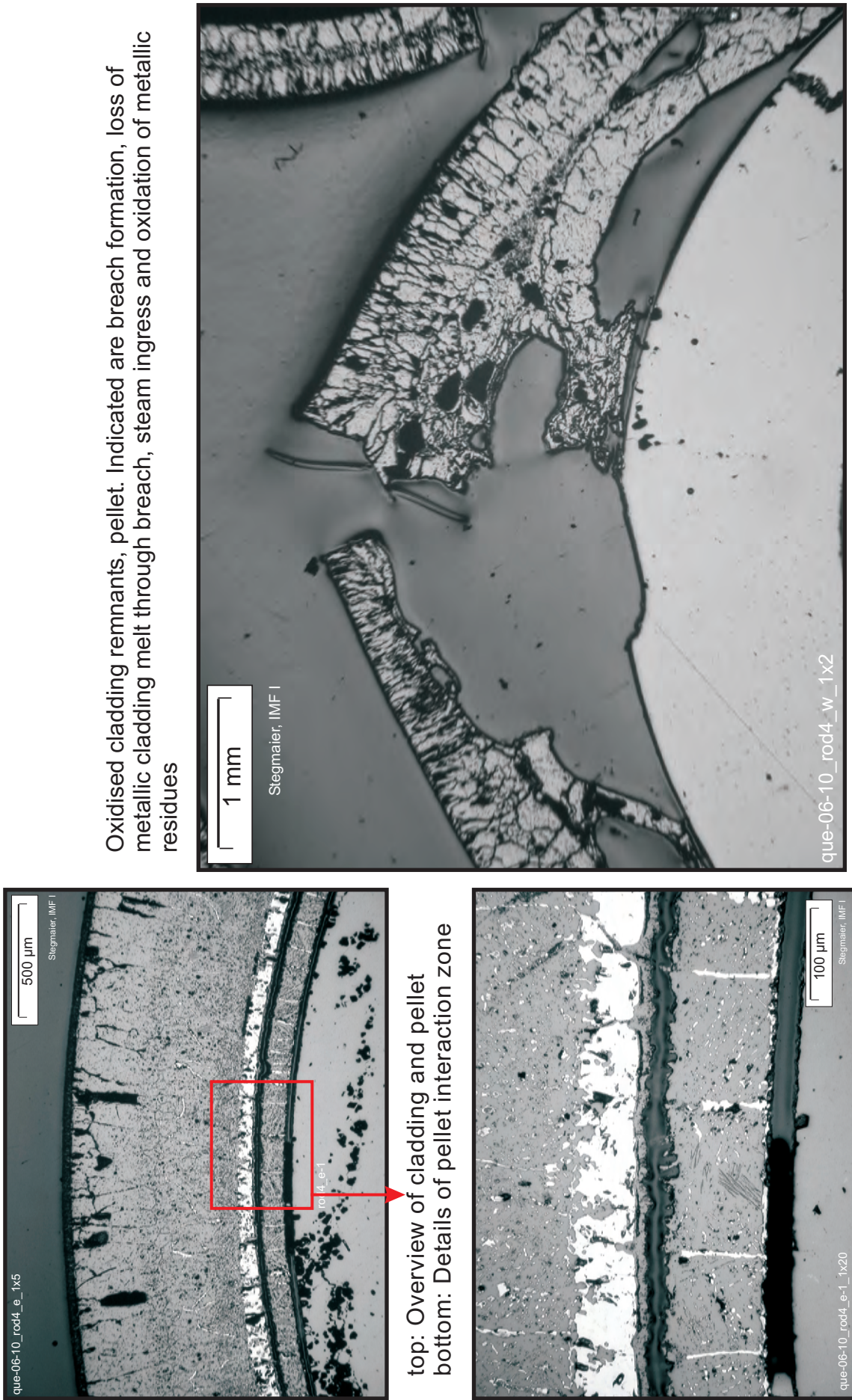
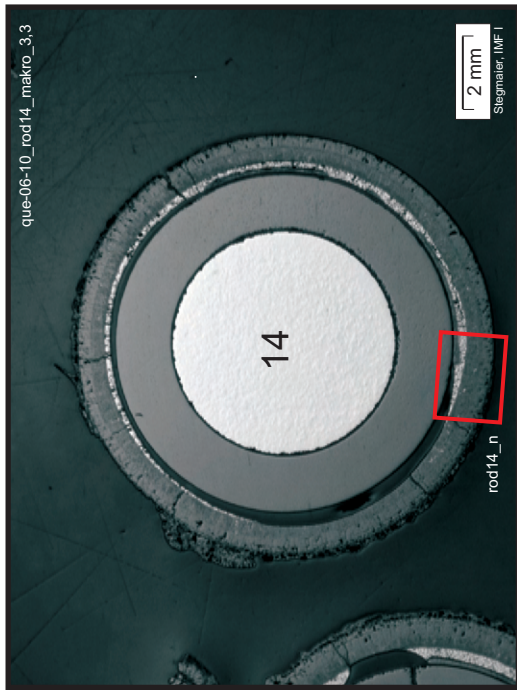
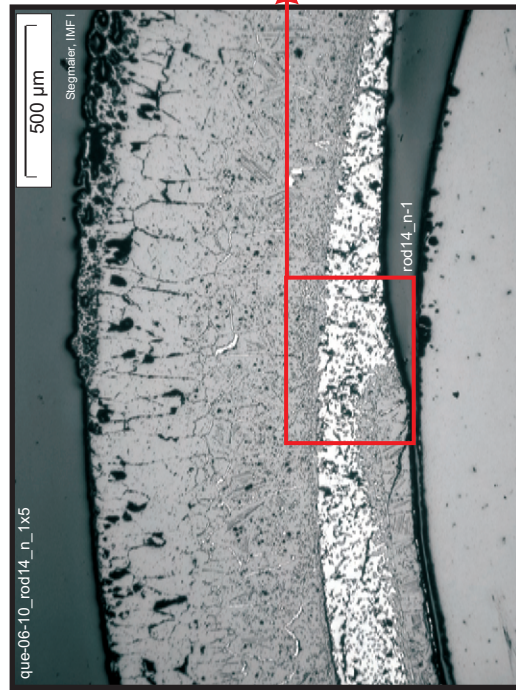


Fig. 65: Cross section at 950 mm bundle elevation (QUE-06-10); oxidation state of rod No. 4 on two opposite sides: advanced α -Zr(O) consumption (left), total oxidation (right).



top: Overview of rod No. 14
 bottom: Melt top layer, pellet interaction zone



Remaining metallic cladding remnants, in contact to external scale (up), pellet interaction layer (down, left) and void from melt relocation (down, right).
 Precipitation of zirconia from α -Zr(O) has taken place.

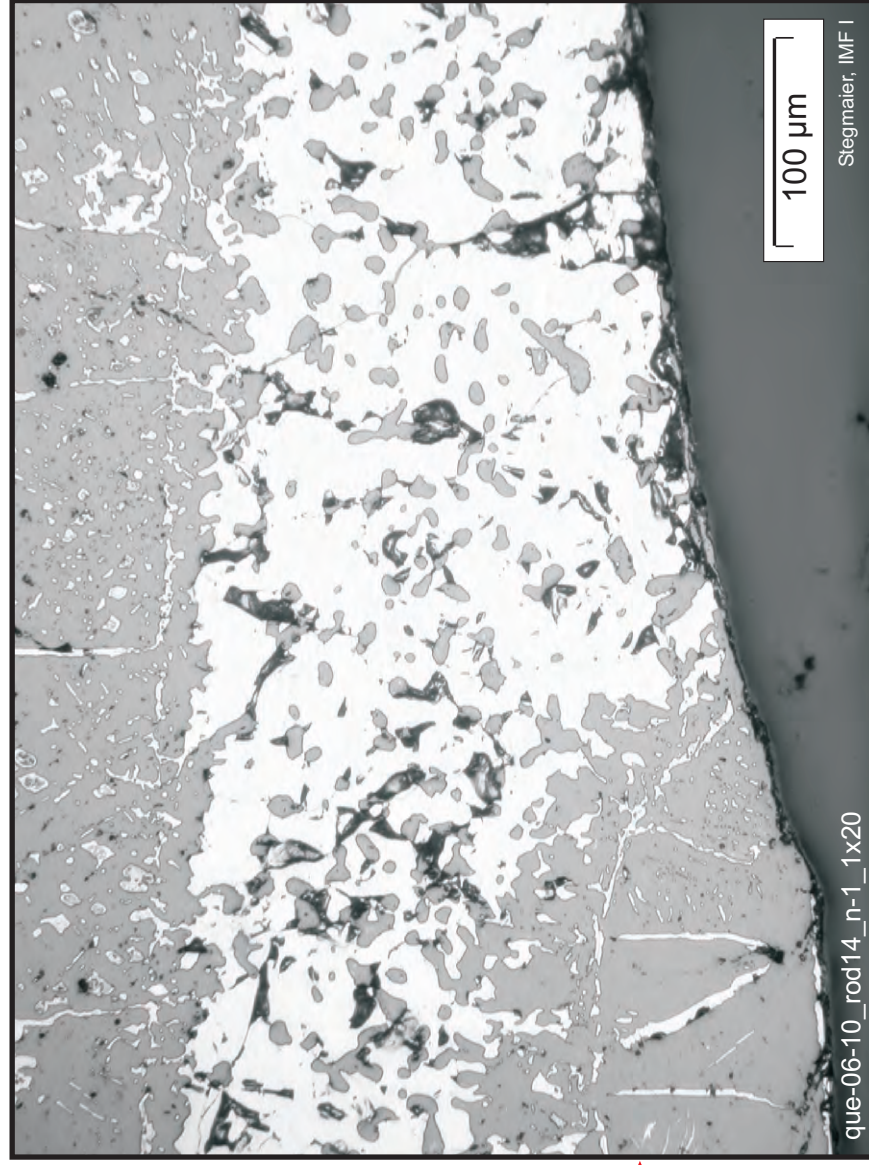


Fig. 66: Cross section at 950 mm bundle elevation (QUE-06-10); oxidation state of rod No. 14, showing local distribution of melt top layer, oxidative cladding consumption and void formation by internal cladding melt relocation.

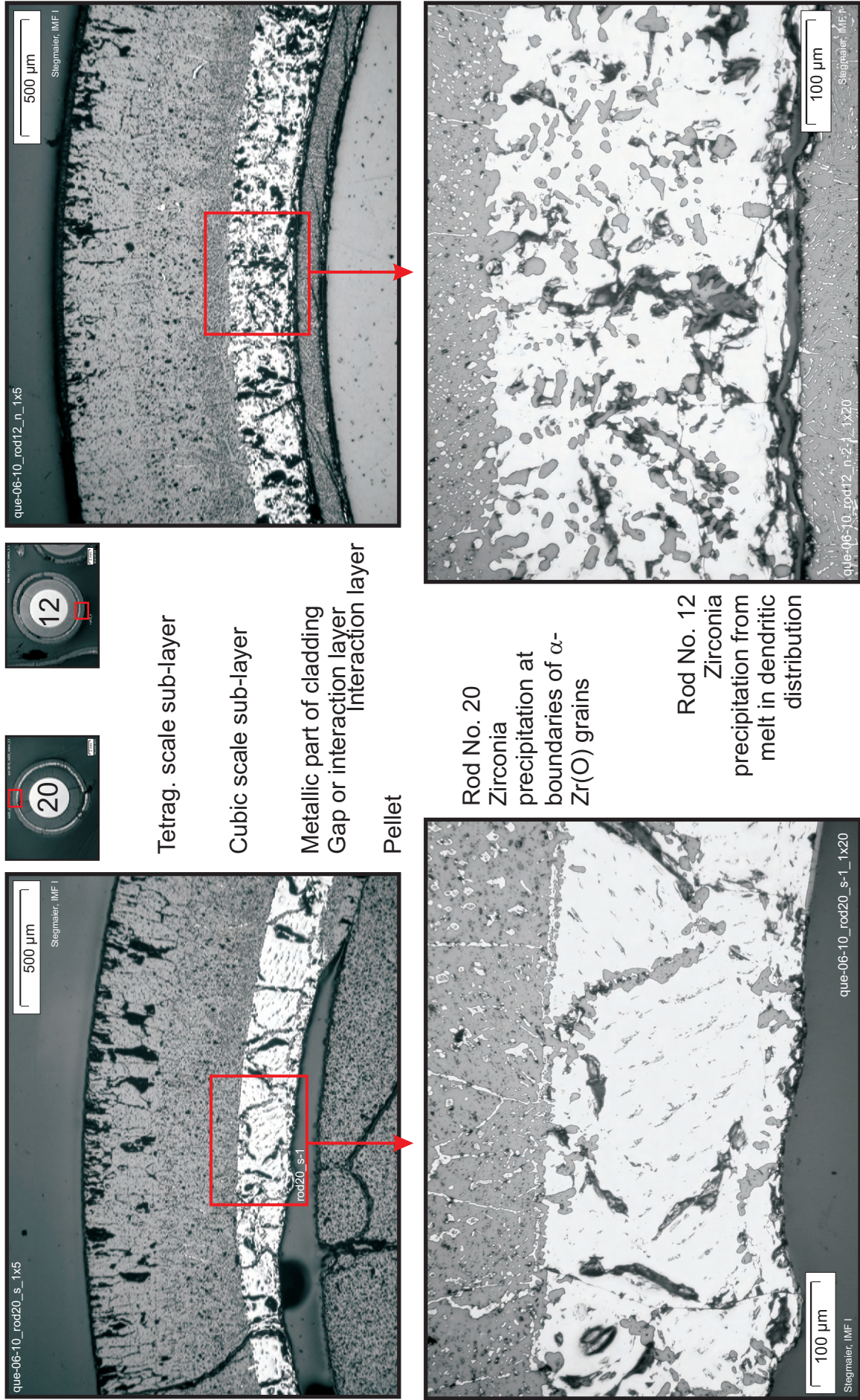
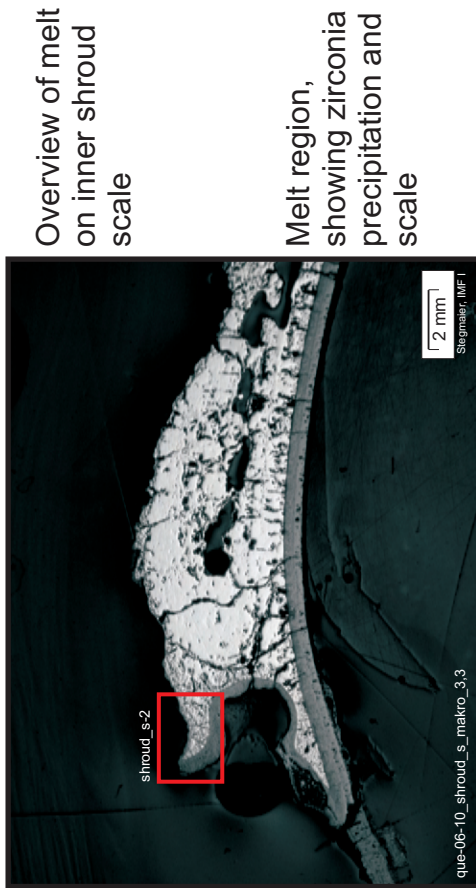


Fig. 67: Cross section at 950 mm bundle elevation (QUE-06-10); rods No. 20 and 12, showing zirconia precipitation from metallic part of cladding, in solid or molten state, respectively



Shroud melt without zirconia precipitates

Melt region, showing zirconia precipitation and scale

Internal shroud scale

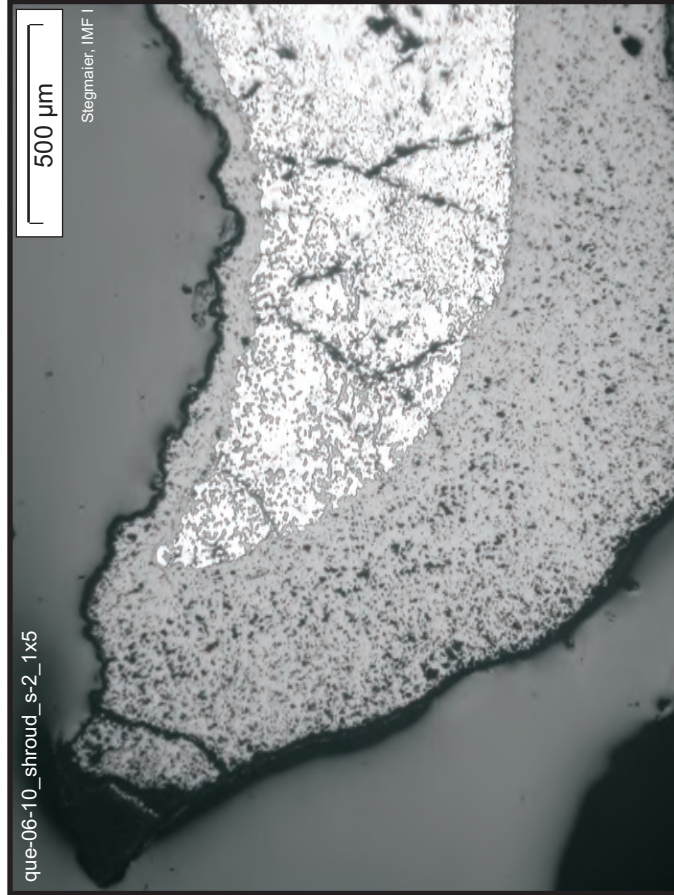
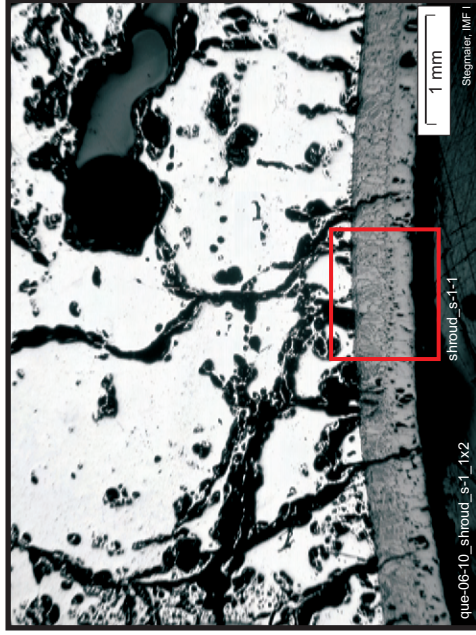
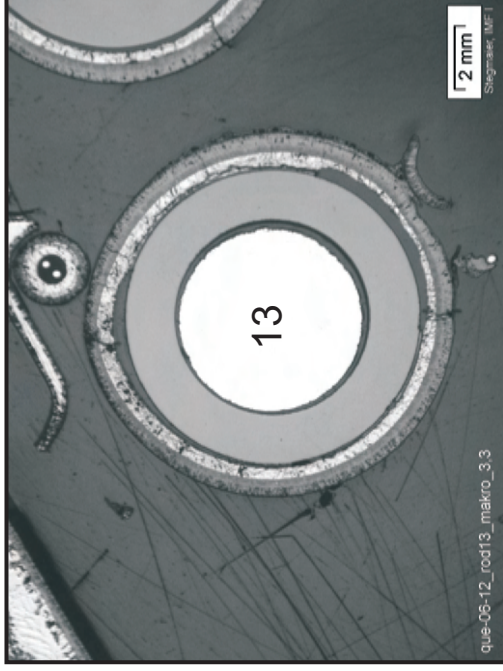
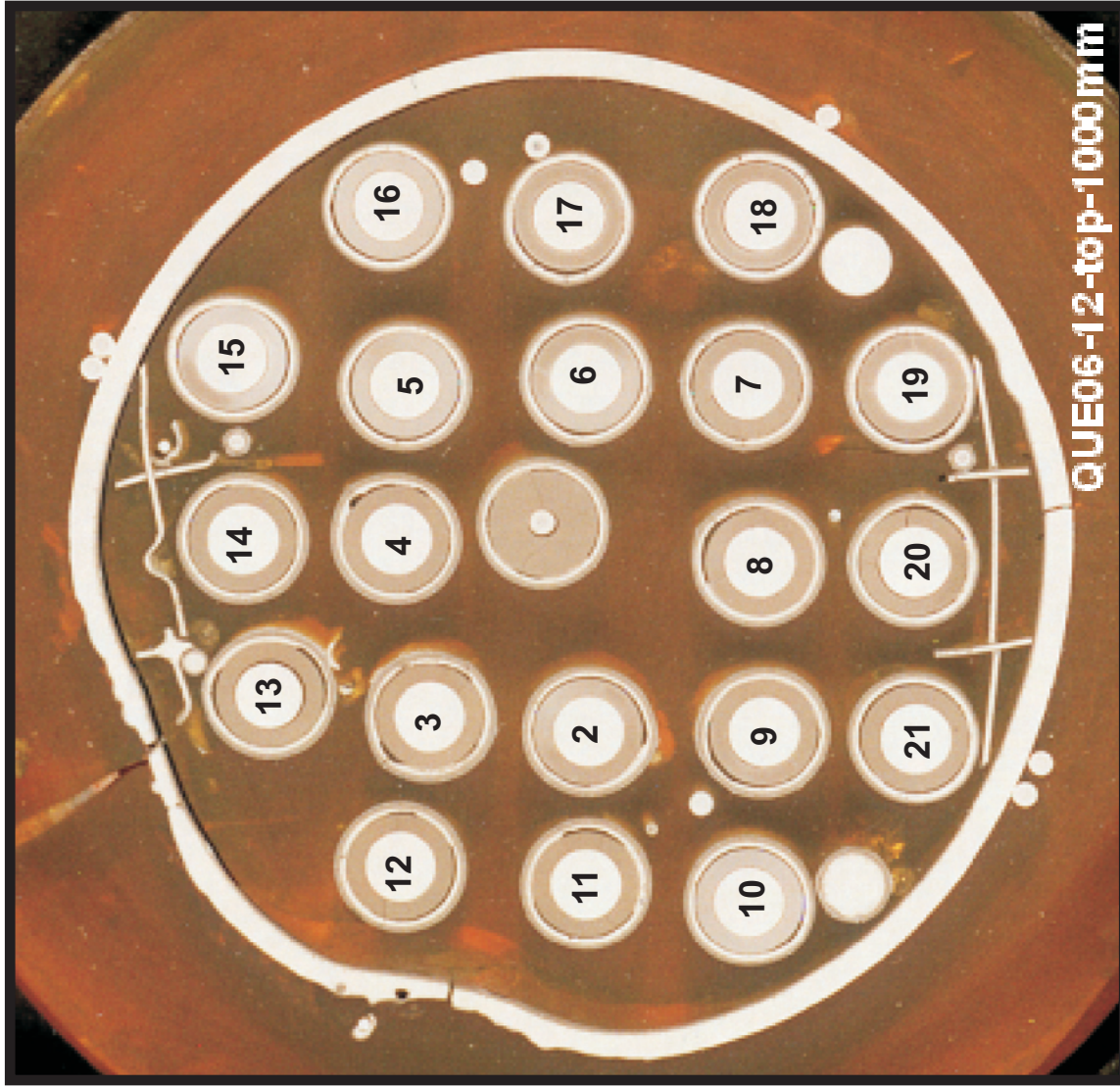


Fig.68: Cross section at 950 mm bundle elevation (QUE-06-10); internal scale of original shroud and oxidation of accumulated shroud melt



Rod No. 13, together with shroud and remnants of spacer and thermocouples

Rod No. 4, showing voids from internal cladding melt relocation

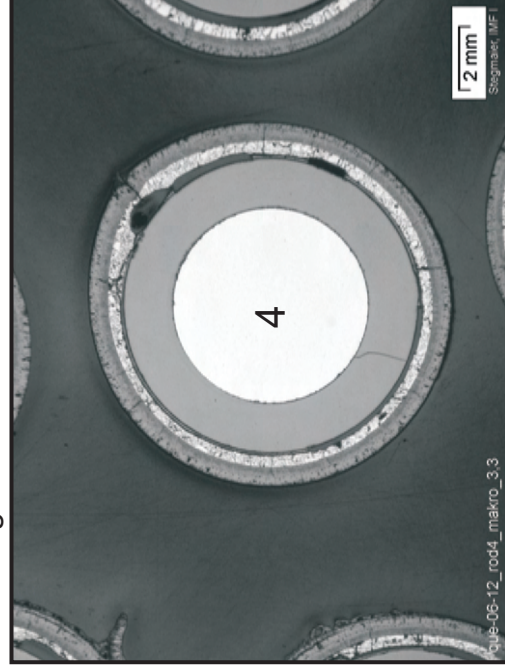
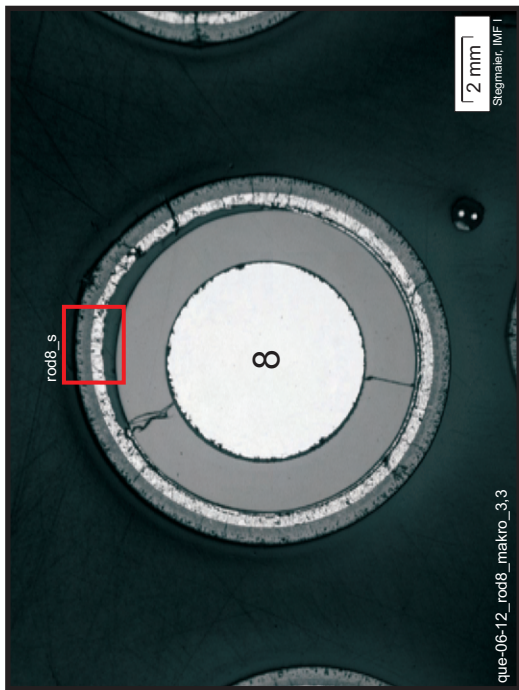
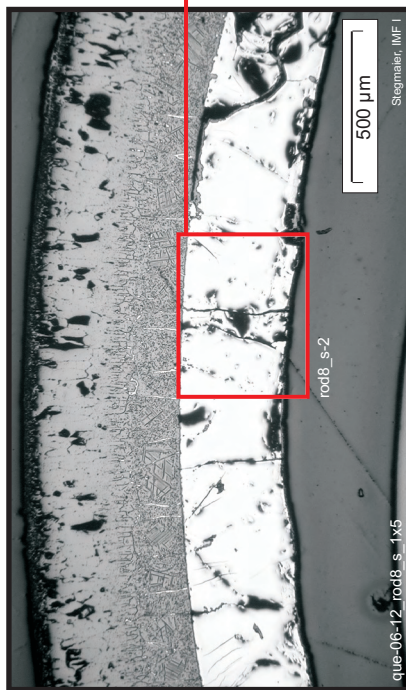


Fig. 69: Cross section at 1000 mm bundle elevation (QUE-06-12); overview, rods No. 13 and 4 as examples



Macrograph of rod No. 8

Cross section, showing (top to bottom): duplex scale, non-molten metallic part of cladding, gap, pellet



Detail micrograph of cladding, showing (top to bottom): Internal part of cubic scale, metallic part of cladding with cracks, partial crack and inner surface oxidation



Fig. 70: Cross section at 1000 mm bundle elevation (QUE-06-12); rod No. 8, showing strong external and slight internal oxidation by steam, and non-molten cladding



Rod No. 8, showing (top to bottom): Scale, α -Zr(O) layer, β -Zr matrix, gap, zirconia protection layer on Mo electrode

Detail: external part of cladding



Fig. 71: Cross section at 1150 mm bundle elevation (QUE-06-14); overview, rod No. 8, showing its components at electrode elevation and its cladding oxidation

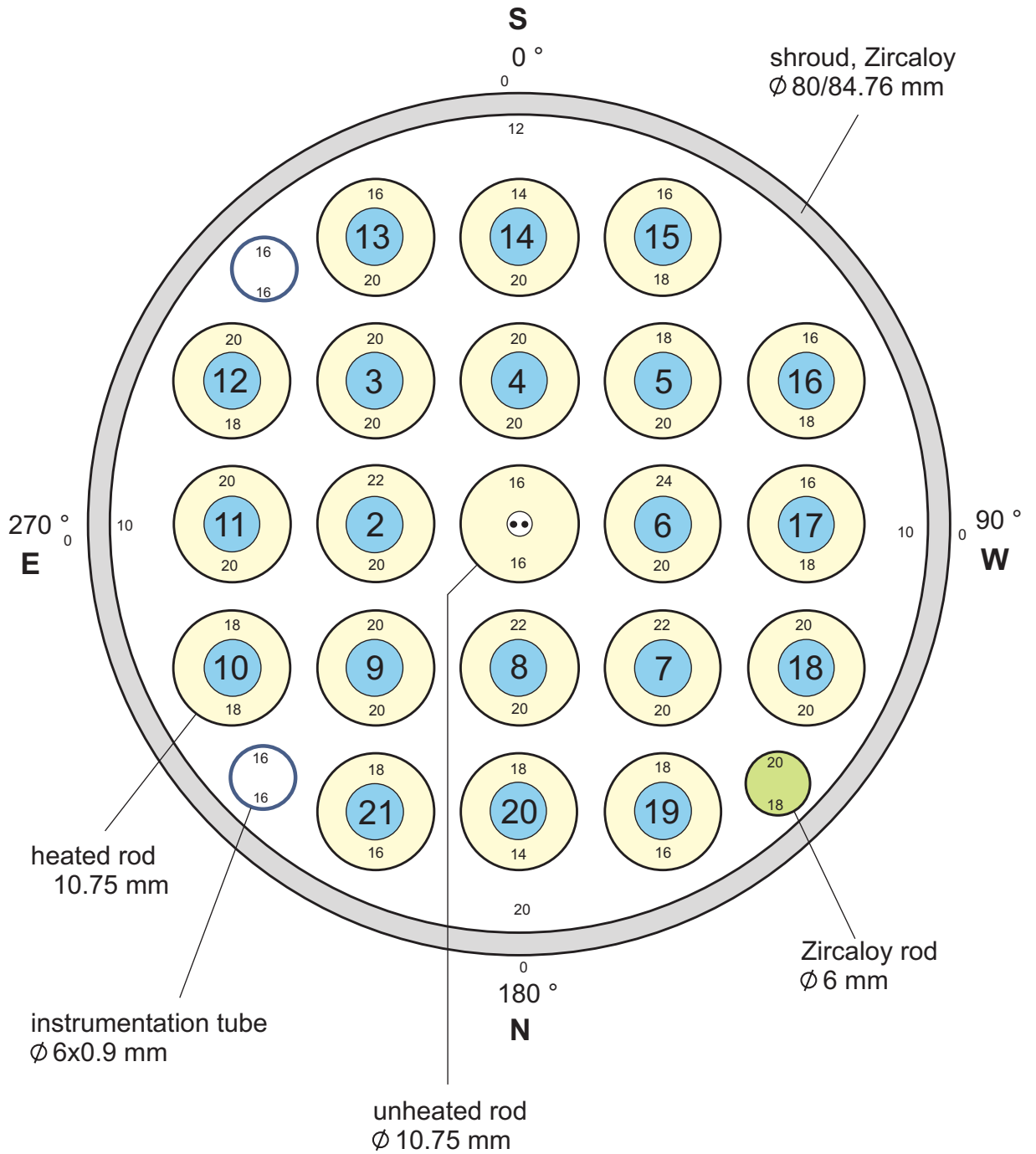


Fig 72-QUE06 cross section QUE-06-2.cdr
11.12.03 - IMF

Fig. 72: QUENCH-06; Oxide layer thicknesses at bundle elevation 550 mm

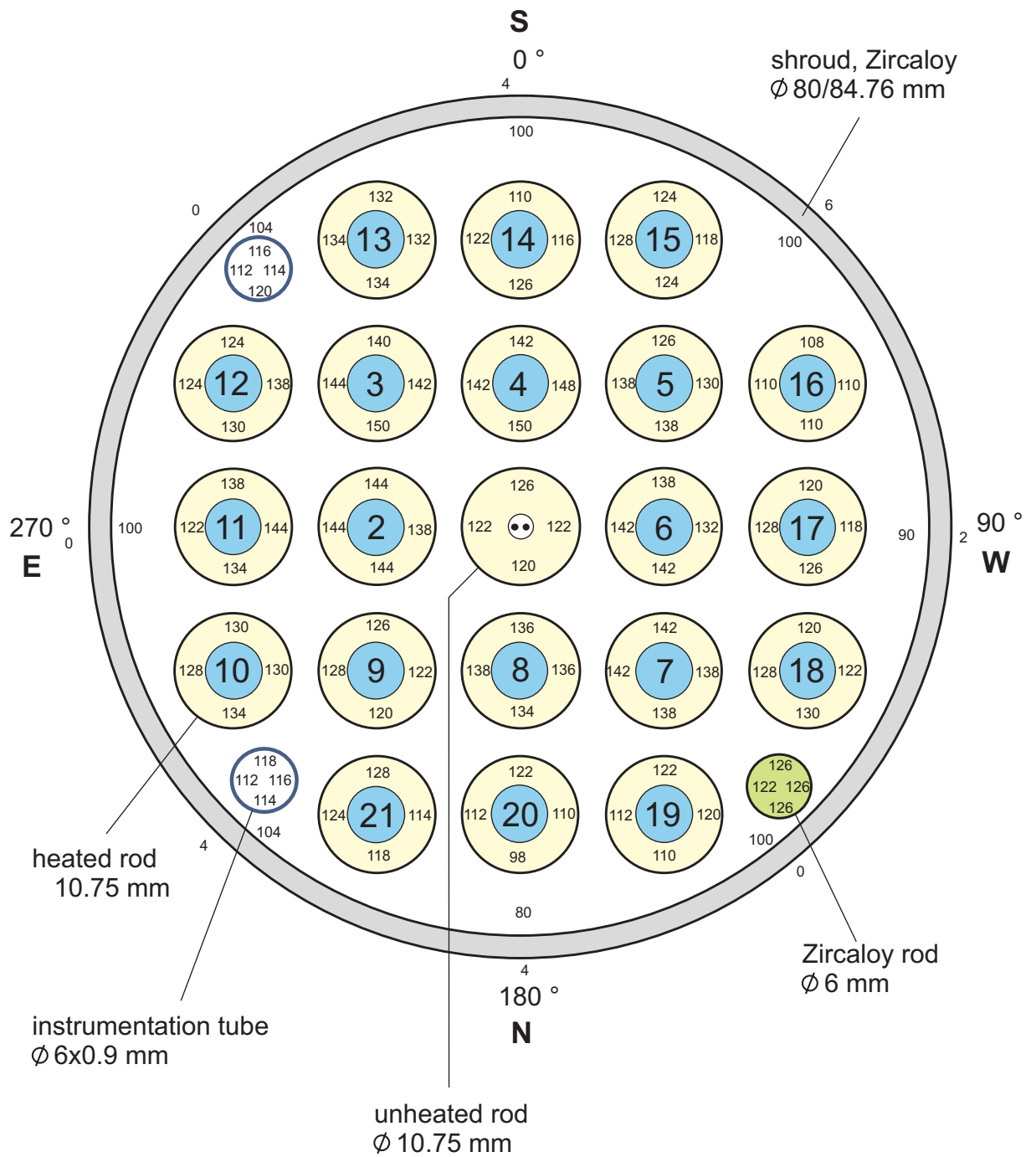


Fig 73-QUE06 cross section QUE-06-4.cdr
11.12.03 - IMF

Fig. 73: QUENCH-06; Oxide layer thicknesses at bundle elevation 750 mm

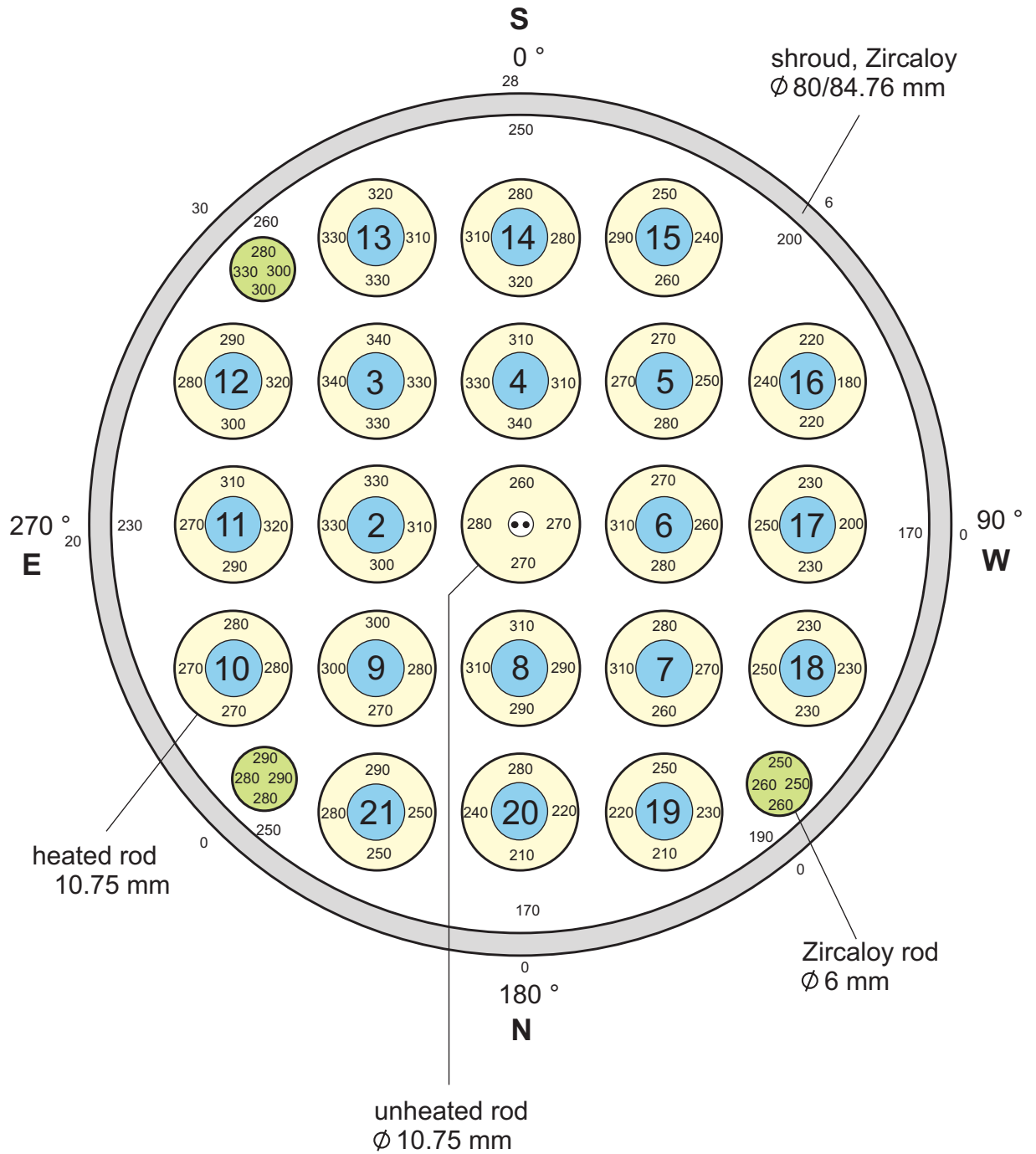


Fig 74-QUE06 cross section QUE-06-6.cdr
11.12.03 - IMF

Fig. 74: QUENCH-06; Oxide layer thicknesses at bundle elevation 850 mm

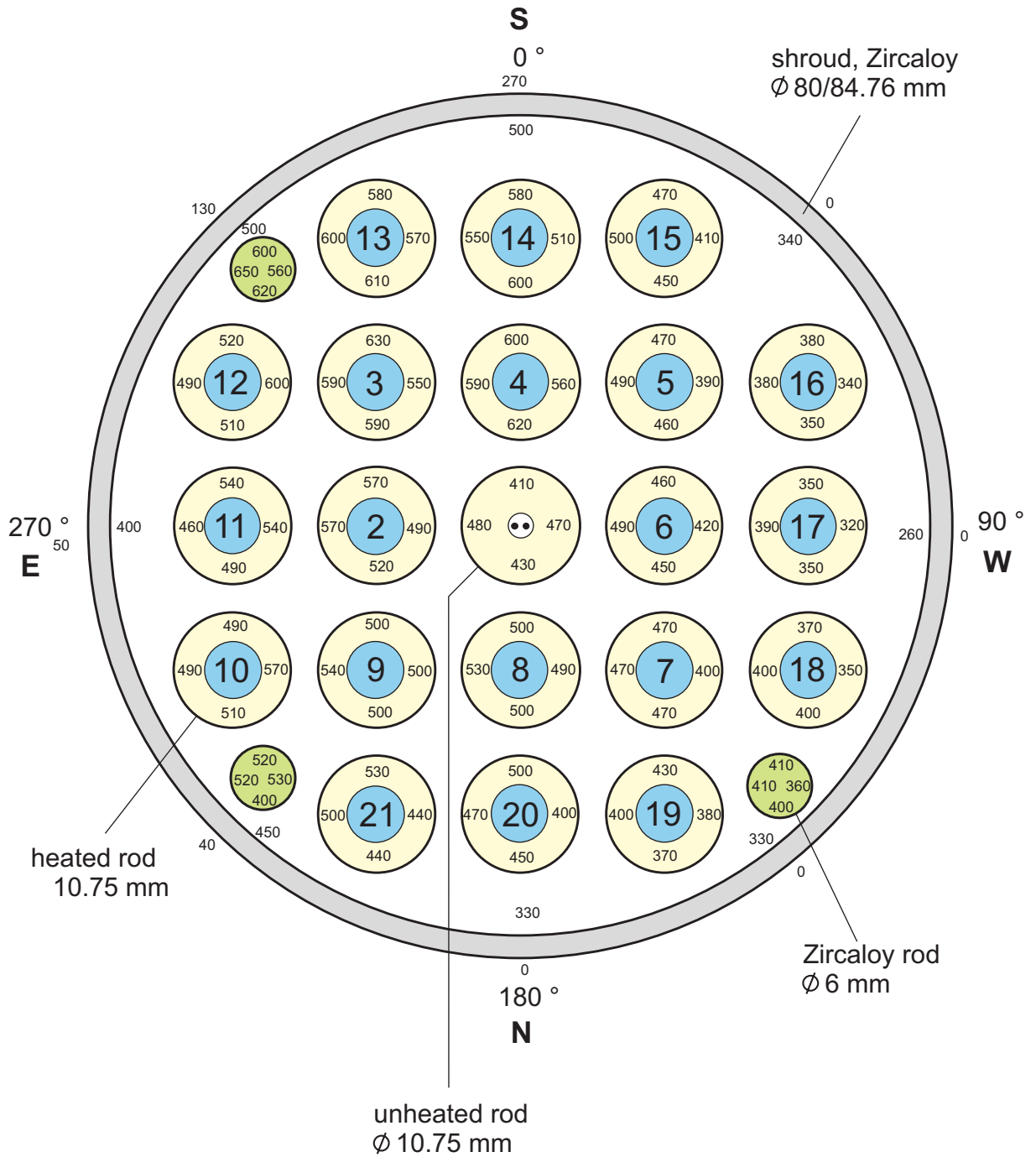


Fig 75-QUE06 cross section QUE-06-8.cdr
11.12.03 - IMF

Fig. 75: QUENCH-06; Oxide layer thicknesses at bundle elevation 900 mm

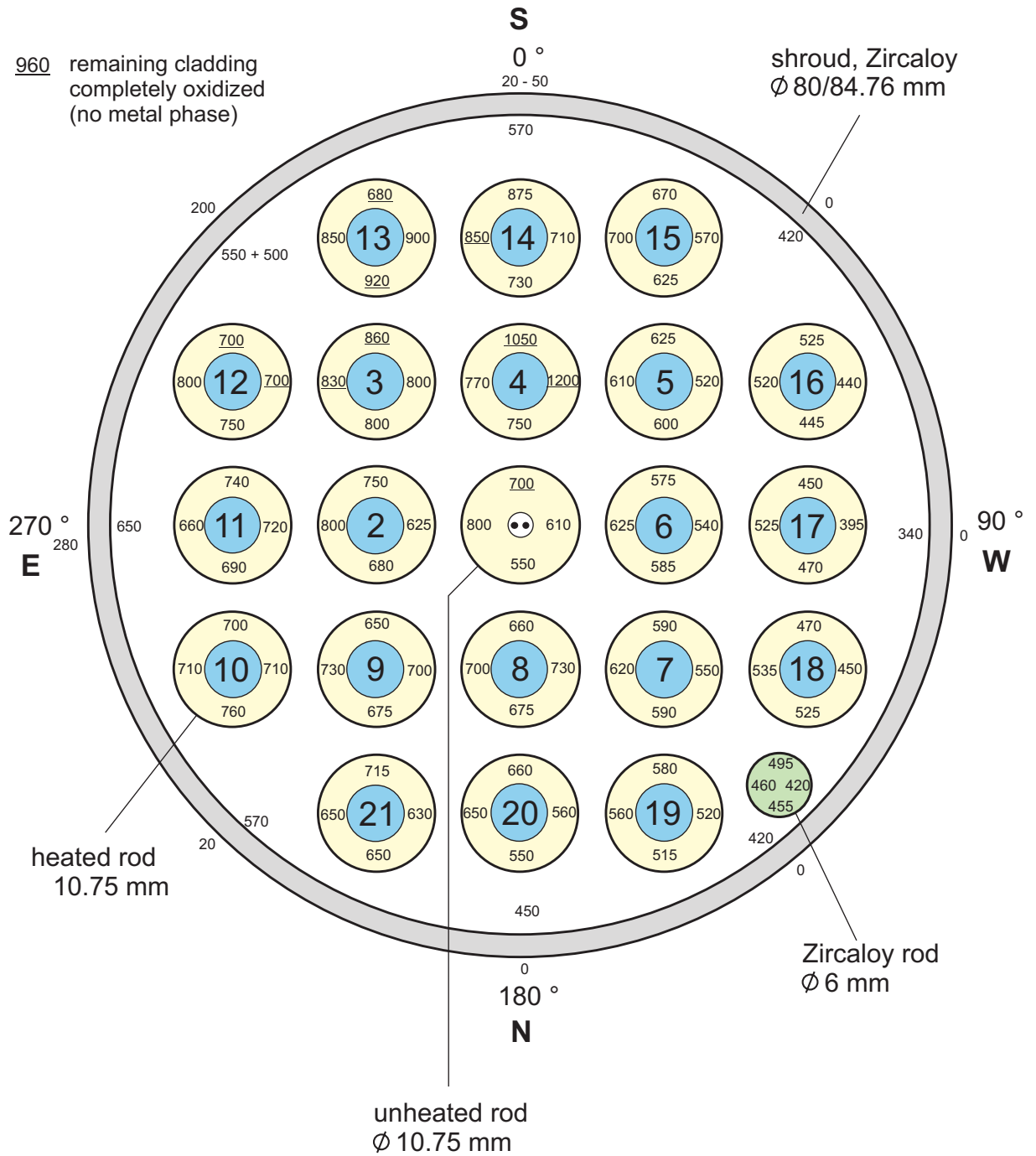


Fig 76-QUE06 cross section QUE-06-10.cdr
11.12.03 - IMF

Fig. 76: QUENCH-06; Oxide layer thicknesses at bundle elevation 950 mm

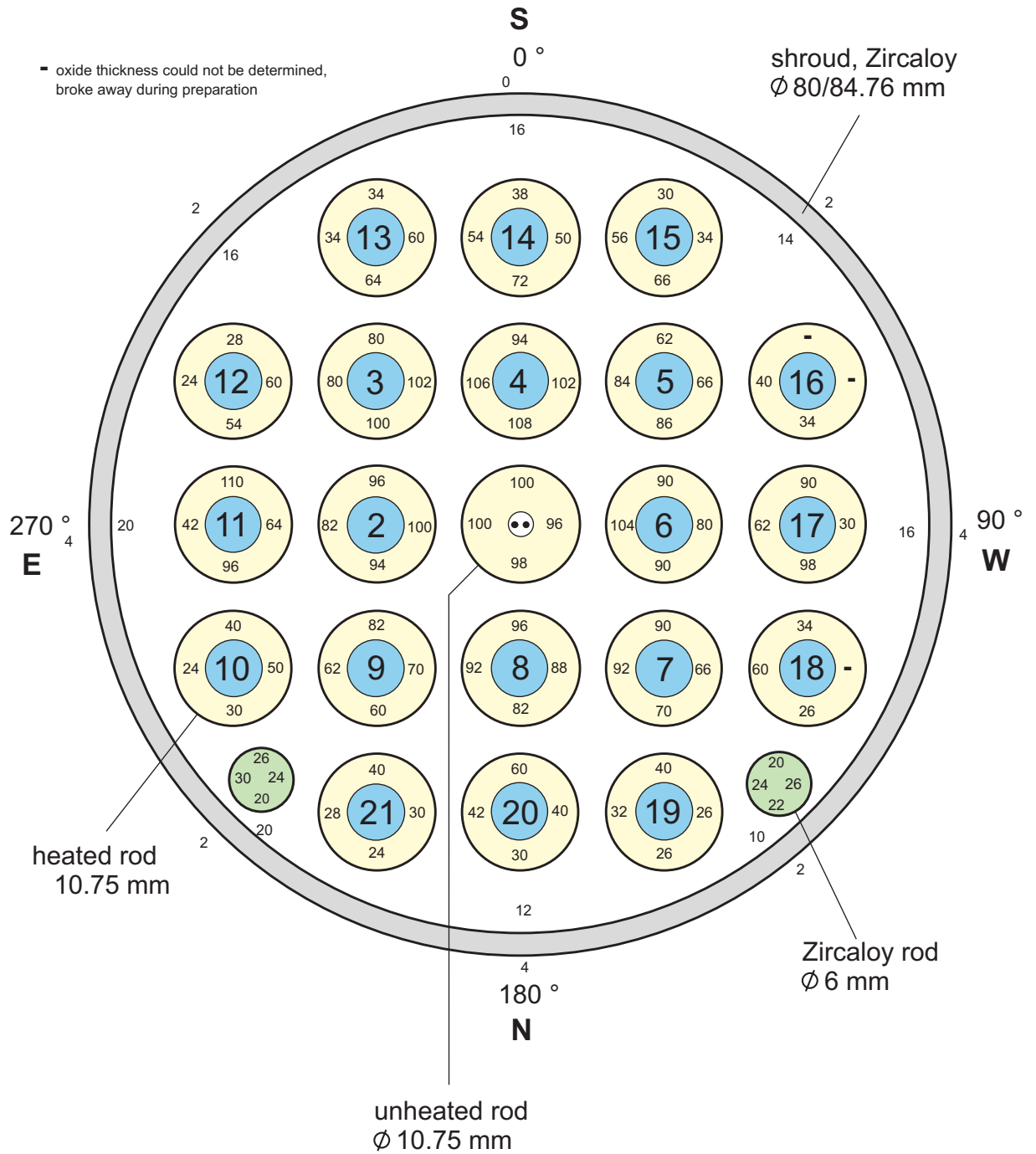


Fig 78-QUE06 cross section QUE-06-14.cdr
11.12.03 - IMF

Fig. 78: QUENCH-06; Oxide layer thicknesses at bundle elevation 1150 mm

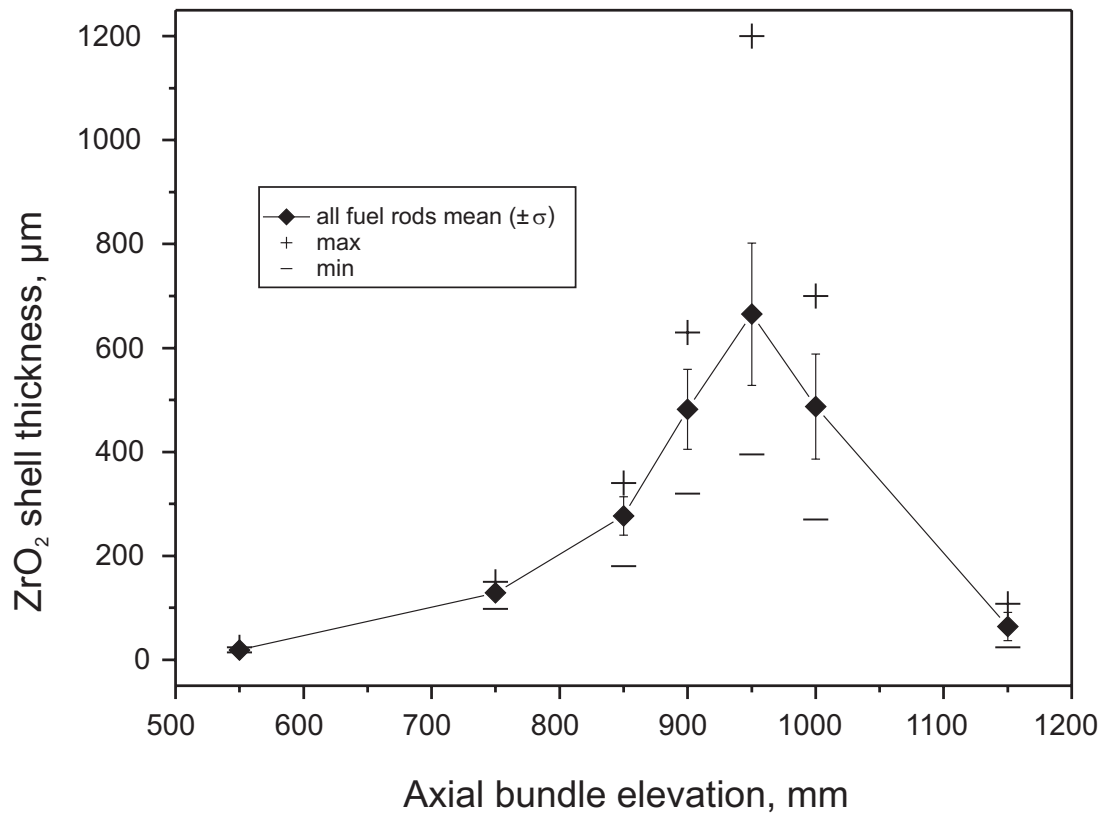
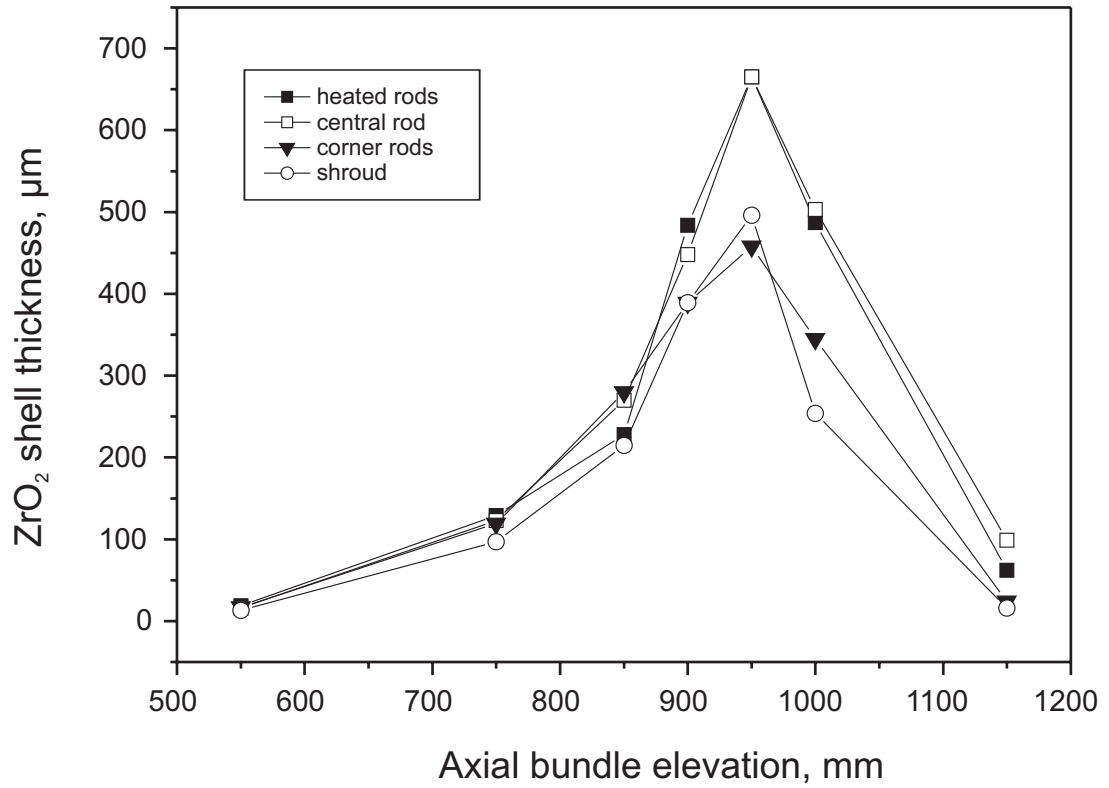


Fig 79-QUE06 Axial oxide layer.cdr
11.12.03 - IMF

Fig. 79: QUENCH-06; Axial oxide layer thickness distribution.

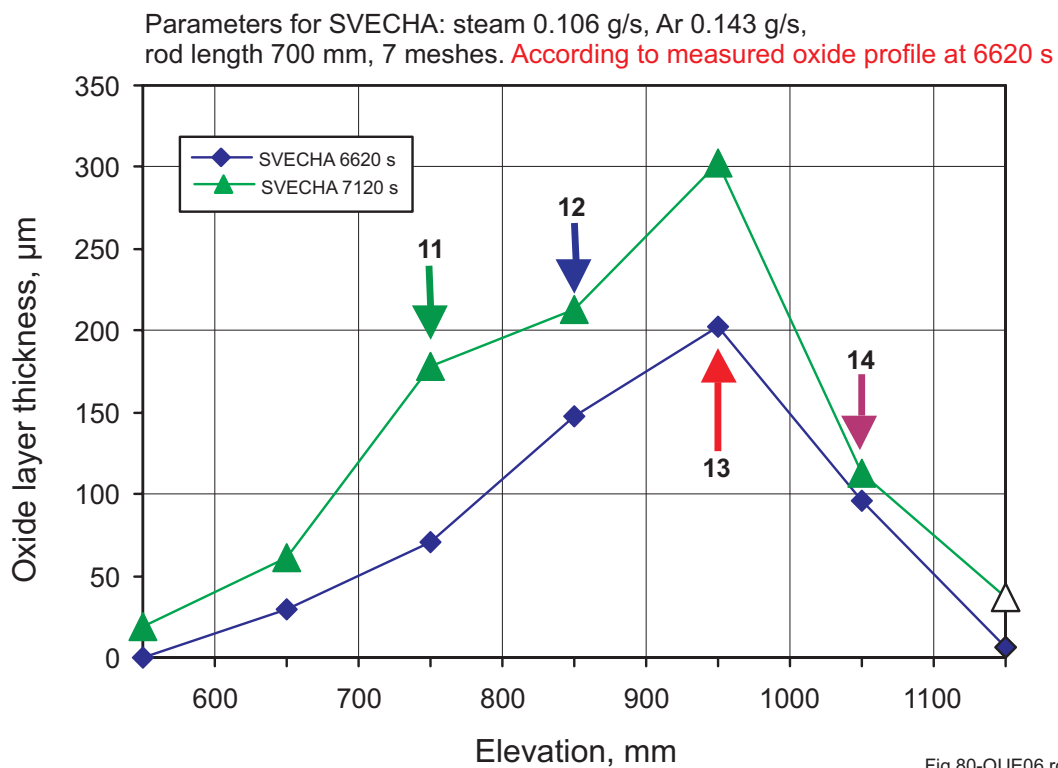
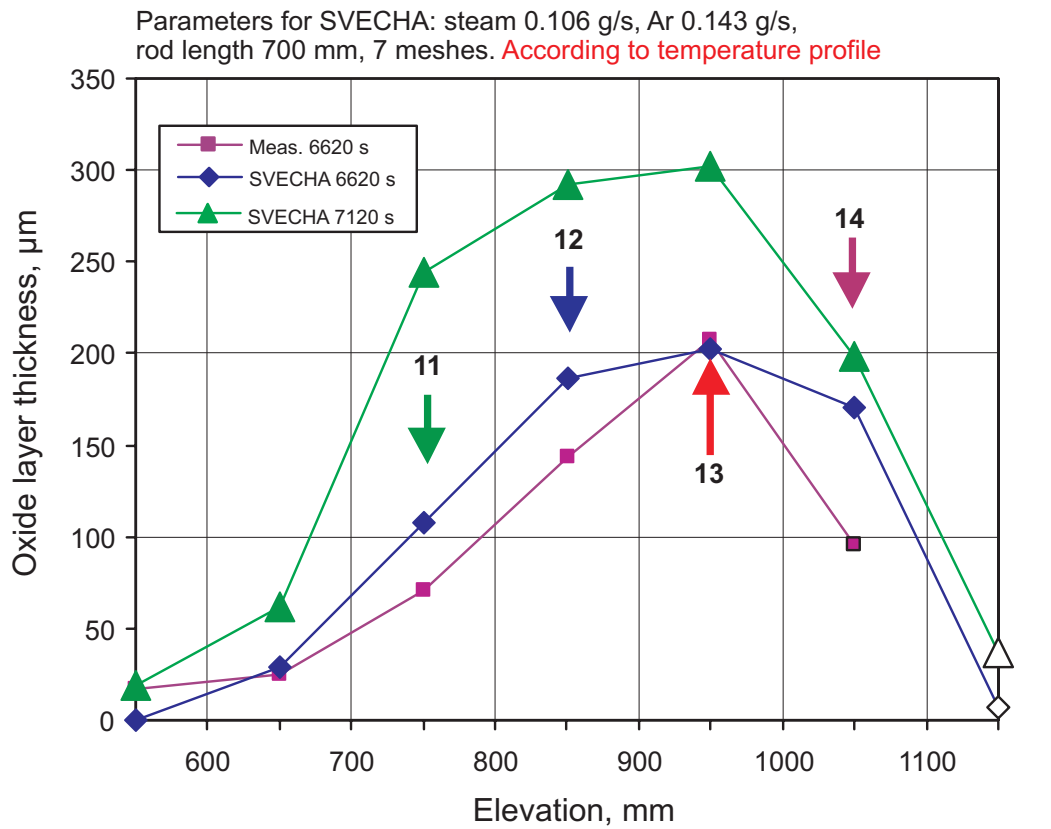


Fig 80-QUE06 rod B S.cdr
11.12.03 - IMF

Fig. 80: QUENCH-06; Calculational results with input of measured temperatures, top, and with input of temperatures according to the oxide profile measured at 6620 s, bottom.

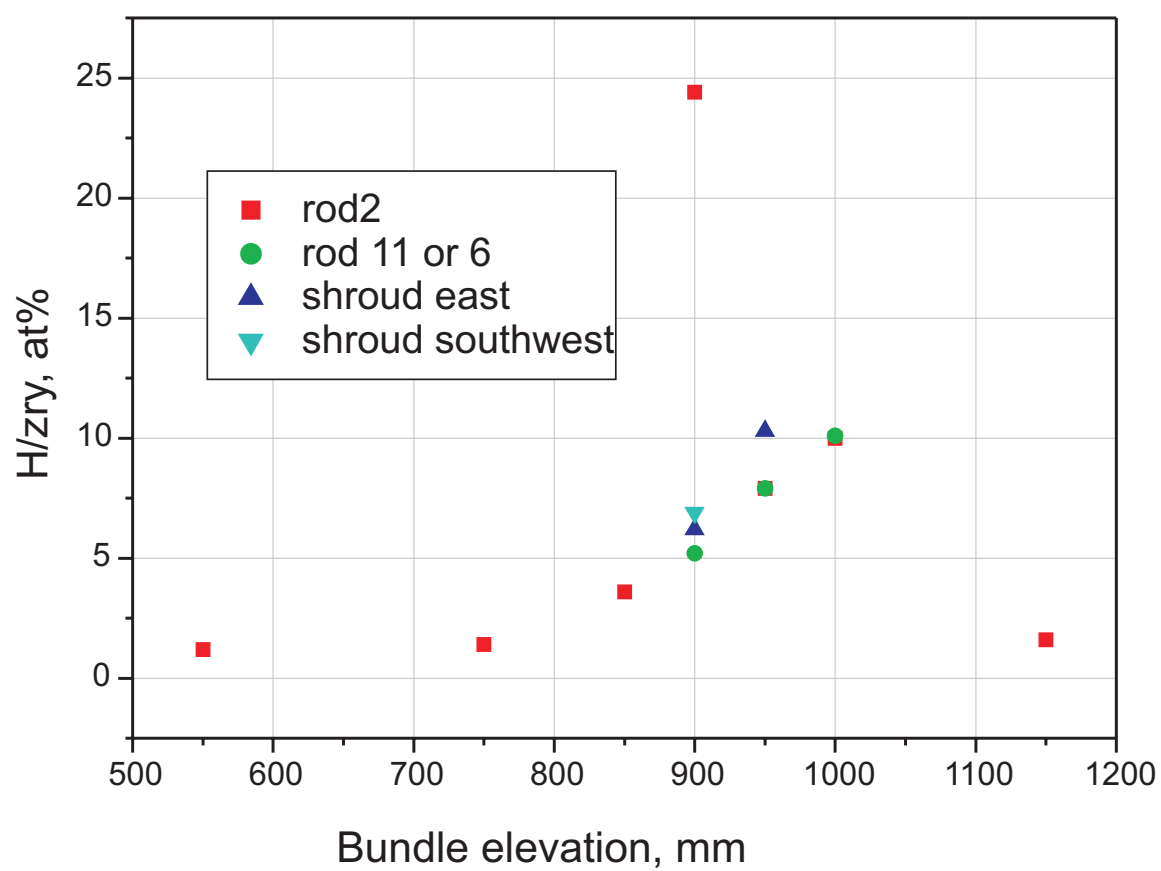


Fig 81-QUE06 Axial profile h2.cdr
11.12.03 - IMF

Fig. 81: QUENCH-06; Axial profile of hydrogen absorbed by the remaining Zr(O) metal phases.

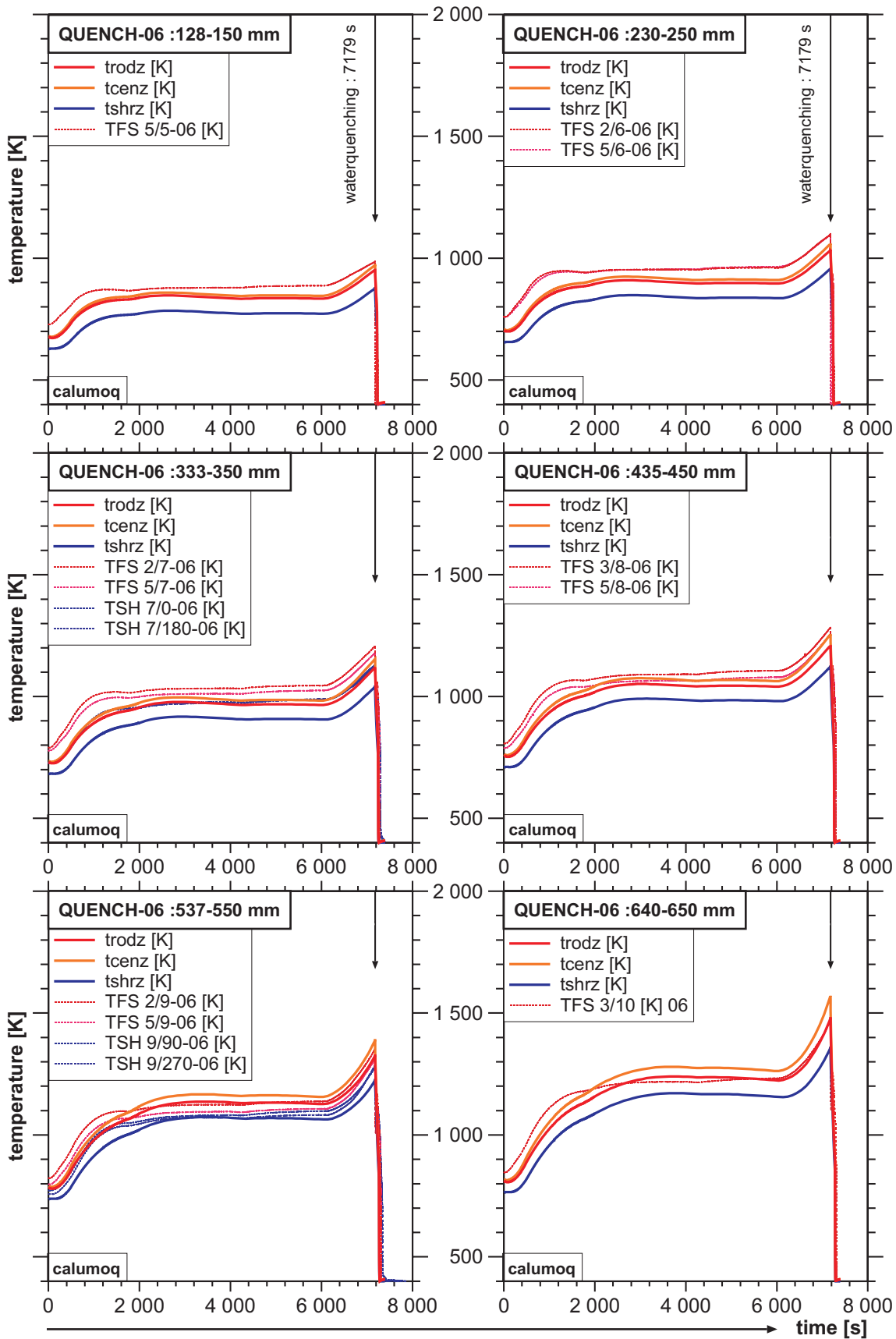


Fig.82-QUE06
11.12.03 - IMF

Fig. 82: QUENCH-06; Calculated average temperature of the entire bundle “trodz”, average temperature of the inner cluster of nine fuel rod simulators “tcenz”, and average shroud temperature “tshrz” compared to the available thermocouple readings at elevations 128 - 650 mm for the entire test duration

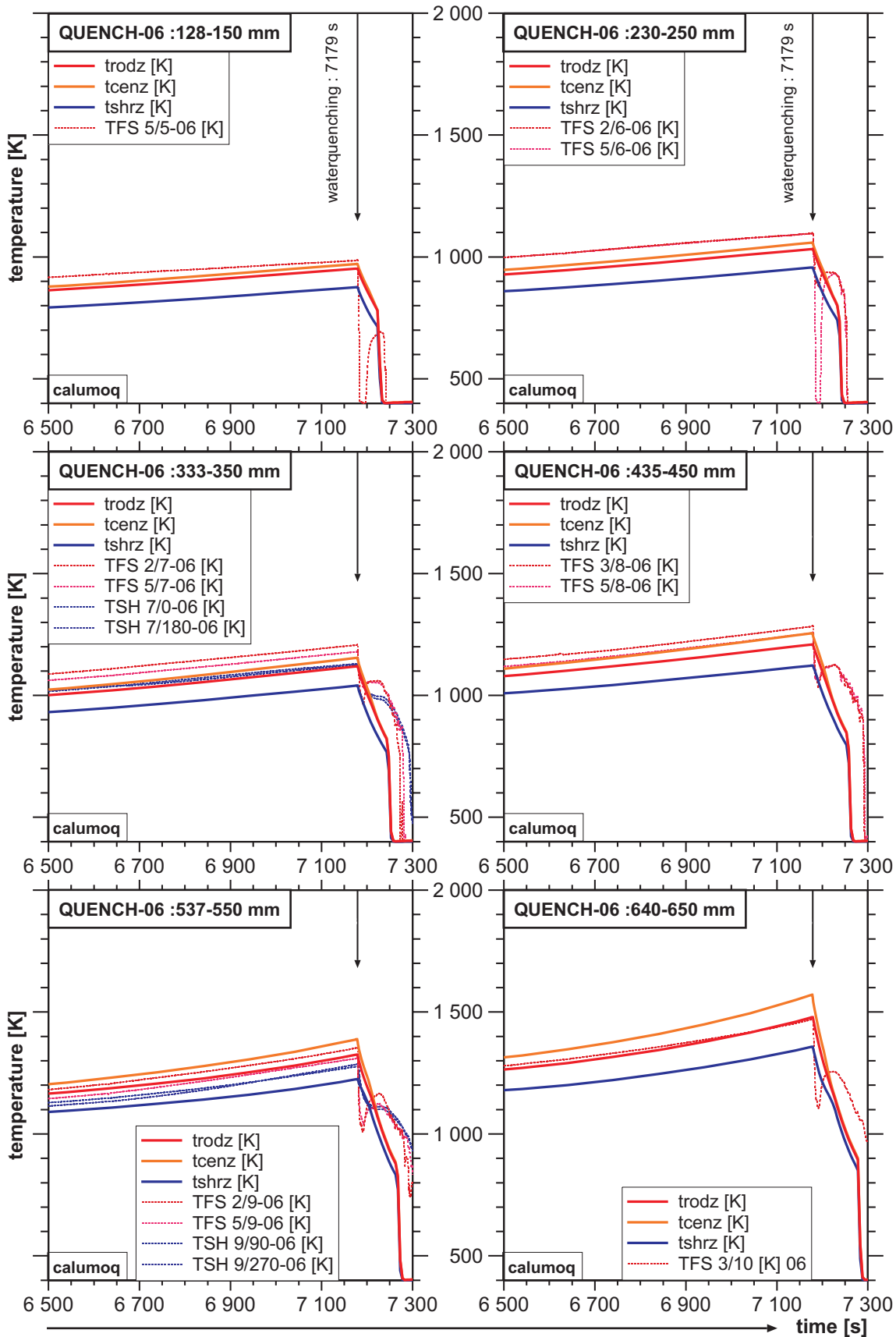


Fig.83-QUE06
11.12.03 - IMF

Fig. 83: QUENCH-06; Calculated average temperature of the entire bundle “trodz”, average temperature of the inner cluster of nine fuel rod simulators “tcenz”, and average shroud temperature “tshrz” compared to the available thermocouple readings at elevations 128 - 650 mm for the test time 6500 - 7300 s

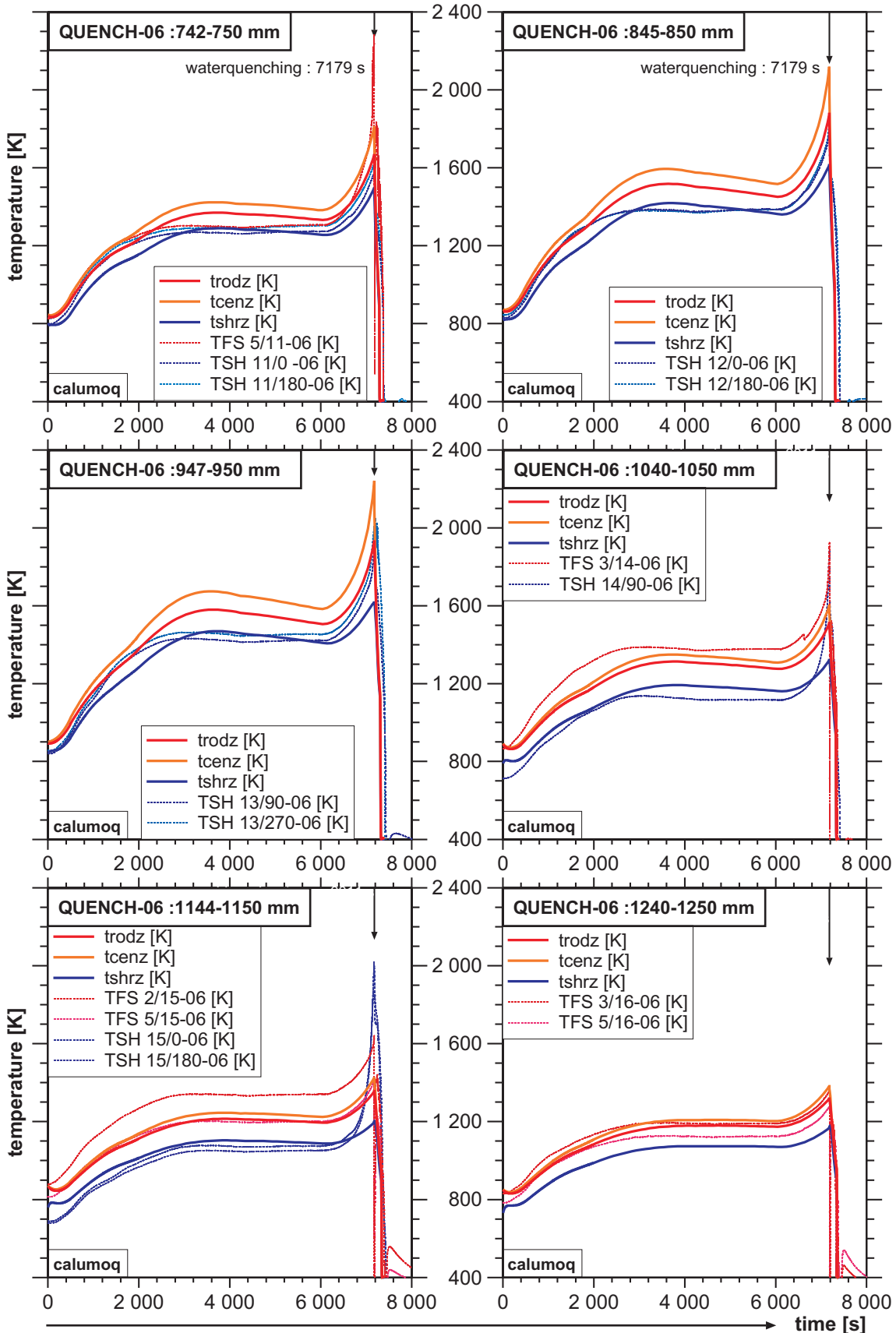


Fig.84-QUE06
11.12.03 - IMF

Fig. 84: QUENCH-06; Calculated average temperature of the entire bundle “trodz”, average temperature of the inner cluster of nine fuel rod simulators “tcenz”, and average shroud temperature “tshrz” compared to the available thermocouple readings at elevations 742 - 1250 mm for the entire test duration.

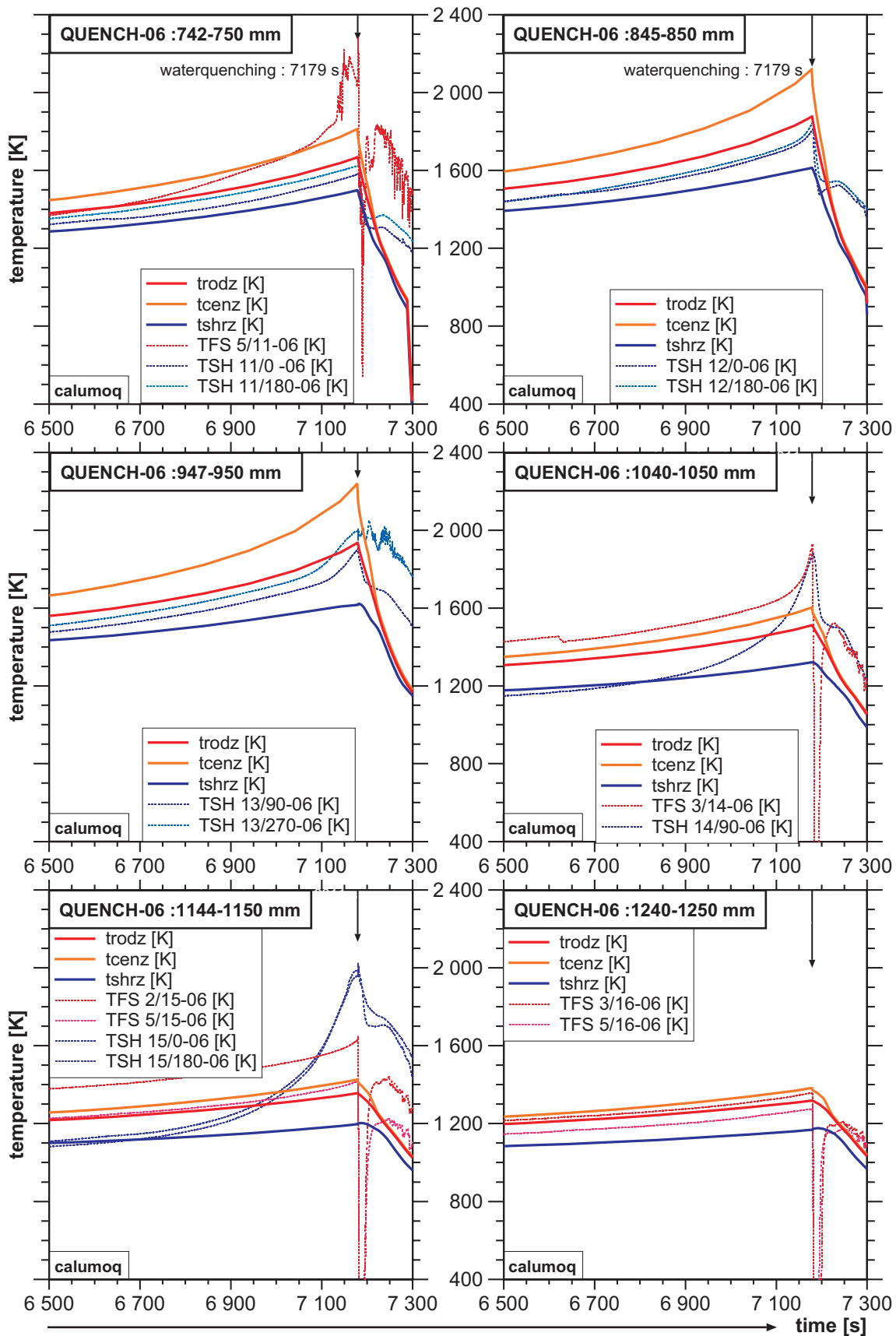


Fig.85-QUE06
11.12.03 - IMF

Fig. 85: QUENCH-06; Calculated average temperature of the entire bundle “trodz”, average temperature of the inner cluster of nine fuel rod simulators “tcentz”, and average shroud temperature “tshrz” compared to the available thermocouple readings at elevations 742 - 1250 mm for the test time 6500 - 7300 s

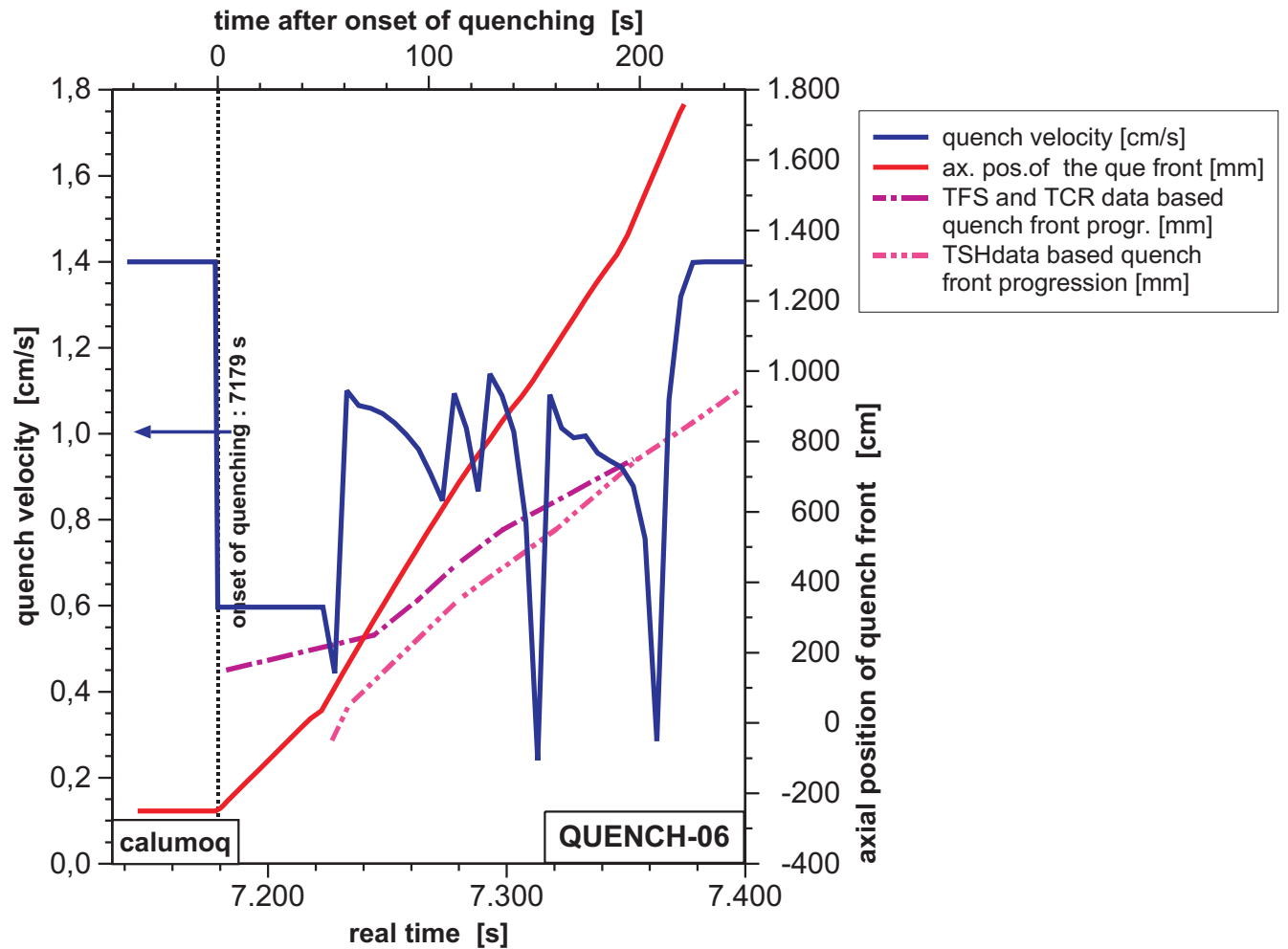


Fig.86-QUE06
11.12.03 - IMF

Fig. 86: QUENCH-06; Calculated quench velocity and axial position of the quench front compared to test data

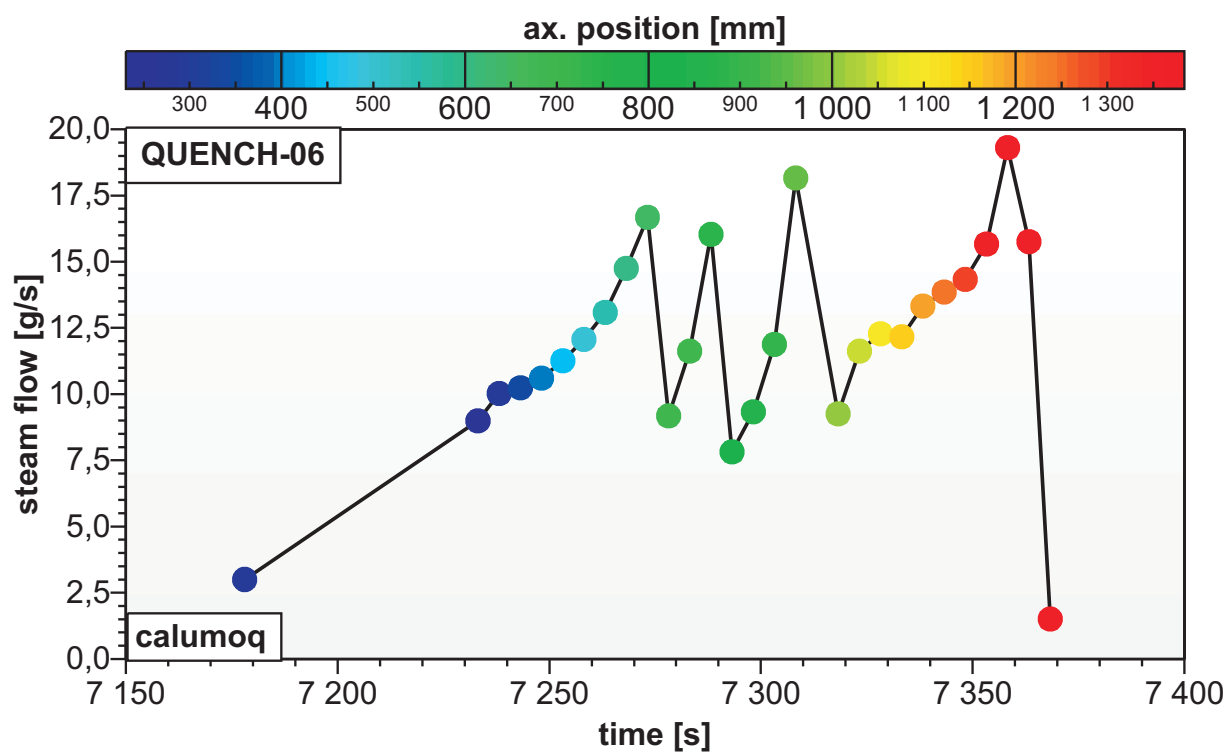


Fig.87-QUE06
11.12.03 - IMF

Fig. 87: QUENCH-06; Calculated steam production during the quench phase

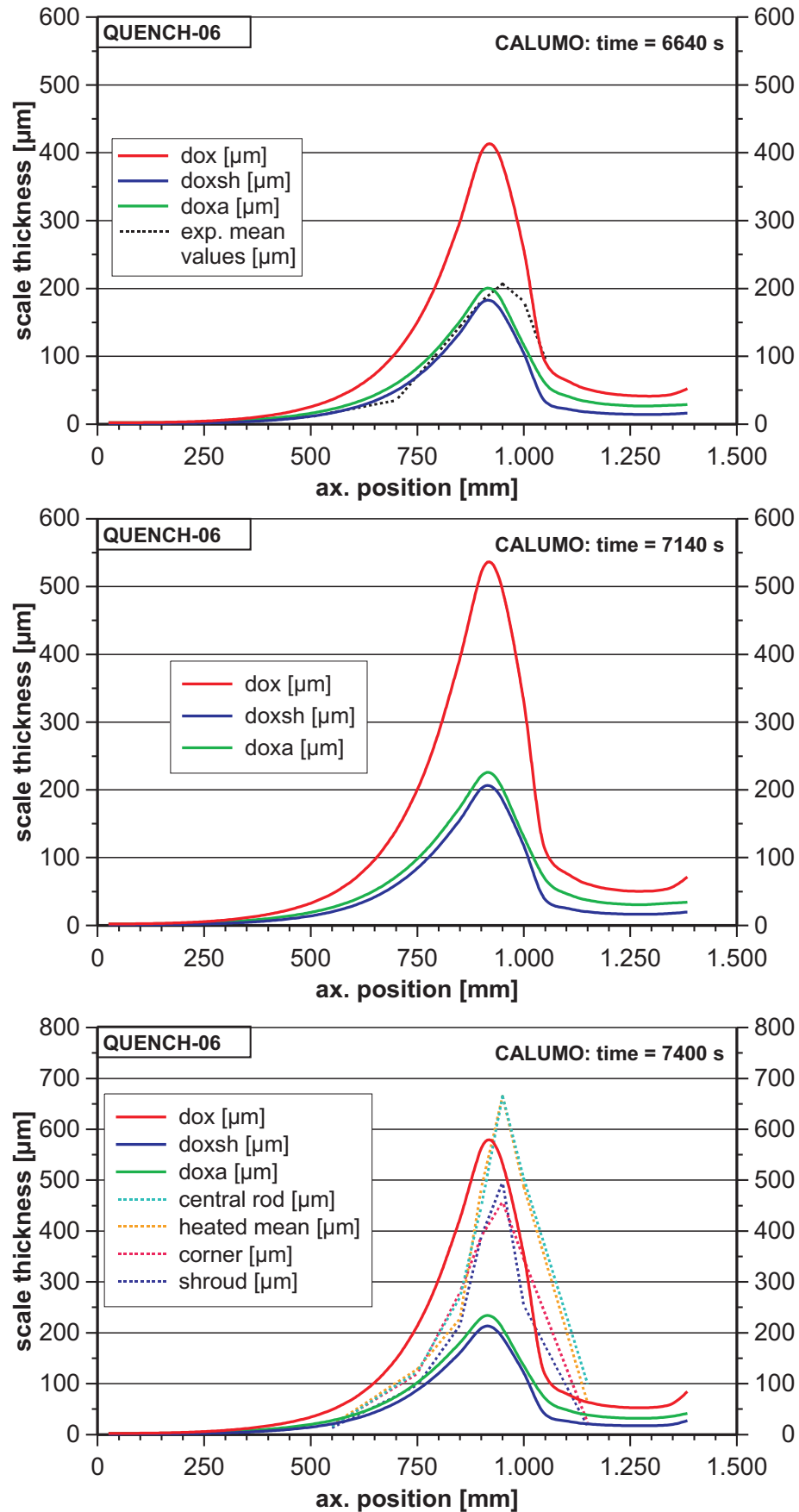


Fig.88-QUE06
11.12.03 - IMF

Fig. 88: QUENCH-06; Axial distributions of the oxide scale thickness for 6640 s (withdrawal of the corner rod B), 7140 s (beginning of the temperature escalation), and 7400 s (after quenching)

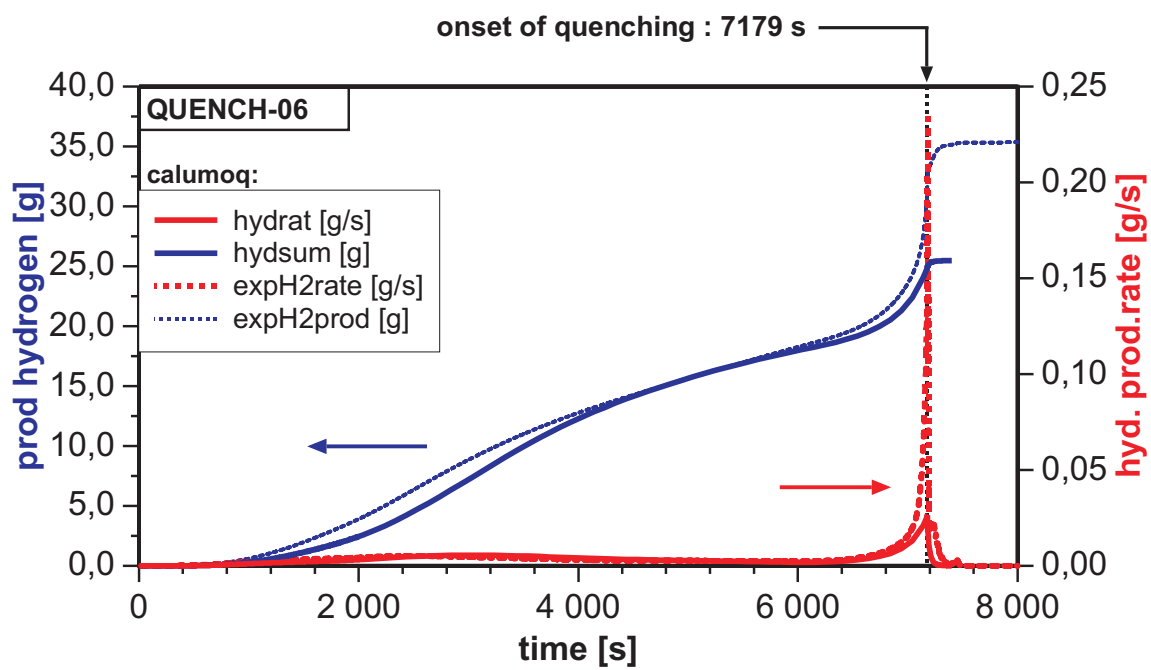


Fig.89-QUE06
11.12.03 - IMF

Fig. 89: QUENCH-06; Comparison of measured and calculated hydrogen production rate and accumulated total hydrogen values.

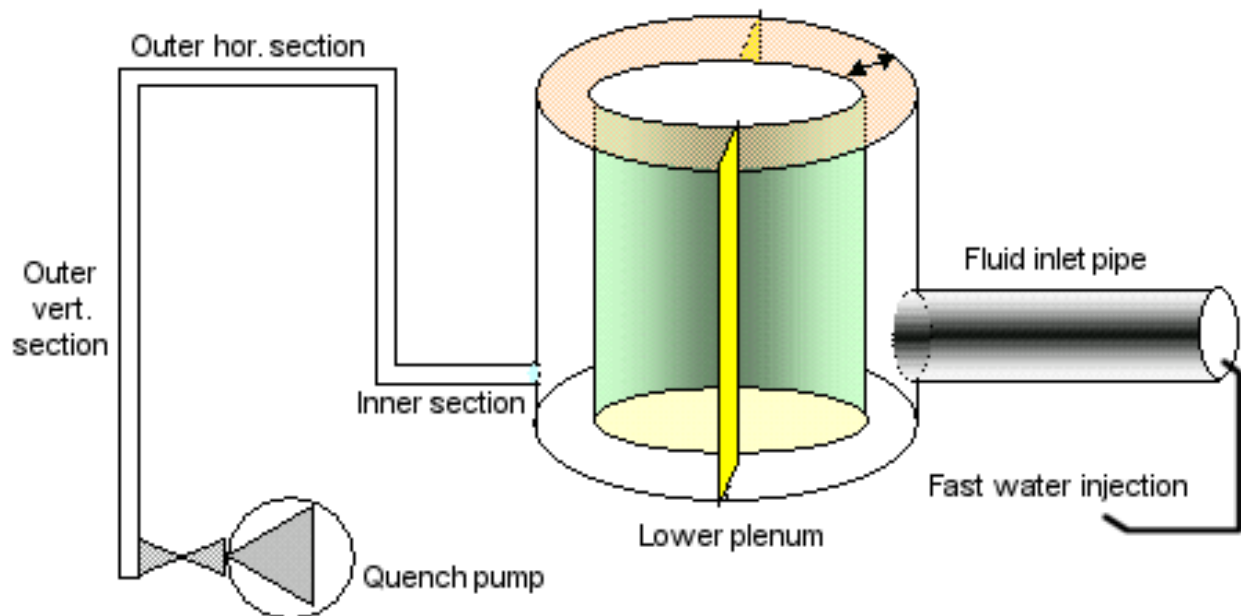
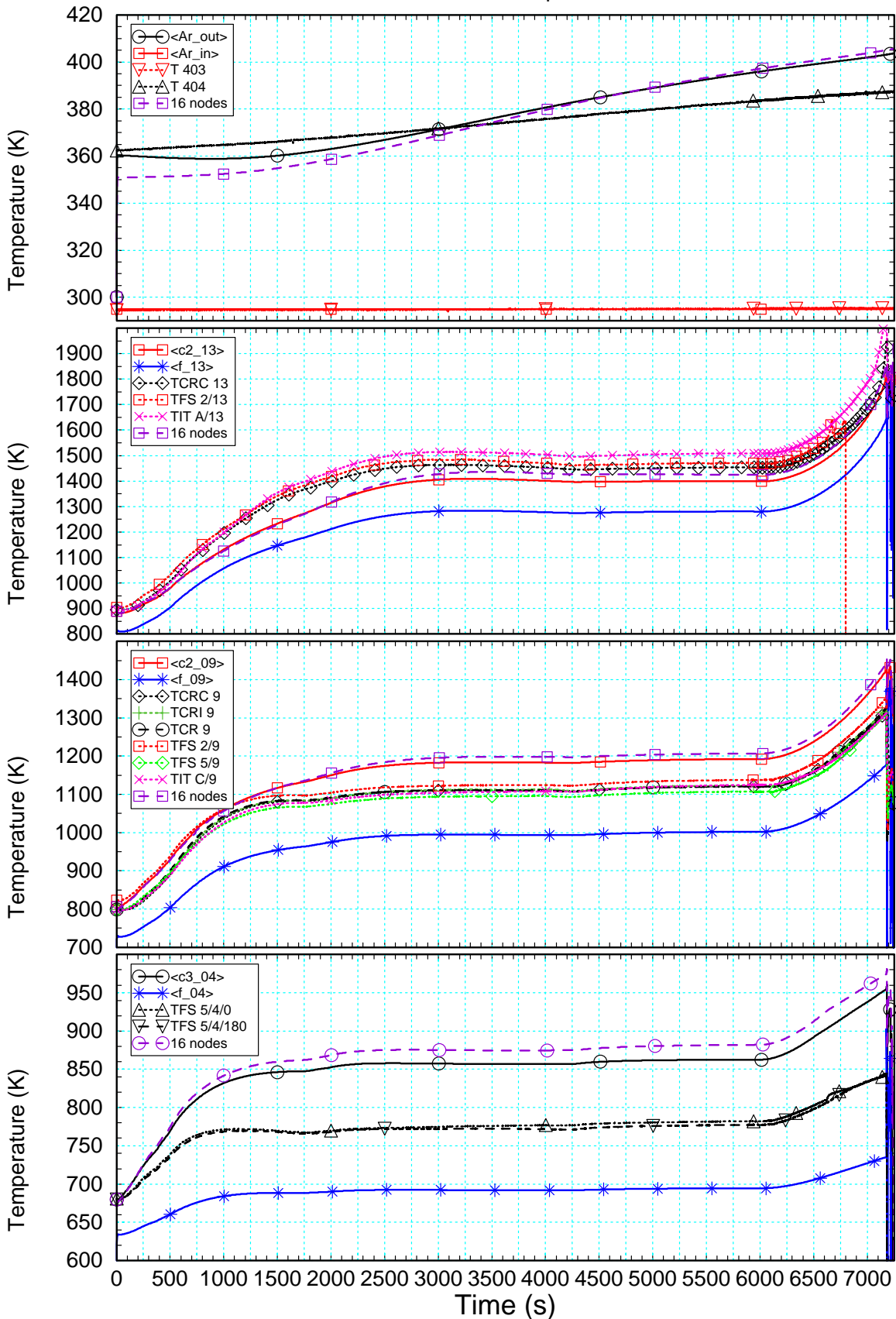


Fig.90 -QUE06.doc
11.12.03 – IMF

Fig. 90: QUENCH-06; Detailed schematics of the inlet volumes including coaxial lower plenum with fluid inlet pipe, fast water injection system (right), and quench water pipe with realistic elevation changes (left) as used for FZK modelling.

QUENCH-06 q06s01



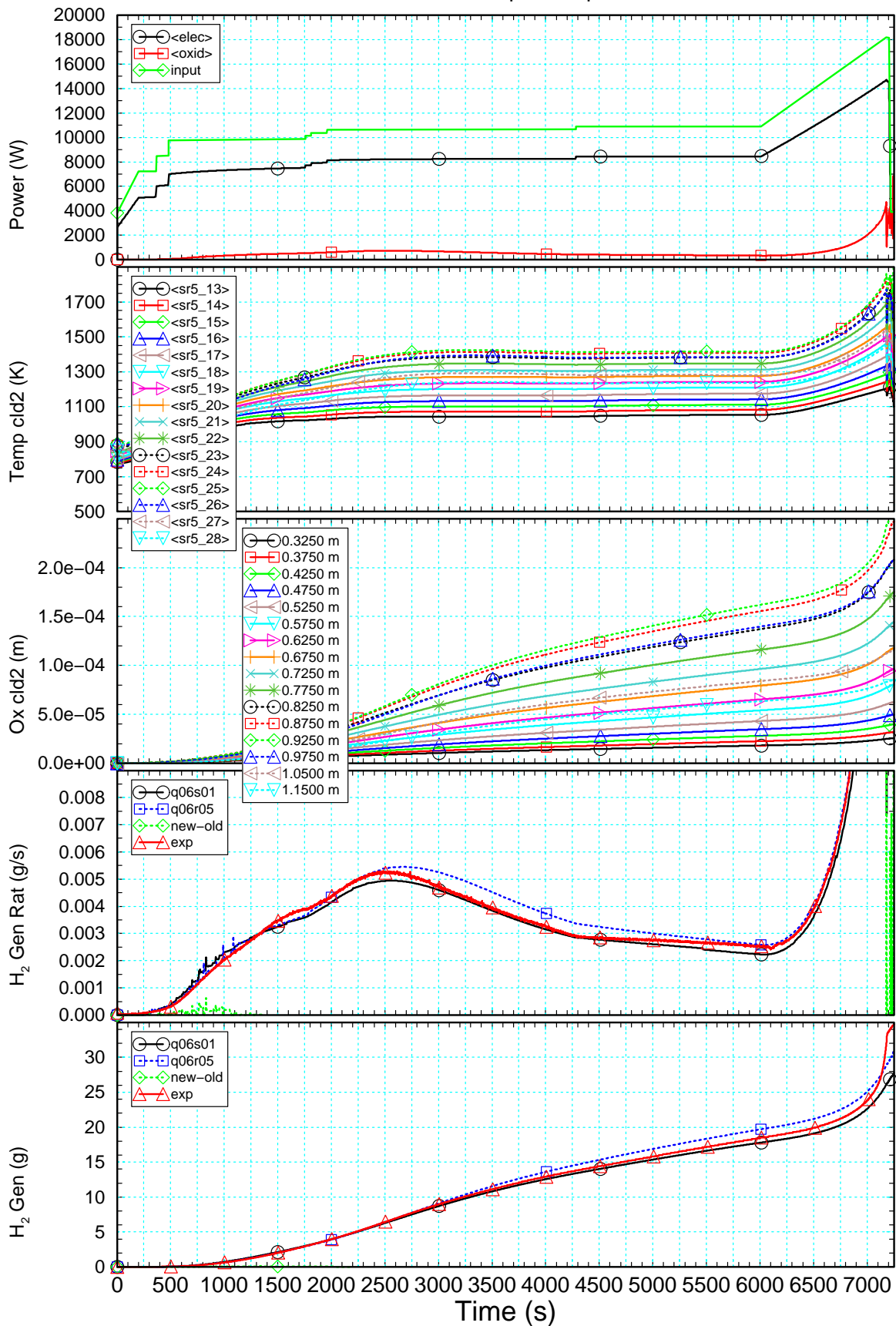
Thu Apr 25 11:00:09 2002

FZK/IRS Ch. Homann sr32.i036i.x

Fig.91-QUE06.doc
11.12.03 – IMF

Fig. 91: QUENCH-06; Comparison of measured and calculated temperature developments at various axial levels in bundle and argon cooling

QUENCH-06 q06s01/q06r05



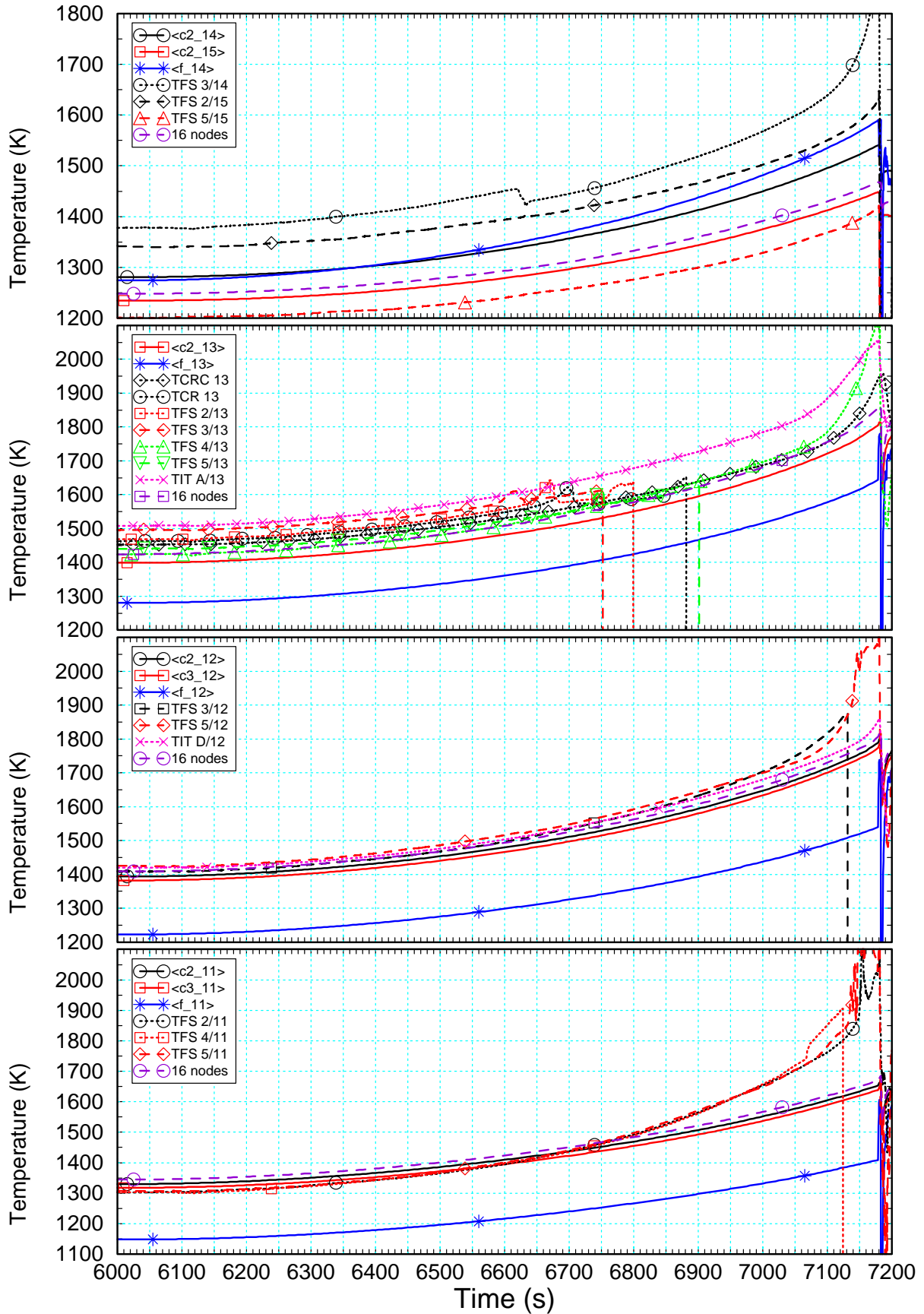
Wed Apr 24 09:17:18 2002

FZK/IRS Ch. Homann sr32.I036i.x

Fig.92-QUE06.doc
11.12.03 - IMF

Fig. 92: QUENCH-06; Power, calculated clad temperatures, and oxide layer thickness, comparison of measured and calculated hydrogen production rate and cumulated hydrogen mass

QUENCH-06 q06s01



Thu Apr 25 14:50:01 2002

FZK/IRS Ch. Homann sr32.i036i.x

Fig.93-QUE06.doc
11.12.03 - IMF

Fig. 93: QUENCH-06; Comparison of measured and calculated temperature developments in the hot zone of the bundle

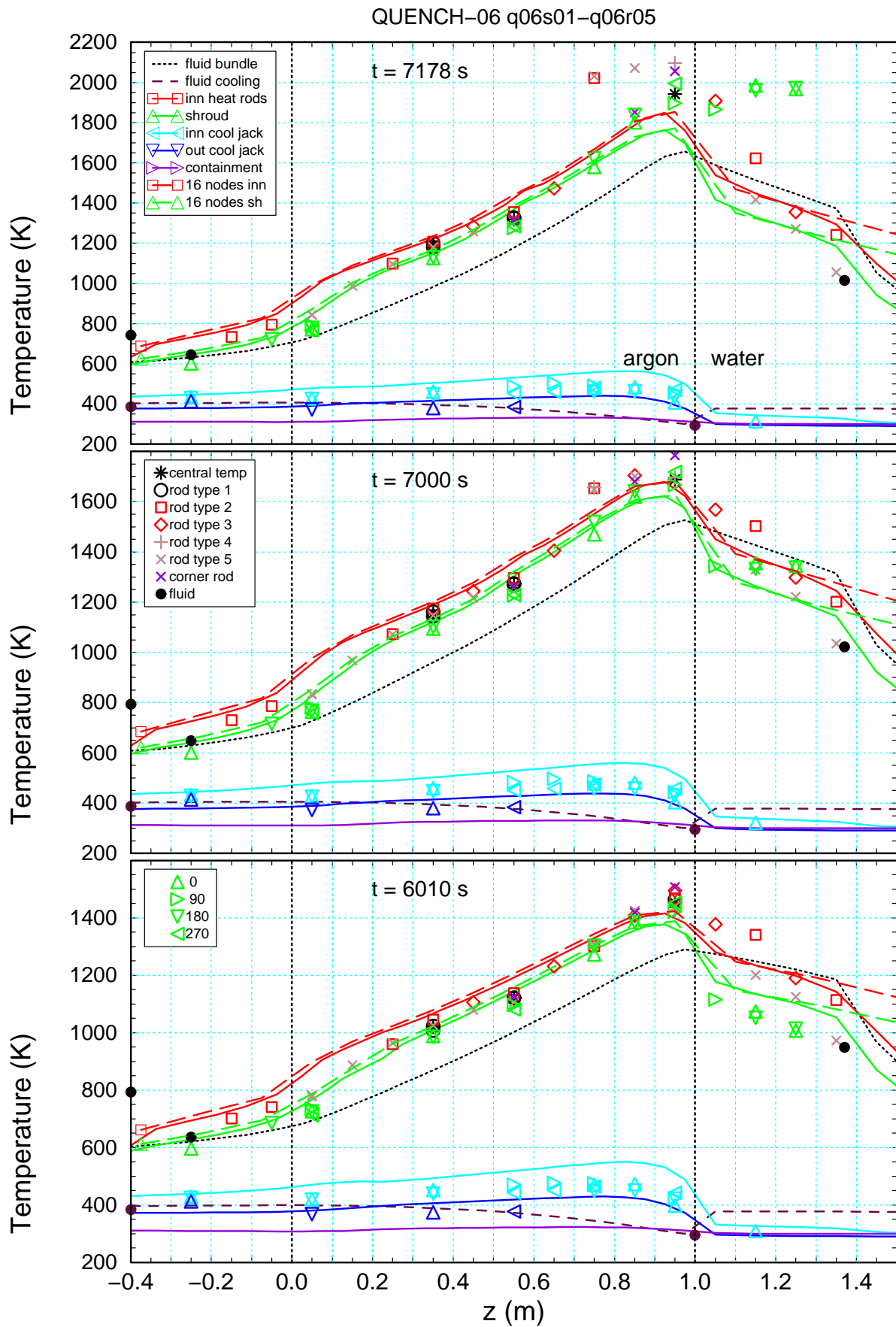
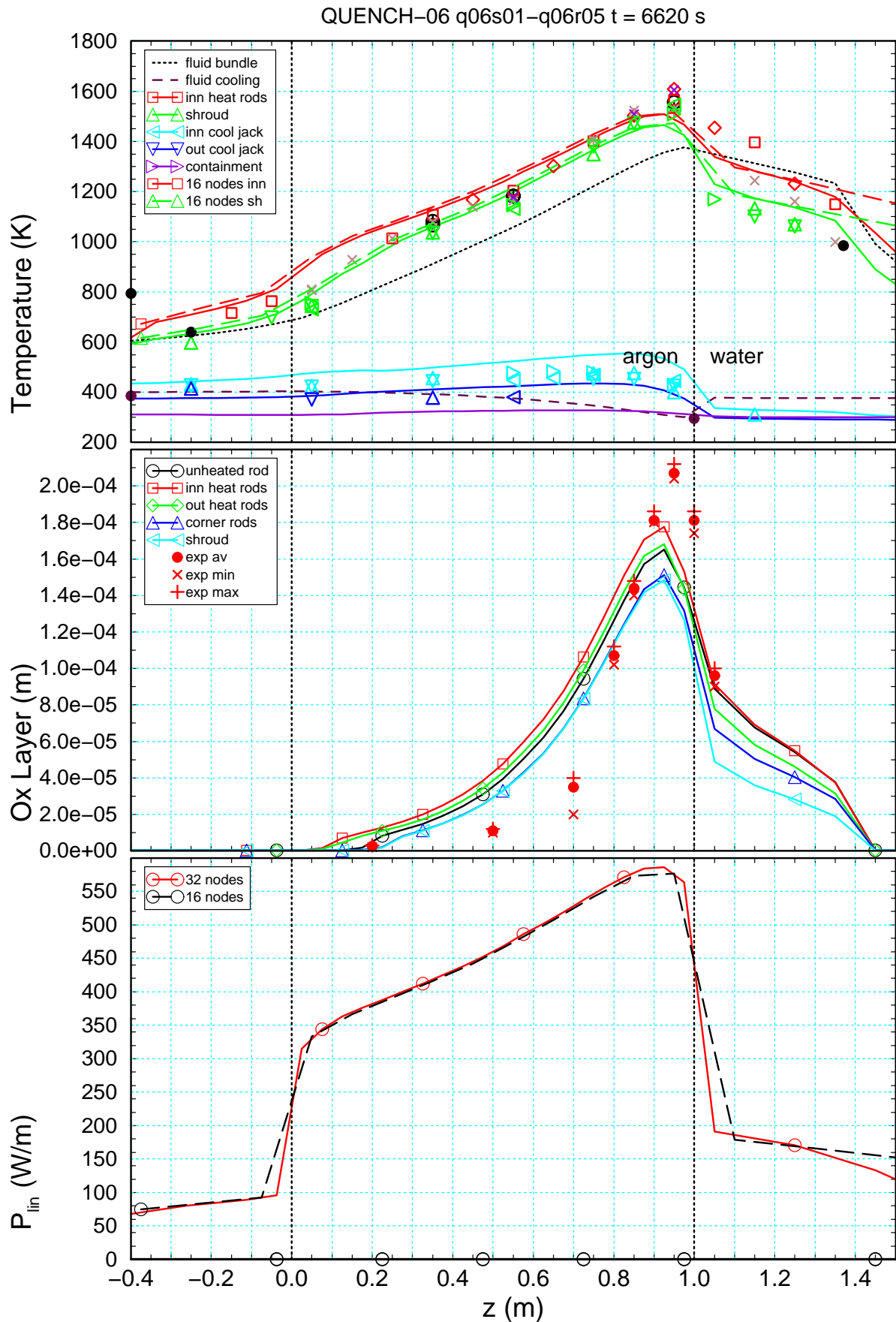


Fig. 94: QUENCH-06; Comparison of measured and calculated axial temperature profiles



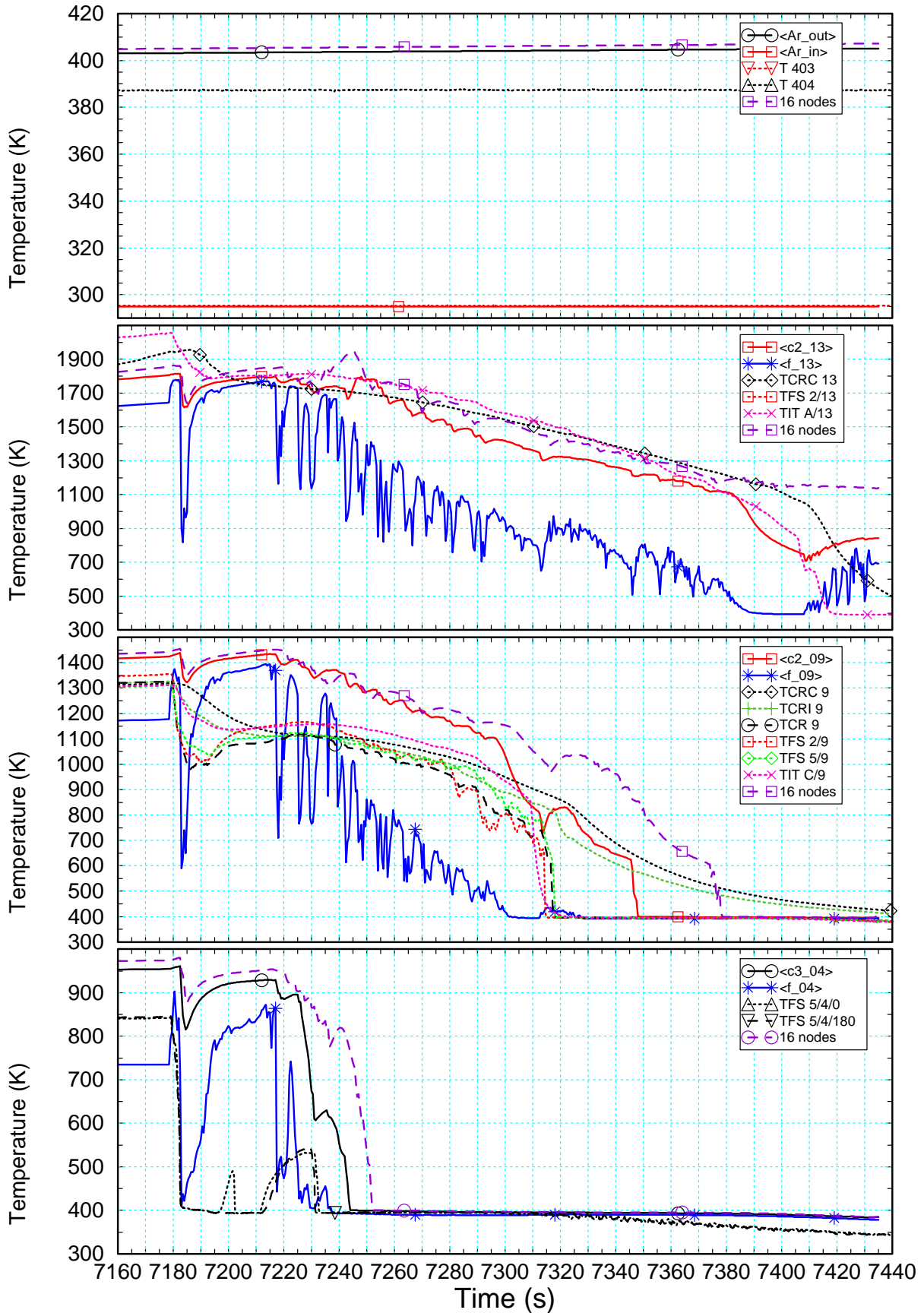
Thu Apr 25 13:19:18 2002

FZK/IRS Ch. Homann sr32.i036i.x

Fig.95-QUE06.doc
11.12.03 - IMF

Fig. 95: QUENCH-06; Comparison of measured and calculated axial temperature and oxide layer thickness profiles and calculated linear pin power profile

QUENCH-06 q06s01



Thu Apr 25 10:57:52 2002

FZK/IRS Ch. Homann sr32.i036i.x

Fig.96-QUE06.doc
11.12.03 - IMF

Fig. 96: QUENCH-06; Comparison of measured and calculated temperature developments at various axial levels in bundle and argon cooling during the quench phase

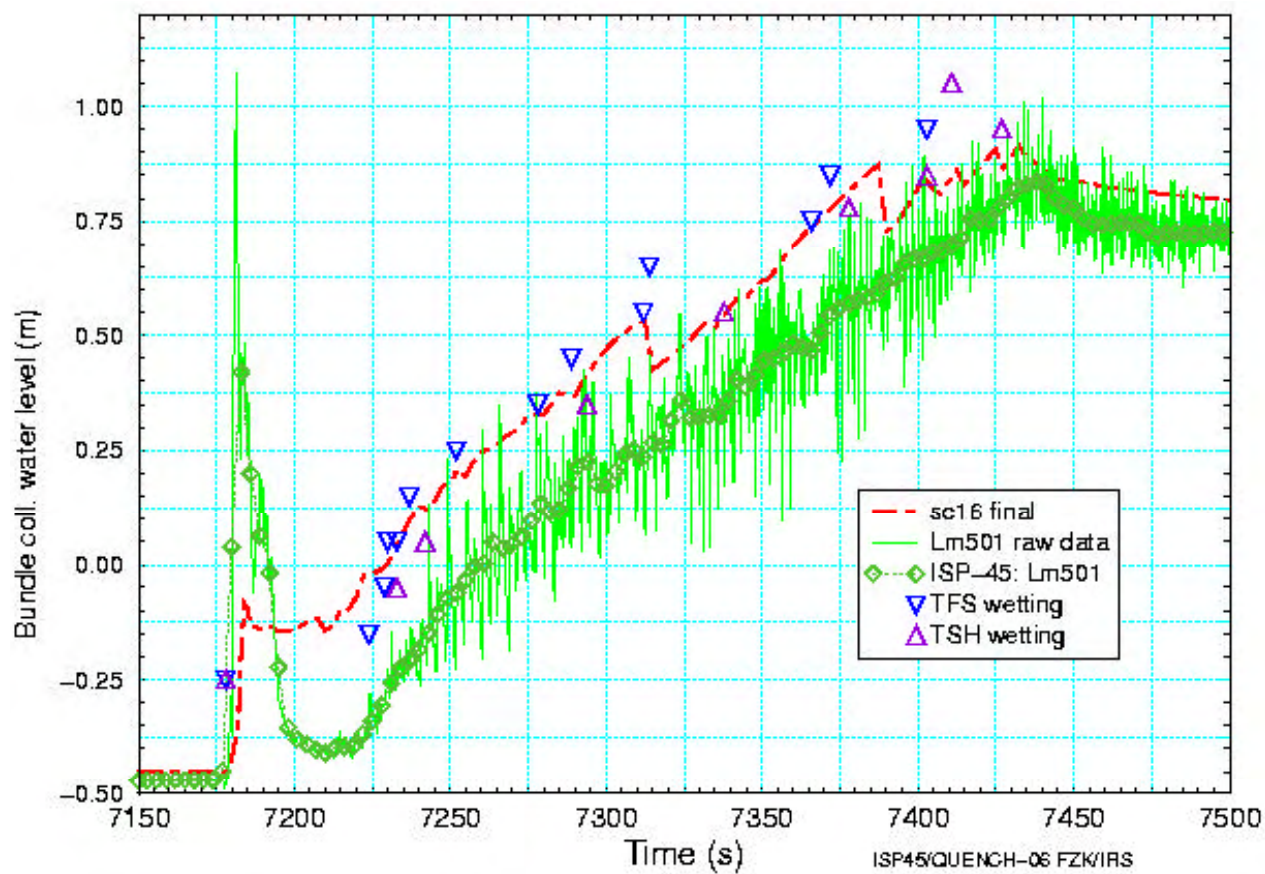


Fig.97-QUE06.doc
11.12.03 – IMF

Fig. 97: QUENCH-06; Water level increase from experimental data and thermocouple readings compared with S/R5irs calculation

Appendix

Appendix

Steam measurements by MS

For test QUENCH-06 the mass spectrometer (MS) was calibrated for steam for the first time with help of an external steam source. For the tests QUENCH-02 through -05 the MS was calibrated by using the 3 g/s Ar plus 3 g/s steam mixture from the facility during the thermal equilibration phase at about 873 K.

Pre-tests recently performed with a dummy bundle showed that a part of the steam may condense in the water and gas cooled off-gas pipe depending on the steam flow rate and the temperature T 601 which is located next to the head of the MS sampling line. The ratio of the steam measured by MS to injected steam mass flow increases with rising steam flow which causes additionally an increase of the temperature in the off-gas pipe, as can be seen in [Table A-1](#).

Table A-1: Dependence of MS steam flow measurement on the injected steam flow rate and temperature at the sampling position.

Injected steam flow rate, g/s	Temp. T 601, °C	Measured steam flow rate, g/s	Ratio measured to injected steam flow rate
3	ca. 140	1.59	0.53
5	ca. 160	4.12	0.82
8	185	6.69	0.84
10	192	9.45	0.95
8	185	7.77	0.97
5	173	4.68	0.94
3	144	1.99	0.66

The conclusion of these new findings is: In earlier tests, the calibration of the MS was wrong. Nevertheless, the steam flow rate measured by MS during the first phases of the experiments with 3 g/s is acceptable because the conditions between the erroneous calibration and measurement did not change significantly. The apparent slight increase of the steam measurement during the transient phase (before quenching) is caused by an increase of the temperature T 601. The steam measurement during the quench phase is overestimated by a factor of about 1.8 as can be concluded from the steam tests QUENCH-04 and QUENCH-05. Originally it was thought, that the accuracy of the MS under these extreme conditions with ca. 98 % steam and only about 1 % Ar (which is the reference gas!) is limited and a relatively high inaccuracy has to be accepted.

For test QUENCH-06 we have the reverse situation: Here, the (external) calibration was correct, therefore the MS measurement underestimates the steam concentration during the

pre-phases with 3 g/s steam (where partial condensation of steam in the off-gas pipe may occur), but the data for the quench phase should be reliable.